

SIMULATION OF HIGH SPEED FLOWS

BY

NADIA KIANVASHRAD

A dissertation submitted to the

School of Graduate Studies

Rutgers, The State University of New Jersey

In partial fulfillment of the requirements

For the degree of

Doctor of Philosophy

Graduate Program in Mechanical and Aerospace Engineering

Written under the direction of

Professor Doyle D. Knight

And approved by

New Brunswick, New Jersey

May, 2020

© 2020

NADIA KIANVASHRAD

ALL RIGHTS RESERVED

ABSTRACT OF THE DISSERTATION

Simulation of High Speed Flows

By NADIA KIANVASHRAD

Dissertation Director:

Professor Doyle D. Knight

There is a reinterest in hypersonic flow. There are several programs all around the world to produce hypersonic aircraft. Computational fluid dynamics (CFD) is an essential tool for high speed aerodynamics. However, it is still under investigation that how reliable is this tool especially at high stagnation enthalpies at high speed flows where non-equilibrium effects are important. For assessment of the CFD capability in the prediction of the aerothermodynamic loading (surface pressure and surface heat transfer) on a hypersonic vehicle, three sample experiments are examined in this dissertation. The models include a hollow cylinder flare, a double cone, and a hemisphere at Mach number range of 10.9 to 14.6. The laminar shock wave boundary layer interaction is investigated at high enthalpy ranges of 9.65 to 21.85 MJ/kg. It is shown that the formation of a supersonic jet as a result of the interaction of the shock waves prevented the highly dissociated gas to reach to the surface and thus the thermally perfect gas model has the best prediction of surface pressure and heat transfer. For hollow cylinder flare, the shock wave boundary layer interaction is weak and therefore, the effect of non-equilibrium modeling is negligible.

The Edney III type shock-shock interaction is studied over a hemisphere at low enthalpy of 2.1 MJ/kg. Edney III interaction can create a region of high pressure and heat transfer over the surface. Therefore, accurate prediction of this phenomenon is essential. The

study in this dissertation shows that the interaction is very sensitive to the location of the interaction of the impinging shock and the bow shock. This can change even the flow regime from laminar to turbulent.

Another challenge facing scientists in producing a hypersonic vehicle is how to rapidly maneuver the vehicle. The common controlling methods are too slow and during their actuation time, the vehicle moves several times its length. One option is to use energy discharge to change the flow structure around the body. This changes the pressure distribution over the body which can create pitching moments for steering the vehicle. Drag reduction is also another benefit that can achieve from energy deposition. If the energy discharge is on the axis of symmetry of the body, only drag reduction is acquired; however, off axis energy discharge provides drag reduction, side force and thus pitching moment. This dissertation has shown that the drag reduction and pitching moment depend on the amount of energy deposited, the location of the discharge, and the shape of the body.

Acknowledgements

My Ph.D. study at Rutgers University is a journey with ups and downs. I was lucky to have lots of good people around me to help me on this path. First, I want to sincerely thank my advisor Professor Doyle Knight who guided me through this way. He helped me not only with my studies but also by adjusting to the American culture. His belief in my ability makes it impossible for me to give up any research. You are the best advisor ever. I will be forever indebted to you.

I am heartfully thankful to my parents who always give me the freedom to choose the ways that I like and guide me toward success. They sacrifice a lot for me. They even give up having the chance of visiting me for several years so I can have the best education possible. How hard can be for parents to not be able to visit their child? I appreciate your sacrifice and will be forever grateful for what you are doing for me.

I'm speechless how I can show my appreciation to my husband (Moji) who quit his job and came to the U.S. and stay by my side so I can follow my dreams. You never give up your hope on me and always see a bright future for me and motivate me to move forward. I'm so lucky to have you by my side.

I want also to thank my sisters, Erfaneh, Niloofar, and Nooshin. Our phone-based communication keeps my spirit high. Talking with my niece, Rosha, on the phone makes life more enjoyable. I'm so happy that I can talk with you so frequently despite the large time gap. You are the best.

I want to thank Dr. Michael Holden (RIP) (and other researchers from CUBRC), Dr. Steve Wilkinson (and other researchers from NASA), and Professor DeMauro for working with me and providing their experimental data to me. Without your data and your collaboration, my Ph.D. study has not been possible.

I want to thank my friends, Elaheh Taghaddos, Shahrzad, and Elaheh Ardalani, who

always be with me, have time for me, and help me.

I want to mention a special thanks to Pat. Her kindness to my family makes life in the U.S. much easier. She is like a family member to us. Thank you so much, Pat, for your acceptance and kindness.

Dedication

To my parents

To my husband

To my sisters

Without them, I would not be here.

Table of Contents

Abstract	ii
Acknowledgements	iv
Dedication	vi
List of Tables	xii
List of Figures	xiv
1. Introduction	4
1.1. Shock-Shock and Shock Boundary Layer Interaction in Hypersonic Flows	7
1.2. Energy Deposition for Flight Control	16
2. Governing Equations	22
2.1. Introduction	22
2.2. Non-Equilibrium Laminar Navier-Stokes Equations	23
2.2.1. Conservation of Mass	23
2.2.2. Conservation of Momentum	24
2.2.3. Conservation of Total Energy	25
2.2.4. Conservation of Vibrational Energy	26
2.2.5. Equation of State	27
2.2.6. Thermodynamic Data and Transport Properties	27
2.2.7. Thermochemistry Model	27
2.3. Special Cases	27
2.3.1. Calorically Perfect	28
2.3.2. Thermally Perfect	28
2.3.3. Non-reactive	28

2.4. Boundary Conditions	29
2.5. Conclusion	29
3. Numerical Algorithm	31
3.1. Introduction	31
3.2. Finite Volume Method	32
3.3. Inviscid Flux Methods	38
3.3.1. Advection Upstream Splitting Method (AUSM)	39
3.3.2. Roe's Method	41
3.3.3. Roe Flux for Non-Equilibrium Equations	45
3.3.4. Van Leer's Method	50
3.4. Reconstruction	52
3.4.1. First Order	52
3.4.2. MUSCLp	53
3.4.3. Min-Mod	57
3.5. Viscous Fluxes	57
3.6. Time Integration	58
3.6.1. DPLR	58
3.6.2. Dual Time Stepping	63
3.6.3. Line Gauss-Seidel	64
3.6.4. Runge-Kutta	65
3.7. Boundary Condition	65
3.7.1. Axisymmetric	66
3.7.2. Fixed	66
3.7.3. No-slip Adiabatic	66
3.7.4. No-slip Isothermal	67
3.7.5. Symmetry	67
3.7.6. Zero-gradient	68
3.8. Message Passing Interface (MPI)	68

3.9. Freestream Conditions	69
3.10. Conclusion	69
I Shock-Shock and Shock Wave Boundary Layer Interaction in Hypersonic Flow	70
4. Prediction of Aerothermodynamic Loading on a Hollow Cylinder Flare	71
4.1. Introduction	71
4.2. Description of Experiment	72
4.3. Methodology	73
4.3.1. Computational Domain	73
4.4. Results	75
4.4.1. Grid Study	75
4.4.2. Comparison with Experiments	77
Effect of Models	78
Effect of Vibrational Energies Boundary Condition at No-Slip Isothermal Wall	81
4.4.3. Analysis of Flow Structure	82
Effect of Calorically Perfect Gas vs. Thermally Perfect Gas Models	92
Effect of Translational-Vibrational Energy Transfer and Vibrational Energies Boundary Condition at No-Slip Isothermal Wall	93
Effect of Park I Thermochemistry Model	96
4.5. Conclusions	97
5. Prediction of Aerothermodynamic Loading on a Double Cone	104
5.1. Introduction	104
5.2. Description of Experiment	105
5.3. Methodology	105
5.3.1. Computational Domain	106
5.4. Results	107

5.4.1. Grid Convergence Study	107
5.4.2. Comparison of Models with Experiment	109
5.4.3. Analysis of Flow Structure	112
5.5. Conclusion	118
6. Prediction of Aerothermodynamic Loading on a Hemisphere Due to Ed-	
ney III Shock-Shock Interaction	127
6.1. Introduction	127
6.2. Description of Experiment	128
6.3. Methodology	129
6.3.1. Computational Domain	129
6.4. Results	130
6.4.1. Results of Case 1	131
Spectrum Analysis	133
6.4.2. Results of Case 2	134
Spectrum Analysis	135
Wavelet Analysis	138
6.4.3. Effect of Numerical Method	139
Effect of Inner Iteration	140
6.5. Conclusion	140
II Energy Deposition for Flight Control in High Speed Flows	146
7. Effect of a Laser Discharge Pulse on a Hemisphere Cylinder	147
7.1. Introduction	147
7.2. Description of Problem	148
7.3. Methodology	149
7.3.1. Computational Domain	149
7.4. Results	151
7.4.1. On Axis Laser Discharge	152

7.4.2. Off Axis Laser Discharge	161
7.5. Conclusion	163
8. Effect of a Laser Discharge Pulse on a Ogive Cylinder	166
8.1. Introduction	166
8.2. Description of Problem	166
8.3. Description of Experiment	169
8.4. Methodology	170
8.4.1. Computational Domain	170
8.5. Results	172
8.5.1. Grid Study	172
8.5.2. Effect of Energy Added to the Gas	174
8.5.3. Effect of the Location of Energy Deposition	175
8.5.4. Flow Structure	181
8.6. Conclusion	182
9. Conclusion	186
10.List of Publications	188
Appendix A. Appendix	191
A.1. Park I Model	191
References	193

List of Tables

2.1. Simplification in Governing Equation for Each Specific Case	29
3.1. ΔQ Values in MUSCL Method	56
3.2. Different MUSCL Methods	57
4.1. Flow conditions	72
4.2. Models Specifications	73
4.3. Grid Properties	74
4.4. Percentage of change between Grid 1 and Grid 2 for Run 2 (10.43 MJ/kg)	77
4.5. Percentage of change between Grid 2 and Grid 3 for Run 5 (21.85 MJ/kg)	78
4.6. Variation of specific heat	92
5.1. Flow conditions	106
5.2. Grid properties	106
5.3. Models specifications	107
6.1. Flow conditions	128
6.2. Experimental Location of Shock Generator Relative to Hemisphere Cylinder	129
6.3. Computational grid	129
6.4. Impinging shock location parameters	131
7.1. Freestream conditions	149
7.2. Heated region initial conditions	149
7.3. Heated region initial conditions	150
7.4. Computational grid (2.16 M cells)	150
7.5. Computational grid for three-dimensional calculation (6.84 M cells)	151
7.6. Gas dynamic energetic efficiency of on-axis laser discharge	161
8.1. Numerical freestream conditions	167
8.2. Ogive cylinder properties and dimensions	168

8.3. Laser discharge initial conditions for Ogive 1	168
8.4. Laser discharge initial conditions for Ogive 2	169
8.5. SWT operation parameters	169
8.6. Computational grid Properties for Ogive 1	171
8.7. Computational grid Properties (5.3 M cells)	172
A.1. Thermochemistry Model Reactions	192

List of Figures

1.1. Artistic impression of the SpaceLiner during ascend (Courtesy of DLR) . .	4
1.2. Artistic impression of the reentry of HTV-2 (Courtesy of DARPA)	5
1.3. SHEFEX II (Courtesy of DLR, CC-BY 3.0)	6
1.4. Artistic impression of X-51A Waverider (Courtesy of US. Air Force)	6
1.5. X-15 damaged pylon	8
1.6. Edney type III and IV interactions	9
1.7. Sample of simple geometries uses for study of shock wave boundary layer interaction	10
1.8. Energy discharge for flow control in hypersonic flight	17
3.1. Reconstruction of interior face of Cell i	53
4.1. Small hollow cylinder flare (dimensions in inches [mm])	72
4.2. Computational domain	74
4.3. Grid study for Run 2 (10.43 MJ/kg) for isothermal Park I model	76
4.4. Grid Study for Run 5 (21.85 MJ/kg) for isothermal Park I model	76
4.5. Grid Study for Run 4 (15.54 MJ/kg) for calorically perfect model	77
4.6. Comparison of different models with experiment for Run 2 (10.43 MJ/kg) .	79
4.7. Comparison of different models with experiment for Run 4 (15.54 MJ/kg) .	80
4.8. Comparison of different models with experiment for Run 5 (21.85 MJ/kg) .	81
4.9. Comparison of different vibrational boundary condition of the non-reactive model with experiment for Run 2 (10.43 MJ/kg)	82
4.10. Comparison of different vibrational boundary condition of the Park I model with experiment for Run 2 (10.43 MJ/kg)	83
4.11. Comparison of different vibrational boundary condition of the non-reactive model with experiment for Run 4 (15.54 MJ/kg)	84

4.12. Comparison of different vibrational boundary condition of the Park I model with experiment for Run 4 (15.54 MJ/kg)	84
4.13. Comparison of different vibrational boundary condition of the non-reactive model with experiment for Run 5 (21.85 MJ/kg)	85
4.14. Comparison of different vibrational boundary condition of the Park I model with experiment for Run 5 (21.85 MJ/kg)	85
4.15. Mach contours and flow structure of Run 2 (10.43 MJ/kg)	86
4.15. Mach contours and flow structure of Run 2 (10.43 MJ/kg)	87
4.16. Mach contours and flow structure of Run 4 (15.54 MJ/kg)	88
4.16. Mach contours and flow structure of Run 4 (15.54 MJ/kg)	89
4.17. Mach contours and flow structure of Run 5 (21.85 MJ/kg)	90
4.17. Mach contours and flow structure of Run 5 (21.85 MJ/kg)	91
4.18. Ratio of transport properties of thermally perfect model to the calorically perfect model of Run 2 (10.43 MJ/kg)	93
4.19. Ratio of transport properties of thermally perfect model to the calorically perfect model of Run 4 (15.54 MJ/kg)	93
4.20. Ratio of transport properties of thermally perfect model to the calorically perfect model of Run 5 (21.85 MJ/kg)	94
4.21. Ratio of vibrational energy to total energy of non-reactive model for Run 5 (21.85 MJ/kg)	95
4.22. Ratio of vibrational energy to total energy of Park I model for Run 5 (21.85 MJ/kg)	96
4.23. Vibrational temperature of N ₂ and O ₂ of non-reactive model for Run 5 (21.85 MJ/kg)	97
4.24. Vibrational temperature of N ₂ and O ₂ of Park I model for Run 5 (21.85 MJ/kg)	98
4.25. Relaxation time nondimensionalized by the time the freestream flow needs to pass the cylinder section of non-reactive model for Run 2 (10.43 MJ/kg)	99

4.26. Relaxation time nondimensionalized by the time the freestream flow needs to pass the cylinder section of non-reactive model for Run 4 (15.54 MJ/kg)	99
4.27. Relaxation time nondimensionalized by the time the freestream flow needs to pass the cylinder section of non-reactive model for Run 5 (21.85 MJ/kg)	100
4.28. Mass fraction of species of Park I model for Run 2 (10.43 MJ/kg)	100
4.29. Mass fraction of species of Park I model for Run 4 (15.54 MJ/kg)	101
4.30. Mass fraction of species of Park I model for Run 5 (21.85 MJ/kg)	102
4.31. Temperature contours of Park I model for Run 2 (10.43 MJ/kg)	102
4.32. Temperature contours of Park I model for Run 4 (15.54 MJ/kg)	103
4.33. Temperature contours of Park I model for Run 5 (21.85 MJ/kg)	103
5.1. Small 25°/55° double cone flare (dimensions in inches [mm] (courtesy of CUBRC)	105
5.2. Computational domain	107
5.3. Grid study for Run 2 (9.65 MJ/kg) for thermally perfect model	108
5.4. Grid study for Run 2 (9.65 MJ/kg) for non-reactive model	109
5.5. Grid study for Run 2 (9.65 MJ/kg) for Park I model	110
5.6. Grid study for Run 4 (21.77 MJ/kg) for thermally perfect model	111
5.7. Grid study for Run 4 (21.77 MJ/kg) for non-reactive model	112
5.8. Grid study for Run 4 (21.77 MJ/kg) for Park I model	113
5.9. Effect of different models on prediction of surface pressure and surface heat transfer for Run 2 (9.65 MJ/kg)	114
5.10. Effect of different models on prediction of surface pressure and surface heat transfer for Run 4 (21.77 MJ/kg)	115
5.11. Mach contours for thermally perfect, non-reactive, and Park I models for Run 2 (9.65 MJ/kg)	119
5.12. Pressure contours for thermally perfect, non-reactive, and Park I models for Run 2 (9.65 MJ/kg)	120
5.13. Mass fraction contours of NO, N, and O for Park I model for Run 2 (9.65 MJ/kg)	121

5.14. Logarithm of ratio of Landau-Teller relaxation and flow characteristic times contours for non-reactive and Park I models for Run 2 (9.65 MJ/kg)	122
5.15. Mach contours for thermally perfect, non-reactive, and Park I models for Run 4 (21.77 MJ/kg)	123
5.16. Pressure contours for thermally perfect, non-reactive, and Park I models for Run 4 (21.77 MJ/kg)	124
5.17. Mass fraction contours of NO, N, and O for Park I model for Run 4 (21.77 MJ/kg)	125
5.18. Logarithm of ratio of Landau-Teller relaxation and flow characteristic times contours for non-reactive and Park I models for Run 4 (21.77 MJ/kg) . . .	126
6.1. Schematic of hemisphere model in hypersonic shock tunnel [1]	128
6.2. Computational domain	130
6.3. Definition of offset location variable used for specifying the location of the impinging shock	131
6.4. Mach contours in the symmetry plane for Case 1	132
6.5. Pressure and temperature contours in the symmetry plane for Case 1	133
6.6. Dimensionless surface pressure and heat transfer <i>vs.</i> time for point P in the interaction region for Case 1	134
6.7. 3-D pressure coefficient and dimensionless heat transfer on hemisphere sur- face for Case 1	135
6.8. Comparison of Surface Pressure Coefficient and Dimensionless Heat Transfer on Plane of Symmetry of Hemisphere with Experimental Data for Case 1 .	136
6.9. Fast Fourier Analysis of surface heat transfer <i>vs.</i> time for point P in the interaction region (Case 1)	137
6.10. Mach contours in the symmetry plane for adjusted oblique shock location (Case 2)	138
6.11. Pressure and temperature contours in the symmetry plane for adjusted oblique shock location (Case 2)	139
6.12. Dimensionless surface pressure and heat transfer <i>vs.</i> time for point P in the interaction region for adjusted oblique shock location	140

6.13. 3-D pressure coefficient and dimensionless heat transfer on hemisphere surface for adjusted oblique shock location (Case 2)	141
6.14. Comparison of Surface Pressure Coefficient and Dimensionless Heat Transfer on Plane of Symmetry of Hemisphere with Experimental Data for adjusted oblique shock location (Case 2)	141
6.15. Fast Fourier Analysis of surface heat transfer <i>vs.</i> time for point P in the interaction region for adjusted oblique shock location (Case 2). The two arrows correspond to $f_{\text{flowfield}}$ and $f_{\text{dissipation}}$	142
6.16. Sample signals and the real parts of their Morse wavelet transform scalograms	143
6.17. Continuous wavelet transform scalogram of the dimensionless surface heat transfer profile given in Figure 6.12(b)	144
6.18. The effect of number of inner iteration on the dimensionless surface pressure and heat transfer <i>vs.</i> time for point P in the interaction region for adjusted oblique shock location (Case 2)	145
7.1. Hemisphere cylinder model	148
7.2. Computational domain	150
7.3. Computational domain for three-dimensional calculation	151
7.4. Contour plots of Mach number and vibrational temperature of N_2 for $\Delta E = 50$ mJ	153
7.5. Contour plots of Mach number and vibrational temperature of N_2 for $\Delta E = 50$ mJ	154
7.6. Numerical schlieren and contour plots of dimensionless pressure for $\Delta E = 50$ mJ	155
7.7. Numerical schlieren and contour plots of dimensionless pressure for $\Delta E = 50$ mJ	156
7.8. Contour plots of Mach number and vibrational temperature of N_2 for three models for $\Delta E = 50$ mJ	157
7.9. Schlieren images and contour plots of dimensionless pressure for three models for $\Delta E = 50$ mJ	158

7.10. Dimensionless pressure force change versus time	160
7.11. Contour plots of Mach number and vibrational temperature of N_2 for off-axis laser discharge	164
7.12. Dimensionless force change versus time for off-axis laser discharge	165
8.1. Schematic of off-axis laser discharge in front of an ogive cylinder	167
8.2. Schematic of ogive-cylinder geometry	167
8.3. Ogive cylinder test article	169
8.4. Computational domain for Ogive 1	170
8.5. Computational domain for Ogive 2	171
8.6. Drag force, side force, and pitching moment coefficients versus time for dif- ferent grids	173
8.7. Drag force, side force, and pitching moment coefficients versus time for dif- ferent energy absorbed by the gas	175
8.8. Pressure for Case 1 ($\epsilon = 82.20$) at $\tau = 1.0$	176
8.9. Pressure for Case 2 ($\epsilon = 163.42$) at $\tau = 1.0$	177
8.10. Pressure for Case 3 ($\epsilon = 328.08$, $z_d/D = 0.25$) at $\tau = 1.0$	178
8.11. Drag force, side force, and pitching moment coefficients versus time for dif- ferent laser discharge location	179
8.12. Pressure for Case 4 ($z_d/D = 0.5$) at $\tau = 1.5$	180
8.13. Pressure for Case 5 ($z_d/D = 0.75$) at $\tau = 2.0$	181
8.14. Drag force and side force coefficients change versus time for different laser discharge locations	182
8.15. Contour plots of Mach number in comparison with shadowgraph images . .	184
8.16. Contour plots of Mach number in comparison with shadowgraph images . .	185

Nomenclature

$A_{\alpha\beta}$	=	variable in Landau-Teller model
$B_{\alpha\beta}$	=	variable in Landau-Teller model
$c_{p\alpha}$	=	specific heat at constant pressure of species α
c_{p_f}	=	mixture specific heat at constant pressure
$c_{v\alpha}$	=	specific heat at constant volume of species α
D	=	diffusivity
e	=	internal energy per unit mass
e_α	=	internal energy per unit mass of species α
e_α^{eq}	=	equilibrium internal energy
e_α^{vib}	=	non-equilibrium internal energy per unit mass of species α due to vibrational excitation
$\dot{e}_\alpha^{\text{vib}}$	=	translational-vibrational energy transfer per unit mass of species α
$e_\alpha^{\text{vib}*}$	=	equilibrium vibrational energy per unit mass of species α
h_α	=	static enthalpy per unit mass of species α
h_f^o	=	enthalpy of formation per unit mass
J	=	number of reactions
k	=	mixture thermal conductivity
k_α	=	thermal conductivity of species α
$k_{e,j}$	=	equilibrium rate of the j^{th} reaction
$k_{f,j}$	=	forward reaction rate of the j^{th} reaction
k_α^{vib}	=	vibrational heat transfer coefficient of species α
Le	=	Lewis number
m	=	number of diatomic species in the gas mixture
M	=	molar concentration
\mathcal{M}	=	molecular weight
n	=	number of gas species in the mixture of gases
p	=	static pressure
q	=	heat transfer vector
$q_{\alpha j}^{\text{vib}}$	=	vibrational heat transfer vector of species α

\mathcal{R}	=	Universal Gas Constant
R_α	=	gas constant for species α
t	=	time
T	=	static temperature
T_α^{vib}	=	vibrational temperature
T_{ref}	=	reference temperature
u	=	mass-averaged velocity
x	=	position
Y	=	mass fraction
δ_{ij}	=	delta function
ε	=	total energy per unit mass
$\Theta_\alpha^{\text{vib}}$	=	characteristic vibrational temperature of species α
μ	=	mixture molecular viscosity
μ_α	=	molecular viscosity of species α
$\nu'_{\alpha,j}$	=	stoichiometric coefficients of the reactants of species X_α in the j^{th} reaction
$\nu''_{\alpha,j}$	=	stoichiometric coefficients of the products of species X_α in the j^{th} reaction
ρ	=	mixture density
ρ_α	=	density of species α
$\dot{\omega}_\alpha^{\text{spe}}$	=	rate of production of species α
$\dot{\omega}_\alpha^{\text{vib}}$	=	Source term in conservation of vibrational energy
τ_{ij}	=	laminar viscous stress tensor
τ_α	=	relaxation time of species α
$\tau_{\alpha\beta}$	=	characteristic relaxation time of species α resulting from collisions with species β

subscripts

i	=	x, y , or z directions
j	=	x, y , or z directions
k	=	x, y , or z directions
w	=	wall
α	=	indicator of species α
β	=	indicator of species β

superscripts

vib = vibrational

Chapter 1

Introduction

There is a recent reinterest in hypersonic flows due to the interest in developing hypersonic vehicles. Several programs are introduced all around the world with the goal of developing a commercial hypersonic aircraft or a passenger spacecraft.

The German Aerospace Center (Deutsches Zentrum für Luft-und Raumfahrt or DLR) is working on a hypersonic passenger transport named SpaceLiner since 2005 intended to cruise at Mach 9.0 or 20.0 depending on the version of the vehicle, in the suborbital altitudes [2]. The SpaceLiner is intended to fly from Europe to Australia in 90 minutes with 50 passengers and two crews [3]. The artistic impression of this aircraft is shown in Figure 1.1.



Figure 1.1: Artistic impression of the SpaceLiner during ascend (Courtesy of DLR)

The “Reaction Engines Limited LAPCAT Configuration A2” called the “LAPCAT A2” is a design study program by the British aerospace engineering. The purpose of this program is to produce a commercial transport aircraft with a maximum Mach number of about 5.0 for about 300 passengers [4]. The LAPCAT A2 would be able to travel from Brussels to Sydney in about 4.6 hours. The “Zero Emission HyperSonic Transport” (ZEHST) introduced by European Aeronautics Defense and Space Company (EADS) in June 2010 is intended to fly Tokyo to Los Angeles or Tokyo to London in less than 2.5 hours at a Mach number greater

than 4.0 [5].

The “High-speed EXperimentntAl FLY Vehicles” (HEXAFLY) [6] and “HEXAFLY-INTernational” (HEXAFLY-INT) [7, 8] experimental flight test vehicles at Mach 7.4 with the goal of approaching toward a high speed civil transportation vehicle. This project moves toward enabling transportation from Brussels to Tokyo in less than two hours and 15 minutes and from Brussels to Sydney in less than three hours.

There are other programs with other missions than passenger transportation. FALCON “Hypersonic Technology Vehicle 2” (HTV-2) flew at up to Mach 20.0 in 2010 and 2011 [9, 10]. From the first flight in 2010, the aerodynamics and performance data was achieved and from the test flight in 2011, the structural and high temperature data was captured. This hypersonic gliding vehicle is shown in Figure 1.2.



Figure 1.2: Artistic impression of the reentry of HTV-2 (Courtesy of DARPA)

The “SHarp Edge Flight Experiment” (SHEFEX) at the DLR is under development since 2005. It is designed to fly at Mach number span of 6.0 to 17.0 [11, 12]. The second design of this program named SHEFEX II is shown in Figure 1.3.

The “Scramjet Powered Accelerator for Reusable Technology Advancement” (SPARTAN) at the University of Queensland will fly at about Mach 10.0 [13]. There were some test flights for different stages of this vehicle. The Chinese DF-ZF Hypersonic Glide Vehicle (HGV) flight tested since 2014 at Mach numbers ranging between 5.0-10.0 [14] and became operational from 2019. The “Hypersonic International Flight Research Experimentation” (HIFiRE) program of the Australian Department of Defense together with the United States Air Force Flight Dynamics Laboratory has test flights from 2009 with the Mach numbers



Figure 1.3: SHEFEX II (Courtesy of DLR, CC-BY 3.0)

ranges from 6.0 to 8.0 [15, 16]. Indian “Advanced Technology Vehicle” (ATV) is a sounding rocket developed for testing a dual-mode air breathing scramjet. It had two successful tests in 2010 and 2016 in which Mach 6.0 flight is achieved. The British Skylon spacecraft is designed to fly at Mach number 5.2. The expected first flight of this spacecraft is 2025 [17]. The Boeing X-51 Waverider is a scramjet experimental aircraft designed for flight at Mach 5.0. Its test flight started in 2010 [18]. In 2013, this vehicle flew for about 210 seconds at Mach number over 5.0. The “Force Application and Launch from CONTinental United States” (FALCON) project [9] of the United States Defense Advanced Research Projects Agency (DARPA) is in progress since 2003. These are some examples of ongoing projects around the world.

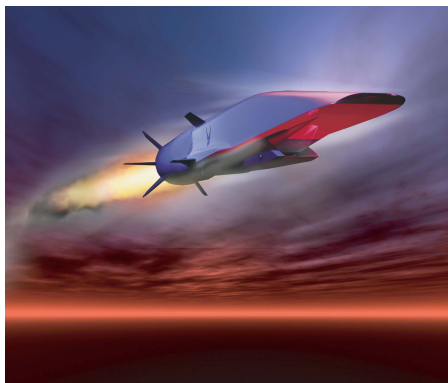


Figure 1.4: Artistic impression of X-51A Waverider (Courtesy of US. Air Force)

Computational fluid dynamics (CFD) became an inseparable part and an important tool for high speed flow aerodynamics at the beginning of the 1970s. One of the first examples of using CFD for simulation of high speed flows is the Robert MacCormack simulation of shock

wave laminar boundary layer interaction in 1971 [19]. He solved the two dimensional Navier-Stokes equations for Mach 2.0 flow. In 1986, Joe Shang performed a full Navier-Stokes simulation of a three dimensional X-24C hypersonic research vehicle at Mach 5.95 [20].

Through time, it is seen that there are more and more computational studies in high speed aerodynamics. The development of new algorithms with higher accuracy is one of the reasons that help this transition. For example, Roe's flux method is introduced in 1981, AUSM in 1991, and Van Leer method in 1997. The enormous advances in computer technology have a big effect on increasing the role of CFD in high speed aerodynamics. The creation of faster processes and the ability to use clusters of hundreds and thousands of processes enables researchers to simulate the phenomena not possible before. The programming software also improves during the years to enhance the experience and abilities of researchers in numerically finding solutions for problems that are very expensive to do by other means such as experiments.

In this Ph.D. dissertation, we choose advance CFD methods in two different areas of high speed aerodynamics: first, shock-shock and shock wave boundary layer interactions and second, energy deposition for flight and flow control.

1.1 Shock-Shock and Shock Boundary Layer Interaction in Hypersonic Flows

The surface pressure and heat transfer also called as aerothermodynamic loads on a hypersonic vehicle is strongly influenced by shock-shock and shock wave boundary layer interaction. There are two examples here to better illustrate this. The space shuttle flight STS-1 had been designed to maintained the body flap angle of 8° to 9° during the reentry to maintain the pitch control. However, in its flight, the trim angle extended to 14° . The postflight analysis of the longitudinal trim characteristics showed that the CFD prediction of the pitch trim were in error due to the wrong prediction of surface pressure distribution on the space shuttle at hypersonic speed. The wrong prediction was a result of not considering the effect of shock wave boundary layer interaction generated by the deployment of the body flap [21, 22]. The pylon of the flight 2-53-97 of the X-15 which was mounted under

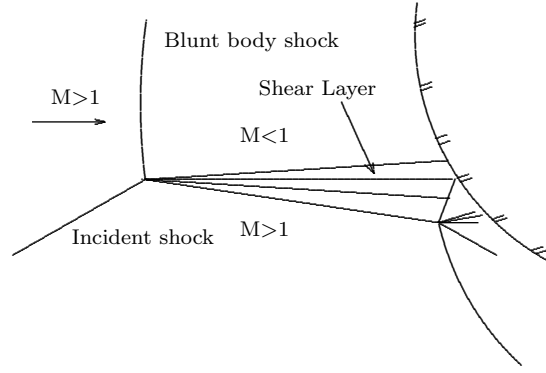
the fuselage was disintegrated. Figure 1.5 shows the damaged pylon of this flight. This material failure was attributed to a shock-shock interaction generating a supersonic jet. This supersonic jet impinged on the pylon surface and resulted in excessive heat transfer and material failure [23]. Later, this kind of interaction was named as Edney IV shock-shock interaction.



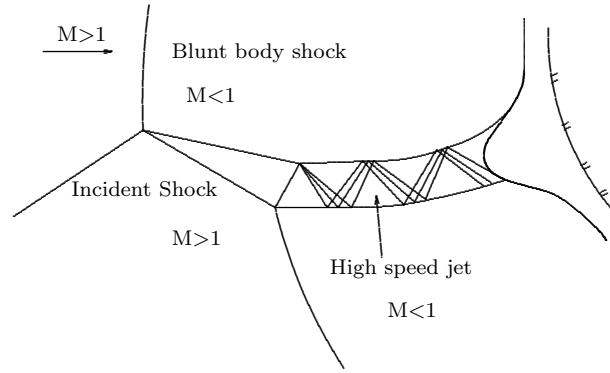
Figure 1.5: X-15 damaged pylon

Edney [24] was the first to categorize the shock-shock interaction. He divided shock-shock interaction into six groups. Among these six groups, Edney III and Edney IV types have the strongest interaction with a region of high surface pressure and high heat transfer. Figure 1.6 shows the schematics of these two interaction types. In the Edney III type, the interaction of the oblique shock and the bow shock creates a shear layer that interacts with the boundary layer, increases the pressure and heat transfer on the surface. In the Edney IV interaction type, the interaction of shocks creates a supersonic jet with many shock waves and expansion waves inside the jet. This jet impinges on the wall surface and creates a region of high pressure and heat transfer.

The need to understand and accurately predict this phenomena has motivated a significant number of research studies both experimentally and numerically in this area over the past 80 years. One of the first researches is the paper published by Liepmann in 1946 [25]. Later on, in 1968, Edney categorized the shock-shock interactions for hypersonic speeds [24]. The focus of the study of shock-shock and shock wave boundary layer interactions at hypersonic speed has been more intense since non-equilibrium effect may be important and thus complicates the problem. The state of the art of the works on this topic is presented



(a) Type III interaction

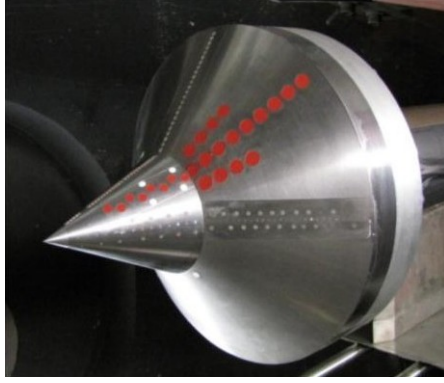


(b) Type IV interaction

Figure 1.6: Edney type III and IV interactions

in Babinsky and Harvey [26]. The majority of the research have focused on simplified geometries (*e.g.*, double cone, double wedge, hollow cylinder flare, cylinder, and hemisphere) to isolate this phenomena and study it without interference of other effect. Examples of these simple geometries are shown in Figure 1.7.

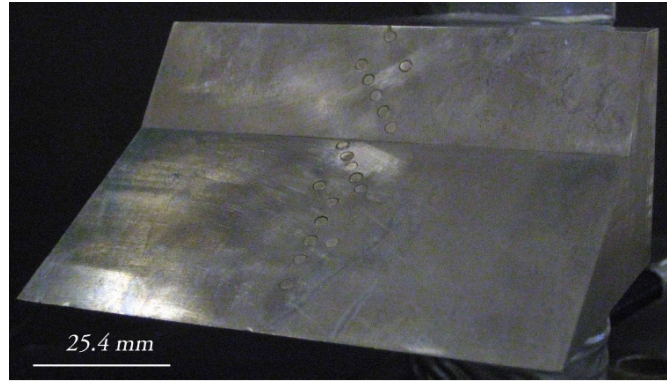
The study of hypersonic shock wave boundary layer interaction may be divided into three main categories from a fluid dynamic viewpoint, 1) purely laminar, 2) transitional in which the transition of the boundary layer from laminar to turbulent occurs ahead of or within the shock boundary layer interaction, and 3) fully turbulent. The fully laminar studies enable researchers to isolate the real gas effects (*i.e.*, dissociation, ionization, vibrational excitation, energy transfer between rotational, vibrational, and translational phases, surface catalycity, etc.) of high enthalpy flows from the other modeling challenges associated with boundary



(a) Double cone (Courtesy of CUBRC)



(b) Hollow cylinder flare (Courtesy of CUBRC)



(c) Double wedge [27]

Figure 1.7: Sample of simple geometries uses for study of shock wave boundary layer interaction

layer transition or turbulence.

The focus of the first part of this dissertation is hypersonic shock-shock and shock wave *laminar* boundary layer interaction at low to high enthalpies to study the capability of the available CFD modeling for accurate prediction of these phenomena. A substantial number of studies have examined the capability of CFD modeling for these interactions, especially in the past twenty years. A selection of these studies is presented here.

Grasso and Marini [28] performed perfect gas Navier-Stokes simulations of several nominally two dimensional compression corners at Mach 14.1 and stagnation enthalpy of 3.6 MJ/kg. A close agreement is achieved by comparison of their results with experimental [29] surface pressure, skin friction, and Stanton number (which is a dimensionless heat transfer).

Chanetz *et al.* [30, 31] conducted perfect gas Navier-Stokes and Direct Simulation Monte Carlo (DSMC) simulations of a 30° hollow cylinder flare at Mach 9.9 and a stagnation

enthalpy of 1.0 MJ/kg. The comparison of the numerical results showed a good agreement with their own experiment.

Olejniczak *et al.* [32] performed Navier-Stokes simulations of a double wedge in nitrogen at Mach numbers of 5.6 to 7.3 and stagnation enthalpies from 23.9 to 28.7 MJ/kg. In their simulations, they included separate equations for conservation of mass of N_2 and N and vibrational energy of N_2 . They incorporated two Park [33, 34] and the Bortner [35] thermochemistry models in their simulations. They also conducted experimental measurements of surface heat transfer. The comparison of their numerical and experimental results showed a smaller separation region for the simulations, although the predicted heat transfer in the separation region was in agreement with the experiment. Possible reasons for this discrepancy include the uncertainty in the dissociation rates (*i.e.*, thermochemistry model), the non-Boltzman distribution of the vibrational energy in the inflow, and the non-continuum effect in the interaction region (*i.e.*, Navier-Stokes equations are not valid).

Wright *et al.* [36] conducted perfect gas Navier-Stokes simulations for $25^\circ/35^\circ$ and $25^\circ/50^\circ$ double cones in the air at freestream Mach 8 and stagnation enthalpy of 0.8 MJ/kg. Comparison of the computed surface heat transfer and the experiment was in close agreement.

Marini [37] performed an extensive perfect gas Navier-Stokes study of a two dimensional compression ramp at Mach 6 to 14.1 and stagnation enthalpies from 1.0 to 3.6 MJ/kg. The comparison of the computational results of surface heat transfer, surface pressure, and skin friction with experimental data [29, 38, 39] showed good agreement. Marini also performed a three dimensional simulation to examine the effect of the finite spanwise width of the experimental compression ramp.

A blind validation study of hypersonic shock wave laminar boundary layer interaction for a 30° hollow cylinder flare and $25^\circ/55^\circ$ double cone was conducted at the AIAA 39th Aerospace Sciences Meeting [40, 41]. The experiments were performed in the 48 inch shock tunnel and LENS I tunnel at the Calspan University of Buffalo Research Center (CUBRC). The Mach number in this experiment ranged from 9.4 to 11.4 and stagnation enthalpies from 3.1 to 3.8 MJ/kg. Seven researchers computed these cases using the Navier-Stokes equations or DSMC. The Navier-Stokes results showed generally good agreement with the

experimental data while the DSMC results showed a significant disagreement in comparison to the experiment.

Gaitonde [42] performed perfect gas Navier-Stokes simulations of a $25^\circ/55^\circ$ double cone in nitrogen at Mach 9.5 and stagnation enthalpy of 4.2 MJ/kg. The comparison of the simulations with the experimental surface pressure and heat transfer data [43, 40] showed good agreement and the predicted peak heat transfer was within 15% of the experimental peak value. His extensive analysis showed that the computational results were not significantly dependent on parameters such as inflow gas (air *vs.* nitrogen), freestream condition and wall temperature.

Roy *et al.* [44, 45] conducted perfect gas Navier-Stokes and DSMC simulations of a blunted $25^\circ/55^\circ$ double cone in nitrogen at Mach 11.3 and stagnation enthalpy 4.0 MJ/kg. The comparison of the computational surface pressure and heat transfer with the experiment [46] showed close agreement for the Navier-Stokes calculation while the DSMC predictions were significantly different. The inability of DSMC to predict the aerothermodynamic loading was related to insufficient grid resolution in the separation region.

Candler *et al.* [47] performed Navier-Stokes simulations of a $25^\circ/55^\circ$ double cone and a 30° hollow cylinder flare at Mach 9.5 to 11.3. They considered the effect of non-equilibrium freestream conditions due to vibrational freezing in the nozzle of the LENS I tunnel and the slip wall boundary condition on the prediction of surface pressure and heat transfer. They showed that considering the non-equilibrium freestream and no-slip boundary condition had a significant effect on the predicted aerothermodynamic loading.

Nompelis *et al.* [48] performed Navier-Stokes simulations for a $25^\circ/55^\circ$ double cone in air and nitrogen at Mach 8.9 and 11.5 and stagnation enthalpies of 7.4 to 9.7 MJ/kg. Their simulations included separate equations for each species and one additional equation for vibrational energy. The comparison of surface pressure and heat transfer with the experimental data showed close agreement for the nitrogen cases while the predicted peak heat transfer for air was significantly below the experimental value. There was an inconsistency in the prediction of the separation region length.

Nompelis *et al.* [49] conducted Navier-Stokes simulations with separate equations for

each species and an equation for the vibrational energy for a $25^\circ/55^\circ$ double cone in nitrogen at nominal Mach 9.5 to 11.3 and stagnation enthalpies of 3.5 to 3.8 MJ/kg. The effect of non-uniformity and non-equilibrium (*i.e.*, vibrationally excited N_2) in the inflow condition, a slip boundary condition with a Maxwell model [50] instead of no-slip wall, and the effect of vibrational energy on the slip wall was considered. The comparison of the numerical results with the experimental surface pressure and heat transfer [43] showed excellent agreement for one case (Run 35) but not for another case (Run 28). For Run 28, using the nominal inflow condition and no-slip boundary condition showed greater disagreement with the experimental data in comparison to other cases.

Druguet *et al.* [51] performed perfect gas Navier-Stokes simulations for a $25^\circ/55^\circ$ double cone in air at Mach 11.3 and stagnation enthalpy of 3.7 MJ/kg. They examined the effect of four inviscid flux algorithms and four inviscid flux limiters (reconstruction methods). They showed that for a sufficiently resolved computational grid, the comparison of the numerical results and experimental surface pressure and heat transfer [40, 41] were in good agreement.

The NATO RTO AVT Task Group 136 [52] conducted a study to assess the capability of CFD to predict hypersonic shock wave boundary layer interactions. In this study, two experiments were used for comparison with the computational results. A $25^\circ/55^\circ$ double cone was tested at CUBRC in nitrogen at Mach 11.5 and stagnation enthalpies of 5.3 and 9.2 MJ/kg. The second experiment was a two-dimensional cylinder (*i.e.*, the cylinder axis is normal to the flow direction) tested at the German Aerospace Center (DLR) in air at Mach 9 and stagnation enthalpies of 13.5 to 22.4 MJ/kg. Six researchers performed Navier-Stokes simulations for these experiments. The comparison of the experimental surface pressure and heat transfer of the double cone with the numerical results showed a close agreement for one case (Run 42), however, for the other case (Run 40), a significant disagreement was observed. All the simulations showed the unsteady behavior for this case while the experiment was steady. The comparison of the calculated surface pressure for the two-dimensional cylinder was in close agreement with the experiment. However, the surface heat transfer prediction agreement depended on the catalytic accommodation coefficient used in the simulations.

Reimann and Hannemann [53] as part of NATO RTO AVT Task Group 136 performed

Navier-Stokes simulations of a $25^\circ/55^\circ$ double cone in nitrogen with inflow gas at thermochemical non-equilibrium. They considered two types of boundary conditions for vibrational energy at the isothermal wall. The “isothermal for vibration” boundary condition was considered for the flow at the thermally non-equilibrium condition. In this situation, the vibrational temperatures are at thermal equilibrium at the isothermal wall. They defined “adiabatic for vibration” boundary condition for the thermally frozen flow when there is barely any transfer of vibrational energy. They claimed that since near the wall the flow is almost vibrationally frozen, the results of the adiabatic for vibration (considering only the Fourier heat transfer term for comparison with the experiment) was valid and showed good agreement with the experiment.

A blind study validation for hypersonic shock wave boundary layer interaction was conducted at AIAA AVIATION Meeting 2014 for a 30° hollow cylinder flare and a $25^\circ/55^\circ$ double cone [54]. The experiments were performed at the CUBRC LENS XX tunnel at Mach numbers 10.9 to 13.2 and stagnation enthalpies 5.3 to 21.9 MJ/kg with freestream air at full equilibrium. Five researchers performed Navier-Stokes simulations for these cases (see, for example, Nompelis and Candler [55]). The comparison of their predicted surface pressure and heat transfer with the experimental data showed consistent significant overprediction of the peak values and overprediction/underprediction of the separation region length for the hollow cylinder flare and double cone, respectively.

NATO STO AVT Task Group 205 performed a study for validation of capability of CFD for prediction of hypersonic shock wave boundary layer heating of a $30^\circ/55^\circ$ double wedge in nitrogen and air at Mach 7.1 and stagnation enthalpies of 2.1 to 8.0 MJ/kg [56]. Experiments were performed in the hypervelocity expansion tube at the University of Illinois Urbana-Champaign [57]. The simulations of all the participated researchers showed unsteady behavior; however, the comparison of the experimental surface heat transfer with numerical results at about the same time as the experimental measurement showed a close agreement. Moreover, the three-dimensional simulations of Komives *et al.* [58] and Tumuklu and Levin [59] indicated that the flow was strongly three-dimensional.

Mason and Berry [60] conducted an experimental study of Edney III and IV shock-shock interaction at Mach 6 over a model with the cylindrical leading edge. They studied

the effect of leading edge radius on the surface heat transfer. They reported that the larger leading edge radius resulted in the larger nondimensional peak heat transfer. Moreover, they showed that the Edney III interaction had a broader peak in comparison to the Edney IV type interaction. The comparison of their experimental nondimensional heat transfer data with the one-dimensional and two-dimensional finite volume code results for the calculation of heat transfer over the surface indicated higher peak values with the two-dimensional calculation.

Windisch *et al.* [61] performed two-dimensional Navier-Stokes simulations of Edney IV type interactions at Mach 6.29 in nitrogen and the Martian atmosphere. They studied the jet structure and the unsteady behavior of this jet very carefully and classified six unsteady mechanisms. The comparison of surface heat transfer with the experimental data was in general agreement.

Hao *et al.* [62] conducted Navier-Stokes simulations of $25^\circ/55^\circ$ double cone at Mach number 10.90 to 13.23 and stagnation enthalpies of 5.44 to 21.77 MJ/kg. To examine the effect of the thermochemistry model, they compared the results of Park's model [33] and coupled vibration-dissociation-vibration (CVDV) model [63] with the experimental surface pressure and heat transfer. They concluded that the CVDV thermochemistry model had a better agreement with the experimental results in the prediction of separation region length. However, their results had still significant discrepancies with the experimental data.

Xiao *et al.* [64] performed an experiment and the corresponding two-dimensional laminar Navier-Stokes simulation of an Edney IV type of interaction on a cylinder with a forward facing cavity at Mach 6. They indicated that the resultant Edney IV interaction can be quasi-steady or unsteady depending on the location that the supersonic jet (created as a result of the Edney IV interaction) impinges on. They observed two different modes of oscillations: 1) high-frequency forward-backward, and 2) low-frequency up-down oscillation modes. The comparison between their experimental and numerical results was in close agreement except for surface pressure.

Hao *et al.* [65] performed Navier-Stokes simulations of a 30° hollow cylinder flare. They studied the effect of thermochemical reaction by using Park's [66] models and an improved version of the Park model based on the quasi-classical trajectory (QCT) calculations and

adding CVDV. The comparison of their results with the experimental surface pressure and heat transfer indicated that the effect of the thermochemistry model on the predicted surface pressure and heat transfer is negligible.

Paoli [67] conducted two dimensional Navier-Stokes simulations of a circular cylinder to study the Edney III and IV types of shock-shock interaction at Mach 9.95. He studied the effect of the location of the impinging shock on the final Edney III and IV type interactions to better understand the characteristics of these interactions.

Durna and Celik [68] performed Navier-Stokes simulations of a double wedge at Mach 7.11 and stagnation enthalpy of 2.1 MJ/kg. They studied the effect of the second wedge angle by changing the second wedge angle from 45° to 60° keeping the first wedge angle constant at 30° . Their results showed that the flow is unsteady with Görtler-like vortices for the aft wedge angle of 50° and above. The results also demonstrated that the two-dimensional study was valid only for the aft wedge angle of 45° .

In summary, there has been no *consistent* demonstration of the capability of CFD in accurate prediction of hypersonic shock-shock and shock wave boundary layer interaction at high stagnation enthalpies. The accurate prediction here defined as the capability to predict the surface pressure and surface heat transfer within the experimental uncertainty (*e.g.*, $\pm 10\%$). This becomes the motivation of the first part of this dissertation. In this regard, instead of adding more complex models into the governing equations, we moved in the direction of simplification of the governing equation to see what are the models that need to be improved.

1.2 Energy Deposition for Flight Control

It is well known that energy deposition can reduce aerodynamic drag. The drag reduction effect of energy deposition has been presented in several experimental and computational works over the past five decades. Adding the energy to the flow creates a heated region that changes the flow structure around the body and hence reduces the drag. The state of the art of energy deposition (*e.g.*, laser discharge, microwave discharge, and DC discharge) and its application for flow control including drag reduction are presented in Knight [69].

Figure 1.8 shows a schematic of using laser discharge for flow control in hypersonic flight. The laser discharge is interchangeable with other means of energy deposition. In this figure, the energy discharge is used for reducing drag, optimizing inlet pressure, and reducing aerothermodynamic loads.

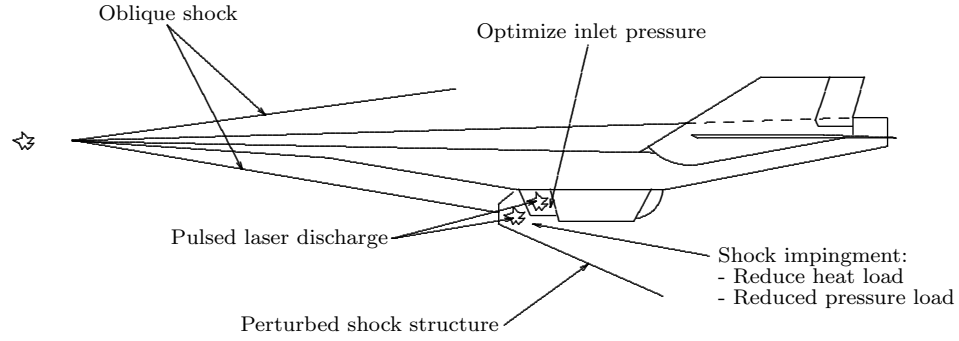


Figure 1.8: Energy discharge for flow control in hypersonic flight

Tretyakov *et al.* [70] conducted an experimental study to examine the effect of CO₂ laser pulse frequency on drag reduction of a 6-mm diameter cylinder with a conical and spherical head at Mach 2. The total length of the model was 20 mm with the conical angle of 60° and the spherical radius of 3 mm. They reported that increasing the frequency of the laser pulses from 12.5 to 100 kHz increased the drag reduction so that at 100 kHz, the drag was 0.55 of the drag at the flow without laser discharge.

Riggins *et al.* [71] performed a series of full non-equilibrium Navier-Stokes simulations of a rectangular (in two-dimensional simulations) and cylindrical (in axisymmetric simulations) energy deposition in front of a blunt body at Mach 6.5 and 10. They studied the effect of the input power for the fixed location of discharge and the effect of the discharge location at fixed discharge power. They reported that at Mach 6.5 and in a two-dimensional simulation, increasing the power at a constant location reduced the ratio of the drag to the drag without the discharge but the ratio asymptotically went toward 0.45. The resulted drag reduction for the axisymmetric flow is less than two-dimensional simulations. Moreover, their results presented the existence of an optimized location for the energy discharge at a specific power level to have the largest drag reduction. If the discharge is located twice the diameter of the blunt body, the drag would be reduce to 0.3 of the initial drag without energy discharge.

Laskov *et al.* [72] conducted a series of experiments to study the effect of microwave discharge on the blunt cylinder, hemisphere, cone, and wedge at Mach 2.1. They showed that for a 20 mm diameter blunt cylinder, the stagnation pressure drops to about one third and the pressure drop lasted for more than 100 μ s. They also examined the effect of off-axis energy discharge and reported that increasing the offset distance from the axis first decreased the maximum stagnation pressure drop and then it even increased the centerline pressure. The interaction of energy discharge with hemisphere showed the same behavior with faster interaction; however, the stagnation pressure drop still lasted for about 100 μ s. On the other hand, they reported that the interaction of the microwave discharge with the cone and wedge are weaker in comparison to blunt bodies. Finally, they concluded that the effect of energy discharge is scalable linearly with the size of the body.

Adelgren *et al.* [73] investigated the effect of the laser discharge in front of a hemisphere at Mach 3.45 for drag reduction and reduction of surface pressure for Edney IV type interaction. The results of this study showed that laser discharge with an energy range of 13 to 283 mJ upstream of a hemisphere bow shock momentarily reduced the centerline pressure by 40%. For the Edney IV interaction case, the laser discharge resulted in a momentarily 30% surface pressure reduction.

Yan and Gaitonde [74] performed three dimensional Reynolds-averaged Navier-Stokes (RANS) simulations of the Adelgren experiment for 283 mJ energy discharge to study the effect of the interaction on the Edney IV shock-shock interaction. Their simulations showed a closed agreement with experimental surface pressure prior to adding the energy discharge. Their simulations illustrated the same behavior as in the experimental schlieren images. Both surface pressure and heat transfer experienced a peak due to the impact of the blast wave on the hemisphere surface followed by a significant decrease due to the interaction of the expansion fan. The interaction of the heated region with the Edney IV interaction drastically increased the surface heat transfer. The time-averaged surface pressure and heat transfer on the vertical plane of symmetry displayed a decrease relative to the surface pressure and heat transfer profile before adding energy discharge to the flow.

Knight *et al.* [75] simulated a microwave discharge passing a hemisphere cylinder with

fully non-equilibrium Navier-Stokes equation with 23 species and 238 reactions. The comparison of the filtered centerline pressure on the hemisphere cylinder showed a close agreement with the experiment. The unfiltered data showed much higher drag reduction compared to the filtered data. The flowfield was significantly non-equilibrium with a high level of atomic oxygen during the entire interaction time.

Schüle in *et al.* [76] performed a combined experimental and numerical study of a series of a single pulse and double pulse energy deposition in front of a hemisphere cylinder at Mach 2. They examined the effect of the energy deposited at the fixed location for a single discharge and reported that peaks and troughs of the time history of the stagnation pressure during interactions became more profound by increasing the amount of energy. They also evaluated the effect of energy added in the second pulse at the fixed location and fixed time delay from the first pulse. Since their simulations used the Euler equations, there was a discrepancy between the flow structure of the simulation and the experimental results which became worse by increasing the second pulse energy. They considered the effect of the physical distance and temporal distance between the two pulses by fixing the energy of the pulse and respectively fixed the time delay and location of the two pulses. There were again discrepancies between the predicted flowfield of the Euler simulations and the experimental data.

Kim *et al.* [77] showed experimentally that at high laser discharge frequencies, the flow structure changed in a way to streamline the body and thus decreased the drag. They performed a series of experiments at Mach 1.94 for a flat head cylinder and showed that increasing the frequency would decrease the drag linearly. Moreover, their results suggested the existence of an optimum energy value for each pulse discharge to achieve the highest efficiency.

In addition to drag reduction and flow control, energy discharge can be used for rapid maneuvering of high speed vehicles, especially at hypersonic speeds. Rapid maneuvering is defined as the ability to change the direction of a vehicle within the time required to travel a distance equal to a body length. The typical flight control methods utilize surface deflection (*e.g.*, ailerons, rudder, flaps). A typical actuation time for full deflection of the conventional control surface is on the order of a tenth of a second [78]. At hypersonic speeds, the vehicle

travels several times its length during this actuation time. Therefore, at high speed flows, the conventional control surfaces are not fast enough for rapid maneuvering. Consequently, the need for investigation of new methods to achieve rapid maneuvering is evident.

The number of studies examining the energy deposition for flight control is very limited. Girgis *et al.* [79] numerically examined the effect of a continuous spherical heated region or an electron beam on a cone cylinder at Mach 2. They first found the optimum location of the heated region on-axis for the fixed input power of the heated region to be $0.4D$ ahead of the cone tip where D is the diameter of the cylinder. The optimized location was the point with the most drag reduction. Then, they changed the radius of the heated region and thus the input power at the optimized location and found the optimized size of the heated region for the maximum drag reduction to be $0.2D$. They moved the heated region off-axis using the optimized size and the optimized location and found the optimized angle of energy deposition between 40 to 50 degrees with a maximum lift to drag ratio of 0.591. Their results showed that the increase in the input power of the heated region would not increase the lift to drag ratio linearly. However, they saw a linear relation between the Mach number and lift to drag ratio and concluded that increasing the Mach number will increase the lift to drag ratio. Moreover, they reported that the drag reduction and lift to drag ratio of the spherical heated region were larger than the electron beam results.

Starikovskiy *et al.* [80] studied the effect of single and multiple pulse laser discharge for flight control of a small rotating projectile at Mach 3. They theoretically analyzed the criterion for having a strong interaction and reported that the weaker the oblique shock, the higher the temperature in the heated region should be. They used 300 mJ energy per pulse in front of a cone cylinder and hemisphere cylinder rotating at 400 Hz. The discharge had a greater impact on the hemisphere cylinder projectile in comparison to the cone cylinder projectile. They concluded that only 2 mJ of energy per pulse would be enough to change the angle of attack of a body by 1° for a 3.5 cm interaction length.

Elias *et al.* [81] conduct an experiment to study the effect of the terawatt femtosecond laser for the steering of high speed vehicles. They added a plasma filament that placed slightly above the axis of the symmetry of a blunt cone at Mach 3. They measured the pressure at the top and bottom of the body using piezoelectric pressure gauges. While the

bottom pressure gauge read almost a constant pressure, the top pressure gauge responded to the interaction of the plasma region with the shock and recorded a variation in pressure. This asymmetric pressure distribution resulted in an upward force on the body which can be used for changing the direction of a vehicle at high speed flows.

Although it is shown that using energy discharge in the flowfield is capable of changing the flow structure and therefore can change the force affecting the body, however, there is limited knowledge on the applicability of this method. For example, the range of the reported performance for drag reduction in the literature is so vast (based on the energy input level, the geometry of the body and the way that the energy is created, frequency of the energy discharge, etc.). There are several questions still need to be answered. Is the force sufficient for steering the body? Is the method scalable to a large body? Is this method efficient? Part two of this dissertation tries to address this problem.

Chapter 2

Governing Equations

In this chapter, the governing equations for high speed flows are described. Due to the high temperatures associated with these flows, the thermochemical reactions are considered, *i.e.*, the dissociation and recombination reaction which produces a new mixture of gas rather than the regular air with the known properties of the air. In addition, the molecules may hold vibrational energy which can be transferred into translational energy and vice versa. Considering air consists of nitrogen and oxygen (dry air at sea level contains 78.09% nitrogen, 20.95% oxygen [82]) and their thermochemical reaction products (NO, N, O), the total number of governing equations are twelve including five equations for conservation of mass of each species, three equations for conservation of momentum, one equation for conservation of total energy and three equations for conservation of vibrational energies.

2.1 Introduction

The first step in solving a problem is to choose the correct governing equations for the problem. It should be considered that neither is it needed to include all the physics in the solution nor it is possible to do so. The best governing equations for a problem are the ones that consider all the important aspects of the problem and ignore modeling of the physics that are not necessary to avoid overcomplicating the problem solving process. For example, when the total enthalpy of flow is small, it's not necessary to consider the full non-equilibrium equations to solve the problem since the maximum possible temperature is not sufficient to dissociate even oxygen.

In this chapter, the full non-equilibrium Navier-Stokes equations for laminar compressible flow are described in Section 2.2. Some simplifications to the complete equations are

described as special cases in Section 2.3. The different types of boundary conditions applicable at the isothermal no-slip wall are also described in Section 2.4.

2.2 Non-Equilibrium Laminar Navier-Stokes Equations

We consider reacting mixture of n gases with density ρ_α for $\alpha = 1, \dots, n$ of which $\alpha = 1, \dots, m$ constitute diatomic (or polyatomic) species and the remainder ($i = m + 1, \dots, n$) represent monatomic species.

2.2.1 Conservation of Mass

The conservation of mass is

$$\frac{\partial \rho_\alpha}{\partial t} + \frac{\partial \rho_\alpha u_j}{\partial x_j} = \dot{\omega}_\alpha^{\text{spe}} + \frac{\partial}{\partial x_j} \left[\rho D \frac{\partial Y_\alpha}{\partial x_j} \right] \quad \text{for } \alpha = 1, \dots, n \quad (2.1)$$

where ρ_α is the density of species α , the mass-averaged velocity is u_j , and ρ is the mixture density

$$\rho = \sum_{\alpha=1}^n \rho_\alpha \quad (2.2)$$

The mass fraction is defined as

$$Y_\alpha = \frac{\rho_\alpha}{\rho} \quad (2.3)$$

The rate of production of species α is denoted as $\dot{\omega}_\alpha^{\text{spe}}$ and defined as

$$\dot{\omega}_\alpha^{\text{spe}} = \mathcal{M}_\alpha \sum_{j=1}^J (\nu''_{\alpha,j} - \nu'_{\alpha,j}) k_{f,j} \left[\prod_{l=1}^n \left(\frac{\rho_l}{\mathcal{M}_l} \right)^{\nu'_{l,j}} - \frac{1}{k_{e,j}} \prod_{l=1}^n \left(\frac{\rho_l}{\mathcal{M}_l} \right)^{\nu''_{l,j}} \right] \quad \text{for } \alpha = 1, \dots, n \quad (2.4)$$

for the general reaction expressions

$$\nu'_{1,j} X_1 + \dots + \nu'_{n,j} X_n \rightleftharpoons \nu''_{1,j} X_1 + \dots + \nu''_{n,j} X_n \quad \text{for } j = 1, \dots, J \quad (2.5)$$

where J is the number of reactions, $k_{f,j}$ and $k_{f,j}/k_{e,j}$ are the forward and backward reaction rates of the j^{th} reaction, and $\nu'_{\alpha,j}$ and $\nu''_{\alpha,j}$ are the stoichiometric coefficients of the reactants and products of species X_α in the j^{th} reaction. \mathcal{M}_α is the molecular weight of species α .

The diffusion of species is modeled by Fick's Law [83] assuming a uniform diffusivity D defined by

$$D = \frac{k}{\rho c_{p_f} Le} \quad (2.6)$$

where $Le = 1.0$ is the constant Lewis number, k is the mixture thermal conductivity [84], and c_{p_f} is the mixture specific heat at constant pressure defined by

$$c_{p_f} = \sum_{\alpha=1}^n Y_{\alpha} c_{p_{\alpha}} \quad (2.7)$$

where $c_{p_{\alpha}}$ is the specific heat at constant pressure of species α . The mixture thermal conductivity is calculated using Wilke's rule [85]

$$k = \sum_{\alpha=1}^n \frac{\chi_{\alpha} k_{\alpha}}{\phi_{\alpha}} \quad (2.8)$$

where k_{α} is the thermal conductivity of species α , and

$$\phi_{\alpha} = \sum_{\beta=1}^n \chi_{\beta} \left[1 + \left(\frac{\mu_{\alpha}}{\mu_{\beta}} \right)^{1/2} \left(\frac{\mathcal{M}_{\beta}}{\mathcal{M}_{\alpha}} \right)^{1/4} \right]^2 \left[\sqrt{8} \left(1 + \frac{\mathcal{M}_{\alpha}}{\mathcal{M}_{\beta}} \right)^{1/2} \right]^{-1} \quad (2.9)$$

and

$$\chi_{\beta} = \frac{C_{\beta}}{C} \quad (2.10)$$

where

$$C_{\beta} = \frac{\rho_{\beta}}{\mathcal{M}_{\beta}} \quad (2.11)$$

and

$$C = \sum_{\beta=1}^n C_{\beta} \quad (2.12)$$

2.2.2 Conservation of Momentum

The conservation of momentum is

$$\frac{\partial \rho u_i}{\partial t} + \frac{\partial \rho u_i u_j}{\partial x_j} = -\frac{\partial p}{\partial x_i} + \frac{\partial \tau_{ij}}{\partial x_j} \quad \text{for } i = 1, 2, 3 \quad (2.13)$$

where τ_{ij} is the laminar viscous stress tensor defined as

$$\tau_{ij} = -\frac{2}{3} \mu \frac{\partial u_k}{\partial x_k} \delta_{ij} + \mu \left(\frac{\partial u_i}{\partial x_j} + \frac{\partial u_j}{\partial x_i} \right) \quad (2.14)$$

The molecular viscosity is defined according to Wilke's rule [85] as

$$\mu = \sum_{\alpha=1}^n \frac{x_{\alpha} \mu_{\alpha}}{\phi_{\alpha}} \quad (2.15)$$

where ϕ_i is defined by Equation (2.9).

2.2.3 Conservation of Total Energy

The total energy per unit mass ε is the sum of the internal energy per unit mass e and the kinetic energy per unit mass

$$\varepsilon = e + \frac{1}{2} u_j u_j \quad (2.16)$$

The internal energy per unit mass e is the sum of the internal energies of each of the n species

$$e = \sum_{\alpha=1}^n Y_{\alpha} e_{\alpha} \quad (2.17)$$

where the internal energy per unit mass of each species e_{α} is the sum of an equilibrium internal energy $e_{\alpha}^{\text{eq}}(T)$ due to random translational energy and rotational energy (in the case of molecules) at a bulk equilibrium temperature T and a non-equilibrium internal energy $e_{\alpha}^{\text{vib}}(T_{\alpha}^{\text{vib}})$ due to vibrational excitation (in the case of molecules)

$$e_{\alpha} = e_{\alpha}^{\text{eq}}(T) + e_{\alpha}^{\text{vib}}(T_{\alpha}^{\text{vib}}) \quad (2.18)$$

The equilibrium internal energy of species α is

$$e_{\alpha}^{\text{eq}}(T) = h_{f_{\alpha}}^o + \int_{T_{\text{ref}}}^T c_{v_{\alpha}}(T) dT \quad (2.19)$$

where $h_{f_{\alpha}}^o$ is the enthalpy of formation of species α at T_{ref} and T_{ref} is reference temperature. $c_{v_{\alpha}}(T)$ is specific heat capacity at constant volume of species α at temperature T .

The conservation of total energy is

$$\frac{\partial \rho \varepsilon}{\partial t} + \frac{\partial}{\partial x_j} (\rho \varepsilon + p) u_j = \frac{\partial \tau_{ji} u_i}{\partial x_j} - \frac{\partial q_j}{\partial x_j} \quad (2.20)$$

where the heat transfer vector is defined by

$$q_j = -k \frac{\partial T}{\partial x_j} - \sum_{\alpha=1}^m k_{\alpha}^{\text{vib}} \frac{\partial T_{\alpha}^{\text{vib}}}{\partial x_j} - \sum_{\alpha=1}^n \rho h_{\alpha} D \frac{\partial Y_{\alpha}}{\partial x_j} \quad (2.21)$$

where k_{α}^{vib} and D are respectively vibrational heat transfer coefficient and diffusivity.

The static enthalpy per unit mass for species α is

$$h_{\alpha} = h_{f_{\alpha}}^o + \int_{T_{\text{ref}}}^T c_{p_{\alpha}}(T) dT \quad (2.22)$$

where $c_{p_{\alpha}}(T)$ is the specific heat capacity at constant pressure of species α at temperature T .

2.2.4 Conservation of Vibrational Energy

The conservation of vibrational energy is

$$\frac{\partial \rho_\alpha e_\alpha^{\text{vib}}}{\partial t} + \frac{\partial \rho_\alpha e_\alpha^{\text{vib}} u_j}{\partial x_j} = -\frac{\partial q_{\alpha j}^{\text{vib}}}{\partial x_j} + \dot{\omega}_\alpha^{\text{vib}} \quad \text{for } \alpha = 1, \dots, m \quad (2.23)$$

The heat transfer vector is

$$q_{\alpha j}^{\text{vib}} = -k_\alpha^{\text{vib}} \frac{\partial T_\alpha^{\text{vib}}}{\partial x_j} - \rho D e_\alpha^{\text{vib}} \frac{\partial Y_\alpha}{\partial x_j} \quad (2.24)$$

The source term is

$$\dot{\omega}_\alpha^{\text{vib}} = \rho_\alpha \dot{e}_\alpha^{\text{vib}} + \dot{\omega}_\alpha^{\text{spe}} e_\alpha^{\text{vib}} \quad (2.25)$$

where $\dot{e}_\alpha^{\text{vib}}$ is the translational-vibrational energy transfer per unit mass of species α defined by the Landau-Teller model [86]

$$\dot{e}_\alpha^{\text{vib}} = \frac{e_\alpha^{\text{vib}*}(T) - e_\alpha^{\text{vib}}(T_\alpha^{\text{vib}})}{\tau_\alpha} \quad (2.26)$$

where $e_\alpha^{\text{vib}*}$ is the equilibrium vibrational energy per unit mass of species α defined by

$$e_\alpha^{\text{vib}*}(T) = \frac{R_\alpha \Theta_\alpha^{\text{vib}}}{\exp(\Theta_\alpha^{\text{vib}}/T) - 1} \quad (2.27)$$

and R_α defines later by Equation (2.34) and τ_α is the relaxation time [87] of species α defined by

$$\tau_\alpha = \frac{\sum_{\beta=1}^n M_\beta}{\sum_{\beta=1}^n M_\beta \tau_{\alpha\beta}} \quad (2.28)$$

where $M_\alpha = \rho_\alpha / \mathcal{M}_\alpha$ is the molar concentration of species α and $\tau_{\alpha\beta}$ is the characteristic relaxation time of species α resulting from collisions with species β defined by [87]

$$\tau_{\alpha\beta} = \frac{1}{p} \exp \left[A_{\alpha\beta} \left(T^{-\frac{1}{3}} - B_{\alpha\beta} \right) - 18.42 \right] \quad (2.29)$$

where $\tau_{\alpha\beta}$ is in seconds and p is in atmospheres, and

$$A_{\alpha\beta} = 0.00116 \mathcal{M}_{\alpha\beta}^{\frac{1}{2}} \Theta_\alpha^{\text{vib} \frac{4}{3}} \quad (2.30)$$

and

$$B_{\alpha\beta} = 0.015 \mathcal{M}_{\alpha\beta}^{\frac{1}{4}} \quad (2.31)$$

and the averaged molecular weight is defined by

$$\mathcal{M}_{\alpha\beta} = \frac{\mathcal{M}_\alpha \mathcal{M}_\beta}{\mathcal{M}_\alpha + \mathcal{M}_\beta} \quad (2.32)$$

where \mathcal{M}_α is the molecular weight of species α . Note that the second term in the numerator in Equation (2.26) is multiplied by ρ_α in Equation (2.25) and is thus $\rho_\alpha e_\alpha^{\text{vib}}$. In the second term in Equation (2.25), there are two possible choices for e_α^{vib} namely, $e_\alpha^{\text{vib}} = \frac{R_\alpha \Theta_\alpha^{\text{vib}}}{\exp(\Theta_\alpha^{\text{vib}}/T) - 1}$ and $e_\alpha^{\text{vib}} = \frac{R_\alpha \Theta_\alpha^{\text{vib}}}{\exp(\Theta_\alpha^{\text{vib}}/T_\alpha^{\text{vib}}) - 1}$.

2.2.5 Equation of State

The equation of state is

$$p = T \sum_{\alpha=1}^n \rho_\alpha R_\alpha \quad (2.33)$$

where the gas constant R_α for species α is

$$R_\alpha = \frac{\mathcal{R}}{\mathcal{M}_\alpha} \quad (2.34)$$

where \mathcal{R} is the Universal Gas Constant.

2.2.6 Thermodynamic Data and Transport Properties

The species thermodynamic data and species transport properties are obtained from Gupta, Yos, Thompson and Lee [88] (NASA-RP-1232) database. The mixture viscosity μ and thermal conductivity k are determined by Wilke's Rule [85]. The vibrational thermal conductivity of species α is

$$k_\alpha^{\text{vib}} = \mu_\alpha R_\alpha \quad (2.35)$$

where μ_α and R_α are the molecular viscosity and gas constant for species α , respectively.

2.2.7 Thermochemistry Model

The non-equilibrium Navier-Stokes simulations used the thermochemistry model proposed by Park [33] comprising five species (N_2 , O_2 , NO , N , O) and seventeen reactions (Table A.1).

2.3 Special Cases

There are several special cases created by simplification of the full non-equilibrium Navier-Stokes equation. The ones are used in this thesis are described below. Table 2.1 presents the simplifications in the governing equation for each of the case below.

2.3.1 Calorically Perfect

In calorically perfect gas which for simplicity called perfect gas, there is no mixture of gases and it is assumed that there is only one gas with density ρ . Therefore, for equation (2.1) the right hand side is zero since there is no diffusion or production and dissociation of species. The gas cannot be vibrationally excited and thus there is no equation for conservation of vibrational energy. Moreover, in the conservation of total energy equation, the heat transfer term in equation (2.21) is simplified to just the first term. Also, viscosity μ and thermal conductivity k are calculated using Sutherland's law and a constant Prandtl number, respectively. The specific heat is constant for a perfect gas.

2.3.2 Thermally Perfect

This terminology is used for the cases with no thermochemical reaction and no vibrational-translational energy transfer. Since there is no thermochemical reaction, therefore, the source term in conservation of mass (see equation (2.1)) is zero, *i.e.*, $\dot{\omega}_\alpha^{\text{spe}} = 0$. Moreover, there is no vibrational-translational energy transfer which means the source term in the conservation of vibrational energy equation (see equation (2.25)) is also zero, *i.e.*, $\dot{\omega}_\alpha^{\text{vib}} = 0$. The thermodynamic data and transport properties are obtained as discussed in Section 2.2.6.

2.3.3 Non-reactive

A mixture of gas with no thermochemical reaction but with vibrational-translational energy transfer is denoted as non-reactive. For this gases, the right hand side of the conservation of mass, equation (2.1) can be simplified due to no thermochemical reaction, *i.e.*, $\dot{\omega}_\alpha^{\text{spe}} = 0$. Moreover, the source term of conservation of vibrational energy, equation (2.25) includes thermochemical reactions and thus can be simplified. Therefore, $\dot{\omega}_\alpha^{\text{vib}} = \rho_\alpha \dot{e}_\alpha^{\text{vib}}$. The thermodynamic data and transport properties are obtained as discussed in Section 2.2.6.

Table 2.1: Simplification in Governing Equation for Each Specific Case

Specific case	Modification to governing equations		Transport properties			
	$\dot{\omega}_\alpha^{\text{spe}}$	$\dot{\omega}_\alpha^{\text{vib}}$	Specific heats	Viscosity	Pr_∞	Le
Calorically perfect gas	n/a	n/a	constant	Sutherland Law	0.72	n/a
Thermally perfect gas	0	0	Gupta <i>et al.</i> database and Wilke's rule		0.737	1.0
Non-reactive gas	0	$\rho_\alpha \dot{e}_\alpha^{\text{vib}}$	Gupta <i>et al.</i> database and Wilke's rule		0.737	1.0
Full non-equilibrium gas	Eq. (2.1) and Park I	Eq. (2.25)	Gupta <i>et al.</i> database and Wilke's rule		0.737	1.0

2.4 Boundary Conditions

The vibrational energy at a no-slip isothermal wall has been treated differently in the literature. The first boundary condition model (denoted “isothermal for vibration”) is [66]

$$e_\alpha^{\text{vib}}|_w = e_\alpha^{\text{vib}*}(T_w) \quad \text{or} \quad T_\alpha^{\text{vib}}|_w = T_w \quad (2.36)$$

The second boundary condition model (denoted “adiabatic for vibration”) is [89]

$$\left(\frac{\partial e_\alpha^{\text{vib}}}{\partial n} \right) \Big|_w = 0 \quad \text{or} \quad \left(\frac{\partial T_\alpha^{\text{vib}}}{\partial n} \right) \Big|_w = 0 \quad (2.37)$$

Reimann and Hannemann [53] explain that when the flow is in vibrationally non-equilibrium (small relaxation time compared to the time flow needed to pass the model) the vibrational energies boundary condition can be considered as “isothermal for vibration” and when the flow is vibrationally frozen (large relaxation time compared to the required time for the flow to pass the entire length of the model) the “adiabatic for vibration” boundary condition can be used since there is almost no vibrational energy transfer to the wall.

2.5 Conclusion

In this chapter, the description of the equations governing the laminar high speed fluid is explained. The possible simplifications to these governing equations are also introduced.

The art of choosing the simplest possible governing equations while any of the important parts of the flow characteristics are missing is one of the key aspects in solving the fluid problem. As Albert Einstein said: “Everything should be made as simple as possible, but no simpler”.

Chapter 3

Numerical Algorithm

In this chapter, the numerical algorithms used for solving the governing equations are described. With the advancement in computer technology, there is a rapid development of numerical methods improving the accuracy of the results. Some of the methods are specifically designed for specific conditions. The availability of numerous numerical methods faces researchers to the new challenge. How to choose the numerical methods that best fits their problem?

3.1 Introduction

Choosing the correct sets of governing equations is the first step for solving the problem. The next step is to choose the numerical methods that are designed for the kind of problem being solved. The governing equations need to be discretized. This discretization is related to the specific method chosen for the problem. To know the values of variables in each cell and at each cell's faces, the reconstruction methods are required to map the change in the variables to the specific accuracy required for solving the problem. The flux calculation method should also be carefully chosen to calculate the flux at the faces. Moreover, the simulation can be time-accurate if unsteady behavior is important, or by iterative methods if only the steady-state solution is desirable.

In this chapter, first, the finite volume method is described in Section 3.2. Then in Section 3.3, several inviscid flux methods are introduced to calculate the flux at each cell's faces including Advection Upstream Splitting method (AUSM), Roe's method, and Van Leer's method. To be able to calculate the flux, the values of the dependent variables should be known at each face. Therefore, reconstruction methods are introduced in Section 3.4. The described methods are first order, MUSCLp, and Min-Mod. The calculation of viscous

fluxes is described in Section 3.5. The time integration methods such as Data Parallel Line Relaxation (DPLR), dual time stepping, and Runge-Kutta are introduced in Section 3.6 for time accurate solutions. The line Gauss-Seidel method is the iterative method introduced in Section 3.6 for the calculation of the steady-state solution.

To be able to solve a problem, the boundary conditions have to be specified. The boundary conditions should also be applied correctly to have a stable simulation for the problem. The boundary conditions such as axisymmetric, fixed, internal, no-slip adiabatic, no-slip isothermal, symmetry, and zero-gradient are described in Section 3.7.

To have the best efficiency, the message passing interface (MPI) is introduced in Section 3.8 to divide the computational domain into several smaller parts which can be solved simultaneously on several processes. This improves performance and reduces the time required to solve a problem.

3.2 Finite Volume Method

The full non-equilibrium laminar Navier-Stokes equations (Equations (2.1), (2.13), (2.20), and (2.23)) can be written in the vector form as

$$\frac{\partial Q}{\partial t} + \frac{\partial E}{\partial x} + \frac{\partial F}{\partial y} + \frac{\partial G}{\partial z} = \frac{\partial R}{\partial x} + \frac{\partial S}{\partial y} + \frac{\partial T}{\partial z} + \dot{S} \quad (3.1)$$

where,

$$Q = \begin{bmatrix} \rho_1 \\ \vdots \\ \rho_n \\ \rho u \\ \rho v \\ \rho w \\ \rho \varepsilon \\ \rho_1 e_1^{\text{vib}} \\ \vdots \\ \rho_m e_m^{\text{vib}} \end{bmatrix}, \quad E = \begin{bmatrix} \rho_1 u \\ \vdots \\ \rho_n u \\ \rho u u + p \\ \rho u v \\ \rho u w \\ (\rho \varepsilon + p) u \\ \rho_1 e_1^{\text{vib}} u \\ \vdots \\ \rho_m e_m^{\text{vib}} u \end{bmatrix}, \quad F = \begin{bmatrix} \rho_1 v \\ \vdots \\ \rho_n v \\ \rho v u \\ \rho v v + p \\ \rho v w \\ (\rho \varepsilon + p) v \\ \rho_1 e_1^{\text{vib}} v \\ \vdots \\ \rho_m e_m^{\text{vib}} v \end{bmatrix}, \quad G = \begin{bmatrix} \rho_1 w \\ \vdots \\ \rho_n w \\ \rho w u \\ \rho w v \\ \rho w w + p \\ (\rho \varepsilon + p) w \\ \rho_1 e_1^{\text{vib}} w \\ \vdots \\ \rho_m e_m^{\text{vib}} w \end{bmatrix} \quad (3.2)$$

$$R = \begin{bmatrix} \rho D \frac{\partial Y_1}{\partial x} \\ \vdots \\ \rho D \frac{\partial Y_n}{\partial x} \\ \tau_{xx} \\ \tau_{xy} \\ \tau_{xz} \\ \tau_{xx}u + \tau_{xy}v + \tau_{xz}w - q_x \\ -q_{1x}^{\text{vib}} \\ \vdots \\ -q_{m_x}^{\text{vib}} \end{bmatrix}, \quad S = \begin{bmatrix} \rho D \frac{\partial Y_1}{\partial y} \\ \vdots \\ \rho D \frac{\partial Y_n}{\partial y} \\ \tau_{xy} \\ \tau_{yy} \\ \tau_{yz} \\ \tau_{xy}u + \tau_{yy}v + \tau_{yz}w - q_y \\ -q_{1y}^{\text{vib}} \\ \vdots \\ -q_{m_y}^{\text{vib}} \end{bmatrix} \quad (3.3)$$

$$T = \begin{bmatrix} \rho D \frac{\partial Y_1}{\partial z} \\ \vdots \\ \rho D \frac{\partial Y_n}{\partial z} \\ \tau_{xz} \\ \tau_{yz} \\ \tau_{zz} \\ \tau_{xz}u + \tau_{yz}v + \tau_{zz}w - q_z \\ -q_{1z}^{\text{vib}} \\ \vdots \\ -q_{m_z}^{\text{vib}} \end{bmatrix}, \quad \dot{S} = \begin{bmatrix} \dot{\omega}_1^{\text{spe}} \\ \vdots \\ \dot{\omega}_n^{\text{spe}} \\ 0 \\ 0 \\ 0 \\ 0 \\ \dot{\omega}_1^{\text{vib}} \\ \vdots \\ \dot{\omega}_m^{\text{vib}} \end{bmatrix} \quad (3.4)$$

These equations need to be transformed into a new set of curvilinear coordinates denoted (ξ, η, ζ) to have a computational domain with cells dimensions of 1. To do this, the chain rule, Jacobian definition (*i.e.* $\frac{\partial(\xi, \eta, \zeta)}{\partial(x, y, z)}$), and the transformation from (x, y, z) to (ξ, η, ζ) and the inverse of the transformation from (ξ, η, ζ) to (x, y, z) are used. The transformed governing equation is

$$\frac{\partial Q'}{\partial t} + \frac{\partial E'}{\partial \xi} + \frac{\partial F'}{\partial \eta} + \frac{\partial G'}{\partial \zeta} = \frac{\partial R'}{\partial \xi} + \frac{\partial S'}{\partial \eta} + \frac{\partial T'}{\partial \zeta} + \dot{S}' \quad (3.5)$$

where,

$$Q' = \frac{1}{J} \begin{bmatrix} \rho_1 \\ \vdots \\ \rho_n \\ \rho u \\ \rho v \\ \rho w \\ \rho \varepsilon \\ \rho_1 e_1^{\text{vib}} \\ \vdots \\ \rho_m e_m^{\text{vib}} \end{bmatrix}, \quad E' = \frac{1}{J} \begin{bmatrix} \rho_1 U' \\ \vdots \\ \rho_n U' \\ \rho u U' + \xi_x p \\ \rho v U' + \xi_y p \\ \rho w U' + \xi_z p \\ (\rho \varepsilon + p) U' \\ \rho_1 e_1^{\text{vib}} U' \\ \vdots \\ \rho_m e_m^{\text{vib}} U' \end{bmatrix} \quad (3.6)$$

$$F' = \frac{1}{J} \begin{bmatrix} \rho_1 V' \\ \vdots \\ \rho_n V' \\ \rho u V' + \eta_x p \\ \rho v V' + \eta_y p \\ \rho w V' + \eta_z p \\ (\rho \varepsilon + p) V' \\ \rho_1 e_1^{\text{vib}} V' \\ \vdots \\ \rho_m e_m^{\text{vib}} V' \end{bmatrix}, \quad G' = \frac{1}{J} \begin{bmatrix} \rho_1 W' \\ \vdots \\ \rho_n W' \\ \rho u W' + \zeta_x p \\ \rho v W' + \zeta_y p \\ \rho w W' + \zeta_z p \\ (\rho \varepsilon + p) W' \\ \rho_1 e_1^{\text{vib}} W' \\ \vdots \\ \rho_m e_m^{\text{vib}} W' \end{bmatrix} \quad (3.7)$$

$$R' = \frac{1}{J} \begin{bmatrix} \rho D \left(\xi_x \frac{\partial Y_1}{\partial x} + \xi_y \frac{\partial Y_1}{\partial y} + \xi_z \frac{\partial Y_1}{\partial z} \right) \\ \vdots \\ \rho D \left(\xi_x \frac{\partial Y_n}{\partial x} + \xi_y \frac{\partial Y_n}{\partial y} + \xi_z \frac{\partial Y_n}{\partial z} \right) \\ \xi_x \tau_{xx} + \xi_y \tau_{xy} + \xi_z \tau_{xz} \\ \xi_x \tau_{xy} + \xi_y \tau_{yy} + \xi_z \tau_{yz} \\ \xi_x \tau_{xz} + \xi_y \tau_{yz} + \xi_z \tau_{zz} \\ \xi_x \beta_x + \xi_y \beta_y + \xi_z \beta_z \\ - \left(\xi_x q_{1x}^{\text{vib}} + \xi_y q_{1y}^{\text{vib}} + \xi_z q_{1z}^{\text{vib}} \right) \\ \vdots \\ - \left(\xi_x q_{m_x}^{\text{vib}} + \xi_y q_{m_y}^{\text{vib}} + \xi_z q_{m_z}^{\text{vib}} \right) \end{bmatrix}, \quad S' = \frac{1}{J} \begin{bmatrix} \rho D \left(\eta_x \frac{\partial Y_1}{\partial x} + \eta_y \frac{\partial Y_1}{\partial y} + \eta_z \frac{\partial Y_1}{\partial z} \right) \\ \vdots \\ \rho D \left(\eta_x \frac{\partial Y_n}{\partial x} + \eta_y \frac{\partial Y_n}{\partial y} + \eta_z \frac{\partial Y_n}{\partial z} \right) \\ \eta_x \tau_{xx} + \eta_y \tau_{xy} + \eta_z \tau_{xz} \\ \eta_x \tau_{xy} + \eta_y \tau_{yy} + \eta_z \tau_{yz} \\ \eta_x \tau_{xz} + \eta_y \tau_{yz} + \eta_z \tau_{zz} \\ \eta_x \beta_x + \eta_y \beta_y + \eta_z \beta_z \\ - \left(\eta_x q_{1x}^{\text{vib}} + \eta_y q_{1y}^{\text{vib}} + \eta_z q_{1z}^{\text{vib}} \right) \\ \vdots \\ - \left(\eta_x q_{m_x}^{\text{vib}} + \eta_y q_{m_y}^{\text{vib}} + \eta_z q_{m_z}^{\text{vib}} \right) \end{bmatrix} \quad (3.8)$$

$$T' = \frac{1}{J} \begin{bmatrix} \rho D \left(\zeta_x \frac{\partial Y_1}{\partial x} + \zeta_y \frac{\partial Y_1}{\partial y} + \zeta_z \frac{\partial Y_1}{\partial z} \right) \\ \vdots \\ \rho D \left(\zeta_x \frac{\partial Y_n}{\partial x} + \zeta_y \frac{\partial Y_n}{\partial y} + \zeta_z \frac{\partial Y_n}{\partial z} \right) \\ \zeta_x \tau_{xx} + \zeta_y \tau_{xy} + \zeta_z \tau_{xz} \\ \zeta_x \tau_{xy} + \zeta_y \tau_{yy} + \zeta_z \tau_{yz} \\ \zeta_x \tau_{xz} + \zeta_y \tau_{yz} + \zeta_z \tau_{zz} \\ \zeta_x \beta_x + \zeta_y \beta_y + \zeta_z \beta_z \\ - \left(\zeta_x q_{1x}^{\text{vib}} + \zeta_y q_{1y}^{\text{vib}} + \zeta_z q_{1z}^{\text{vib}} \right) \\ \vdots \\ - \left(\zeta_x q_{m_x}^{\text{vib}} + \zeta_y q_{m_y}^{\text{vib}} + \zeta_z q_{m_z}^{\text{vib}} \right) \end{bmatrix}, \quad \dot{S}' = \frac{1}{J} \begin{bmatrix} \dot{\omega}_1^{\text{spe}} \\ \vdots \\ \dot{\omega}_n^{\text{spe}} \\ 0 \\ 0 \\ 0 \\ 0 \\ \dot{\omega}_1^{\text{vib}} \\ \vdots \\ \dot{\omega}_m^{\text{vib}} \end{bmatrix} \quad (3.9)$$

where

$$U' = \xi_x u + \xi_y v + \xi_z w \quad (3.10)$$

$$V' = \eta_x u + \eta_y v + \eta_z w \quad (3.11)$$

$$W' = \zeta_x u + \zeta_y v + \zeta_z w \quad (3.12)$$

$$(3.13)$$

and

$$\beta_x = \tau_{xx}u + \tau_{xy}v + \tau_{xz}w - q_x \quad (3.14)$$

$$\beta_y = \tau_{xy}u + \tau_{yy}v + \tau_{yz}w - q_y \quad (3.15)$$

$$\beta_z = \tau_{xz}u + \tau_{yz}v + \tau_{zz}w - q_z \quad (3.16)$$

$$(3.17)$$

Using the divergence theorem and Leibniz's integral rule, the governing equations can be written for a control volume (a cell in the computational domain) as below:

$$\begin{aligned} \frac{d}{dt} (\mathbf{Q}_{ijk} V_{ijk}) &+ \left(\mathbf{E}_{i+\frac{1}{2},jk} - \mathbf{E}_{i-\frac{1}{2},jk} \right) + \\ &\left(\mathbf{F}_{i,j+\frac{1}{2},k} - \mathbf{F}_{i,j-\frac{1}{2},k} \right) + \left(\mathbf{G}_{ij,k+\frac{1}{2}} - \mathbf{G}_{ij,k-\frac{1}{2}} \right) = \\ &\left(\mathbf{R}_{i+\frac{1}{2},jk} - \mathbf{R}_{i-\frac{1}{2},jk} \right) + \left(\mathbf{S}_{i,j+\frac{1}{2},k} - \mathbf{S}_{i,j-\frac{1}{2},k} \right) + \\ &\left(\mathbf{T}_{ij,k+\frac{1}{2}} - \mathbf{T}_{ij,k-\frac{1}{2}} \right) + \dot{\mathbf{S}}_{ijk} V_{ijk} \end{aligned} \quad (3.18)$$

where for simplicity E', F', G', R', S', T' , and \dot{S}' are written as E, F, G, R, S, T , and \dot{S} . These vectors can be simplified by defining

$$\vec{l}' = \frac{\vec{\nabla} \xi d\eta d\zeta}{J} \quad (3.19)$$

$$\vec{m}' = \frac{\vec{\nabla} \eta d\xi d\zeta}{J} \quad (3.20)$$

$$\vec{n}' = \frac{\vec{\nabla} \zeta d\xi d\eta}{J} \quad (3.21)$$

where \vec{l}' is a vector pointing normal to the ξ -face in positive xi -direction with magnitude equal to the area of the face. A similar definition applies to \vec{m}' and \vec{n}' . U, V , and W are defined as

$$U = \frac{U' d\eta d\zeta}{J} = \vec{V} \cdot \vec{l}' \quad (3.22)$$

$$V = \frac{V' d\xi d\zeta}{J} = \vec{V} \cdot \vec{m}' \quad (3.23)$$

$$W = \frac{W' d\xi d\eta}{J} = \vec{V} \cdot \vec{n}' \quad (3.24)$$

The vectors Q, E, F, G, R, S, T , and \dot{S} in the governing equations (Equation 3.19) can be simplified to

$$Q = \begin{bmatrix} \rho_1 \\ \vdots \\ \rho_n \\ \rho u \\ \rho v \\ \rho w \\ \rho \varepsilon \\ \rho_1 e_1^{\text{vib}} \\ \vdots \\ \rho_m e_m^{\text{vib}} \end{bmatrix}, \quad E = \begin{bmatrix} \rho_1 U \\ \vdots \\ \rho_n U \\ \rho u U + l'_x p \\ \rho v U + l'_y p \\ \rho w U + l'_z p \\ (\rho \varepsilon + p) U \\ \rho_1 e_1^{\text{vib}} U \\ \vdots \\ \rho_m e_m^{\text{vib}} U \end{bmatrix} \quad (3.25)$$

$$F = \begin{bmatrix} \rho_1 V \\ \vdots \\ \rho_n V \\ \rho u V + m'_x p \\ \rho v V + m'_y p \\ \rho w V + m'_z p \\ (\rho \varepsilon + p) V \\ \rho_1 e_1^{\text{vib}} V \\ \vdots \\ \rho_m e_m^{\text{vib}} V \end{bmatrix}, \quad G = \begin{bmatrix} \rho_1 W \\ \vdots \\ \rho_n W \\ \rho u W + n'_x p \\ \rho v W + n'_y p \\ \rho w W + n'_z p \\ (\rho \varepsilon + p) W \\ \rho_1 e_1^{\text{vib}} W \\ \vdots \\ \rho_m e_m^{\text{vib}} W \end{bmatrix} \quad (3.26)$$

$$R = \begin{bmatrix} \rho D \left(l'_x \frac{\partial Y_1}{\partial x} + l'_y \frac{\partial Y_1}{\partial y} + l'_z \frac{\partial Y_1}{\partial z} \right) \\ \vdots \\ \rho D \left(l'_x \frac{\partial Y_n}{\partial x} + l'_y \frac{\partial Y_n}{\partial y} + l'_z \frac{\partial Y_n}{\partial z} \right) \\ l'_x \tau_{xx} + l'_y \tau_{xy} + l'_z \tau_{xz} \\ l'_x \tau_{xy} + l'_y \tau_{yy} + l'_z \tau_{yz} \\ l'_x \tau_{xz} + l'_y \tau_{yz} + l'_z \tau_{zz} \\ l'_x \beta_x + l'_y \beta_y + l'_z \beta_z \\ - \left(l'_x q_{1x}^{\text{vib}} + l'_y q_{1y}^{\text{vib}} + l'_z q_{1z}^{\text{vib}} \right) \\ \vdots \\ - \left(l'_x q_{m_x}^{\text{vib}} + l'_y q_{m_y}^{\text{vib}} + l'_z q_{m_z}^{\text{vib}} \right) \end{bmatrix}, \quad S = \begin{bmatrix} \rho D \left(m'_x \frac{\partial Y_1}{\partial x} + m'_y \frac{\partial Y_1}{\partial y} + m'_z \frac{\partial Y_1}{\partial z} \right) \\ \vdots \\ \rho D \left(m'_x \frac{\partial Y_n}{\partial x} + m'_y \frac{\partial Y_n}{\partial y} + m'_z \frac{\partial Y_n}{\partial z} \right) \\ m'_x \tau_{xx} + m'_y \tau_{xy} + m'_z \tau_{xz} \\ m'_x \tau_{xy} + m'_y \tau_{yy} + m'_z \tau_{yz} \\ m'_x \tau_{xz} + m'_y \tau_{yz} + m'_z \tau_{zz} \\ m'_x \beta_x + m'_y \beta_y + m'_z \beta_z \\ - \left(m'_x q_{1x}^{\text{vib}} + m'_y q_{1y}^{\text{vib}} + m'_z q_{1z}^{\text{vib}} \right) \\ \vdots \\ - \left(m'_x q_{m_x}^{\text{vib}} + m'_y q_{m_y}^{\text{vib}} + m'_z q_{m_z}^{\text{vib}} \right) \end{bmatrix} \quad (3.27)$$

$$T = \begin{bmatrix} \rho D \left(n'_x \frac{\partial Y_1}{\partial x} + n'_y \frac{\partial Y_1}{\partial y} + n'_z \frac{\partial Y_1}{\partial z} \right) \\ \vdots \\ \rho D \left(n'_x \frac{\partial Y_n}{\partial x} + n'_y \frac{\partial Y_n}{\partial y} + n'_z \frac{\partial Y_n}{\partial z} \right) \\ n'_x \tau_{xx} + n'_y \tau_{xy} + n'_z \tau_{xz} \\ n'_x \tau_{xy} + n'_y \tau_{yy} + n'_z \tau_{yz} \\ n'_x \tau_{xz} + n'_y \tau_{yz} + n'_z \tau_{zz} \\ n'_x \beta_x + n'_y \beta_y + n'_z \beta_z \\ - \left(n'_x q_{1x}^{\text{vib}} + n'_y q_{1y}^{\text{vib}} + n'_z q_{1z}^{\text{vib}} \right) \\ \vdots \\ - \left(n'_x q_{m_x}^{\text{vib}} + n'_y q_{m_y}^{\text{vib}} + n'_z q_{m_z}^{\text{vib}} \right) \end{bmatrix}, \quad \dot{S} = \begin{bmatrix} \dot{\omega}_1^{\text{spe}} \\ \vdots \\ \dot{\omega}_n^{\text{spe}} \\ 0 \\ 0 \\ 0 \\ 0 \\ \dot{\omega}_1^{\text{vib}} \\ \vdots \\ \dot{\omega}_m^{\text{vib}} \end{bmatrix} \quad (3.28)$$

3.3 Inviscid Flux Methods

Due to the discontinuity of the conservative variables in the adjacent cells, it is necessary to use some methods to calculate a unique flux between the adjacent cells despite the existence of a discontinuity between the two cells. Several methods are developed over the years to calculate inviscid fluxes. Some of these methods are based on the exact or approximate solution of the Riemann problem (known as Godunov, Riemann, or Flux Difference

Splitting Methods), while others used flux vector splitting. In this dissertation, three inviscid flux method are used namely Advection Upstream Splitting Method (AUSM) [90], Roe's Method [91, 92], and Van Leer's Method [92]. Roe's method is a Godunov method while AUSM and Van Leer's methods are flux vector splitting methods. The description of inviscid fluxes are limited to one-dimensional perfect gas flows; however, the extension to three-dimensional and non-equilibrium flows is straight forward.

3.3.1 Advection Upstream Splitting Method (AUSM)

To have a better understanding of how the flux method works, the one-dimensional Euler equations presented in Equation 3.29 are used. Extension of the method to three-dimension is straight forward.

$$\frac{\partial \mathbf{Q}}{\partial t} + \frac{\partial \mathbf{F}}{\partial x} = \mathbf{0} \quad (3.29)$$

where,

$$\mathbf{Q} = \begin{bmatrix} \rho \\ \rho u \\ \rho \varepsilon \end{bmatrix} \quad \mathbf{F} = \begin{bmatrix} \rho u \\ \rho u^2 + p \\ u(\rho \varepsilon + p) \end{bmatrix} \quad (3.30)$$

where,

$$\rho \varepsilon = \frac{p}{(\gamma - 1)} + \frac{1}{2} \rho u^2 \quad (3.31)$$

and the specific total energy is

$$\varepsilon = H - \frac{p}{\rho} \quad (3.32)$$

where H is the total enthalpy per unit mass.

The inviscid flux is consist of two physical distinct parts: convective part (\mathbf{F}^c) and pressure part

$$\mathbf{F} = u \begin{pmatrix} \rho \\ \rho u \\ \rho H \end{pmatrix} + \begin{pmatrix} 0 \\ p \\ 0 \end{pmatrix} = \mathbf{F}^c + \begin{pmatrix} 0 \\ p \\ 0 \end{pmatrix} \quad (3.33)$$

The convective term (\mathbf{F}^c) is, therefore, a vector of scalars convected by the velocity u at the cell interface while the pressure term is propagated by the acoustic wave speed. Thus,

these two terms could be treated separately. If the face value is indicated by $\frac{1}{2}$ and the face value at its left and right identified by L and R respectively, the convective term can be written as

$$\mathbf{F}_{\frac{1}{2}}^c = u_{\frac{1}{2}} \begin{pmatrix} \rho \\ \rho u \\ \rho H \end{pmatrix}_{L/R} = M_{\frac{1}{2}} \begin{pmatrix} \rho a \\ \rho a u \\ \rho a H \end{pmatrix}_{L/R} \quad (3.34)$$

where

$$(\bullet)_{L/R} = \begin{cases} (\bullet)_L, & \text{if } M_{\frac{1}{2}} \geq 0 \\ (\bullet)_R, & \text{otherwise} \end{cases} \quad (3.35)$$

One way to calculate the convective Mach number ($M_{\frac{1}{2}}$) is to consider a combination of the wave speeds ($M \pm 1$) from both left and right cells traveling toward the face. Therefore,

$$M_{\frac{1}{2}} = M_L^+ + M_R^- \quad (3.36)$$

where Mach number M^\pm is defined using Van Leer splitting

$$M^\pm = \begin{cases} \pm \frac{1}{4} (M \pm 1)^2, & \text{if } |M| \leq 1 \\ \frac{1}{2} (M \pm |M|), & \text{otherwise} \end{cases} \quad (3.37)$$

The pressure term can be written as

$$p_{\frac{1}{2}} = p_L^+ + p_R^- \quad (3.38)$$

The pressure is weighted splitting using second order polynomial expansion of characteristic speeds ($M \pm 1$)

$$p^\pm = \begin{cases} \frac{p}{4} (M \pm 1)^2 (2 \mp M), & \text{if } |M| \leq 1 \\ \frac{p}{2} \frac{(M \pm |M|)}{M}, & \text{otherwise} \end{cases} \quad (3.39)$$

The flux term can be written as

$$\begin{pmatrix} \rho u \\ \rho u u + p \\ \rho u H \end{pmatrix}_{\frac{1}{2}} = \frac{M_{\frac{1}{2}}}{2} \left[\begin{pmatrix} \rho a \\ \rho a u \\ \rho a H \end{pmatrix}_L + \begin{pmatrix} \rho a \\ \rho a u \\ \rho a H \end{pmatrix}_R \right] - \frac{1}{2} |M_{\frac{1}{2}}| \Delta_{\frac{1}{2}} \begin{pmatrix} \rho a \\ \rho a u \\ \rho a H \end{pmatrix} + \begin{pmatrix} 0 \\ p_L^+ + p_R^- \\ 0 \end{pmatrix} \quad (3.40)$$

where

$$\Delta_{\frac{1}{2}}(\bullet) = (\bullet)_R - (\bullet)_L \quad (3.41)$$

The first term in the right hand side is a Mach number weighted average of the left and right fluxes, the second term is a numerical dissipation making the flux upwind, and the last term is the pressure term. This method is faster than the Roe method in calculating flux terms (Roe method will be discussed in Section 3.3.2) since it needs only to calculate the scalar values $|M_{\frac{1}{2}}|$, p_L^+ , and p_R^- rather than a matrix used in the Roe's method.

3.3.2 Roe's Method

Consider one-dimensional Euler equations (Equation 3.29 and 3.30) again. Consider a parameterization vector ν as

$$\nu = \begin{bmatrix} \nu_1 \\ \nu_2 \\ \nu_3 \end{bmatrix} = \begin{bmatrix} \sqrt{\rho} \\ \sqrt{\rho}u \\ \sqrt{\rho}H \end{bmatrix} \quad (3.42)$$

Vectors \mathbf{Q} and \mathbf{F} can be written as

$$\mathbf{Q} = \begin{bmatrix} \nu_1^2 \\ \nu_1\nu_2 \\ \frac{1}{\gamma}\nu_1\nu_3 + \frac{\gamma-1}{2\gamma}\nu_2^2 \end{bmatrix} \quad \mathbf{F} = \begin{bmatrix} \nu_1\nu_2 \\ \frac{\gamma-1}{\gamma}\nu_1\nu_3 + \frac{\gamma+1}{2\gamma}\nu_2^2 \\ \nu_2\nu_3 \end{bmatrix} \quad (3.43)$$

\mathbf{Q} and \mathbf{F} are quadratic relative to the vector ν elements. Thus, it is possible to find matrix B and C such that

$$\Delta\mathbf{Q} = B\Delta\nu \quad (3.44)$$

$$\Delta\mathbf{F} = C\Delta\nu \quad (3.45)$$

where $\Delta(\bullet) = (\bullet)_l - (\bullet)_r$. The matrices B and C are given in Equations (3.46) and (3.47), respectively.

$$B = \begin{bmatrix} 2\bar{\nu}_1 & 0 & 0 \\ \bar{\nu}_2 & \bar{\nu}_1 & 0 \\ \frac{1}{\gamma}\bar{\nu}_3 & \frac{\gamma-1}{\gamma}\bar{\nu}_2 & \frac{1}{\gamma}\bar{\nu}_1 \end{bmatrix} \quad (3.46)$$

$$C = \begin{bmatrix} \bar{\nu}_2 & \bar{\nu}_1 & 0 \\ \frac{\gamma-1}{\gamma}\bar{\nu}_3 & \frac{\gamma+1}{\gamma}\bar{\nu}_2 & \frac{\gamma-1}{\gamma}\bar{\nu}_1 \\ 0 & \bar{\nu}_3 & \bar{\nu}_2 \end{bmatrix} \quad (3.47)$$

where $\bar{\bullet} \equiv \frac{1}{2}(\bullet_l + \bullet_r)$.

Thus,

$$\Delta \mathbf{F} = A \Delta \mathbf{Q} \quad (3.48)$$

$$C \Delta \nu = AB \Delta \nu \quad (3.49)$$

$$\Delta \nu = C^{-1} AB \Delta \nu \quad (3.50)$$

$$A = CB^{-1} \quad (3.51)$$

Therefore, the A matrix is

$$A = \begin{bmatrix} 0 & 1 & 0 \\ \frac{\gamma-3}{2} \left(\frac{\bar{\nu}_2}{\bar{\nu}_1} \right)^2 & (3-\gamma) \frac{\bar{\nu}_2}{\bar{\nu}_1} & \gamma-1 \\ -\frac{\bar{\nu}_2 \bar{\nu}_3}{\bar{\nu}_1^2} + \frac{\gamma-1}{2} \left(\frac{\bar{\nu}_2}{\bar{\nu}_1} \right)^3 & \frac{\bar{\nu}_3}{\bar{\nu}_1} - (\gamma-1) \left(\frac{\bar{\nu}_2}{\bar{\nu}_1} \right)^2 & \gamma \frac{\bar{\nu}_2}{\bar{\nu}_1} \end{bmatrix} \quad (3.52)$$

which can be simplified as

$$A = \begin{bmatrix} 0 & 1 & 0 \\ \frac{\gamma-3}{2} \tilde{u}^2 & (3-\gamma) \tilde{u} & \gamma-1 \\ -\tilde{u} \tilde{H} + \frac{\gamma-1}{2} \tilde{u}^3 & \tilde{H} - (\gamma-1) \tilde{u}^2 & \gamma \tilde{u} \end{bmatrix} \quad (3.53)$$

where

$$\begin{aligned} \tilde{u} &\equiv \frac{\bar{\nu}_2}{\bar{\nu}_1} = \frac{\sqrt{\rho_l} u_l + \sqrt{\rho_r} u_r}{\sqrt{\rho_l} + \sqrt{\rho_r}} \\ \tilde{H} &\equiv \frac{\bar{\nu}_3}{\bar{\nu}_1} = \frac{\sqrt{\rho_l} H_l + \sqrt{\rho_r} H_r}{\sqrt{\rho_l} + \sqrt{\rho_r}} \end{aligned} \quad (3.54)$$

The quantity \tilde{u} is Roe-averaged velocity and \tilde{H} is Roe-averaged total enthalpy. The matrix A in Equation 3.53 is the Roe matrix.

The eigenvalues of matrix A can be found out by solving

$$\det(A - \lambda I) = 0 \quad (3.55)$$

This equation simplifies in the algebraic equation in Equation 3.56.

$$(\lambda - \tilde{u}) [\lambda - (\tilde{u} + \tilde{a})] [\lambda - (\tilde{u} - \tilde{a})] = 0 \quad (3.56)$$

where

$$\tilde{a} = \sqrt{(\gamma-1) \left(\tilde{H} - \frac{1}{2} \tilde{u}^2 \right)} \quad (3.57)$$

Therefore, eigenvalues of matrix A are

$$\begin{aligned}\lambda_1 &= \tilde{u} \\ \lambda_2 &= \tilde{u} + \tilde{a} \\ \lambda_3 &= \tilde{u} - \tilde{a}\end{aligned}\tag{3.58}$$

The corresponding eigenvectors for this eigenvalues of matrix A are

$$\mathbf{e}_1 = \begin{bmatrix} 1 \\ \tilde{u} \\ \frac{1}{2}\tilde{u}^2 \end{bmatrix} \quad \mathbf{e}_2 = \begin{bmatrix} 1 \\ \tilde{u} + \tilde{a} \\ \tilde{H} + \tilde{u}\tilde{a} \end{bmatrix} \quad \mathbf{e}_3 = \begin{bmatrix} 1 \\ \tilde{u} - \tilde{a} \\ \tilde{H} - \tilde{u}\tilde{a} \end{bmatrix}\tag{3.59}$$

The Roe matrix could be diagonalized as

$$A = S\Lambda S^{-1}\tag{3.60}$$

where S is the matrix of right eigenvectors of matrix A

$$S = \begin{bmatrix} 1 & 1 & 1 \\ \tilde{u} & \tilde{u} + \tilde{a} & \tilde{u} - \tilde{a} \\ \frac{1}{2}\tilde{u}^2 & \tilde{H} + \tilde{u}\tilde{a} & \tilde{H} - \tilde{u}\tilde{a} \end{bmatrix}\tag{3.61}$$

and

$$S^{-1} = \begin{bmatrix} 1 - \frac{\gamma-1}{2}\frac{\tilde{u}^2}{\tilde{a}^2} & (\gamma-1)\frac{\tilde{u}}{\tilde{a}^2} & -(\gamma-1)\frac{1}{\tilde{a}^2} \\ \frac{\gamma-1}{4}\frac{\tilde{u}^2}{\tilde{a}^2} - \frac{1}{2}\frac{\tilde{u}}{\tilde{a}} & \frac{1}{2\tilde{a}} - \frac{\gamma-1}{2}\frac{\tilde{u}}{\tilde{a}^2} & \frac{\gamma-1}{2}\frac{1}{\tilde{a}^2} \\ \frac{\gamma-1}{4}\frac{\tilde{u}^2}{\tilde{a}^2} + \frac{1}{2}\frac{\tilde{u}}{\tilde{a}} & -\frac{1}{2\tilde{a}} - \frac{\gamma-1}{2}\frac{\tilde{u}}{\tilde{a}^2} & \frac{\gamma-1}{2}\frac{1}{\tilde{a}^2} \end{bmatrix}\tag{3.62}$$

Semi-discrete form of Equation (3.29) is

$$\frac{d\mathbf{Q}_i}{dt} + \frac{\mathbf{F}_{i+\frac{1}{2}} - \mathbf{F}_{i-\frac{1}{2}}}{\Delta x} = \mathbf{0}\tag{3.63}$$

Considering the definition of Roe matrix, and Equation (3.60), the flux $\mathbf{F}_{i+\frac{1}{2}}$ becomes

$$\mathbf{F}_{i+\frac{1}{2}} = (A\mathbf{Q})_{i+\frac{1}{2}} = A\mathbf{Q}_{i+\frac{1}{2}} = (S\Lambda S^{-1})\mathbf{Q}_{i+\frac{1}{2}}\tag{3.64}$$

Using definition

$$\mathbf{R} = S^{-1}\mathbf{Q}\tag{3.65}$$

Equation (3.64) turns into

$$\mathbf{F}_{i+\frac{1}{2}} = (S\Lambda S^{-1})(S\mathbf{R})_{i+\frac{1}{2}} = S\Lambda\mathbf{R}_{i+\frac{1}{2}} \quad (3.66)$$

Using the Riemann problem solution and get advantage of characteristic lines

$$R_{k_{i+\frac{1}{2}}}^{n+1} = \frac{1}{2}(R_{k_l} + R_{k_r})^n + \frac{1}{2}\text{sign}(\lambda_k)(R_{k_l} - R_{k_r})^n \quad (3.67)$$

where R_k is the k^{th} element of vector \mathbf{R} and $k = 1, 2, 3$, r and l are respectively reconstructed right and left face values, and

$$\text{sign}(\lambda_k) = \begin{cases} +1, & \lambda_k > 0 \\ 0, & \lambda_k = 0 \\ -1, & \lambda_k < 0 \end{cases} \quad (3.68)$$

Therefore,

$$\mathbf{F}_{i+\frac{1}{2}} = \frac{1}{2}S\Lambda(\mathbf{R}_l + \mathbf{R}_r) + \frac{1}{2}S|\Lambda|(\mathbf{R}_l - \mathbf{R}_r) \quad (3.69)$$

where

$$|\Lambda| = \begin{bmatrix} |\lambda_1| & 0 & 0 \\ 0 & |\lambda_2| & 0 \\ 0 & 0 & |\lambda_3| \end{bmatrix} = \begin{bmatrix} |\tilde{u}| & 0 & 0 \\ 0 & |\tilde{u} + \tilde{a}| & 0 \\ 0 & 0 & |\tilde{u} - \tilde{a}| \end{bmatrix} \quad (3.70)$$

changing \mathbf{R} to \mathbf{Q} again

$$\mathbf{F}_{i+\frac{1}{2}} = \frac{1}{2}[S\Lambda S^{-1}(\mathbf{Q}_l + \mathbf{Q}_r) + S|\Lambda|S^{-1}(\mathbf{Q}_l - \mathbf{Q}_r)] \quad (3.71)$$

The final form of Roe method for calculation of inviscid flux is

$$\mathbf{F} = \frac{1}{2}[\mathbf{F}_l + \mathbf{F}_r + S|\Lambda|S^{-1}(\mathbf{Q}_l - \mathbf{Q}_r)] \quad (3.72)$$

It should be noted that Roe's method can produce a discontinuous expansion or expansion shock. Harten proposed to replace the Roe eigenvalues $|\lambda|$ with the approximate eigenvalues $|\tilde{\lambda}|$

$$|\tilde{\lambda}| = \begin{cases} \tilde{\lambda}_i^2 / (4\varepsilon\hat{a}) + \varepsilon\hat{a}, & \text{for } |\tilde{\lambda}| < 2\varepsilon\hat{a} \\ |\tilde{\lambda}_i|, & \text{for } |\tilde{\lambda}| \geq 2\varepsilon\hat{a} \end{cases} \quad (3.73)$$

where \hat{a} is a suitable velocity scale, and ε is a small positive number. This method satisfies $|\tilde{\lambda}| > 0$ for $i = 1, 2, 3$ and therefore, the determinant of matrix $S|\Lambda|S^{-1}$ is always positive.

In the calculations for this dissertation, $\hat{a} = \tilde{a}$ and $\varepsilon = 0.1$.

3.3.3 Roe Flux for Non-Equilibrium Equations

The one dimensional Euler equation in the direction normal to the face at which flux calculated for the non-equilibrium flow calculation is

$$\frac{\partial \mathbf{Q}}{\partial t} + \frac{\partial \mathbf{F}}{\partial x} = \mathbf{0} \quad (3.74)$$

where,

$$\mathbf{Q} = \begin{bmatrix} Q_1 \\ \vdots \\ Q_n \\ Q_{n+1} \\ Q_{n+2} \\ Q_{n+3} \\ Q_{n+4} \\ Q_{n+5} \\ \vdots \\ Q_{n+m+4} \end{bmatrix} = \begin{bmatrix} \rho_1 \\ \vdots \\ \rho_n \\ \rho u \\ \rho v \\ \rho w \\ \rho \varepsilon \\ \rho_1 e_1^{vib} \\ \vdots \\ \rho_m e_m^{vib} \end{bmatrix} \quad \mathbf{F} = \begin{bmatrix} F_1 \\ \vdots \\ F_n \\ F_{n+1} \\ F_{n+2} \\ F_{n+3} \\ F_{n+4} \\ F_{n+5} \\ \vdots \\ F_{n+m+4} \end{bmatrix} = \begin{bmatrix} \rho_1 u \\ \vdots \\ \rho_n u \\ \rho u^2 + p \\ \rho uv \\ \rho uw \\ u(\rho \varepsilon + p) \\ \rho_1 e_1^{vib} u \\ \vdots \\ \rho_m e_m^{vib} u \end{bmatrix} \quad (3.75)$$

where n is the number of species and m is the number of diatomic or polyatomic species.

Following the same procedure as was done for the perfect gas case, define

$$\begin{aligned} \tilde{u} &= \frac{\sqrt{\rho_l} u_l + \sqrt{\rho_r} u_r}{\sqrt{\rho_l} + \sqrt{\rho_r}} \\ \tilde{v} &= \frac{\sqrt{\rho_l} v_l + \sqrt{\rho_r} v_r}{\sqrt{\rho_l} + \sqrt{\rho_r}} \\ \tilde{w} &= \frac{\sqrt{\rho_l} w_l + \sqrt{\rho_r} w_r}{\sqrt{\rho_l} + \sqrt{\rho_r}} \\ \tilde{H} &= \frac{\sqrt{\rho_l} H_l + \sqrt{\rho_r} H_r}{\sqrt{\rho_l} + \sqrt{\rho_r}} \\ \tilde{Y}_i &= \frac{\sqrt{\rho_l} Y_{i_l} + \sqrt{\rho_r} Y_{i_r}}{\sqrt{\rho_l} + \sqrt{\rho_r}} \quad \text{for } i = 1, \dots, n \end{aligned} \quad (3.76)$$

The Roe matrix A is

$$A = \frac{\partial \mathbf{F}}{\partial \mathbf{Q}} \quad (3.77)$$

The eigenvalues of matrix A are

$$\begin{aligned}
 \lambda_j &= \tilde{u} \quad \text{for } j = 1, \dots, n+2 \\
 \lambda_{n+3} &= \tilde{u} + \tilde{a} \\
 \lambda_{n+4} &= \tilde{u} - \tilde{a} \\
 \lambda_{n+4+k} &= \tilde{u}^2 \quad \text{for } k = 1, \dots, m
 \end{aligned} \tag{3.78}$$

The Roe matrix could be diagonalized as

$$A = S \Lambda S^{-1} \tag{3.79}$$

where S is the matrix of right eigenvectors of matrix A

$$S = \begin{bmatrix}
 1 & \dots & 0 & \dots & 0 & 0 & 0 & \tilde{Y}_1 & \tilde{Y}_1 & 1 & \dots & 0 & \dots & 0 \\
 \vdots & \ddots & \vdots & \ddots & \vdots & \vdots & \vdots & \vdots & \vdots & \vdots & \ddots & \vdots & \ddots & \vdots \\
 0 & \dots & 1 & \dots & 0 & 0 & 0 & \tilde{Y}_j & \tilde{Y}_j & 0 & \dots & \delta_{jk} & \dots & \delta_{jm} \\
 \vdots & \ddots & \vdots & \ddots & \vdots & \vdots & \vdots & \vdots & \vdots & \vdots & \ddots & \vdots & \ddots & \vdots \\
 0 & \dots & 0 & \dots & 1 & 0 & 0 & \tilde{Y}_n & \tilde{Y}_n & 0 & \dots & 0 & \dots & 0 \\
 \tilde{u} & \dots & \tilde{u} & \dots & \tilde{u} & 0 & 0 & \tilde{u} + \tilde{a} & \tilde{u} - \tilde{a} & \tilde{u} & \dots & \tilde{u} & \dots & \tilde{u} \\
 \tilde{v} & \dots & \tilde{v} & \dots & \tilde{v} & 1 & 0 & \tilde{v} & \tilde{v} & \tilde{v} & \dots & \tilde{v} & \dots & \tilde{v} \\
 \tilde{w} & \dots & \tilde{w} & \dots & \tilde{w} & 0 & 1 & \tilde{w} & \tilde{w} & \tilde{w} & \dots & \tilde{w} & \dots & \tilde{w} \\
 \tilde{\Delta}_1 & \dots & \tilde{\Delta}_j & \dots & \tilde{\Delta}_n & \tilde{v} & \tilde{w} & \tilde{H} + \tilde{u}\tilde{a} & \tilde{H} - \tilde{u}\tilde{a} & 0 & \dots & 0 & \dots & 0 \\
 0 & \dots & 0 & \dots & 0 & 0 & 0 & \tilde{\alpha}_1 & \tilde{\alpha}_1 & -\tilde{\Delta}_1 & \dots & 0 & \dots & 0 \\
 \vdots & \ddots & \vdots & \ddots & \vdots & \vdots & \vdots & \vdots & \vdots & \vdots & \ddots & \vdots & \ddots & \vdots \\
 0 & \dots & 0 & \dots & 0 & 0 & 0 & \tilde{\alpha}_k & \tilde{\alpha}_k & 0 & \dots & -\tilde{\Delta}_k & \dots & 0 \\
 \vdots & \ddots & \vdots & \ddots & \vdots & \vdots & \vdots & \vdots & \vdots & \vdots & \ddots & \vdots & \ddots & \vdots \\
 0 & \dots & 0 & \dots & 0 & 0 & 0 & \tilde{\alpha}_m & \tilde{\alpha}_m & 0 & \dots & 0 & \dots & -\tilde{\Delta}_m
 \end{bmatrix} \tag{3.80}$$

where

$$\tilde{\alpha}_i = \tilde{Y}_i \tilde{e}_i^{\text{vib}} \quad \text{for } i = 1, \dots, m \tag{3.81}$$

and

$$\tilde{\Delta}_j = \tilde{h}_j - \frac{\tilde{\Gamma}}{\tilde{\Gamma} - 1} \frac{1}{\gamma_\infty M_\infty^2} \frac{\tilde{T}}{M_j} + \frac{1}{2} (\tilde{u}^2 + \tilde{v}^2 + \tilde{w}^2) \quad \text{for } j = 1, \dots, n \tag{3.82}$$

The function δ_{ij} is defines as

$$\delta_{ij} = \begin{cases} 1, & i = j \\ 0, & i \neq k \end{cases} \quad (3.83)$$

Matrix S^{-1} is

where

$$\tilde{\beta}_i = \tilde{\Delta}_i - (\tilde{u}^2 + \tilde{v}^2 + \tilde{w}^2) \quad (3.85)$$

and

$$\tilde{\nu}_i = \frac{\tilde{\Gamma} - 1}{\tilde{a}^2} \frac{1}{\tilde{\Delta}_i} (\tilde{\Delta}_i \tilde{Y}_i + \tilde{\alpha}_i) \quad (3.86)$$

and

$$\tilde{\delta} = \frac{\tilde{\Gamma} - 1}{\tilde{a}^2} \quad (3.87)$$

and

$$\tilde{\mu} = \frac{\tilde{u}\tilde{a}}{\tilde{\Gamma} - 1} \quad (3.88)$$

The final form of Roe method for calculation of flux is

$$\mathbf{F}_{i+\frac{1}{2}} = \frac{1}{2} [\mathbf{F}_l + \mathbf{F}_r + S|\Lambda|S^{-1}(\mathbf{Q}_l - \mathbf{Q}_r)] \quad (3.89)$$

where

$$\begin{aligned}
 |\Lambda| &= \begin{bmatrix} |\lambda_1| & \dots & 0 & 0 & 0 & 0 & 0 & 0 & \dots & 0 \\ \vdots & \ddots & \vdots & \vdots & \vdots & \vdots & \vdots & \vdots & \ddots & \vdots \\ 0 & \dots & |\lambda_n| & 0 & 0 & 0 & 0 & 0 & \dots & 0 \\ 0 & \dots & 0 & |\lambda_{n+1}| & 0 & 0 & 0 & 0 & \dots & 0 \\ 0 & \dots & 0 & 0 & |\lambda_{n+2}| & 0 & 0 & 0 & \dots & 0 \\ 0 & \dots & 0 & 0 & 0 & |\lambda_{n+3}| & 0 & 0 & \dots & 0 \\ 0 & \dots & 0 & 0 & 0 & 0 & |\lambda_{n+4}| & 0 & \dots & 0 \\ 0 & \dots & 0 & 0 & 0 & 0 & 0 & |\lambda_{n+4+1}| & \dots & 0 \\ \vdots & \ddots & \vdots & \vdots & \vdots & \vdots & \vdots & \vdots & \ddots & \vdots \\ 0 & \dots & 0 & 0 & 0 & 0 & 0 & 0 & \dots & |\lambda_{n+4+m}| \end{bmatrix} \\
 &= \begin{bmatrix} |\tilde{u}| & \dots & 0 & 0 & 0 & 0 & 0 & 0 & \dots & 0 \\ \vdots & \ddots & \vdots & \vdots & \vdots & \vdots & \vdots & \vdots & \ddots & \vdots \\ 0 & \dots & |\tilde{u}| & 0 & 0 & 0 & 0 & 0 & \dots & 0 \\ 0 & \dots & 0 & |\tilde{u}| & 0 & 0 & 0 & 0 & \dots & 0 \\ 0 & \dots & 0 & 0 & |\tilde{u}| & 0 & 0 & 0 & \dots & 0 \\ 0 & \dots & 0 & 0 & 0 & |\tilde{u} + \tilde{a}| & 0 & 0 & \dots & 0 \\ 0 & \dots & 0 & 0 & 0 & 0 & |\tilde{u} - \tilde{a}| & 0 & \dots & 0 \\ 0 & \dots & 0 & 0 & 0 & 0 & 0 & |\tilde{u}^2| & \dots & 0 \\ \vdots & \ddots & \vdots & \vdots & \vdots & \vdots & \vdots & \vdots & \ddots & \vdots \\ 0 & \dots & 0 & 0 & 0 & 0 & 0 & 0 & \dots & |\tilde{u}^2| \end{bmatrix} \tag{3.90}
 \end{aligned}$$

3.3.4 Van Leer's Method

Let's start with the one-dimensional Euler equations (Equation 3.29 and 3.30) again. The flux vector can be rewritten in the following form

$$\mathbf{F} = \begin{bmatrix} \rho a M \\ \frac{\rho a^2}{\gamma} (\gamma M^2 + 1) \\ \rho a^3 M \left(\frac{1}{\gamma-1} + \frac{1}{2} M^2 \right) \end{bmatrix} \tag{3.91}$$

In Van Leer's method, the term involving M splits into two parts while ρ and a evaluates

at the left and right side of each face denoted respectively by subscript l and r . For the mass flux, the term involving Mach number and thus needs to split is simply M . Therefore,

$$M = M^+ + M^- \quad (3.92)$$

and the mass flux is

$$\rho u = \rho_l a_l M^+ + \rho_r a_r M^- \quad (3.93)$$

where

$$M^\pm = \begin{cases} \pm \frac{1}{4} (M \pm 1)^2, & \text{if } |M| < 1 \\ \frac{1}{2} (M \pm |M|), & \text{otherwise} \end{cases} \quad (3.94)$$

The Mach number M is the average Mach number at the interface

$$M = \frac{u_l + u_r}{a_l + a_r} \quad (3.95)$$

For the momentum flux, the term involving Mach number is $(\gamma M^2 + 1)$ and it splits as

$$\gamma M^2 + 1 = (\gamma M^2 + 1)^+ + (\gamma M^2 + 1)^- \quad (3.96)$$

Therefore, the momentum flux splits as

$$\rho u^2 + p = \frac{\rho_l a_l^2}{\gamma} (\gamma M^2 + 1)^+ + \frac{\rho_r a_r^2}{\gamma} (\gamma M^2 + 1)^- \quad (3.97)$$

where

$$(\gamma M^2 + 1)^\pm = \begin{cases} \pm \frac{1}{4} (M \pm 1)^2 [(\gamma - 1) M \pm 2], & \text{if } |M| < 1 \\ \frac{1}{2M} [M (\gamma M^2 + 1) \pm |M (\gamma M^2 + 1)|], & \text{otherwise} \end{cases} \quad (3.98)$$

For the energy flux, the term involving the Mach number is $M \left[(\gamma - 1)^{-1} + \frac{1}{2} M^2 \right]$ and it splits as

$$M \left(\frac{1}{\gamma - 1} + \frac{1}{2} M^2 \right) = \left[M \left(\frac{1}{\gamma - 1} + \frac{1}{2} M^2 \right) \right]^+ + \left[M \left(\frac{1}{\gamma - 1} + \frac{1}{2} M^2 \right) \right]^- \quad (3.99)$$

The energy flux is then

$$(\rho e + p) u = \rho_l a_l^3 \left[M \left(\frac{1}{\gamma - 1} + \frac{1}{2} M^2 \right) \right]^+ + \rho_r a_r^3 \left[M \left(\frac{1}{\gamma - 1} + \frac{1}{2} M^2 \right) \right]^- \quad (3.100)$$

where

$$\left[M \left(\frac{1}{\gamma - 1} + \frac{1}{2} M^2 \right) \right]^\pm = \begin{cases} \pm \frac{1}{8} \frac{1}{(\gamma + 1)(\gamma - 1)} (M \pm 1)^2 [(\gamma - 1) M \pm 2]^2, & \text{if } |M| < 1 \\ \frac{1}{2} \left[M \left(\frac{1}{\gamma - 1} + \frac{1}{2} M^2 \right) \pm \left| M \left(\frac{1}{\gamma - 1} + \frac{1}{2} M^2 \right) \right| \right], & \text{otherwise} \end{cases} \quad (3.101)$$

3.4 Reconstruction

Reconstruction is a function used to approximate the distribution of dependent variables (\mathbf{Q}) in a cell. In the finite volume method, the value of \mathbf{Q} is stored at the center of each cell. However, to be able to calculate the flux values at faces, it is necessary to estimate the values of \mathbf{Q} at each face. This estimation for \mathbf{Q} provided using different reconstruction methods with different accuracy. Several reconstruction methods have been developed such as the Modified Upwind Scheme for Conservative Laws (MUSCL), Essentially Non-Oscillatory (ENO), and Weighted ENO (WENO) methods, each has its benefits and drawbacks. The reconstruction methods used for the simulations in this dissertation are first order reconstruction, third order accurate MUSCL based on primitive variables (MUSCLp), and Min-Mod reconstructions which will be explained in the next sections.

3.4.1 First Order

Consider the semi-discrete form of the Euler equation for the cell i shown in Figure 3.1.

$$\frac{d\mathbf{Q}_i}{dt} + \frac{\mathbf{F}_{i+\frac{1}{2}} - \mathbf{F}_{i-\frac{1}{2}}}{\Delta x} = 0 \quad (3.102)$$

where \mathbf{Q}_i , the average of dependent variable vector over the cell, is given by

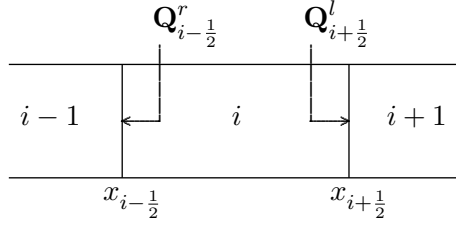
$$\mathbf{Q}_i(t) = \frac{1}{V_i} \int_{V_i} \mathcal{Q} dx dy dz \quad (3.103)$$

and $\mathbf{F}_{i\pm\frac{1}{2}}$, the spatial flux quadrature, are given by

$$\mathbf{F}_{i\pm\frac{1}{2}} = \frac{1}{A_{i\pm\frac{1}{2}}} \int_{x_{i\pm\frac{1}{2}}} \mathcal{F} dy dz \quad (3.104)$$

in which $A_{i\pm\frac{1}{2}} = \Delta y \Delta z$ is the area of faces at $x_{i\pm\frac{1}{2}}$.

To be able to calculate the fluxes in the x -direction, the values of dependent variables at the left and right sides of each face should be determined. A polynomial is used in each cell to approximate \mathcal{Q} . The polynomial that estimates the value of \mathcal{Q} at the left face of the cell i , which is the right side of the face at $x_{i-\frac{1}{2}}$, is $\mathbf{Q}_{i-\frac{1}{2}}^r$ and the $\mathbf{Q}_{i+\frac{1}{2}}^l$ is the approximate value for the left side of the face at $x_{i+\frac{1}{2}}$ which is the right face of the cell i (see Fig. 3.1). In the same way, by approximation of \mathcal{Q} in each cell, the left and right values at each cell will be

Figure 3.1: Reconstruction of interior face of Cell i

defined. The flux value at each face then be calculated using the right and left approximate values at that face.

The simplest possible reconstruction is the first order reconstruction. In this method, the conservative vector in each cell is reconstructed by

$$\mathbf{Q}_i(x) = \mathbf{Q}_i \quad (3.105)$$

Since the function has a constant value in the cell, the face values of cell i are

$$\mathbf{Q}_{i-\frac{1}{2}}^r = \mathbf{Q}_{i+\frac{1}{2}}^l = \mathbf{Q}_i \quad (3.106)$$

It should be noted that this method is numerically diffusive.

3.4.2 MUSCLp

The MUSCLp reconstruction method employs the cell average values of \mathbf{Q}_{i-1} , \mathbf{Q}_i , and \mathbf{Q}_{i+1} to approximate \mathbf{Q} at cell i . A primitive function $\mathbf{I}(x)$ is defined as

$$\mathbf{I}(x) = \int_{x_{i-\frac{3}{2}}}^x \mathbf{Q} dx \quad \text{for } x_{i-\frac{3}{2}} \leq x \leq x_{i+\frac{3}{2}} \quad (3.107)$$

where $\Delta x_i = x_{i+\frac{1}{2}} - x_{i-\frac{1}{2}}$ is a variable and it can change from one cell to its adjacent cell.

The definition of $\mathbf{I}(x)$ is valid for x in cells $i-1$, i , and $i+1$. Thus,

$$\begin{aligned} \mathbf{I}(x_{i-\frac{3}{2}}) &= 0 \\ \mathbf{I}(x_{i-\frac{1}{2}}) &= \Delta x_{i-1} \mathbf{Q}_{i-1} \\ \mathbf{I}(x_{i+\frac{1}{2}}) &= \Delta x_{i-1} \mathbf{Q}_{i-1} + \Delta x_i \mathbf{Q}_i \\ \mathbf{I}(x_{i+\frac{3}{2}}) &= \Delta x_{i-1} \mathbf{Q}_{i-1} + \Delta x_i \mathbf{Q}_i + \Delta x_{i+1} \mathbf{Q}_{i+1} \end{aligned} \quad (3.108)$$

There is a unique third order polynomial $\mathbf{P}(x)$ to approximate $\mathbf{I}(x)$ at four points $x_{i-\frac{3}{2}}$, $x_{i-\frac{1}{2}}$, $x_{i+\frac{1}{2}}$, and $x_{i+\frac{3}{2}}$. This polynomial is given as below by using Newton's formula

$$\begin{aligned}\mathbf{P}(x) = & \mathbf{a}_0 + \mathbf{a}_1(x - x_{i-\frac{3}{2}}) + \mathbf{a}_2(x - x_{i-\frac{3}{2}})(x - x_{i-\frac{1}{2}}) \\ & + \mathbf{a}_3(x - x_{i-\frac{3}{2}})(x - x_{i-\frac{1}{2}})(x - x_{i+\frac{1}{2}})\end{aligned}\quad (3.109)$$

where

$$\begin{aligned}\mathbf{a}_0 &= \mathbf{I}[x_{i-\frac{3}{2}}] \\ \mathbf{a}_1 &= \mathbf{I}[x_{i-\frac{3}{2}}, x_{i-\frac{1}{2}}] \\ \mathbf{a}_2 &= \mathbf{I}[x_{i-\frac{3}{2}}, x_{i-\frac{1}{2}}, x_{i+\frac{1}{2}}] \\ \mathbf{a}_3 &= \mathbf{I}[x_{i-\frac{3}{2}}, x_{i-\frac{1}{2}}, x_{i+\frac{1}{2}}, x_{i+\frac{3}{2}}]\end{aligned}\quad (3.110)$$

where

$$\begin{aligned}\mathbf{I}[x_{i-\frac{3}{2}}] &= \mathbf{I}(x_{i-\frac{3}{2}}) \\ \mathbf{I}[x_{i-\frac{3}{2}}, x_{i-\frac{1}{2}}] &= \frac{\mathbf{I}[x_{i-\frac{1}{2}}] - \mathbf{I}[x_{i-\frac{3}{2}}]}{x_{i-\frac{1}{2}} - x_{i-\frac{3}{2}}} \\ \mathbf{I}[x_{i-\frac{3}{2}}, x_{i-\frac{1}{2}}, x_{i+\frac{1}{2}}] &= \frac{\mathbf{I}[x_{i-\frac{1}{2}}, x_{i+\frac{1}{2}}] - \mathbf{I}[x_{i-\frac{3}{2}}, x_{i-\frac{1}{2}}]}{x_{i+\frac{1}{2}} - x_{i-\frac{3}{2}}} \\ \mathbf{I}[x_{i-\frac{3}{2}}, x_{i-\frac{1}{2}}, x_{i+\frac{1}{2}}, x_{i+\frac{3}{2}}] &= \frac{\mathbf{I}[x_{i-\frac{1}{2}}, x_{i+\frac{1}{2}}, x_{i+\frac{3}{2}}] - \mathbf{I}[x_{i-\frac{3}{2}}, x_{i-\frac{1}{2}}, x_{i+\frac{1}{2}}]}{x_{i+\frac{3}{2}} - x_{i-\frac{3}{2}}}\end{aligned}\quad (3.111)$$

The reconstruction function for \mathcal{Q} denotes $\mathbf{Q}(x)$ and defines as

$$\mathbf{Q}_i(x) = \frac{d\mathbf{P}}{dx} \quad \text{for } x_{i-\frac{1}{2}} \leq x \leq x_{i+\frac{1}{2}} \quad (3.112)$$

Thus,

$$\begin{aligned}\mathbf{Q}_i(x) = & \mathbf{a}_1 + \mathbf{a}_2 \left[(x - x_{i-\frac{1}{2}}) + (x - x_{i-\frac{3}{2}}) \right] \\ & + \mathbf{a}_3 \left[(x - x_{i-\frac{1}{2}})(x - x_{i+\frac{1}{2}}) + (x - x_{i-\frac{3}{2}})(x - x_{i+\frac{1}{2}}) + \right. \\ & \left. (x - x_{i-\frac{3}{2}})(x - x_{i-\frac{1}{2}}) \right]\end{aligned}\quad (3.113)$$

Using Equations (3.108), (3.110), and (3.111) and defining $\Delta\mathbf{Q}_{i+\frac{1}{2}} = \mathbf{Q}_{i+1} - \mathbf{Q}_i$ where the

\mathbf{Q}_i is the cell averaged value, the coefficient for reconstruction function become

$$\begin{aligned} \mathbf{a}_1 &= \mathbf{Q}_{i-1} \\ \mathbf{a}_2 &= (\Delta x_i + \Delta x_{i-1})^{-1} \Delta \mathbf{Q}_{i-\frac{1}{2}} \\ \mathbf{a}_3 &= [\Delta x_{i+1} + \Delta x_i + \Delta x_{i-1}]^{-1} \left(\frac{\Delta \mathbf{Q}_{i+\frac{1}{2}}}{\Delta x_{i+1} + \Delta x_i} - \frac{\Delta \mathbf{Q}_{i-\frac{1}{2}}}{\Delta x_i + \Delta x_{i-1}} \right) \end{aligned} \quad (3.114)$$

The left and right faces of cell i are identified as $i - \frac{1}{2}$ and $i + \frac{1}{2}$. Using Equation (3.113), the left and right reconstruction to the faces of cell i would be given as

$$\begin{aligned} \mathbf{Q}_{i+\frac{1}{2}}^l &= \mathbf{Q}_i + \Delta \mathbf{Q}_{i+\frac{1}{2}} \frac{(\Delta x_i + \Delta x_{i-1}) \Delta x_i}{(\Delta x_{i+1} + \Delta x_i) (\Delta x_{i+1} + \Delta x_i + \Delta x_{i-1})} \\ &\quad + \Delta \mathbf{Q}_{i-\frac{1}{2}} \frac{\Delta x_{i+1} \Delta x_i}{(\Delta x_i + \Delta x_{i-1}) (\Delta x_{i+1} + \Delta x_i + \Delta x_{i-1})} \\ \mathbf{Q}_{i-\frac{1}{2}}^r &= \mathbf{Q}_i - \Delta \mathbf{Q}_{i+\frac{1}{2}} \frac{\Delta x_i \Delta x_{i-1}}{(\Delta x_{i+1} + \Delta x_i) (\Delta x_{i+1} + \Delta x_i + \Delta x_{i-1})} \\ &\quad - \Delta \mathbf{Q}_{i-\frac{1}{2}} \frac{(\Delta x_i + \Delta x_{i+1}) \Delta x_i}{(\Delta x_i + \Delta x_{i-1}) (\Delta x_{i+1} + \Delta x_i + \Delta x_{i-1})} \end{aligned} \quad (3.115)$$

These equations could be rewritten as below

$$\begin{aligned} \mathbf{Q}_{i+\frac{1}{2}}^l &= \mathbf{Q}_i + \Delta \mathbf{Q}_{i+\frac{1}{2}} \kappa_{i+\frac{1}{2}}^l + \Delta \mathbf{Q}_{i-\frac{1}{2}} \kappa_{i-\frac{1}{2}}^l \\ \mathbf{Q}_{i-\frac{1}{2}}^r &= \mathbf{Q}_i - \Delta \mathbf{Q}_{i+\frac{1}{2}} \kappa_{i+\frac{1}{2}}^r - \Delta \mathbf{Q}_{i-\frac{1}{2}} \kappa_{i-\frac{1}{2}}^r \end{aligned} \quad (3.116)$$

where

$$\begin{aligned} \kappa_{i+\frac{1}{2}}^l &= \frac{(\Delta x_i + \Delta x_{i-1}) \Delta x_i}{(\Delta x_{i+1} + \Delta x_i) (\Delta x_{i+1} + \Delta x_i + \Delta x_{i-1})} \\ \kappa_{i-\frac{1}{2}}^l &= \frac{\Delta x_{i+1} \Delta x_i}{(\Delta x_i + \Delta x_{i-1}) (\Delta x_{i+1} + \Delta x_i + \Delta x_{i-1})} \\ \kappa_{i+\frac{1}{2}}^r &= \frac{\Delta x_i \Delta x_{i-1}}{(\Delta x_{i+1} + \Delta x_i) (\Delta x_{i+1} + \Delta x_i + \Delta x_{i-1})} \\ \kappa_{i-\frac{1}{2}}^r &= \frac{(\Delta x_i + \Delta x_{i+1}) \Delta x_i}{(\Delta x_i + \Delta x_{i-1}) (\Delta x_{i+1} + \Delta x_i + \Delta x_{i-1})} \end{aligned} \quad (3.117)$$

As it is denoted by these equations, the left value of the right face and the right value of the left face of cell i are calculated using cell averaged values of cells $i - 1$, i , and $i + 1$.

When there is no discontinuity in the flowfield, the reconstructed values at the faces would not create a new maximum or minimum values relative to the cells that they are reconstructed from. However, in the case of discontinuities in the flowfield such as the

existence of a shock wave, new extrema may be created which results in instability. Thus there are restrictions implemented on the flow as

$$\begin{aligned}
Q_{i+\frac{1}{2}}^l &\leq \max(Q_{i-1}, Q_i, Q_{i+1}) \\
Q_{i+\frac{1}{2}}^l &\geq \min(Q_{i-1}, Q_i, Q_{i+1}) \\
Q_{i-\frac{1}{2}}^r &\leq \max(Q_{i-1}, Q_i, Q_{i+1}) \\
Q_{i-\frac{1}{2}}^r &\geq \min(Q_{i-1}, Q_i, Q_{i+1})
\end{aligned} \tag{3.118}$$

Applying these restrictions to the flow is indicated as Modified Upwind Scheme for Conservation Laws which has the abbreviation of MUSCL.

Implying this restriction would end up to the following equations

$$\begin{aligned}
Q_{i+\frac{1}{2}}^l &= Q_i + \widehat{\Delta Q}_{i+\frac{1}{2}} \kappa_{i+\frac{1}{2}}^l + \widehat{\Delta Q}_{i-\frac{1}{2}} \kappa_{i-\frac{1}{2}}^l \\
Q_{i-\frac{1}{2}}^r &= Q_i - \widehat{\Delta Q}_{i+\frac{1}{2}} \kappa_{i+\frac{1}{2}}^r - \widehat{\Delta Q}_{i-\frac{1}{2}} \kappa_{i-\frac{1}{2}}^r
\end{aligned} \tag{3.119}$$

where the values of $\widehat{\Delta Q}_{i+\frac{1}{2}}$ and $\widehat{\Delta Q}_{i-\frac{1}{2}}$ are calculated using Table 3.1.

Table 3.1: ΔQ Values in MUSCL Method

$\Delta Q_{i+\frac{1}{2}} \geq 0$	$\widehat{\Delta Q}_{i-\frac{1}{2}} = \min \left(\Delta Q_{i-\frac{1}{2}}, \left(\frac{1-\kappa_{i+\frac{1}{2}}^l}{\kappa_{i-\frac{1}{2}}^l} \right) \Delta Q_{i+\frac{1}{2}} \right)$
$\Delta Q_{i-\frac{1}{2}} \geq 0$	$\widehat{\Delta Q}_{i+\frac{1}{2}} = \min \left(\Delta Q_{i+\frac{1}{2}}, \left(\frac{1-\kappa_{i-\frac{1}{2}}^r}{\kappa_{i+\frac{1}{2}}^r} \right) \Delta Q_{i-\frac{1}{2}} \right)$
$\Delta Q_{i+\frac{1}{2}} \leq 0$	$\widehat{\Delta Q}_{i-\frac{1}{2}} = \max \left(\Delta Q_{i-\frac{1}{2}}, -\frac{\kappa_{i+\frac{1}{2}}^l}{\kappa_{i-\frac{1}{2}}^l} \Delta Q_{i+\frac{1}{2}} \right)$
$\Delta Q_{i-\frac{1}{2}} \leq 0$	$\widehat{\Delta Q}_{i+\frac{1}{2}} = \min \left(\Delta Q_{i+\frac{1}{2}}, -\frac{\kappa_{i-\frac{1}{2}}^r}{\kappa_{i+\frac{1}{2}}^r} \Delta Q_{i-\frac{1}{2}} \right)$
$\Delta Q_{i+\frac{1}{2}} \leq 0$	$\widehat{\Delta Q}_{i-\frac{1}{2}} = \max \left(\Delta Q_{i-\frac{1}{2}}, \left(\frac{1-\kappa_{i+\frac{1}{2}}^l}{\kappa_{i-\frac{1}{2}}^l} \right) \Delta Q_{i+\frac{1}{2}} \right)$
$\Delta Q_{i-\frac{1}{2}} \leq 0$	$\widehat{\Delta Q}_{i+\frac{1}{2}} = \max \left(\Delta Q_{i+\frac{1}{2}}, \left(\frac{1-\kappa_{i-\frac{1}{2}}^r}{\kappa_{i+\frac{1}{2}}^r} \right) \Delta Q_{i-\frac{1}{2}} \right)$
$\Delta Q_{i+\frac{1}{2}} \leq 0$	$\widehat{\Delta Q}_{i-\frac{1}{2}} = \min \left(\Delta Q_{i-\frac{1}{2}}, -\frac{\kappa_{i+\frac{1}{2}}^l}{\kappa_{i-\frac{1}{2}}^l} \Delta Q_{i+\frac{1}{2}} \right)$
$\Delta Q_{i-\frac{1}{2}} \geq 0$	$\widehat{\Delta Q}_{i+\frac{1}{2}} = \max \left(\Delta Q_{i+\frac{1}{2}}, -\frac{\kappa_{i-\frac{1}{2}}^r}{\kappa_{i+\frac{1}{2}}^r} \Delta Q_{i-\frac{1}{2}} \right)$

There are different types of MUSCL reconstructions based on the variables used in the method which Table 3.2 gives a brief explanation for each one.

Table 3.2: Different MUSCL Methods

Method	Value Reconstructed
MUSCL	$\rho, \rho u, \rho v, \rho w, \rho e$
MUSCLp	ρ, u, v, w, p
MUSCLq	ρ, u, v, w, T

3.4.3 Min-Mod

This method is actually a part of MUSCL reconstruction, but due to its popularity, it has its own specific name. This is an upwind second-order reconstruction that uses values of cells $i - 1$ and i to calculate $\mathbf{Q}_{i+\frac{1}{2}}^l$ and cell values of i and $i + 1$ to calculate $\mathbf{Q}_{i-\frac{1}{2}}^r$.

$$\begin{aligned}\mathbf{Q}_{i+\frac{1}{2}}^l &= \mathbf{Q}_i + \frac{\Delta x_i}{\Delta x_i + \Delta x_{i-1}} \widehat{\Delta \mathbf{Q}}_{i-\frac{1}{2}} \\ \mathbf{Q}_{i-\frac{1}{2}}^r &= \mathbf{Q}_i - \frac{\Delta x_i}{\Delta x_i + \Delta x_{i+1}} \widehat{\Delta \mathbf{Q}}_{i+\frac{1}{2}}\end{aligned}\quad (3.120)$$

where

$$\begin{aligned}\widehat{\Delta \mathbf{Q}}_{i-\frac{1}{2}} &= \text{minmod} \left(\Delta \mathbf{Q}_{i-\frac{1}{2}}, b \Delta \mathbf{Q}_{i+\frac{1}{2}} \right) \\ \widehat{\Delta \mathbf{Q}}_{i+\frac{1}{2}} &= \text{minmod} \left(b' \Delta \mathbf{Q}_{i-\frac{1}{2}}, \Delta \mathbf{Q}_{i+\frac{1}{2}} \right)\end{aligned}\quad (3.121)$$

and b and b' are

$$\begin{aligned}b &= \frac{\Delta x_i + \Delta x_{i-1}}{\Delta x_i} \\ b' &= \frac{\Delta x_i + \Delta x_{i+1}}{\Delta x_i}\end{aligned}\quad (3.122)$$

The minmod function is defined as

$$\text{minmod}(x, y) = \begin{cases} x, & \text{if } |x| \leq |y| \text{ and } xy > 0 \\ y, & \text{if } |x| > |y| \text{ and } xy > 0 \\ 0, & \text{if } xy < 0 \end{cases}\quad (3.123)$$

3.5 Viscous Fluxes

Consider a 1-D viscous flow in a one species fluid. The governing equation for this flow is

$$\frac{\partial \mathbf{Q}}{\partial t} + \frac{\partial \mathbf{F}}{\partial x} = \frac{\partial \mathbf{R}}{\partial x}\quad (3.124)$$

where

$$\mathbf{Q} = \begin{bmatrix} \rho \\ \rho u \\ \rho \varepsilon \end{bmatrix} \quad \mathbf{F} = \begin{bmatrix} \rho u \\ \rho u^2 + p \\ u(\rho \varepsilon + p) \end{bmatrix} \quad \mathbf{R} = \begin{bmatrix} 0 \\ \tau \\ \tau u - q \end{bmatrix} \quad (3.125)$$

and \mathbf{R} is the viscous flux vector. The viscous fluxes are calculated using the second order central differencing method

$$\mathbf{R}_{i+\frac{1}{2}} = \frac{\mathbf{R}_{i+1} - \mathbf{R}_i}{\Delta x_i} \quad (3.126)$$

3.6 Time Integration

Time integration methods are used to move forward in time to get an unsteady solution or reach a steady state solution. There are several different methods for solving time dependent problems numerically among which three different time integration methods are used for this dissertation. These three methods are data-parallel line relaxation (DPLR) method [93], Dual-Time Stepping [94, 89], and second order Runge-Kutta method [92] which are described below. The line Gauss-Seidel [95, 89] is also a method used for finding the steady solution through iteration in time, however, this method is not time accurate.

3.6.1 DPLR

The data-parallel line relaxation method (DPLR) is a first order method in time that has the fast convergence properties of the Gauss-Seidel line relaxation method and high efficiency for parallel computations. In this method, the solution is implicit in the direction normal to the surface due to the stronger viscous effect in this direction and is explicit in the two other directions. Define ξ as the direction along the surface, η as the direction normal to the surface, and ζ as the third normal direction in the right hand system.

Consider Equation (3.19) which is the semi-discrete governing equation of the forementioned system if η is chosen in the correct direction. This equation can be expanded in the

following way

$$\begin{aligned}
& \frac{(\mathbf{Q}_{ijk}^{n+1} - \mathbf{Q}_{ijk}^n) V_{ijk}}{\Delta t} + \left(\mathbf{E}_{i+\frac{1}{2},jk}^{n+1} - \mathbf{E}_{i-\frac{1}{2},jk}^{n+1} \right) + \\
& \left(\mathbf{F}_{i,j+\frac{1}{2},k}^{n+1} - \mathbf{F}_{i,j-\frac{1}{2},k}^{n+1} \right) + \left(\mathbf{G}_{ij,k+\frac{1}{2}}^{n+1} - \mathbf{G}_{ij,k-\frac{1}{2}}^{n+1} \right) = \\
& \left(\mathbf{R}_{i+\frac{1}{2},jk}^{n+1} - \mathbf{R}_{i-\frac{1}{2},jk}^{n+1} \right) + \left(\mathbf{S}_{i,j+\frac{1}{2},k}^{n+1} - \mathbf{S}_{i,j-\frac{1}{2},k}^{n+1} \right) + \\
& \left(\mathbf{T}_{ij,k+\frac{1}{2}}^{n+1} - \mathbf{T}_{ij,k-\frac{1}{2}}^{n+1} \right) + \dot{\mathbf{S}}_{ijk}^{n+1} V_{ijk}
\end{aligned} \tag{3.127}$$

Starting with the inviscid flux term in ξ direction, using linearization in time

$$\mathbf{E}^{n+1} \simeq \mathbf{E}^n + \left(\frac{\partial \mathbf{E}}{\partial \mathbf{Q}} \right)^n (\mathbf{Q}^{n+1} - \mathbf{Q}^n) + \mathcal{O}(\Delta \mathbf{Q})^2 \tag{3.128}$$

the inviscid flux terms in Equation (3.127) become

$$\begin{aligned}
\mathbf{E}_{i+\frac{1}{2},jk}^{n+1} - \mathbf{E}_{i-\frac{1}{2},jk}^{n+1} &= \mathbf{E}_{i+\frac{1}{2},jk}^n + \left(\frac{\partial \mathbf{E}}{\partial \mathbf{Q}} \right)_{i+\frac{1}{2},jk}^n (\mathbf{Q}^{n+1} - \mathbf{Q}^n)_{i+\frac{1}{2},jk} \\
&- \mathbf{E}_{i-\frac{1}{2},jk}^n - \left(\frac{\partial \mathbf{E}}{\partial \mathbf{Q}} \right)_{i-\frac{1}{2},jk}^n (\mathbf{Q}^{n+1} - \mathbf{Q}^n)_{i-\frac{1}{2},jk}
\end{aligned} \tag{3.129}$$

The Jacobian matrix defines as

$$\frac{\partial \mathbf{E}}{\partial \mathbf{Q}} = A = A^+ + A^- \tag{3.130}$$

where A^+ and A^- are respectively Jacobians related to the nonnegative and negative eigenvalues. Hence,

$$\begin{aligned}
\mathbf{E}_{i+\frac{1}{2},jk}^{n+1} - \mathbf{E}_{i-\frac{1}{2},jk}^{n+1} &= \mathbf{E}_{i+\frac{1}{2},jk}^n - \mathbf{E}_{i-\frac{1}{2},jk}^n \\
&+ (A^+ + A^-)_{i+\frac{1}{2},jk} (\mathbf{Q}^{n+1} - \mathbf{Q}^n)_{i+\frac{1}{2},jk} \\
&- (A^+ + A^-)_{i-\frac{1}{2},jk} (\mathbf{Q}^{n+1} - \mathbf{Q}^n)_{i-\frac{1}{2},jk}
\end{aligned} \tag{3.131}$$

Note that characteristic lines for positive eigenvalues are right running and left running for negative eigenvalues. Therefore,

$$\begin{aligned}
\mathbf{E}_{i+\frac{1}{2},jk}^{n+1} - \mathbf{E}_{i-\frac{1}{2},jk}^{n+1} &= \mathbf{E}_{i+\frac{1}{2},jk}^n - \mathbf{E}_{i-\frac{1}{2},jk}^n \\
&+ A_{i+\frac{1}{2},jk}^+ \delta \mathbf{Q}_{ijk}^n + A_{i+\frac{1}{2},jk}^- \delta \mathbf{Q}_{i+1,jk}^n \\
&- A_{i-\frac{1}{2},jk}^+ \delta \mathbf{Q}_{i-1,jk}^n - A_{i-\frac{1}{2},jk}^- \delta \mathbf{Q}_{ijk}^n
\end{aligned} \tag{3.132}$$

where

$$\delta \mathbf{Q}^n = \mathbf{Q}^{n+1} - \mathbf{Q}^n \quad (3.133)$$

The final form for inviscid flux in ξ direction is

$$\begin{aligned} \mathbf{E}_{i+\frac{1}{2},jk}^{n+1} - \mathbf{E}_{i-\frac{1}{2},jk}^{n+1} &= \mathbf{E}_{i+\frac{1}{2},jk}^n - \mathbf{E}_{i-\frac{1}{2},jk}^n + A_{i+\frac{1}{2},jk}^- \delta \mathbf{Q}_{i+1,jk}^n \\ &+ \left(A_{i+\frac{1}{2},jk}^+ - A_{i-\frac{1}{2},jk}^- \right) \delta \mathbf{Q}_{ijk}^n - A_{i-\frac{1}{2},jk}^+ \delta \mathbf{Q}_{i-1,jk}^n \end{aligned} \quad (3.134)$$

Similarly, the inviscid flux in the η and ζ directions are respectively

$$\begin{aligned} \mathbf{F}_{i,j+\frac{1}{2},k}^{n+1} - \mathbf{F}_{i,j-\frac{1}{2},k}^{n+1} &= \mathbf{F}_{i,j+\frac{1}{2},k}^n - \mathbf{F}_{i,j-\frac{1}{2},k}^n + B_{i,j+\frac{1}{2},k}^- \delta \mathbf{Q}_{i,j+1,k}^n \\ &+ \left(B_{i,j+\frac{1}{2},k}^+ - B_{i,j-\frac{1}{2},k}^- \right) \delta \mathbf{Q}_{ijk}^n - B_{i,j-\frac{1}{2},k}^+ \delta \mathbf{Q}_{i,j-1,k}^n \end{aligned} \quad (3.135)$$

and

$$\begin{aligned} \mathbf{G}_{ij,k+\frac{1}{2}}^{n+1} - \mathbf{G}_{ij,k-\frac{1}{2}}^{n+1} &= \mathbf{G}_{ij,k+\frac{1}{2}}^n - \mathbf{G}_{ij,k-\frac{1}{2}}^n + C_{ij,k+\frac{1}{2}}^- \delta \mathbf{Q}_{ij,k+1}^n \\ &+ \left(C_{ij,k+\frac{1}{2}}^+ - C_{ij,k-\frac{1}{2}}^- \right) \delta \mathbf{Q}_{ijk}^n - C_{ij,k-\frac{1}{2}}^+ \delta \mathbf{Q}_{ij,k-1}^n \end{aligned} \quad (3.136)$$

where B and C are Jacobian matrices define as

$$\begin{aligned} B &= \frac{\partial \mathbf{F}}{\partial \mathbf{Q}} \\ C &= \frac{\partial \mathbf{G}}{\partial \mathbf{Q}} \end{aligned} \quad (3.137)$$

The source term $\dot{\mathbf{S}}$ is linearized as

$$\dot{\mathbf{S}}_{ijk}^{n+1} = \dot{\mathbf{S}}_{ijk}^n + D_{ijk} \delta \mathbf{Q}_{ijk}^n \quad (3.138)$$

where

$$D = \frac{\partial \dot{\mathbf{S}}}{\partial \mathbf{Q}} \quad (3.139)$$

For linearizing the viscous flux in ξ direction, first, it is written as

$$\mathbf{R}_{i+\frac{1}{2},jk}^{n+1} = R_\xi \left(\frac{\partial \hat{\mathbf{Q}}}{\partial \xi} \right)_{i+\frac{1}{2},jk}^{n+1} + R_\eta \left(\frac{\partial \hat{\mathbf{Q}}}{\partial \eta} \right)_{i+\frac{1}{2},jk}^{n+1} + R_\zeta \left(\frac{\partial \hat{\mathbf{Q}}}{\partial \zeta} \right)_{i+\frac{1}{2},jk}^{n+1} \quad (3.140)$$

where R_ξ , R_η , and R_ζ are not derivatives. The $\hat{\mathbf{Q}}$ is the primitive variables vector. Using

$$\hat{\mathbf{Q}}^{n+1} = \hat{\mathbf{Q}}^n + \delta \hat{\mathbf{Q}}^n \quad (3.141)$$

Equation (3.140) turns into

$$\begin{aligned} \mathbf{R}_{i+\frac{1}{2},jk}^{n+1} &= R_\xi \left(\frac{\partial \hat{\mathbf{Q}}}{\partial \xi} \right)_{i+\frac{1}{2},jk}^n + R_\xi \left(\frac{\partial \delta \hat{\mathbf{Q}}}{\partial \xi} \right)_{i+\frac{1}{2},jk}^n + R_\eta \left(\frac{\partial \hat{\mathbf{Q}}}{\partial \eta} \right)_{i+\frac{1}{2},jk}^n \\ &+ R_\eta \left(\frac{\partial \delta \hat{\mathbf{Q}}}{\partial \eta} \right)_{i+\frac{1}{2},jk}^n + R_\zeta \left(\frac{\partial \hat{\mathbf{Q}}}{\partial \zeta} \right)_{i+\frac{1}{2},jk}^n + R_\zeta \left(\frac{\partial \delta \hat{\mathbf{Q}}}{\partial \zeta} \right)_{i+\frac{1}{2},jk}^n \end{aligned} \quad (3.142)$$

Similar to Equation (3.140), we have

$$\mathbf{R}_{i+\frac{1}{2},jk}^n = R_\xi \left(\frac{\partial \hat{\mathbf{Q}}}{\partial \xi} \right)_{i+\frac{1}{2},jk}^n + R_\eta \left(\frac{\partial \hat{\mathbf{Q}}}{\partial \eta} \right)_{i+\frac{1}{2},jk}^n + R_\zeta \left(\frac{\partial \hat{\mathbf{Q}}}{\partial \zeta} \right)_{i+\frac{1}{2},jk}^n \quad (3.143)$$

Therefore,

$$\mathbf{R}_{i+\frac{1}{2},jk}^{n+1} = \mathbf{R}_{i+\frac{1}{2},jk}^n + R_\xi \left(\frac{\partial \delta \hat{\mathbf{Q}}}{\partial \xi} \right)_{i+\frac{1}{2},jk}^n + R_\eta \left(\frac{\partial \delta \hat{\mathbf{Q}}}{\partial \eta} \right)_{i+\frac{1}{2},jk}^n + R_\zeta \left(\frac{\partial \delta \hat{\mathbf{Q}}}{\partial \zeta} \right)_{i+\frac{1}{2},jk}^n \quad (3.144)$$

Neglecting the derivatives along with η and ζ direction at the $i + \frac{1}{2}$ surface,

$$\mathbf{R}_{i+\frac{1}{2},jk}^{n+1} = \mathbf{R}_{i+\frac{1}{2},jk}^n + R_\xi \left(\frac{\partial \delta \hat{\mathbf{Q}}}{\partial \xi} \right)_{i+\frac{1}{2},jk}^n \quad (3.145)$$

Discretize the derivation, it becomes

$$\mathbf{R}_{i+\frac{1}{2},jk}^{n+1} = \mathbf{R}_{i+\frac{1}{2},jk}^n + R_{\xi_{i+\frac{1}{2},jk}} \frac{\delta \hat{\mathbf{Q}}_{i+1,jk}^n - \delta \hat{\mathbf{Q}}_{ijk}^n}{\Delta \xi} \quad (3.146)$$

Considering $\Delta \xi = \Delta \eta = \Delta \zeta = 1$ (see Section 3.2) and

$$\delta \hat{\mathbf{Q}} = M \delta \mathbf{Q} \quad (3.147)$$

then

$$\mathbf{R}_{i+\frac{1}{2},jk}^{n+1} = \mathbf{R}_{i+\frac{1}{2},jk}^n + (R_\xi M)_{i+\frac{1}{2},jk} [\delta \mathbf{Q}_{i+1,jk}^n - \delta \mathbf{Q}_{ijk}^n] \quad (3.148)$$

Similarly,

$$\mathbf{R}_{i-\frac{1}{2},jk}^{n+1} = \mathbf{R}_{i-\frac{1}{2},jk}^n + (R_\xi M)_{i-\frac{1}{2},jk} [\delta \mathbf{Q}_{ijk}^n - \delta \mathbf{Q}_{i-1,jk}^n] \quad (3.149)$$

Thus, the total viscous flux in the ξ direction is

$$\begin{aligned} \mathbf{R}_{i+\frac{1}{2},jk}^{n+1} - \mathbf{R}_{i-\frac{1}{2},jk}^{n+1} &= \mathbf{R}_{i+\frac{1}{2},jk}^n - \mathbf{R}_{i-\frac{1}{2},jk}^n \\ &+ (R_\xi M)_{i+\frac{1}{2},jk} [\delta \mathbf{Q}_{i+1,jk}^n - \delta \mathbf{Q}_{ijk}^n] \\ &- (R_\xi M)_{i-\frac{1}{2},jk} [\delta \mathbf{Q}_{ijk}^n - \delta \mathbf{Q}_{i-1,jk}^n] \end{aligned} \quad (3.150)$$

Likewise, the viscous fluxes in the η and ζ direction respectively are

$$\begin{aligned}
\mathbf{S}_{i,j+\frac{1}{2},k}^{n+1} - \mathbf{S}_{i,j-\frac{1}{2},k}^{n+1} &= \mathbf{S}_{i,j+\frac{1}{2},k}^n - \mathbf{S}_{i,j-\frac{1}{2},k}^n \\
&+ (S_\eta M)_{i,j+\frac{1}{2},k} [\delta \mathbf{Q}_{i,j+1,k}^n - \delta \mathbf{Q}_{ijk}^n] \\
&- (S_\eta M)_{i,j-\frac{1}{2},k} [\delta \mathbf{Q}_{ijk}^n - \delta \mathbf{Q}_{i,j-1,k}^n]
\end{aligned} \tag{3.151}$$

and

$$\begin{aligned}
\mathbf{T}_{ij,k+\frac{1}{2}}^{n+1} - \mathbf{T}_{ij,k-\frac{1}{2}}^{n+1} &= \mathbf{T}_{ij,k+\frac{1}{2}}^n - \mathbf{T}_{ij,k-\frac{1}{2}}^n \\
&+ (T_\zeta M)_{ij,k+\frac{1}{2}} [\delta \mathbf{Q}_{ij,k+1}^n - \delta \mathbf{Q}_{ijk}^n] \\
&- (T_\zeta M)_{ij,k-\frac{1}{2}} [\delta \mathbf{Q}_{ijk}^n - \delta \mathbf{Q}_{ij,k-1}^n]
\end{aligned} \tag{3.152}$$

Inserting all the viscous and inviscid fluxes given by Equations (3.134), (3.135), (3.136), (3.150), (3.151), and (3.152) in Equation (3.127), and considering that η direction related to j variation is the implicit direction, the complete discretized equation is

$$\begin{aligned}
\hat{B}_{ijk} \delta \mathbf{Q}_{i,j+1,k}^n + \hat{A}_{ijk} \delta \mathbf{Q}_{ijk}^n + \hat{C}_{ijk} \delta \mathbf{Q}_{i,j-1,k}^n = \hat{\mathbf{R}}_{ijk} - \\
\frac{\Delta t}{V_{ijk}} \left[\left(A_{i+\frac{1}{2},jk}^- - (R_\xi M)_{i+\frac{1}{2},jk} \right) \delta \mathbf{Q}_{i+1,jk}^n - \right. \\
\left(A_{i-\frac{1}{2},jk}^+ + (R_\xi M)_{i-\frac{1}{2},jk} \right) \delta \mathbf{Q}_{i-1,jk}^n + \\
\left(C_{ij,k+\frac{1}{2}}^- - (T_\zeta M)_{ij,k+\frac{1}{2}} \right) \delta \mathbf{Q}_{ij,k+1}^n - \\
\left. \left(C_{ij,k-\frac{1}{2}}^+ + (T_\zeta M)_{ij,k-\frac{1}{2}} \right) \delta \mathbf{Q}_{ij,k-1}^n \right]
\end{aligned} \tag{3.153}$$

where

$$\begin{aligned}
\hat{A}_{ijk} = I + \frac{\Delta t}{V_{ijk}} \left[\left(A_{i+\frac{1}{2},jk}^+ - A_{i-\frac{1}{2},jk}^- \right) + (R_\xi M)_{i+\frac{1}{2},jk} + (R_\xi M)_{i-\frac{1}{2},jk} + \right. \\
\left(B_{i,j+\frac{1}{2},k}^+ - B_{i,j-\frac{1}{2},k}^- \right) + (S_\eta M)_{i,j+\frac{1}{2},k} + (S_\eta M)_{i,j-\frac{1}{2},k} + \\
\left(C_{ij,k+\frac{1}{2}}^+ - C_{ij,k-\frac{1}{2}}^- \right) + (T_\zeta M)_{ij,k+\frac{1}{2}} + (T_\zeta M)_{ij,k-\frac{1}{2}} - \\
\left. D_{ijk} V_{ijk} \right]
\end{aligned} \tag{3.154}$$

$$\hat{B}_{ijk} = \frac{\Delta t}{V_{ijk}} \left[B_{i,j+\frac{1}{2},k}^- - (S_\eta M)_{i,j+\frac{1}{2},k} \right] \tag{3.155}$$

$$\hat{C}_{ijk} = \frac{\Delta t}{V_{ijk}} \left[-B_{i,j-\frac{1}{2},k}^+ - (S_\eta M)_{i,j-\frac{1}{2},k} \right] \quad (3.156)$$

$$\begin{aligned} \hat{\mathbf{R}}_{ijk} = & -\frac{\Delta t}{V_{ijk}} \left[\left(\mathbf{F}_{i+\frac{1}{2},jk}^n - \mathbf{F}_{i-\frac{1}{2},jk}^n \right) + \left(\mathbf{G}_{i,j+\frac{1}{2},k}^n - \mathbf{G}_{i,j-\frac{1}{2},k}^n \right) + \left(\mathbf{H}_{ij,k+\frac{1}{2}}^n - \mathbf{H}_{ij,k-\frac{1}{2}}^n \right) - \right. \\ & \left. \left(\mathbf{R}_{i+\frac{1}{2},jk}^n - \mathbf{R}_{i-\frac{1}{2},jk}^n \right) - \left(\mathbf{S}_{i,j+\frac{1}{2},k}^n - \mathbf{S}_{i,j-\frac{1}{2},k}^n \right) - \left(\mathbf{T}_{ij,k+\frac{1}{2}}^n - \mathbf{T}_{ij,k-\frac{1}{2}}^n \right) - \right. \\ & \left. - \dot{\mathbf{S}}_{ijk}^n V_{ijk} \right] \quad (3.157) \end{aligned}$$

For solving this system of equations, $k_{max} + 1$ inner iterations are used in each iteration. In the first step, only $\hat{\mathbf{R}}$ is considered on the right hand side of Equation (3.153) and $\delta \mathbf{Q}^{(0)}$ is calculated.

$$\hat{B}_{ijk} \delta \mathbf{Q}_{i,j+1,k}^{(0)} + \hat{A}_{ijk} \delta \mathbf{Q}_{ijk}^{(0)} + \hat{C}_{ijk} \delta \mathbf{Q}_{i,j-1,k}^{(0)} = \hat{\mathbf{R}}_{ijk} \quad (3.158)$$

Then k_{max} relaxation steps are solved to find $\delta \mathbf{Q}^{(k_{max})}$ which is equal to $\delta \mathbf{Q}^n$.

$$\begin{aligned} \hat{B}_{ijk} \delta \mathbf{Q}_{i,j+1,k}^{(k)} + \hat{A}_{ijk} \delta \mathbf{Q}_{ijk}^{(k)} + \hat{C}_{ijk} \delta \mathbf{Q}_{i,j-1,k}^{(k)} = & \hat{\mathbf{R}}_{ijk} - \\ & \frac{\Delta t}{V_{ijk}} \left[\left(A_{i+\frac{1}{2},jk}^- - (R_\xi M)_{i+\frac{1}{2},jk} \right) \delta \mathbf{Q}_{i+1,jk}^{(k-1)} - \right. \\ & \left(A_{i-\frac{1}{2},jk}^+ + (R_\xi M)_{i-\frac{1}{2},jk} \right) \delta \mathbf{Q}_{i-1,jk}^{(k-1)} + \\ & \left(C_{ij,k+\frac{1}{2}}^- - (T_\zeta M)_{ij,k+\frac{1}{2}} \right) \delta \mathbf{Q}_{ij,k+1}^{(k-1)} - \\ & \left. \left(C_{ij,k-\frac{1}{2}}^+ + (T_\zeta M)_{ij,k-\frac{1}{2}} \right) \delta \mathbf{Q}_{ij,k-1}^{(k-1)} \right] \quad (3.159) \end{aligned}$$

3.6.2 Dual Time Stepping

This method has two different time integration: the first one is the usual time shows the real time of computation (t), and second a pseudo-time inner time integration (τ). For convergence of the pseudo-time, any method including the implicit methods which do not maintain time accuracy can be used while the outer time integration is implicit. This is because the accuracy of time integration is defined by the outer layer or real time integration. The implicit time integration of the one-dimensional governing equations with pseudo-time inner iterations are

$$\frac{\partial}{\partial \tau} \iiint \mathbf{Q} dV = - \left(\frac{\partial}{\partial t} \iiint_{V(t)} \mathbf{Q} dV + \iint_{S(t)} (\mathbf{E} - \mathbf{R}) \cdot \mathbf{n} dS - \iiint_{V(t)} \dot{\mathbf{S}} dV \right)^{m+1} \quad (3.160)$$

where m represents the pseudo time step. In each outer time step, the pseudo time integration will be converged or reached to the maximum iteration specified. The converged solution of the inner iteration is set as the result of the next real timestep.

3.6.3 Line Gauss-Seidel

The line Gauss-Seidel iteration method is used as a way to find a steady state solution in the GASPeX code. In this method, the computational domain is swept line by line several times until the solution reached the convergence criterion. The governing equation for this case can be written as

$$\frac{1}{\Delta t}\Delta\mathbf{Q} + \frac{1}{\Delta x}A\Delta\mathbf{Q} + \frac{1}{\Delta y}B\Delta\mathbf{Q} + \frac{1}{\Delta z}C\Delta\mathbf{Q} = \mathbf{0} \quad (3.161)$$

where A , B , and C matrices are Jacobians of fluxes in each direction and the right hand side is zero since the calculation is perfect gas and thus, there is no source term. This equation is simplified as

$$\left(\frac{1}{\Delta t}I + \frac{1}{\Delta x}A + \frac{1}{\Delta y}B + \frac{1}{\Delta z}C \right) \Delta\mathbf{Q} = \mathbf{0} \quad (3.162)$$

If direction j is considered as the implicit direction, Equation (3.162) can be expanded as

$$D_{ijk}\Delta\mathbf{Q}_{i-1,jk}^{n+1} + E_{ijk}\Delta\mathbf{Q}_{i+1,jk}^{n+1} + F_{ijk}\Delta\mathbf{Q}_{ijk}^{n+1} + G_{ijk}\Delta\mathbf{Q}_{ij,k-1}^{n+1} + H_{ijk}\Delta\mathbf{Q}_{ij,k+1}^{n+1} = \mathbf{R}_{ijk}^n - L_{ijk}\Delta\mathbf{Q}_{i,j-1,k}^{n+1} \quad (3.163)$$

where the matrices D , E , F , G , H , L , and vector R are defined by knowing the reconstruction method. Values of $\Delta\mathbf{Q}_{i,j-1,k}^{n+1}$ are known since the values of line $j - 1$ was calculated before line j . The j is varied over its entire domain and then using matrix solution for five-diagonal matrix, the unknown values of $\Delta\mathbf{Q}_{ijk}^{n+1}$ is solved. The n values start from 0 which is the initial condition and increased to the point that convergence criterion for $\Delta\mathbf{Q}_{ijk}^{n+1}$ is reached.

3.6.4 Runge-Kutta

Consider the governing equations given in Equation (3.1). This equation can be rewritten as

$$\frac{d\mathbf{Q}}{dt} = \frac{\partial(\mathbf{R} - \mathbf{E})}{\partial x} + \frac{\partial(\mathbf{S} - \mathbf{G})}{\partial y} + \frac{\partial(\mathbf{T} - \mathbf{H})}{\partial z} + \dot{\mathbf{S}} \quad (3.164)$$

The semi-discretized format of this equation is

$$\frac{d\mathbf{Q}_{ijk}}{dt} = \mathbf{Re}_{ijk} \quad (3.165)$$

where

$$\mathbf{Re}_{ijk} = \frac{\partial(\mathbf{R} - \mathbf{E})}{\partial x} + \frac{\partial(\mathbf{S} - \mathbf{G})}{\partial y} + \frac{\partial(\mathbf{T} - \mathbf{H})}{\partial z} + \dot{\mathbf{S}} \quad (3.166)$$

There are several types of Runge-Kutta time integration methods with different accuracy. One of the common Runge-Kutta methods is called the two-stage Runge-Kutta method which is second order accurate. In this method, there are two inner steps for each iteration in time. The entire procedure for iteration n of two-stage Runge-Kutta method is as follows

$$\begin{aligned} \mathbf{Q}_{ijk}^{(0)} &= \mathbf{Q}_{ijk}^n \\ \mathbf{Q}_{ijk}^{(1)} &= \mathbf{Q}_{ijk}^{(0)} + \frac{\Delta t}{2} \mathbf{Re}_{ijk}^{(0)} \\ \mathbf{Q}_{ijk}^{(2)} &= \mathbf{Q}_{ijk}^{(0)} + \Delta t \mathbf{Re}_{ijk}^{(0)} \\ \mathbf{Q}_{ijk}^{n+1} &= \mathbf{Q}_{ijk}^{(2)} \end{aligned} \quad (3.167)$$

3.7 Boundary Condition

The Numerical implementation of boundary conditions is very important. The boundary conditions should represent physics and be numerically stable. The boundary condition can be applied in different ways. One method is by using ghost cells. Ghost cells are imaginary cells that extend beyond the physical domain. If the dependent variables vector is defined appropriately in these ghost cells, the flux at the boundary is calculated as a regular cell. In this method, the main challenge is to define the dependent variables vector at the ghost cells. Another method for applying the boundary condition is to apply the boundary conditions directly to the boundary by calculating the flux at the boundary condition's boarder. In this section, the boundary conditions used in this dissertation are described.

3.7.1 Axisymmetric

The flux at the face with the axisymmetric boundary condition is zero because the surface area is zero.

3.7.2 Fixed

The fixed boundary condition is the freestream boundary condition for flow with Mach number above sonic. In such a case, all the eigenvalues are positive and thus, no information propagates upstream. Hence, the dependent variables vector can be fixed at the boundary with the values of the freestream. This boundary condition applied using ghost cells and the values of dependent variables at the ghost cells are also fixed at the freestream values.

$$\mathbf{Q}_{\text{gh}} = \mathbf{Q}_{\infty} \quad (3.168)$$

where \mathbf{Q}_{gh} is the dependent variables vector at the ghost cell and \mathbf{Q}_{∞} is the dependent variables vector at freestream.

3.7.3 No-slip Adiabatic

The no-slip adiabatic boundary condition for a non-catalytic wall defines as

$$\begin{aligned} \mathbf{V} &= 0 \\ \frac{\partial Y_i}{\partial n} &= 0 \\ \frac{\partial T}{\partial n} &= 0 \\ \frac{\partial e_i^{\text{vib}}}{\partial n} &= 0 \\ \frac{\partial p}{\partial n} &= 0 \end{aligned} \quad (3.169)$$

Ghost cells become handy for implementing this boundary condition.

3.7.4 No-slip Isothermal

The no-slip isothermal boundary condition for a non-catalytic wall is

$$\begin{aligned}
 \mathbf{V} &= 0 \\
 T &= T_w \\
 \frac{\partial Y_\alpha}{\partial n} &= 0 \\
 \frac{\partial p}{\partial n} &= 0
 \end{aligned} \tag{3.170}$$

where T_w is fixed wall temperature. For this boundary condition, there are two possible conditions for vibrational energies which are the same as having conditions on vibrational temperatures. These two conditions called “adiabatic for vibration” and “isothermal for vibration” (see Section 2.4).

There are two ways for implementing no-slip isothermal boundary condition in this dissertation, the first method is with using ghost cells and the second method is applying the boundary condition directly to the boundary face by calculation of the flux at the wall surface. In all the calculations presented here, the boundary condition is implemented using ghost cells except for the calculation of the hollow cylinder flare in Chapter 4.

3.7.5 Symmetry

The symmetry boundary condition is defined as

$$\begin{aligned}
 \mathbf{V} \cdot \hat{\mathbf{n}} &= 0 \\
 \frac{\partial (\mathbf{V} \times \hat{\mathbf{n}})}{\partial n} &= 0 \\
 \frac{\partial \rho_i}{\partial n} &= 0 \\
 \frac{\partial P}{\partial n} &= 0 \\
 \frac{\partial T}{\partial n} &= 0 \\
 \frac{\partial (\rho_i e_i^{\text{vib}})}{\partial n} &= 0
 \end{aligned} \tag{3.171}$$

where $\hat{\mathbf{n}}$ is the unit normal vector at wall. For implementing this boundary condition, ghost cells are used.

3.7.6 Zero-gradient

The zero-gradient boundary condition is used as an outflow boundary condition. For supersonic and hypersonic flow, this is justifiable by knowing that all the characteristic lines of the flow move downstream. If the outflow boundary location is far from any rapid change in the flow, the change normal to this direction can simply be ignored. In the case of the existence of a small subsonic region in the form of the boundary layer, the assumption of fully developed boundary layer - which is valid considering the length of the boundary layer over the surface in comparison to its thickness - reduces the governing equations to have a parabolic nature and thus the information can march downstream only and not upstream. Again, since there is no rapid change in the boundary layer, we can simply ignore any changes in the normal direction to the outflow boundary condition. The mathematical representation of the zero-gradient boundary condition is

$$\frac{\partial \mathbf{Q}}{\partial n} = 0 \quad (3.172)$$

where n is the direction normal to the boundary. This boundary condition is implemented using ghost cells as

$$\mathbf{Q}_{\text{gh}} = \mathbf{Q}_{il} \quad (3.173)$$

where \mathbf{Q}_{il} is the dependent variables vector at the last cell in the computational domain next to the boundary itself.

3.8 Message Passing Interface (MPI)

MPI is a programmer interface with related protocols and logical specifications to enable communication between processes. MPI is used for high-performance computing on a distributed memory system since it is portable and scalable. Using MPI, the calculation can be divided into smaller pieces called zones and assigned to several processors. MPI is an essential part of all the calculations in this dissertation.

3.9 Freestream Conditions

In the simulations, the mass fraction of the polyatomic species should be greater than zero to avoid the instability for calculation in the calculation of the vibrational temperature of that species. To avoid this problem, whenever the mass fraction of a polyatomic species in the freestream of the experiment is zero, the mass fraction of that species is considered as a small value (*e.g.*, 0.01). For example, in many of the calculations in this dissertation, the freestream mass fractions of N_2 , O_2 , and NO are 0.76, 0.23, and 0.01 for the calculation with Park I thermochemistry while the experimental mass fractions are 0.765, 0.235, and 0.0. This process is validated by comparison of the resultant surface heat transfer and surface pressure for the Park I calculation of a double cone (Chapter 5) while the mass fraction of NO is reduced.

3.10 Conclusion

In this chapter, the numerical methods of this dissertation are described. Choosing the correct numerical methods is an art that any researcher who works in the computational field should learn. The inconsistency between the methods introduces instability and even worst, unexpected unphysical results. Knowing the limits of each method in addition to the advantages and drawbacks of that method, enables any researcher to combine the methods that best work for the problem that is solved.

Part I

Shock-Shock and Shock Wave Boundary Layer Interaction in Hypersonic Flow

Chapter 4

Prediction of Aerothermodynamic Loading on a Hollow Cylinder Flare

The recent renewed interest in hypersonic flight brought attention to the capability of CFD methods for the prediction of hypersonic laminar shock wave boundary layer interactions. The recent set of experiments performed at Calspan University of Buffalo Research Center (CUBRC) showed the incapability of current CFD models in prediction of even simple geometries in high enthalpy hypersonic flows. The blind study based on this experiment at AVIATION 2014 showed the need for evaluation and examination of the current models for this type of flows.

4.1 Introduction

The blind study of AVIATION 2014 [96, 97] makes it evident that there is a problem in the prediction of aerothermodynamic loading in high enthalpy hypersonic flows. The separation region size was not predicted correctly and therefore the peak values of surface heat transfer and pressure were in error too. Different researchers who participated in this blind study used different CFD tools and thus the problem should be in the models used in their CFD modeling and not in their numerical methods.

In this chapter, different models are considered to evaluate which part of the modeling introduces the error to the solution. For this purpose, the hollow cylinder flare model of the CUBRC data set used for the AVIATION 2014 blind study is selected. The models are 1) full non-equilibrium laminar Navier-Stokes with Park I thermochemistry, 2) non-reactive model, 3) thermally perfect, and 4) calorically perfect. The effect of vibrational boundary condition type at the surface, namely, adiabatic for vibration and isothermal for vibration for non-reactive and Park I models are also evaluated.

4.2 Description of Experiment

Figure 4.1 shows the experimental model. The overall length of this hollow cylinder flare is 220 mm. The surface of this model equipped with eighteen pressure transducers and fifty one heat transfer gauges to measure the surface pressure and surface heat transfer. The experimental uncertainty of both surface pressure and heat transfer measurements is 10% [98]. Five sets of experiments were conducted in the LENS XX expansion tunnel at CUBRC at stagnation enthalpies ranges from 5.07 to 21.85 MJ/kg and Mach numbers from 11.3 to 13.2. Details of this tunnel are presented in Dufrene *et al.* [99, 100] The Reynolds number based on the freestream condition and the length of the hollow cylinder (*i.e.*, 101.6 mm) is from 12,192 to 57,912 ensure fully laminar flow [54]. Three of these five experiments are considered and listed in Table 4.1. These experiments are chosen as examples of the low, medium, and high stagnation enthalpies. The inflow gas is air in full thermochemical and chemical equilibrium with mass fractions of 0.765 and 0.235 respectively for N₂ and O₂. The surface of the model is isothermal at 300 K.

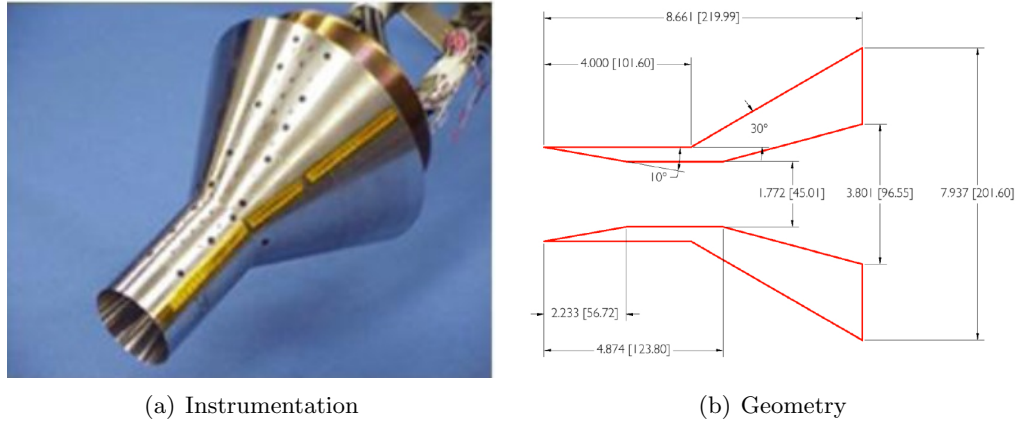


Figure 4.1: Small hollow cylinder flare (dimensions in inches [mm])

Table 4.1: Flow conditions

Run No.	Total Enthalpy (MJ/kg)	Mach Number	Pitot Pressure (kPa)	Unit Reynolds (/10 ⁶ m ⁻¹)	Velocity (km/s)	Density (g/m ³)	Temperature (K)
2	10.43	12.6	9.7	0.12	4.497	0.499	318
4	15.54	11.5	64.0	0.42	5.470	2.216	569
5	21.85	13.2	39.0	0.20	6.515	0.947	618

4.3 Methodology

The governing equations are the non-equilibrium laminar Navier-Stokes equation (see Section 2.2) with its simplified version corresponding to the simplified models used in this chapter. Table 4.2 gives a list of all the models used in this study. Roe's method with MUSCLp reconstruction is used to calculate the inviscid fluxes. DPLR method is used for time integration which enables usage of timesteps as large as the one achieved by CFL numbers in the order of several hundred. The simulation is initialized by freestream conditions and converged to the steady state solution. The calorically perfect results are calculated using GASPex software [89].

Table 4.2: Models Specifications

Model	Modification to governing equations		Transport Properties		Vibrational Energy B.C. at No-Slip Isothermal Wall
	$\dot{\omega}_\alpha^{\text{spe}}$	$\dot{\omega}_\alpha^{\text{vib}}$	Pr_∞	Le	
Calorically perfect	n/a	n/a	0.72	n/a	n/a
Thermally perfect	0	0	0.737	1.0	n/a
Isothermal non-reactive	0	$\rho_\alpha \dot{e}_\alpha^{\text{vib}}$	0.737	1.0	$T_\alpha^{\text{vib}} _w = T_w$
Adiabatic non-reactive	0	$\rho_\alpha \dot{e}_\alpha^{\text{vib}}$	0.737	1.0	$\left(\frac{\partial T_\alpha^{\text{vib}}}{\partial n}\right)\Big _w = 0$
Isothermal Park I	Eq. (2.4) and Park I	Eq. (2.25)	0.737	1.0	$T_\alpha^{\text{vib}} _w = T_w$
Adiabatic Park I	Eq. (2.4) and Park I	Eq. (2.25)	0.737	1.0	$\left(\frac{\partial T_\alpha^{\text{vib}}}{\partial n}\right)\Big _w = 0$

4.3.1 Computational Domain

The schematic of the computational domain is shown in Figure 4.2. The boundary conditions are symmetry from A to B, non-catalytic (*i.e.*, $\partial Y_\alpha / \partial n = 0$ where n is normal to the wall) non-slip isothermal wall from B to C, zero gradient outflow boundary conditions from

C to D, and fixed at freestream conditions from A to E and E to D. The use of non-catalytic wall for a stainless steel is justified based on the study by Rouhi Youssefi and Knight [101] in which the results of catalytic and non-catalytic wall for a stainless steel double cone at the same tunnel and similar conditions predicted no significant change on the peak values of surface pressure and heat transfer.

Three different sets of grids used for the simulations of this chapter consists of 0.6 M, 2.5 M, and 9.8 M cells. The grid properties of these grids are shown in Table 4.3. The GASPex software used three sequences of grids: 1.04 M cells, 4.18 M cells, and 16.7 M cells.

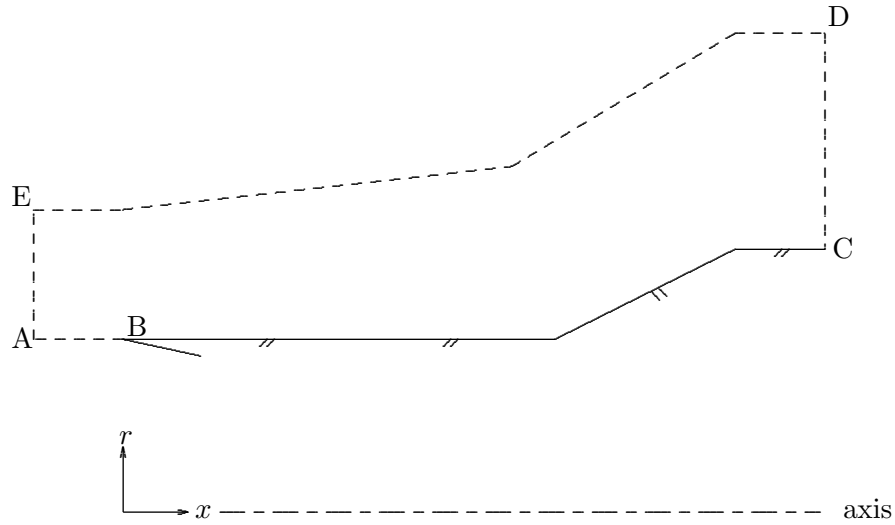


Figure 4.2: Computational domain

Table 4.3: Grid Properties

Grid Name	Total Cell Numbers	il	jl	kl	$\Delta\xi$ (μm)	$\Delta\eta_{min}$ (μm)	$\Delta\zeta$ (degree)
Grid 1	614,400	635	160	6	454	50	2.5
Grid 2	2,457,600	1270	320	6	227	25	2.5
Grid 3	9,830,400	2540	640	6	113.5	12.5	2.5

NOTE:

il is number of points along the wall

jl is number of points normal to the wall

kl is number of points in azimuthal direction

$\Delta\xi$ is spacing along the wall

$\Delta\eta$ is spacing normal to the wall

$\Delta\zeta$ is the axial spacing

4.4 Results

Four different models are used in this chapter to test the effect of each model on the prediction of surface pressure and heat transfer. These models are: 1) full non-equilibrium laminar Navier-Stokes equations with Park I [33] thermochemistry denoted “Park I” (see Section 2.2), 2) non-reactive (see Section 2.3.3), 3) thermally perfect (see Section 2.3.2), and 4) calorically perfect (see Section 2.3.1). Two of these models, namely Park I and non-reactive models, have two possible boundary conditions, adiabatic for vibration and isothermal for vibration, as described in Section 2.4. Here, for simplicity, the non-reactive model with isothermal for vibration and adiabatic for vibration boundary conditions are respectively called “isothermal non-reactive” and “adiabatic non-reactive”. Similarly, the Park I model with isothermal for vibrations is denoted as “isothermal Park I” while the Park I model with adiabatic for vibration boundary condition is named “adiabatic Park I”. Table 4.2 lists all these models with the specifications of each model.

The result section comprises three subsections: grid convergence study, comparison with experiments, and analysis of the flow structure.

4.4.1 Grid Study

In this dissertation, we conclude a solution is grid converged if the average difference between the two finest successive grids is significantly below the experimental uncertainty and the maximum difference also does not exceed the experimental uncertainty.

For the grid study, the isothermal Park I model is selected since it is the most complicated model in this dissertation. It is assumed that if grid convergence is achieved for this model, the solution of the simpler models is also grid converged. The surface pressure and heat transfer of Run 2 (10.43 MJ/kg) and Run 5 (21.85 MJ/kg) of isothermal Park I model are shown in Figures 4.3 and 4.4, respectively. Additionally, Tables 4.4 and 4.5 present the averaged change between two finest grid and the change at the peak location for Run 2 and Run 5 in the axial range of 2 cm to 20 cm. The finest grids are Grid 1 and Grid 2 for Run 2 and Grid 2 and Grid 3 for Run 5. From these figures and tables, the grid convergence of the calculations for Run 2 and Run 5 is concluded. This result is extended to Run 4

(15.54 MJ/kg) and thus it is considered that Grid 2 will provide a grid converged solution for all the cases. Figure 4.5 shows the grid study using three sets of grids used for the GASPex calculation (1.04 M cells, 4.18 M cells, and 16.7 M cells) for calorically perfect calculation. Thus, the results obtained by GASPex are also grid converged.

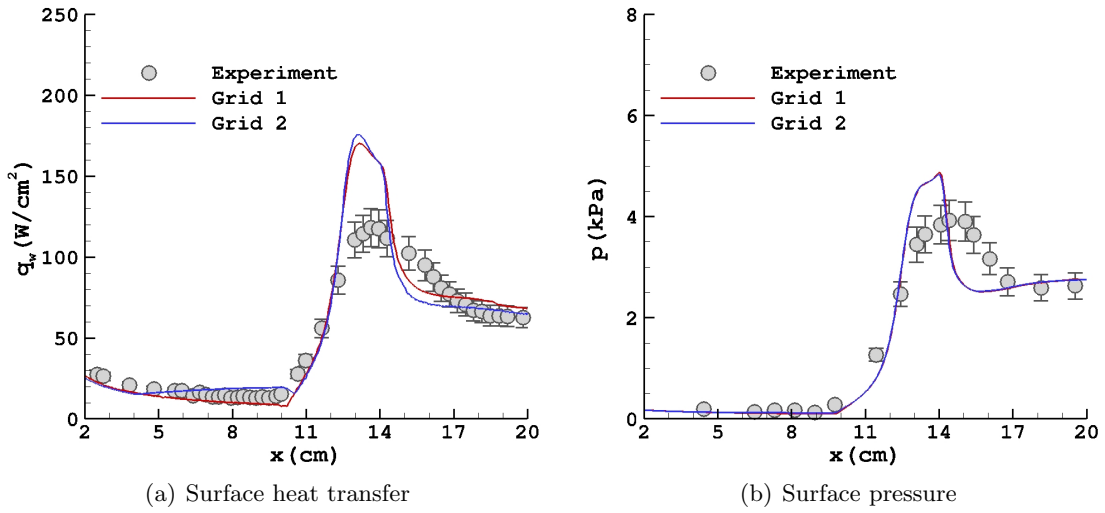


Figure 4.3: Grid study for Run 2 (10.43 MJ/kg) for isothermal Park I model

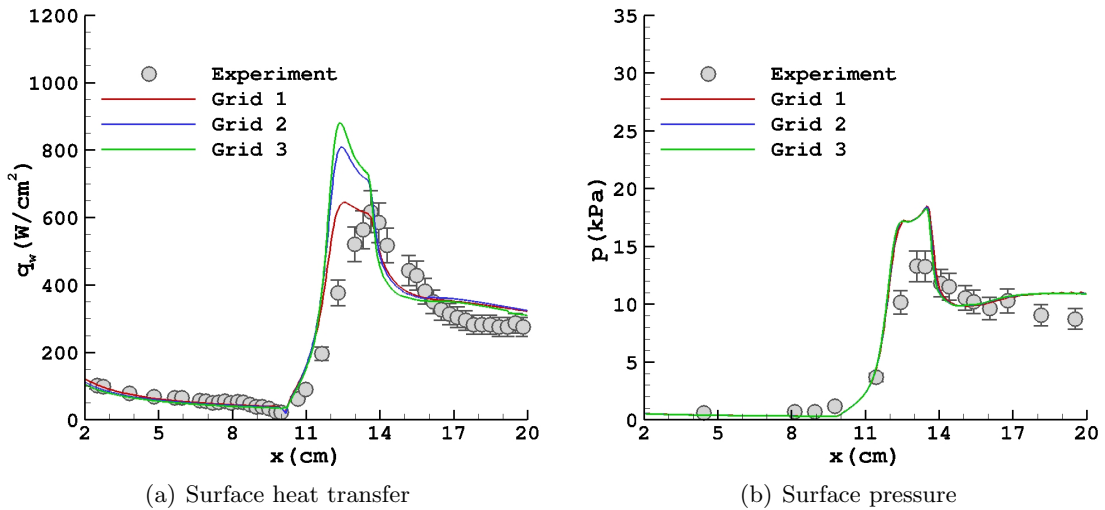


Figure 4.4: Grid Study for Run 5 (21.85 MJ/kg) for isothermal Park I model

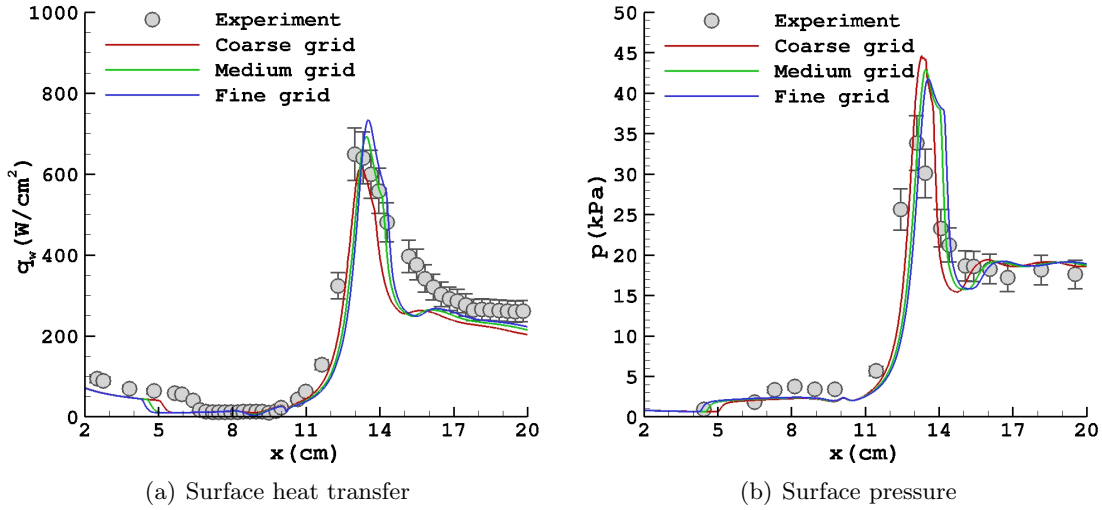


Figure 4.5: Grid Study for Run 4 (15.54 MJ/kg) for calorically perfect model

Table 4.4: Percentage of change between Grid 1 and Grid 2 for Run 2 (10.43 MJ/kg)

Model	q_w^1		p^1	
	Average	At peak	Average	At peak
Thermally perfect	4.74%	3.71%	0.70%	0.95%
Isothermal non-reactive	5.72%	3.34%	0.68%	0.96%
Adiabatic non-reactive	4.53%	4.20%	0.46%	0.79%
Isothermal Park I	5.83%	3.25%	0.69%	0.90%
Adiabatic Park I	4.71%	3.96%	0.69%	0.94%

NOTE:

¹ Experimental uncertainty is $\pm 10\%$

4.4.2 Comparison with Experiments

In this section, the computed surface heat transfer and surface pressure are compared with experimental data. The results are divided into two parts: first, the results of the main models, namely, Park I, non-reactive, thermally perfect, and calorically perfect are compared with experimental measurements. In the second part, the effect of the two boundary conditions, adiabatic for vibration and isothermal vibration, on the prediction of surface loadings are evaluated for Park I and non-reactive models.

The comparison of the results of these models also enables us to better understand the important modeling issue for this kind of problem. The comparison of the calorically perfect with thermally perfect results enables us to realize how effective the temperature dependency of specific heat and transport model is. The comparison of the non-reactive

Table 4.5: Percentage of change between Grid 2 and Grid 3 for Run 5 (21.85 MJ/kg)

Model	q_w^1		p^1	
	Average	At peak	Average	At peak
Thermally perfect	4.05%	8.92%	0.39%	0.70%
Isothermal non-reactive	4.68%	9.21%	0.42%	0.68%
Adiabatic non-reactive	3.89%	9.48%	0.44%	0.67%
Isothermal Park I	4.79%	9.15%	0.44%	0.68%
Adiabatic Park I	3.94%	9.35%	0.39%	0.66%

NOTE:

¹ Experimental uncertainty is $\pm 10\%$

prediction with thermally perfect enlightens the effect of vibrational-translational modeling. Finally, the comparison of the non-reactive and Park I model shows how important is the thermochemistry for these simulations.

Effect of Models

The comparison of computational and experimental results for surface heat transfer and surface pressure for Run 2 (10.43 MJ/kg) are presented in Figure 4.6. The adiabatic non-reactive and adiabatic Park I are denoted “non-reactive” and “Park I”, respectively. The results of thermally perfect, non-reactive and Park I models are almost identical except for the region before the rise in the surface heat transfer in which the non-reactive model has a lower prediction compared to the thermally perfect and Park I models. The predicted surface heat transfer by all four models over the hollow cylinder part are within the experimental uncertainty except in the beginning of the cylinder. The rise in the surface heat transfer due to shock wave boundary layer interaction is predicted accurately by all models. The calorically perfect model predicts peak heat transfer within the experimental uncertainty while thermally perfect, non-reactive and Park I models overpredict peak surface heat transfer by about 50%. The surface heat transfer at the end of the flare is slightly underpredicted by the calorically perfect model.

The predicted surface pressure over the hollow cylinder part is predicted accurately within the experimental uncertainty by all models. The surface pressure rise is predicted accurately by all four models; however, the peak surface pressure is overpredicted by all models by about 25%. The surface pressure at the aft part of the flare is predicted within

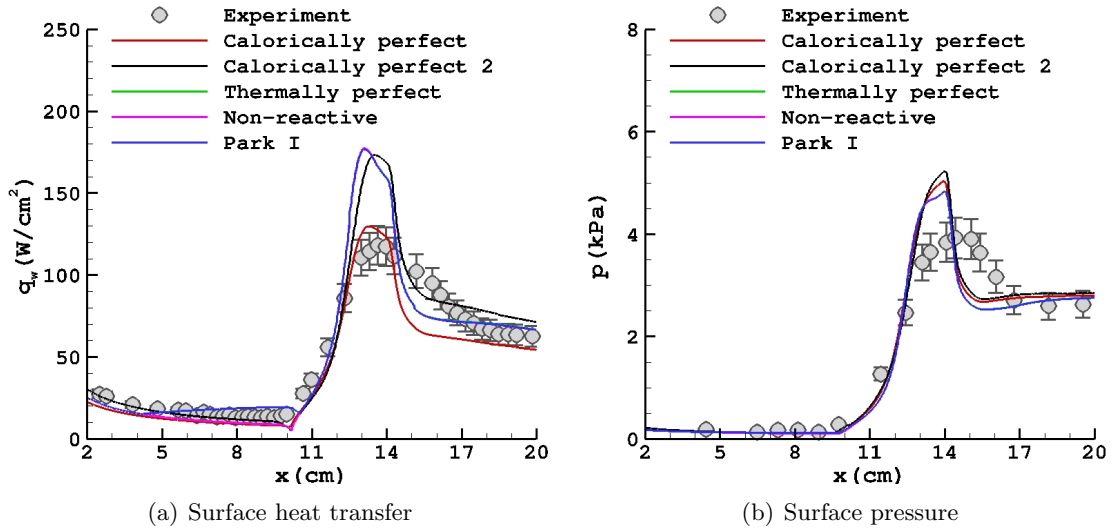


Figure 4.6: Comparison of different models with experiment for Run 2 (10.43 MJ/kg)

the experimental uncertainty by all models. These graphs suggest that while changing from calorically perfect to thermally perfect model has a significant effect especially in the surface heat transfer calculation (as we expected due to the change of specific heat according to temperature), the translational-vibrational energy exchange and thermochemical reactions have negligible effect in this calculation.

The comparison of the experimental and numerical results of the four models for Run 4 (15.54 MJ/kg) are presented in Figure 4.7. All four models predict the surface heat transfer over the hollow cylinder within the experimental uncertainty. The calorically perfect model predicts a larger separation region than the experiment while the thermally perfect, non-reactive and Park I models predict the separation region in agreement with the experiment. The rise in surface heat transfer starts at a larger axial distance for the calorically perfect model while the thermally perfect, non-reactive and Park I models predict the correct location. The calorically perfect model predicts peak heat transfer within the experimental uncertainty while thermally perfect, non-reactive and Park I models overpredict it by 40% to 45%. The heat transfer at the aft flare is accurately predicted by the calorically perfect model but overpredicted by thermally perfect, non-reactive and Park I models.

The surface pressure prediction over the hollow cylinder is within the experimental uncertainty for all the models. The surface pressure plateau in the separation region is

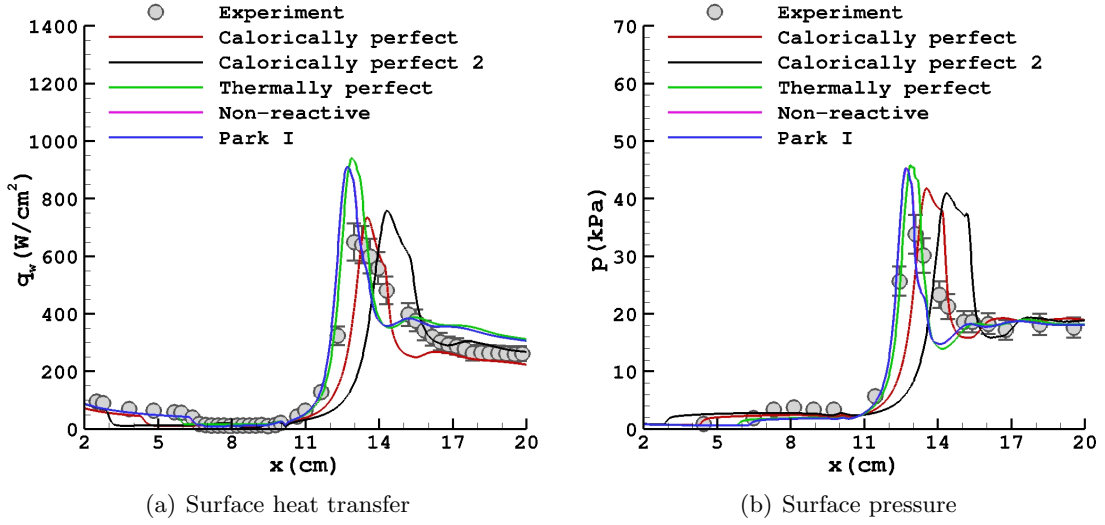


Figure 4.7: Comparison of different models with experiment for Run 4 (15.54 MJ/kg)

slightly underpredicted by all four models. The rising point of the surface pressure for the thermally perfect, non-reactive and Park I models is located at an axial distance comparable to the experiment while the calorically perfect model prediction is at greater axial distance compared to the experiment. The peak surface pressure is overpredicted by all models; however, the calorically perfect model overpredicts surface pressure by 23% while thermally perfect, non-reactive, and Park I models overpredict it by about 35%. All models accurately predict surface pressure at the end of the flare. Figure 4.7 shows again that changing from the calorically perfect to the thermally perfect model has a significant effect on the predicted surface pressure and heat transfer while translational-vibrational energy transfer and Park I thermochemistry effects on the predicted aerothermodynamic loading are negligible.

The comparison of the numerical and experimental results of the four models for Run 5 (21.85 MJ/kg) are presented in Figure 4.8. All models predict the surface heat transfer over the hollow cylinder within the experimental uncertainty. The calorically perfect model predicts a separation region while the thermally perfect, non-reactive and Park I models have no separation region. The rise in surface heat transfer starts at a smaller axial distance for the thermally perfect, non-reactive and Park I models relative to the calorically perfect model. The calorically perfect model overpredicts peak heat transfer by 30% while thermally perfect, non-reactive and Park I models overpredict it by about 45%. The heat transfer at

the aft flare is accurately predicted by the calorically perfect model but overpredicted by thermally perfect, non-reactive and Park I models.

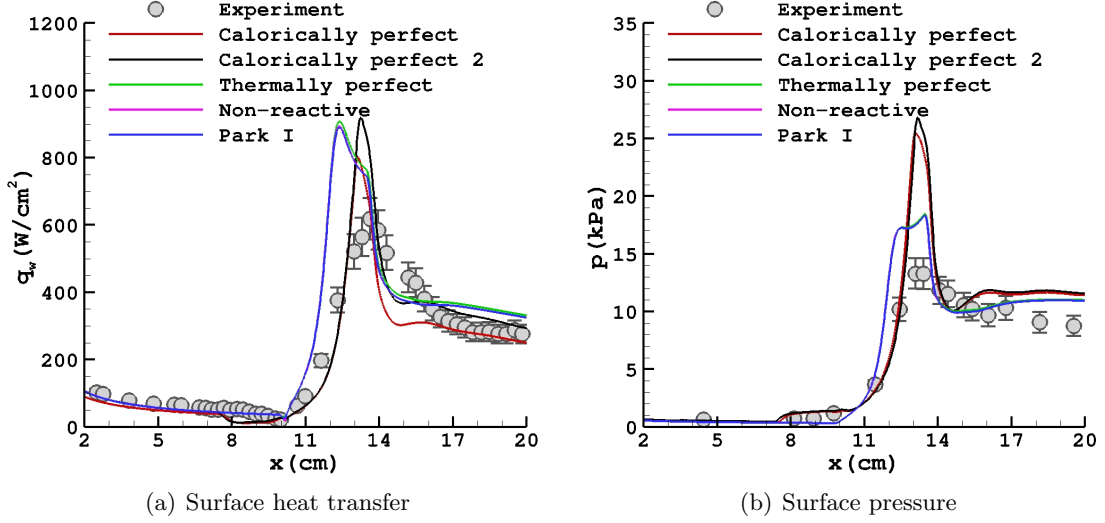


Figure 4.8: Comparison of different models with experiment for Run 5 (21.85 MJ/kg)

Similarly, the surface pressure prediction over the hollow cylinder is within the experimental uncertainty for all the models. The rising point of the surface pressure for the thermally perfect, non-reactive and Park I models is located at lower axial distance compared to the experimental data while the calorically perfect model prediction is comparable to the experiment. The peak surface pressure is overpredicted by all models; however, the calorically perfect model overpredicts surface pressure by 92% while thermally perfect, non-reactive, and Park I models overpredict it by about 38%. All models overpredict surface pressure at the end of the flare. Again from these figure, it is seen that while the effect of translational-vibrational energy transfer and Park I thermochemistry is negligible, there is a considerable change in the predicted surface heat transfer and surface pressure by changing from calorically perfect to thermally perfect model.

Effect of Vibrational Energies Boundary Condition at No-Slip Isothermal Wall

The computed and experimental results for surface heat transfer and surface pressure for the non-reactive and Park I models with two different possible vibrational energies boundary conditions at a no-slip isothermal wall namely, 1) isothermal for vibration and 2) adiabatic

for vibration, are presented in this section.

Figures 4.9 to 4.14 show respectively the comparison of the computational surface heat transfer and surface pressure of isothermal non-reactive and adiabatic non-reactive and isothermal Park I and adiabatic Park I respectively for Run 2 (10.43 MJ/kg), Run 4 (15.54 MJ/kg) and Run 5 (21.85 MJ/kg). There is no significant change in predicted surface heat transfer and surface pressure due to the change in the vibrational boundary condition at the wall.

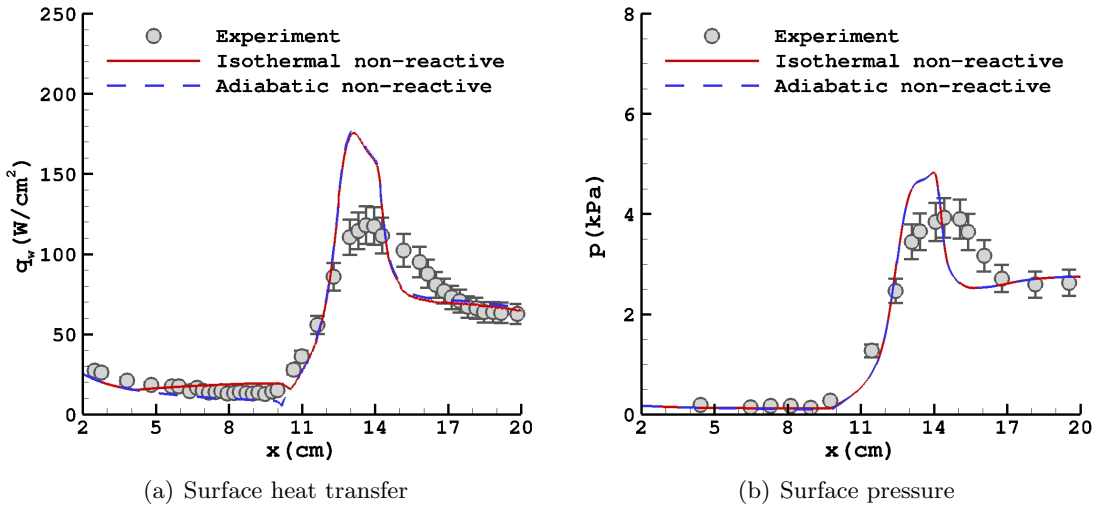


Figure 4.9: Comparison of different vibrational boundary condition of the non-reactive model with experiment for Run 2 (10.43 MJ/kg)

4.4.3 Analysis of Flow Structure

The Mach contours of the four models for Run 2 (10.43 MJ/kg) are shown in Figure 4.15. The non-reactive and Park I model presented here have the adiabatic for vibration boundary condition type. The displacement thickness shock interacts with the flare oblique shock. No separation region is created as a result of this interaction for any of the models simulations. The Mach contour plots shows no significant difference between the four main models.

Figure 4.16 shows Mach contours of the four models for Run 4 (15.54 MJ/kg). The boundary condition at the no-slip wall for the non-reactive and Park I models are adiabatic for vibration. In this case, the boundary layer is separated for all models due to the

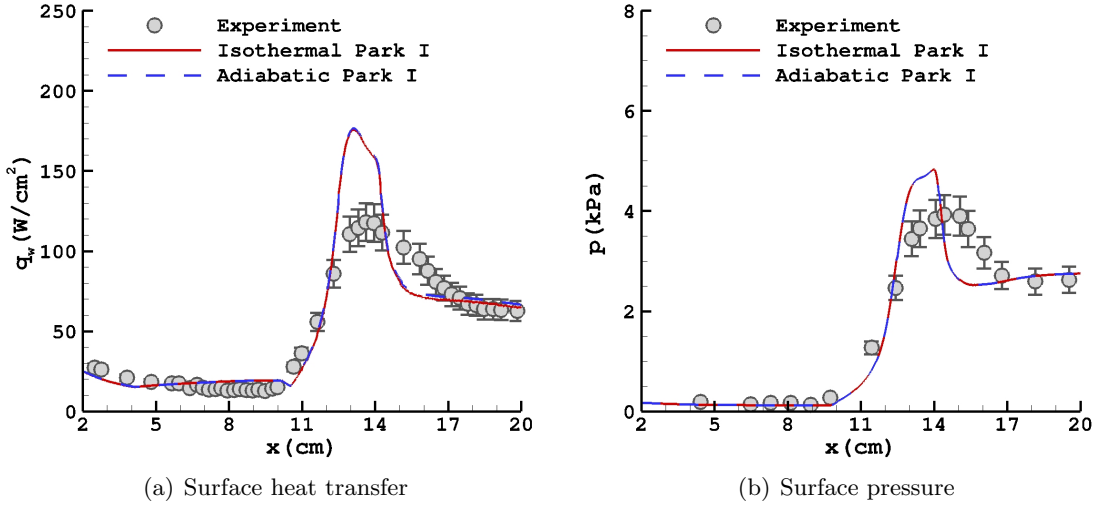


Figure 4.10: Comparison of different vibrational boundary condition of the Park I model with experiment for Run 2 (10.43 MJ/kg)

adverse pressure resulting from the interaction of the flare shock and the boundary layer displacement shock. The separation region creates a separation shock which interacts with the two other shocks at approximately the same location as the displacement shock for thermally perfect, non-reactive and Park I models while for the calorically perfect model, the boundary layer displacement shock and separation shock first interacts with each other and then the resultant shock interacts with the flare shock.

Figure 4.17 presents Mach contours of all models for Run 5 (21.85 MJ/kg). Again, the adiabatic non-reactive and adiabatic Park I are used for representing the results. In the calorically perfect gas model, the adverse pressure due to the interaction of the displacement thickness shock and the flare shock is strong enough to separate the boundary layer while for other models, there is no separation region. The separation region itself creates a separation shock which interacts with the flare shock at approximately the location of reattachment point.

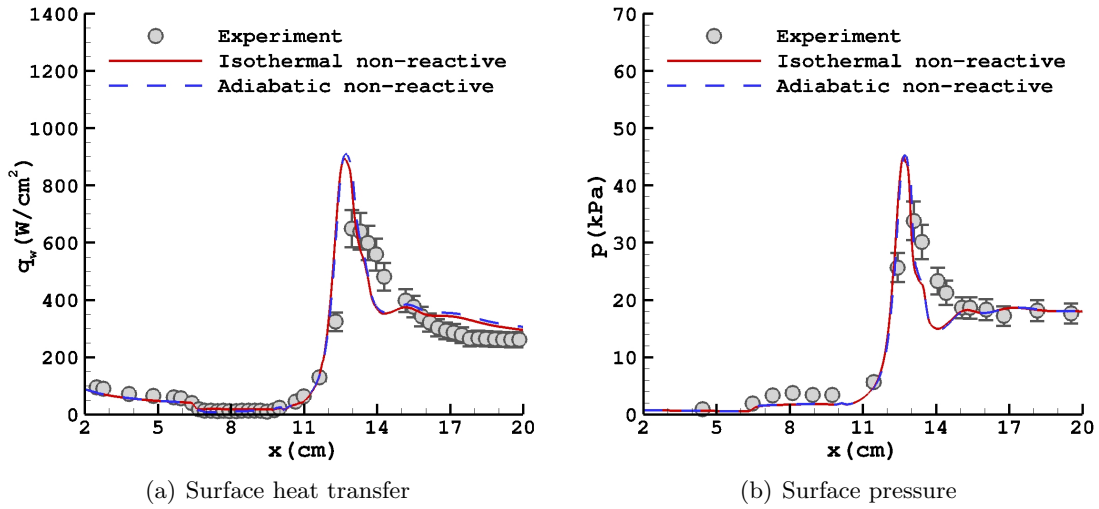


Figure 4.11: Comparison of different vibrational boundary condition of the non-reactive model with experiment for Run 4 (15.54 MJ/kg)

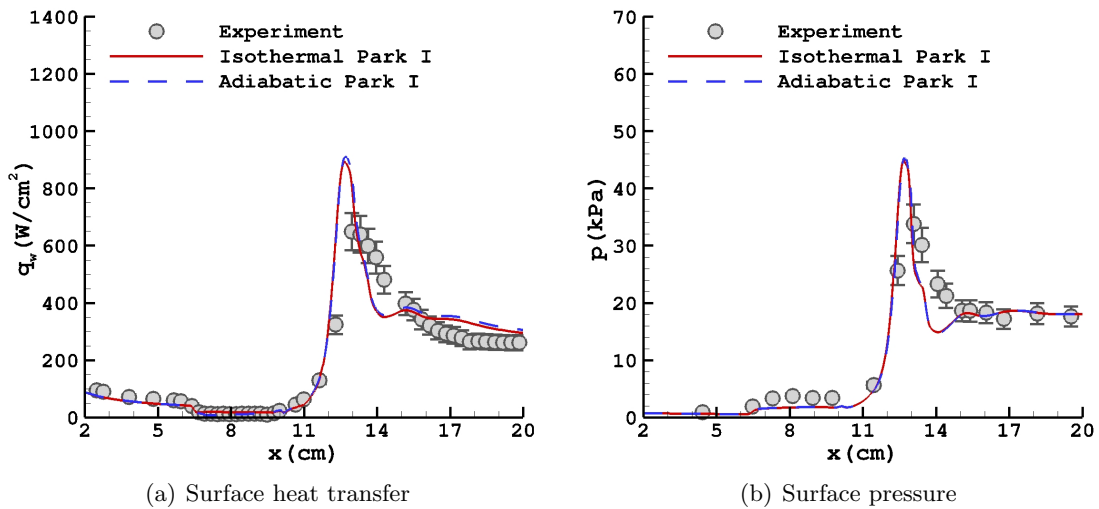


Figure 4.12: Comparison of different vibrational boundary condition of the Park I model with experiment for Run 4 (15.54 MJ/kg)

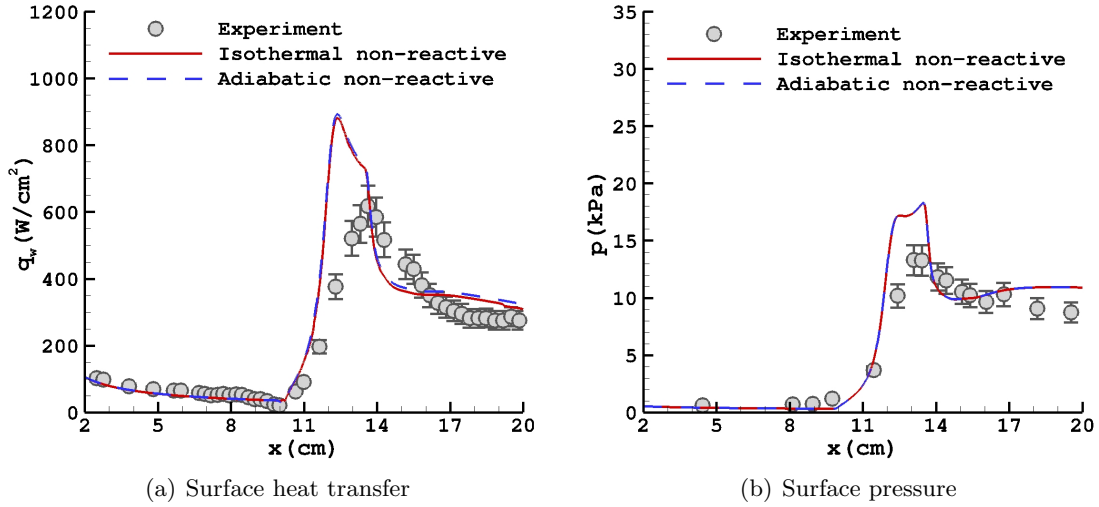


Figure 4.13: Comparison of different vibrational boundary condition of the non-reactive model with experiment for Run 5 (21.85 MJ/kg)

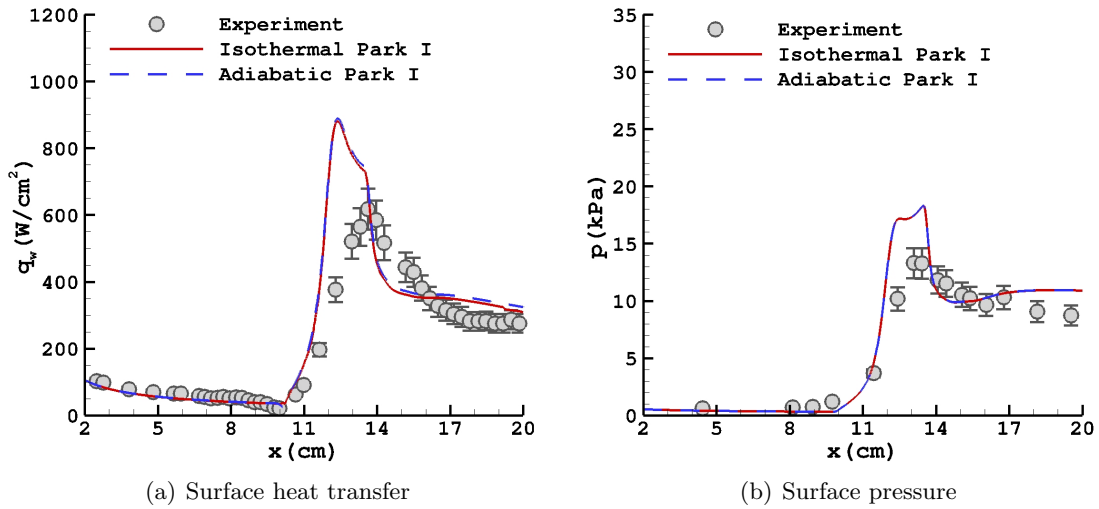


Figure 4.14: Comparison of different vibrational boundary condition of the Park I model with experiment for Run 5 (21.85 MJ/kg)

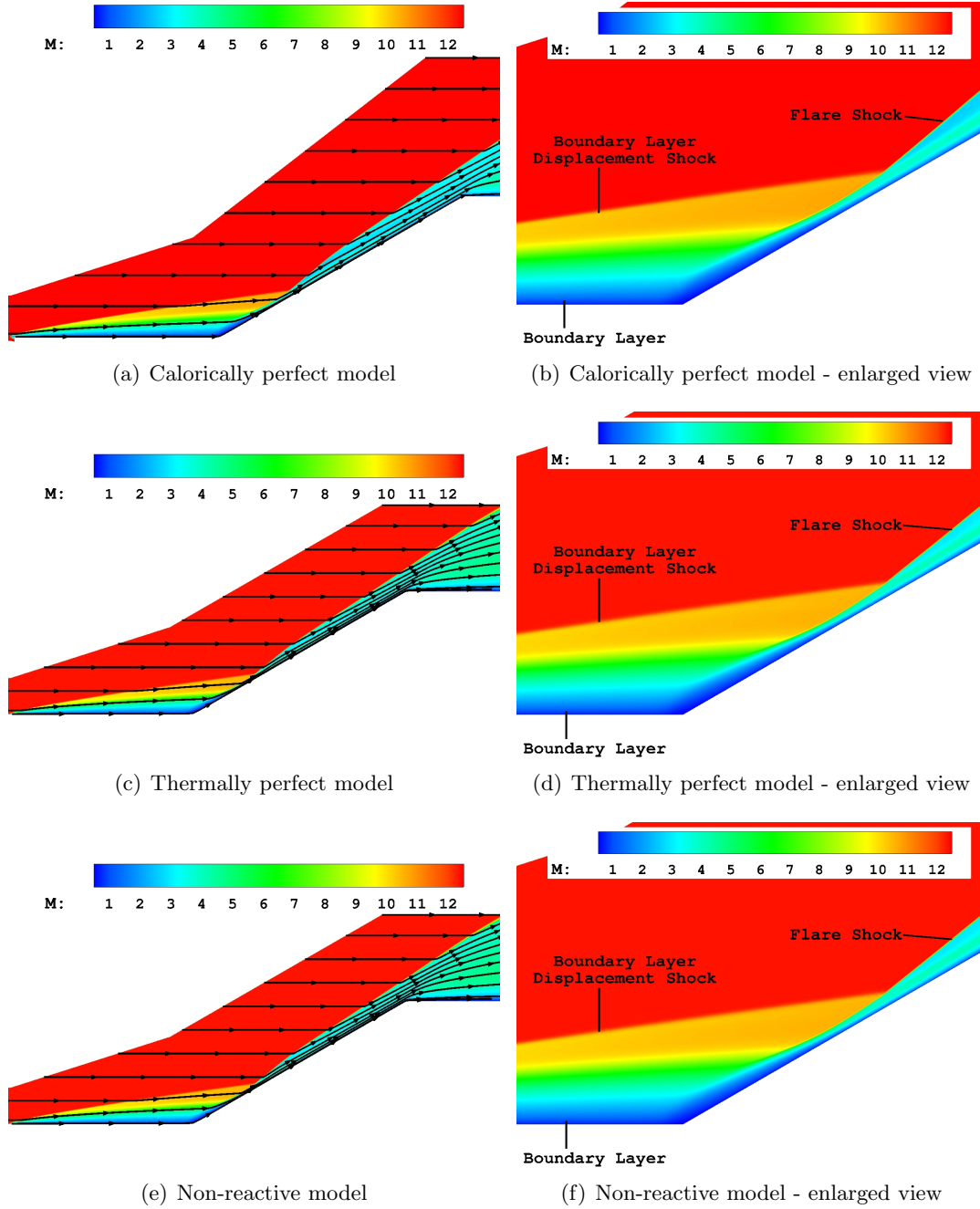


Figure 4.15: Mach contours and flow structure of Run 2 (10.43 MJ/kg)

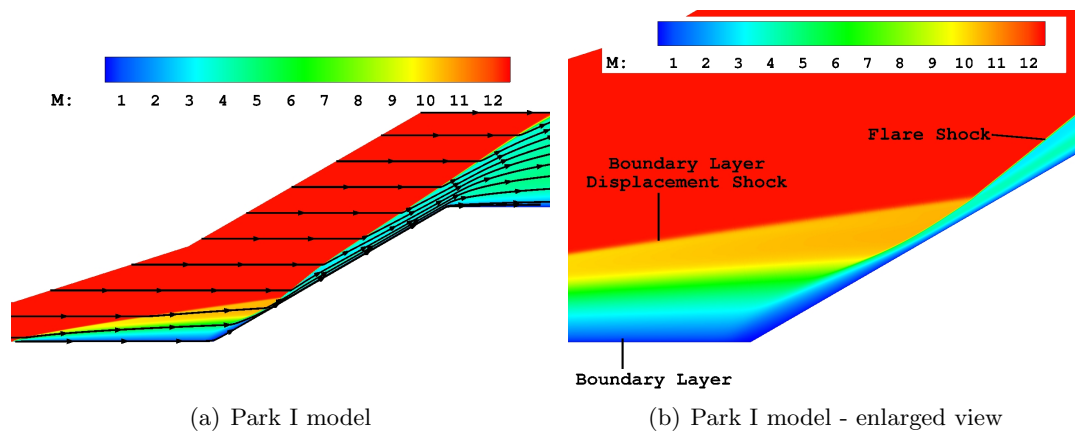


Figure 4.15: Mach contours and flow structure of Run 2 (10.43 MJ/kg)

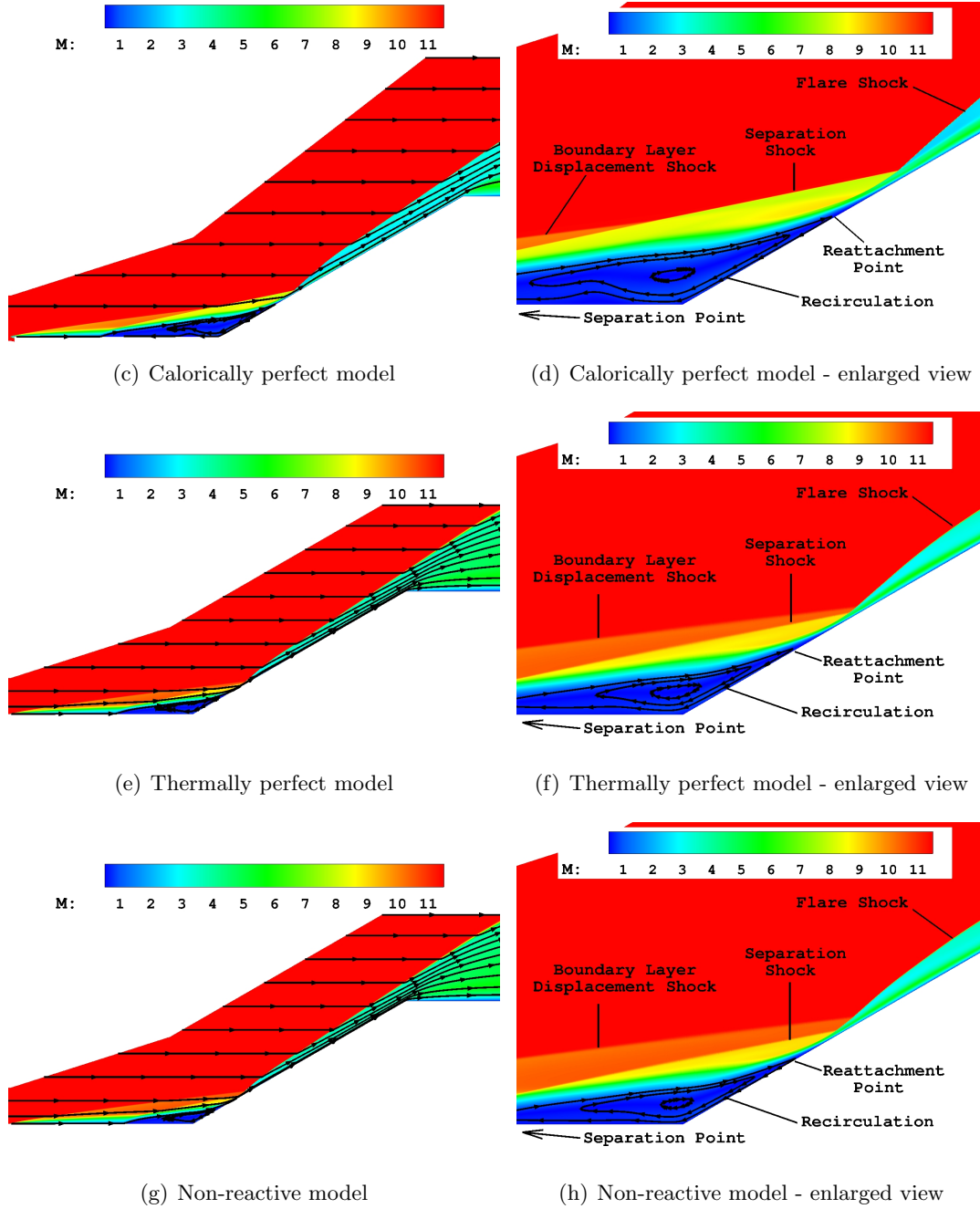
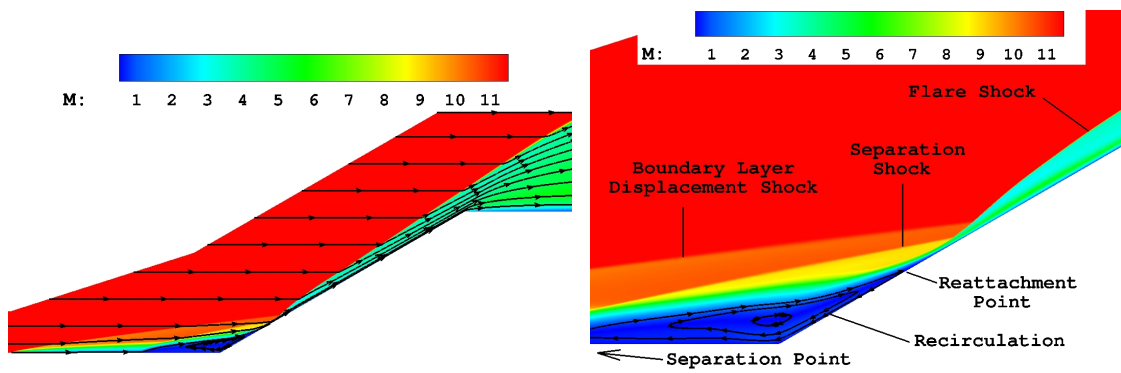


Figure 4.16: Mach contours and flow structure of Run 4 (15.54 MJ/kg)



(a) Park I model

(b) Park I model - enlarged view

Figure 4.16: Mach contours and flow structure of Run 4 (15.54 MJ/kg)

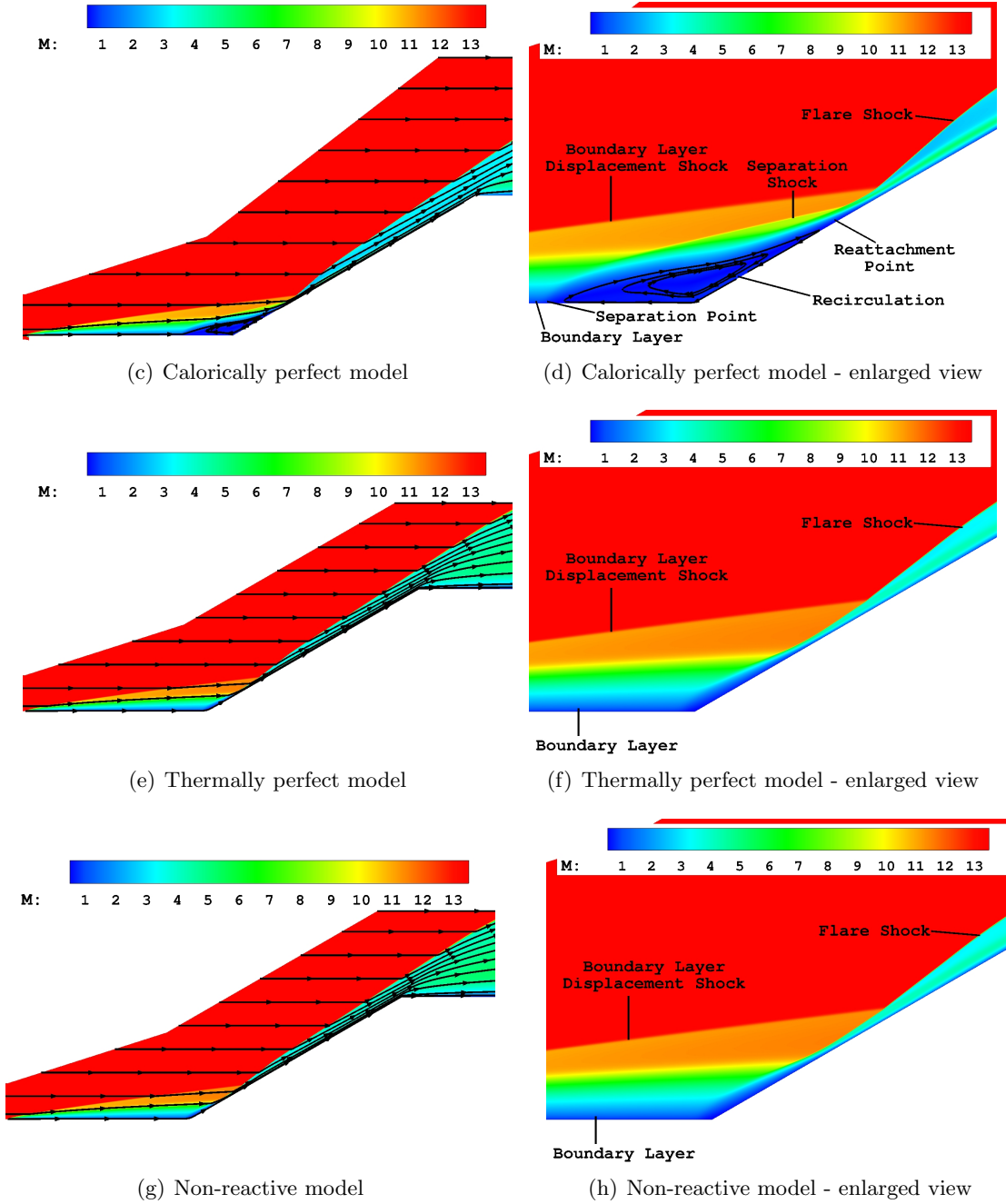


Figure 4.17: Mach contours and flow structure of Run 5 (21.85 MJ/kg)

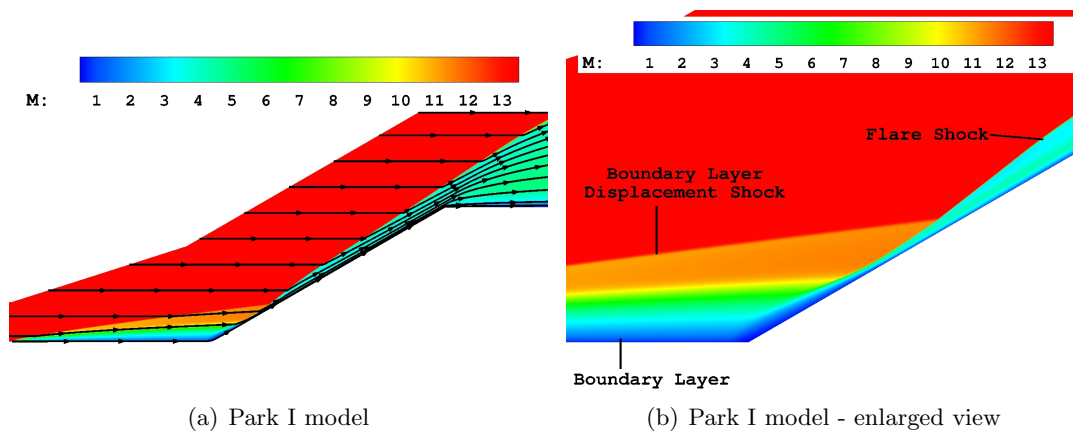


Figure 4.17: Mach contours and flow structure of Run 5 (21.85 MJ/kg)

Effect of Calorically Perfect Gas vs. Thermally Perfect Gas Models

To better understand the effect of thermally perfect model *vs.* calorically perfect model, the minimum and maximum values of the specific heat c_p for all models are presented in Table 4.6. The change in the specific heat of the thermally perfect model for Run 2, Run 4 and Run 5 are 30%, 35% and 36%, respectively. The percentage of change in the specific heat for the isothermal non-reactive, adiabatic non-reactive, isothermal Park I, and adiabatic Park I models are also about 30%, 35% and 36% respectively for Run 2, Run 4 and Run 5. This change in specific heat mostly occurs in the high temperature region related to the interaction of the shock wave and boundary layer, and is the same location which creates the peak heat transfer and peak pressure. Therefore, the change in specific heat may have a significant effect on the prediction of surface heat transfer and surface pressure especially the peak values.

Table 4.6: Variation of specific heat

Model	c_p (J/kg·K)					
	Run 2		Run 4		Run 5	
	min	max	min	max	min	max
Calorically perfect	1004.15	1004.15	1004.15	1004.15	1004.15	1004.15
Thermally perfect	1010.76	1318.89	1015.29	1371.77	1013.92	1379.46
Isothermal non-reactive	1010.77	1318.75	1015.58	1367.24	1015.58	1379.38
Adiabatic non-reactive	1011.66	1319.20	1012.66	1368.03	1013.16	1377.08
Isothermal Park I	1010.77	1318.75	1015.60	1367.24	1015.34	1379.38
Adiabatic Park I	1010.78	1318.77	1012.66	1368.02	1013.26	1379.39

In the thermally perfect gas model, along with the temperature dependency of specific heat, viscosity and thermal conductivity calculations are changed from Sutherland's law to the Gupta *et al.* database. In order to recognize the importance of the change of these two variables, the ratio of viscosity and thermal conductivity of thermally perfect gas calculated using Gupta *et al.* database denoted as μ and k to the calorically perfect gas values calculated by Sutherland's law represented as $\mu_{sutherland}$ and $k_{sutherland}$ are shown in Figures 4.18 to 4.20 for Run 2, Run 4 and Run 5, respectively. The maximum change in viscosity and thermal conductivity for Run 2 are respectively 18% and 61%, for Run 4 are respectively 36% and 84%, and for Run 5 the changes are 38% and 88%, respectively. These percentage of change are significant for Run 2, Run 4 and Run 5.

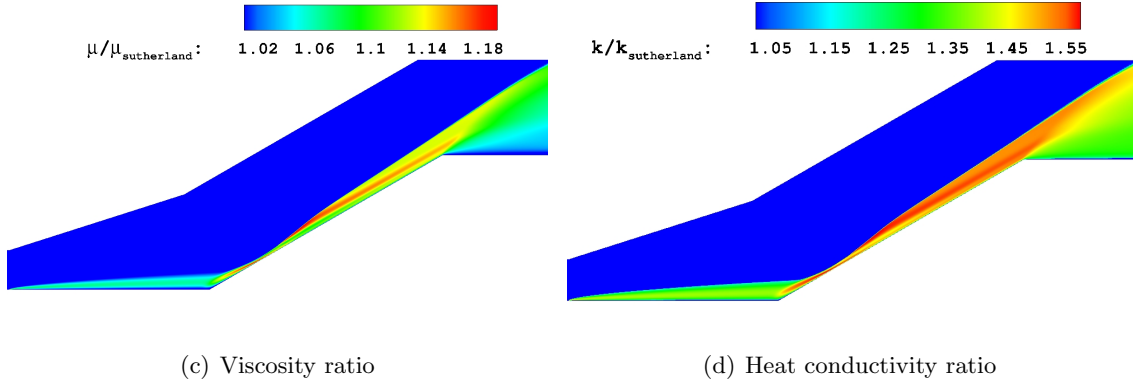


Figure 4.18: Ratio of transport properties of thermally perfect model to the calorically perfect model of Run 2 (10.43 MJ/kg)

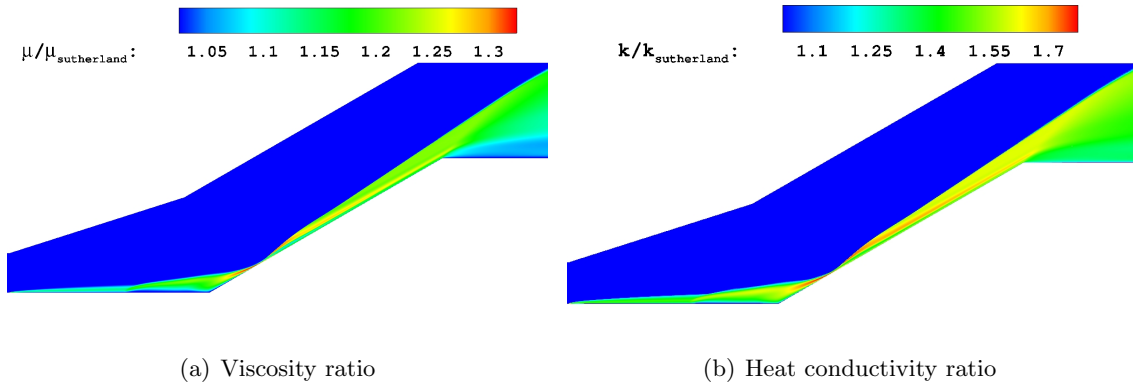


Figure 4.19: Ratio of transport properties of thermally perfect model to the calorically perfect model of Run 4 (15.54 MJ/kg)

Effect of Translational-Vibrational Energy Transfer and Vibrational Energies Boundary Condition at No-Slip Isothermal Wall

For better understanding the effect of translational-vibrational energy transfer and why adding it to the calculation does not change the calculated surface heat transfer and surface pressure, the ratio of vibrational energies of each species to the total energy for both isothermal for vibration and adiabatic for vibration boundary condition of non-reactive and Park I are illustrated in Figures 4.21 and 4.22 for Run 5 (21.85 MJ/kg). The fraction of the total energy in the vibrational modes in Run 2 is 1.2%, in Run 4 is 7.46% (not including the separation region; in separation region the energy goes to vibrational modes is about 32%)

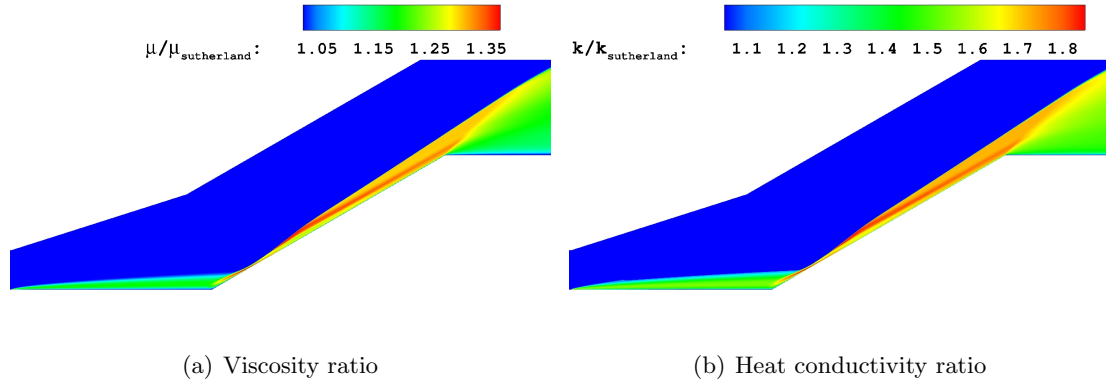


Figure 4.20: Ratio of transport properties of thermally perfect model to the calorically perfect model of Run 5 (21.85 MJ/kg)

and in Run 5 is 7.61% for the isothermal vibrational boundary condition. This amount of energy is so small and therefore the effect of translational-vibrational energy exchange model is insignificant. The percentage of vibrational energy in the flow after the shock wave boundary layer interaction and near the flare increased to about 6%, 16% (not including the separation region; in separation region the energy goes to vibrational modes is about 28.54%) and 23% for adiabatic vibrational energy boundary condition at wall.

To see the effect of the vibrational boundary condition on the flow structure, the contour plots of the normalized difference between the vibrational temperatures of N_2 and O_2 and the static temperature nondimensionalized by the static temperature are shown in Figures 4.23 and 4.24 for Run 5 (21.85 MJ/kg) for the non-reactive and Park I models. In the boundary layer over the hollow cylinder, there is a lag of vibrational temperatures relative to the static temperature except for the separation region of Run 4. Comparison of these figures shows that the zero gradient boundary condition leads to the higher vibrational temperatures after the shock waves and specifically near the walls.

Dimensionless vibrational relaxation time of N_2 and O_2 which is the ratio of vibrational relaxation time and the time required for the freestream flow to pass over the cylinder part of the model (time that freestream needs to travel length equal to 101.6 mm) are shown in Figures 4.25 to 4.27 for non-reactive model. For Run 2 (10.43 MJ/kg), the relaxation time of N_2 and O_2 are greater than the required time for the freestream flow to pass the

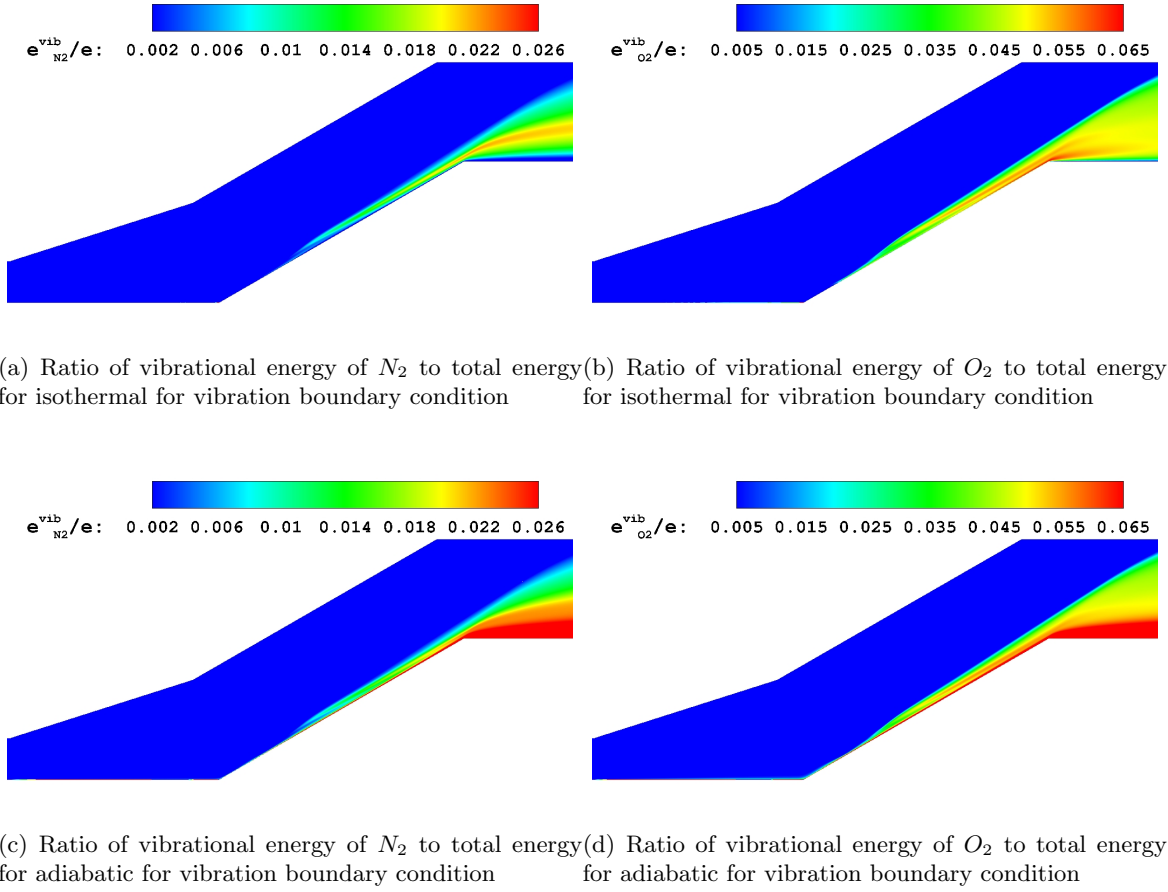
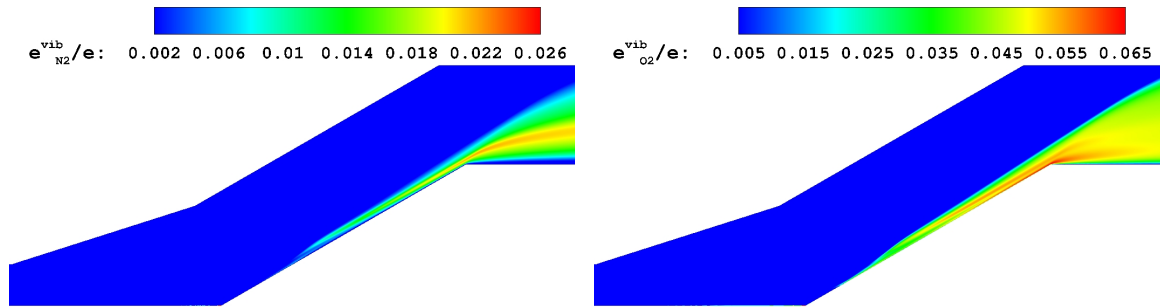
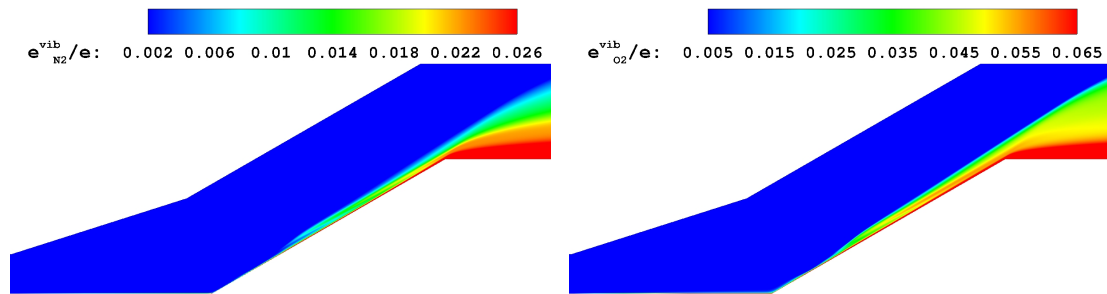


Figure 4.21: Ratio of vibrational energy to total energy of non-reactive model for Run 5 (21.85 MJ/kg)

entire hollow cylinder flare model. Therefore, the vibrational modes of energy of species do not have enough time to interact with translational-rotational modes and relax, *i.e.*, the vibrational temperatures remain nearly constant. However, for Run 4 (15.54 MJ/kg) and Run 5 (21.85 MJ/kg), while the relaxation time of N_2 is still greater than the time of passing over the model and hence the vibrational temperature of N_2 is almost frozen as seen in Figures 4.26(a) and 4.27(a), in some regions after the flare shock, the relaxation time of O_2 is less than the flare length (which is longer than cylinder part) and thus, the vibrational temperature is at equilibrium with static temperature (see Figures 4.26(b) and 4.27(b)).



(a) Ratio of vibrational energy of N_2 to total energy for isothermal for vibration boundary condition (b) Ratio of vibrational energy of O_2 to total energy for isothermal for vibration boundary condition



(c) Ratio of vibrational energy of N_2 to total energy for adiabatic for vibration boundary condition (d) Ratio of vibrational energy of O_2 to total energy for adiabatic for vibration boundary condition

Figure 4.22: Ratio of vibrational energy to total energy of Park I model for Run 5 (21.85 MJ/kg)

Effect of Park I Thermochemistry Model

Figures 4.28 to 4.33 show the mass fraction of species NO, N, and O and temperature contours for the Park I model respectively for Run 2 (10.43 MJ/kg), Run 4 (15.54 MJ/kg) and Run 5 (21.85 MJ/kg). The adiabatic for vibration boundary condition is shown for all cases. The maximum temperature for Run 2 (10.43 MJ/kg), Run 4 (15.54 MJ/kg) and Run 5 (21.85 MJ/kg) are respectively 3538 K, 6063 K, and 6867 K. The mass fraction of species NO, N, and O are less than 2% for Run 2 (10.43 MJ/kg), Run 4 (15.54 MJ/kg) and Run 5 (21.85 MJ/kg) (the freestream mass fraction of NO is 1%) which is an indication of why there is no significant change in the predicted surface pressure and surface heat transfer between the Park I and non-reactive models.

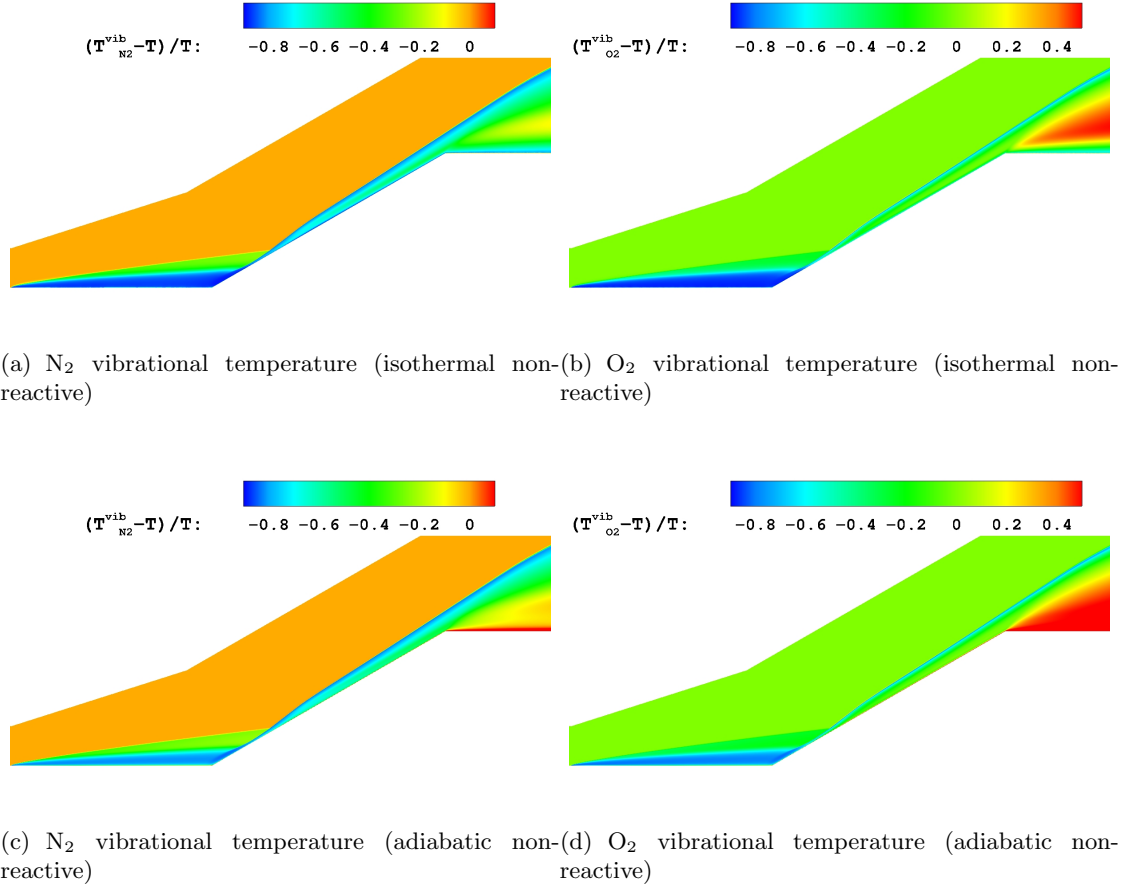
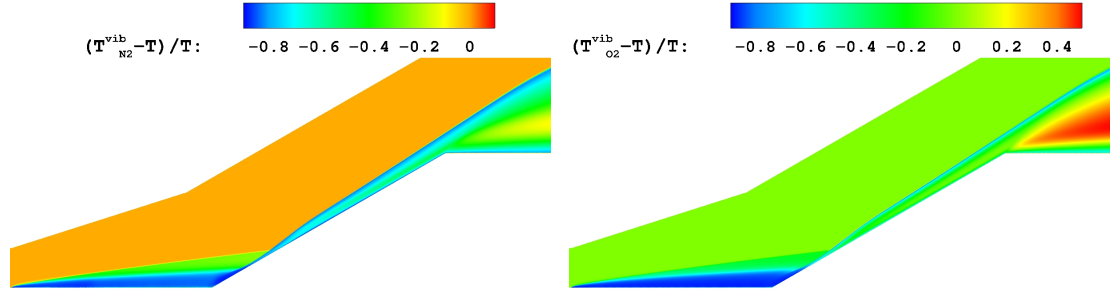


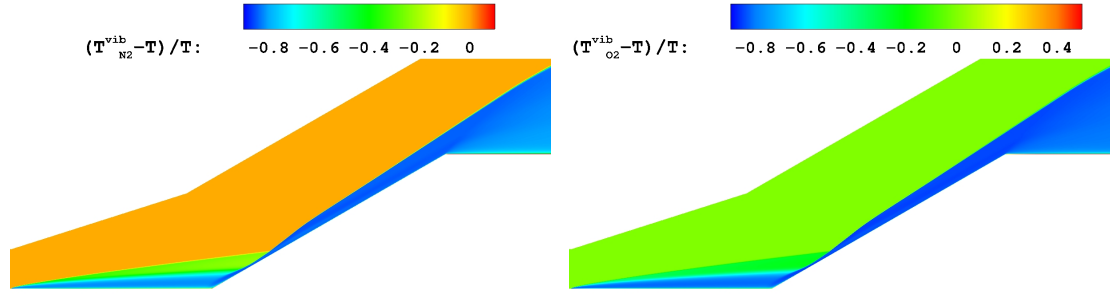
Figure 4.23: Vibrational temperature of N_2 and O_2 of non-reactive model for Run 5 (21.85 MJ/kg)

4.5 Conclusions

In this chapter a total of four models - calorically perfect, thermally perfect, non-reactive and Park I - are considered for a laminar hypersonic flow past a hollow cylinder flare at Mach numbers range from 12.6 to 13.2 and stagnation enthalpies from 10.43 to 21.85 MJ/kg. Two sets of boundary conditions for vibrational energies at an isothermal surface are also considered. The objective of this paper is to examine the effect of 1) calorically perfect gas *vs.* thermally perfect gas models, 2) translational-vibrational energy transfer, 3) Park I thermochemistry, and 4) isothermal or adiabatic boundary condition for vibrational energies at no-slip isothermal wall on the prediction of peak surface heat transfer and peak surface pressure for the hollow cylinder flare.



(a) N₂ vibrational temperature (isothermal Park I) (b) O₂ vibrational temperature (isothermal Park I)



(c) N₂ vibrational temperature (adiabatic Park I) (d) O₂ vibrational temperature (adiabatic Park I)

Figure 4.24: Vibrational temperature of N₂ and O₂ of Park I model for Run 5 (21.85 MJ/kg)

Four key results are obtained in this research. First, the temperature dependency of specific heats has a significant effect on prediction of surface heat transfer and surface pressure. However, this effect does not uniformly improve the results. The thermally perfect model can accurately predict the separation point location while the calorically perfect model overpredict the separation size. On the other hand, the calorically perfect model has better prediction for peak surface heat transfer. The predicted peak surface pressure is comparable for both thermally perfect and calorically perfect models except for the highest enthalpy case (21.85 MJ/kg) in which the calorically perfect prediction is worse than the thermally perfect. Surprisingly, the thermally perfect model consistently improves prediction of the aerothermodynamic loading in the double cone experiment [102]. More research is required to understand the contradictory effect of adding temperature dependency of specific heats. Second, the translational-vibrational energy exchange has no

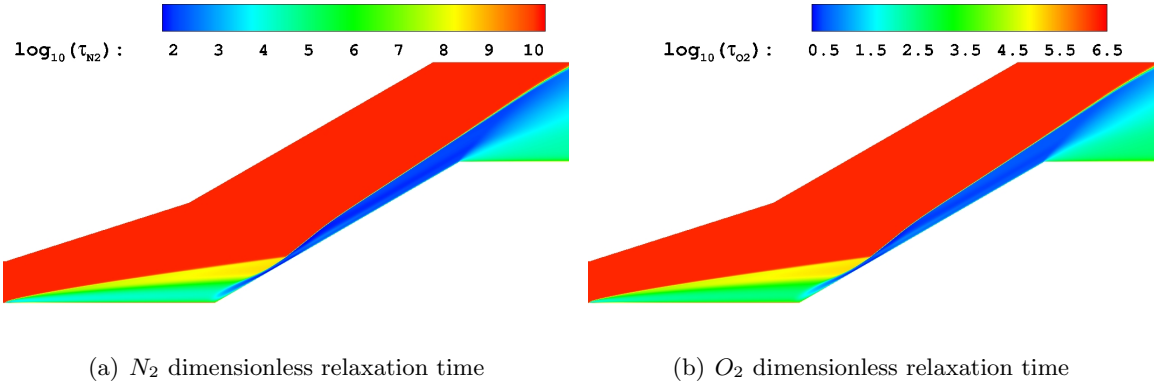


Figure 4.25: Relaxation time nondimensionalized by the time the freestream flow needs to pass the cylinder section of non-reactive model for Run 2 (10.43 MJ/kg)

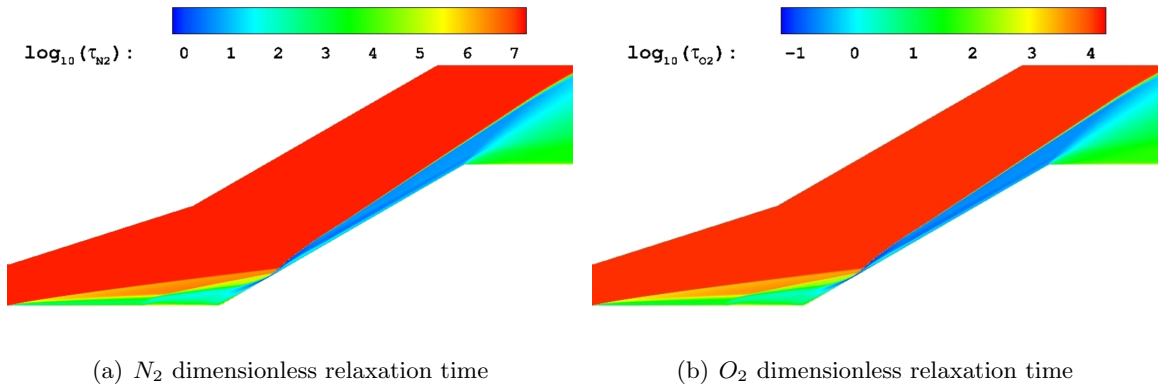


Figure 4.26: Relaxation time nondimensionalized by the time the freestream flow needs to pass the cylinder section of non-reactive model for Run 4 (15.54 MJ/kg)

significant effect on the prediction of surface heat transfer and surface pressure since the time required for the energy transfer between vibrational and translational modes is larger or at least comparable to the time required for the freestream flow to pass the length of the experimental model. Third, the effect of isothermal or adiabatic boundary condition for vibrational energies at a no-slip isothermal wall is negligible on the prediction of peak values. Fourth, the Park I thermochemistry model does not improve the prediction of aerothermodynamic loading because the mass fraction of dissociated gas in the flowfield is negligible. These conclusions are specific to this hollow cylinder flare experiment.

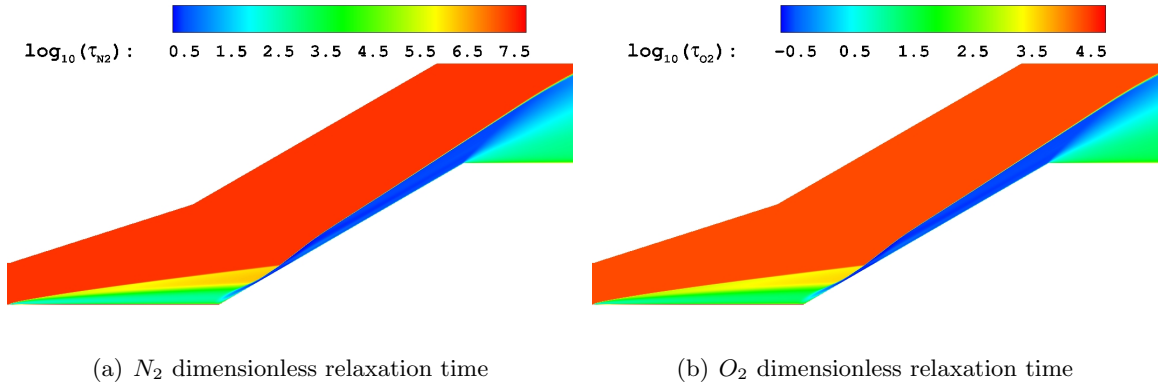


Figure 4.27: Relaxation time nondimensionalized by the time the freestream flow needs to pass the cylinder section of non-reactive model for Run 5 (21.85 MJ/kg)

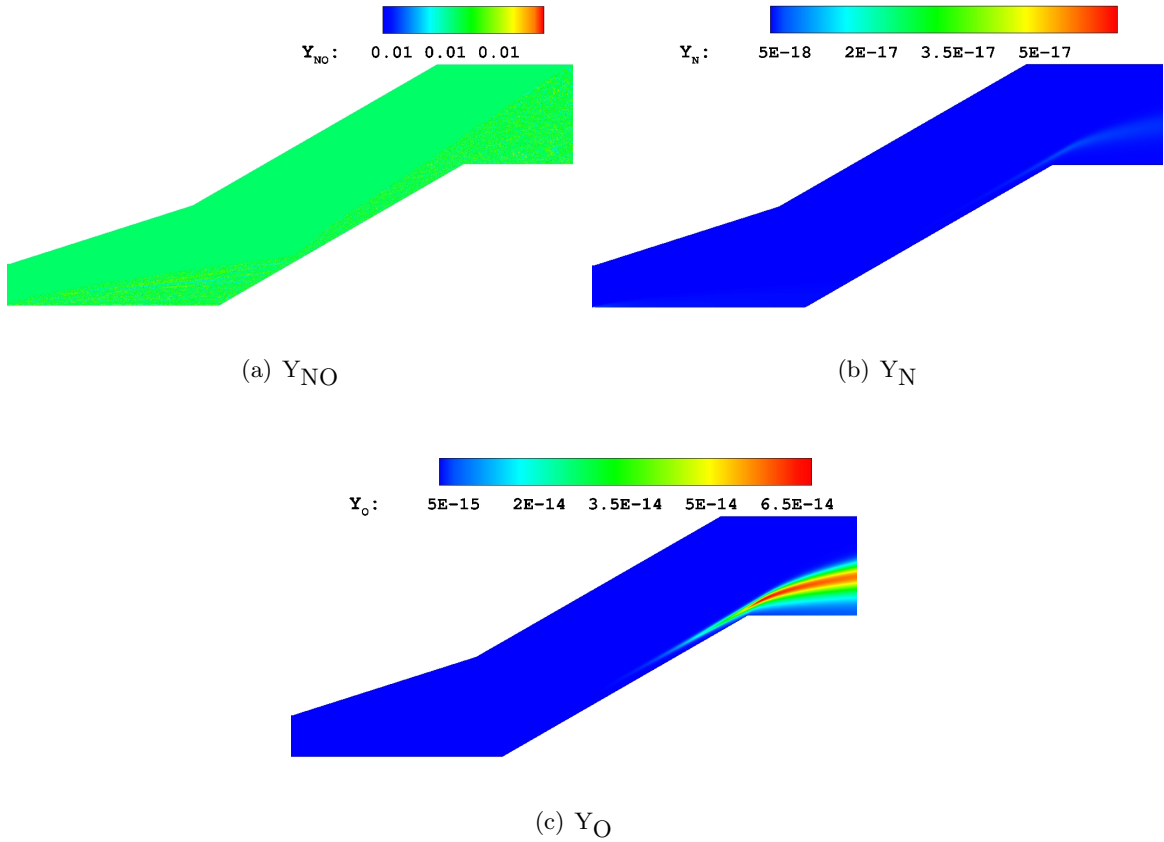


Figure 4.28: Mass fraction of species of Park I model for Run 2 (10.43 MJ/kg)

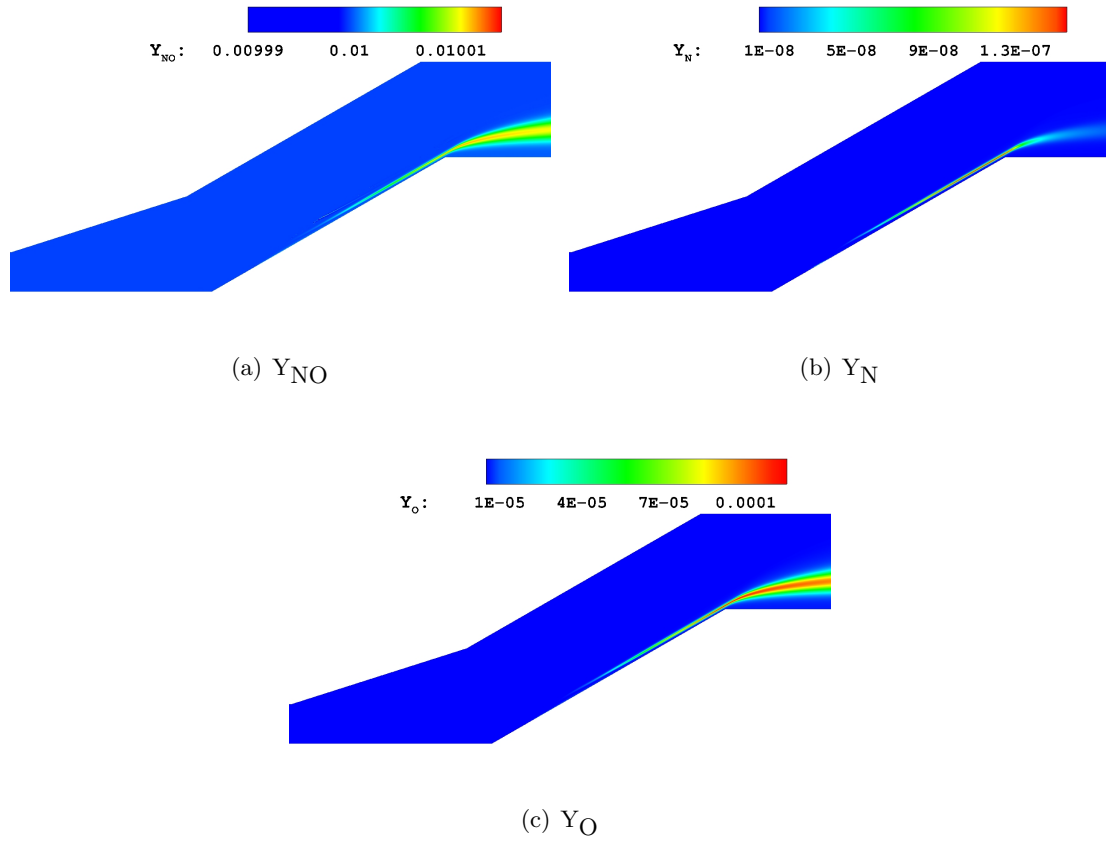


Figure 4.29: Mass fraction of species of Park I model for Run 4 (15.54 MJ/kg)

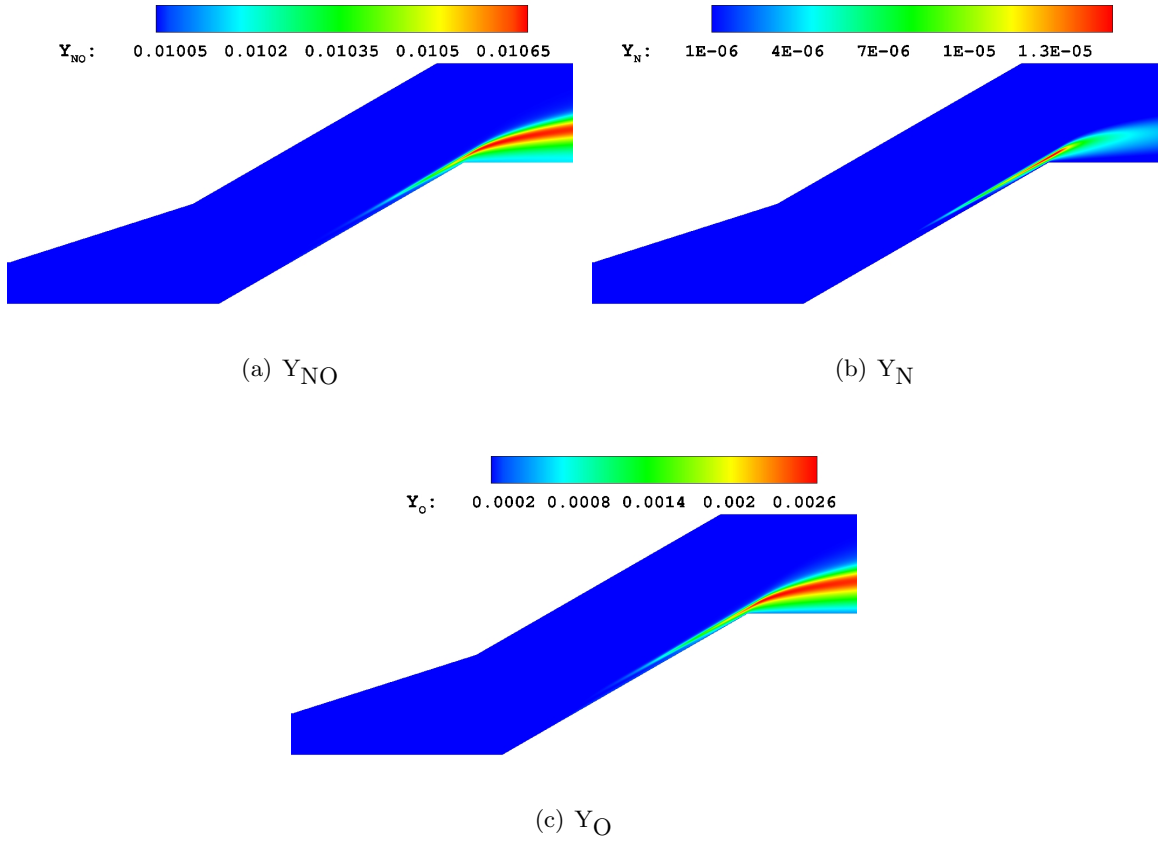


Figure 4.30: Mass fraction of species of Park I model for Run 5 (21.85 MJ/kg)

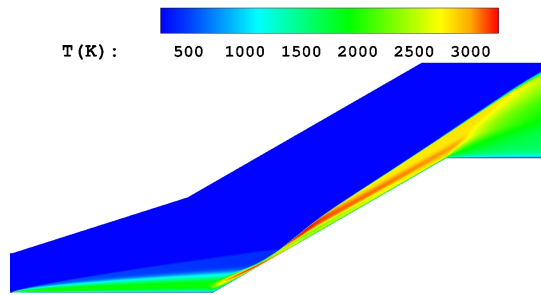


Figure 4.31: Temperature contours of Park I model for Run 2 (10.43 MJ/kg)

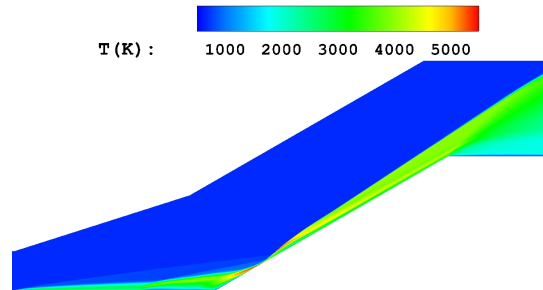


Figure 4.32: Temperature contours of Park I model for Run 4 (15.54 MJ/kg)

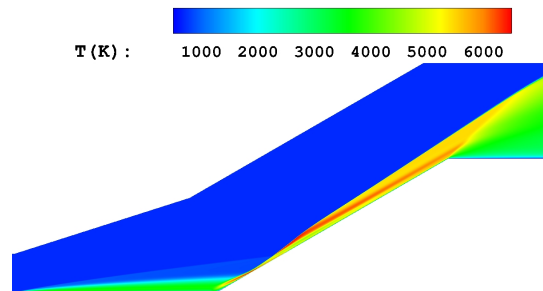


Figure 4.33: Temperature contours of Park I model for Run 5 (21.85 MJ/kg)

Chapter 5

Prediction of Aerothermodynamic Loading on a Double Cone

In this chapter, the computational fluid dynamics is used for the prediction of aerothermodynamic loading (surface pressure and heat transfer) over a simple geometry called “double cone”. This geometry produces a stronger interaction between shocks and boundary layer in comparison to the hollow cylinder flare studies in Chapter 4 and thus, the analysis of this case enables us to better examine our available tools.

5.1 Introduction

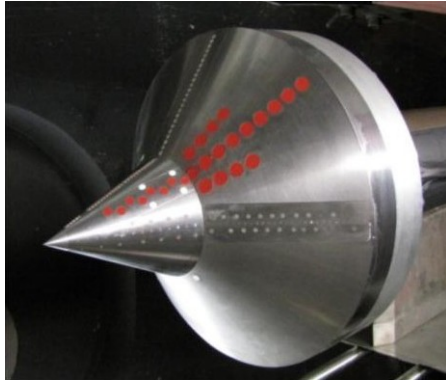
The recent reinterest in hypersonic flight brings along the question of capability of numerical simulation. A recent set of experiments with equilibrium freestream conditions was performed at the Calspan University of Buffalo Research Center (CUBRC) and is a bench test for assessment of CFD capabilities. Originally, these data were used for a blind test study at 2014 [96, 97]. The results of the blind study in addition to the other studies performed over this geometry afterward showed significant discrepancies between numerical and experimental peak surface heat transfer and pressure.

In this chapter, the non-equilibrium laminar Navier-Stokes equations and several of its simplified forms are considered to examine the effect of each model on the prediction of surface pressure and surface heat transfer for the $25^\circ/55^\circ$ double cone of CUBRC. In this chapter, the effect of 1) translational-vibrational relaxation through the transfer of energy between translational-rotational and vibrational modes of energies, and 2) the effect of Park I thermochemistry model are presented.

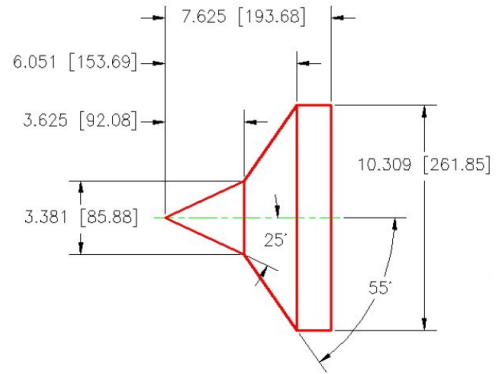
5.2 Description of Experiment

The experimental model of this experiment is the $25^\circ/55^\circ$ double cone shown in Figure 5.1. The total length of this model is 194 mm (see Figure 5.1(b)). The model is instrumented with twenty three pressure transducers and forty nine heat transfer gauges (see Figure 5.1(a)). The experiment includes six cases denoted Runs 1 to 6 with a stagnation enthalpies range of 5.44 MJ/kg to 21.77 MJ/kg and Mach numbers of 10.90 to 13.23, and were conducted in the LENS XX expansion tunnel. The freestream gas is air in full chemical and thermochemical equilibrium with mass fractions of 0.765 and 0.235 respectively for N_2 and O_2 . The surface of the double cone is an isothermal wall at 300° K. Details of the LENS XX facility are presented in Dufrene *et al* [99, 100].

In this section, two of the six cases, namely Run 2 and Run 4, are considered. The conditions of these experiments are given in Table 5.1. It should be noted here that the Reynolds number based on the freestream condition and the axial length of the first cone (which is 92.08 mm from Figure 5.1(b)) are respectively 17426 and 18136 for Run 2 and Run 4. These Reynolds numbers are low enough to assure a fully laminar flow.



(a) Instrumentation



(b) Geometry

Figure 5.1: Small $25^\circ/55^\circ$ double cone flare (dimensions in inches [mm] (courtesy of CUBRC)

5.3 Methodology

The governing equations are the non-equilibrium laminar Navier-Stokes equations for thermally perfect compressible viscous flow described in Section 2.2. The special cases of the

Table 5.1: Flow conditions

Run No.	Total Enthalpy (MJ/kg)	Mach Number	Pitot Pressure (kPa)	Unit Reynolds (/10 ⁶ m ⁻¹)	Velocity (km/s)	Density (g/m ³)	Temperature (K)
2	9.65	10.90	17.5	0.19	4.303	0.984	389
4	21.77	12.82	39.5	0.20	6.497	0.964	652

full non-equilibrium equations are also considered here. The special cases for this study are 1) thermally perfect and 2) non-reactive.

The governing equations are solved using a block structured grid finite volume time accurate C⁺⁺ code partially developed by the author. Roe's method is used for calculation of inviscid fluxes with MUSCL reconstruction and the central differencing method is used for calculation of viscous fluxes. The DPLR method is used to achieve high computational efficiency. The problem is initialized by freestream conditions and converged to the steady state solution.

5.3.1 Computational Domain

The schematic of the computational domain is shown in Figure 5.2. The boundary conditions for these simulations are axisymmetric from A to B, no-slip, non-catalytic isothermal wall with adiabatic for vibration (see Section 2.4) from B to C, zero-gradient from C to D, and fixed at freestream condition from D to E and E to A. The grid properties of the three sets of grids used for the simulations of this chapter are given in Table 5.2.

Table 5.2: Grid properties

Grid Name	Total Cell Numbers	il	jl	kl	$\Delta\xi$ (μm)	$\Delta\eta_{min}$ (μm)	$\Delta\zeta$ (degree)
Grid 1	1,228,800	1280	160	6	227.57	50	2.5
Grid 2	3,225,600	2560	210	6	113.78	25	2.5
Grid 3	4,515,840	3584	210	6	81.27	12.5	2.5

NOTE:

il is number of points along ABC (see Figure 5.2)

jl is number of points along AE(CD) (see Figure 5.2)

kl is number of points in azimuthal direction

$\Delta\xi$ is spacing along the wall

$\Delta\eta$ is spacing normal to the wall

$\Delta\zeta$ is the axial spacing

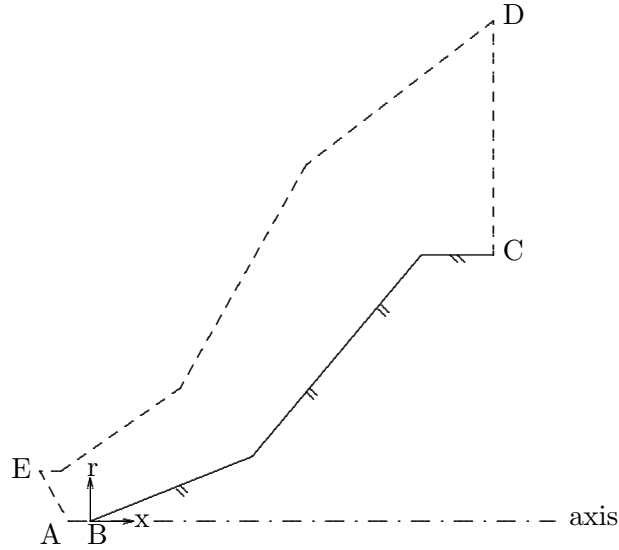


Figure 5.2: Computational domain

5.4 Results

Three models are considered in this chapter to better understand the source of the observed discrepancies between the numerical results and the experimental data: 1) non-equilibrium laminar Navier-Stokes with Park thermochemistry [33] denoted “Park I”, 2) non-reactive (see Section 2.3.3), and 3) thermally perfect (see Section 2.3.2). Table 5.3 presents the specification of each models.

Table 5.3: Models specifications

Model	Modification to governing equations		Transport properties	
	$\dot{\omega}_{\alpha}^{\text{spe}}$	$\dot{\omega}_{\alpha}^{\text{vib}}$	Pr_{∞}	Le
Park I	Eq. (2.4) and Park I	Eq. (2.25)	0.736	1.0
Non-reactive	0	$\rho_{\alpha} \dot{e}_{\alpha}^{\text{vib}}$	0.736	1.0
Thermally perfect	0	0	0.736	1.0

5.4.1 Grid Convergence Study

To study the grid independency of the results, for each of the three models mentioned in Table 5.3 and for both Run 2 (9.65 MJ/kg) and Run 4 (21.77MJ/kg), three sets of grids, namely Grid 1, Grid 2, and Grid 3 are used. All the calculations are converged to steady state. The minimum final dimensionless time for Run 2 and Run 4 calculations with Grid 2 are 79.91 and 89.91, respectively. Using Grid 3, the final time of the calculations increased

to 106.91 for both Run 2 and Run 4 calculations. One dimensionless time is the time required for the freestream to pass the first cone. At the convergence point, the change in the separation region length for the Park I, non-reactive, and thermally perfect models are respectively less than a micron over the last 27 dimensionless time, less than a micron over the last 37 dimensionless time, and less than 0.5 millimeter over the last 36 dimensionless time.

Figures 5.3 to 5.8 show the surface pressure and heat transfer of the three grids and the exact solution. The “exact” solutions are obtained using Richardson extrapolation of Grid 2 and Grid 3. The regions where the percentage of change between Grid 3 (*i.e.*, finest grid) and the exact solutions exceeds 10% (*i.e.*, experimental uncertainty) are limited to the immediate neighborhood of the separation region point on the first cone and the region near to the peak values. The typical length of regions with the difference above 10% between the solutions is approximately less than the experimental gauge spacing. Elsewhere, the change from Grid 3 to the exact solution is less than 2%. Moreover, the change in the peak surface pressure and peak heat transfer is less than 10% for all the cases. Thus, the exact solution is concluded as grid converged.

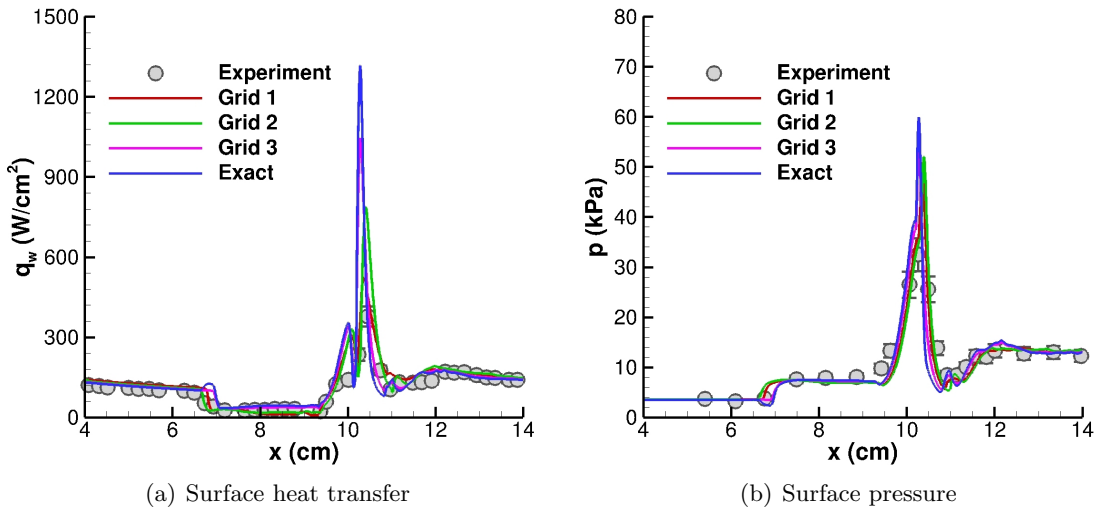


Figure 5.3: Grid study for Run 2 (9.65 MJ/kg) for thermally perfect model

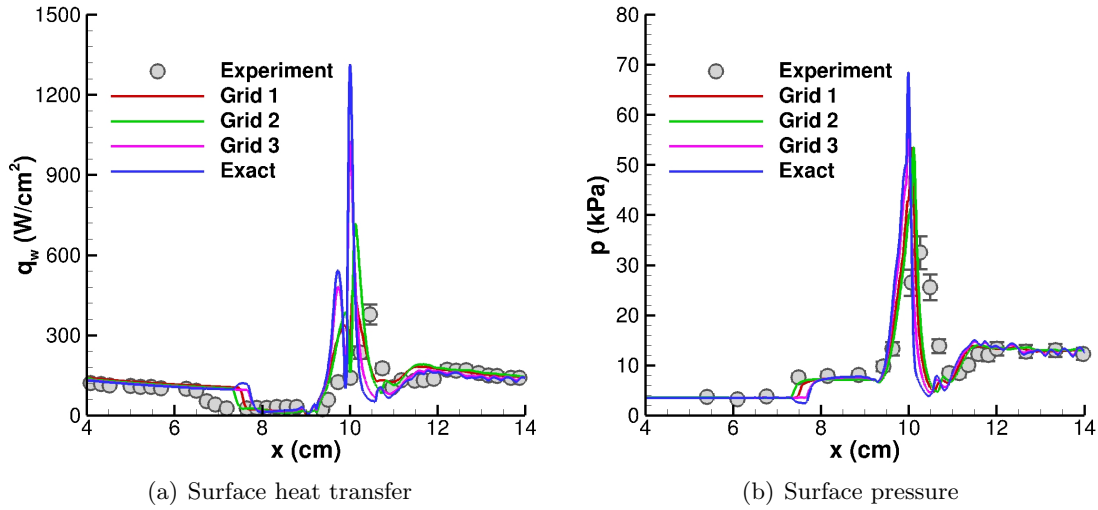


Figure 5.4: Grid study for Run 2 (9.65 MJ/kg) for non-reactive model

5.4.2 Comparison of Models with Experiment

Figure 5.9 shows the comparison of the exact results of the thermally perfect, non-reactive, and Park I models with the experimental measurement for Run 2 (9.65 MJ/kg). All three models predict virtually identical surface heat transfer and in close agreement with the experiment on the forward cone. The separation point is predicted accurately by the thermally perfect model while both non-reactive and Park I model predictions of the separation region reduce the separation region size to about two-third of the experimental data. The peak values are overpredicted by all models ranges from 210% to 250%. However, the comparison of the heat transfer in the vicinity of the peak region is indeterminant. The spacing between the gauge in the experiment shows the maximum heat transfer and the gauge before and after is 0.22 cm and 0.28 cm which is about 50 times larger than the numerical spacing (*i.e.*, 0.0047 cm). Therefore, the measured peak heat transfer may not correspond to the actual experimental peak surface heat transfer. The predicted location of peak heat transfer for thermally perfect, non-reactive, and Park I is respectively $x = 10.28$, 10.00, and 9.99 cm while the measured location for the peak heat transfer at the experiment is 10.46 cm. This data shows that the thermally perfect peak heat transfer location is in better agreement with the experimental data. The recovery of the heat transfer in the aft cone is similar for all three models and agrees with the experiment within the experimental uncertainty.

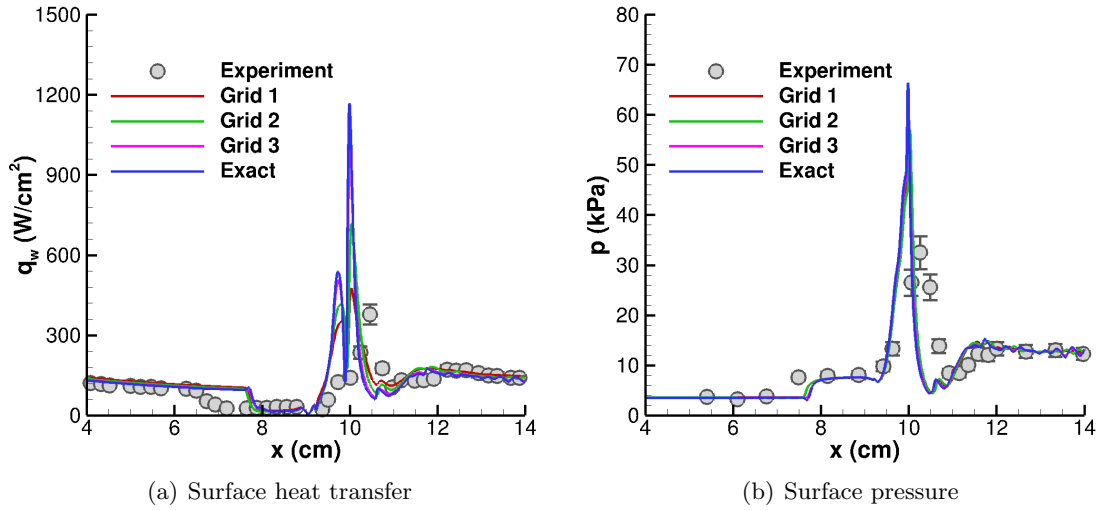


Figure 5.5: Grid study for Run 2 (9.65 MJ/kg) for Park I model

All three models predict virtually identical forward cone surface pressure and the prediction is in close agreement with the experiment. As indicated above, the separation point is predicted accurately by the thermally perfect model while it is not accurately predicted by both non-reactive and Park I model. The plateau pressure is virtually identical for all three models and in agreement with the experimental measurement. The peak values are overpredicted by all models ranges from 85% to 110%. However, the comparison of the surface pressure in the vicinity of the peak region is indeterminant. The spacing between the gauge in the experiment shows the maximum pressure and the gauge before and after is 0.20 cm and 0.43 cm which is about 50 times larger than the numerical spacing (*i.e.*, 0.0047 cm). Therefore, the measured peak pressure may not correspond to the actual experimental peak surface pressure. The predicted location of peak pressure for thermally perfect, non-reactive, and Park I is respectively $x = 10.27$, 9.99, and 9.98 cm while the measured location for the peak heat transfer at the experiment is 10.26 cm. This data shows that the thermally perfect peak pressure location is in better agreement with the experimental data. The recovery of the surface pressure in the aft cone region is similar for all three models and agrees with the experiment within the experimental uncertainty.

Figure 5.10 shows the comparison of the surface pressure and heat transfer of the exact solution for the three numerical models, namely thermally perfect, non-reactive, and

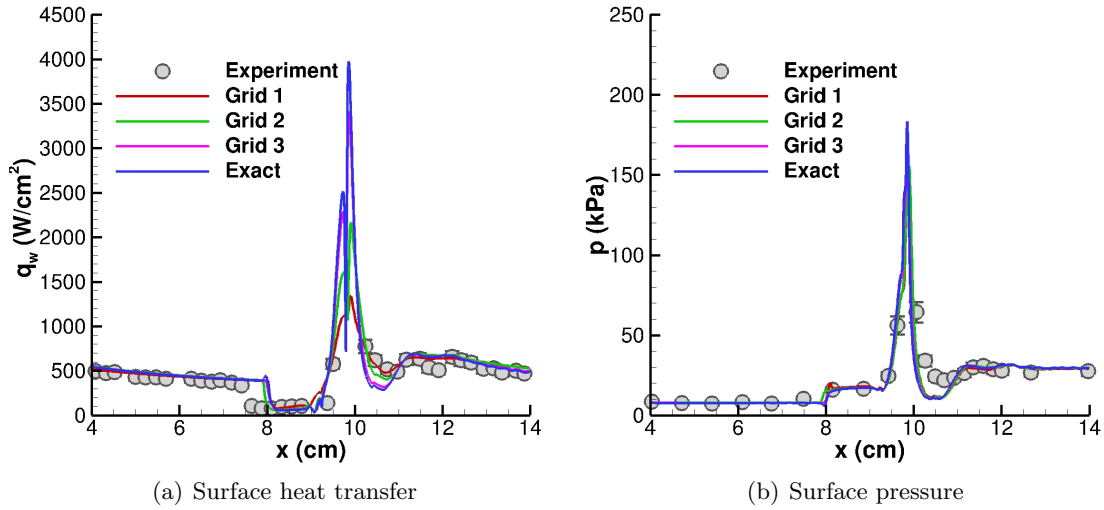


Figure 5.6: Grid study for Run 4 (21.77 MJ/kg) for thermally perfect model

Park I and the experimental measurements for Run 4 (21.77 MJ/kg). The predicted surface heat transfer on the forward cone is essentially identical for all three models and is in agreement with the experimental data. The separation point is underpredicted by all the models; however, the thermally perfect model predicts the largest separation region and the Park I model predicts a slightly smaller separation region compared to the non-reactive model. The predicted peak heat transfer exceeds the experimental peak by 250% to 415%. However, the comparison between the peak surface heat transfer and predicted numerical peaks is indeterminant. There is no experimental measurement between $x = 9.50$ cm and $x = 10.24$ cm which is 157 times the numerical grid spacing (*i.e.* 0.0047 cm). This region is exactly where the numerical peaks are located. Thus, the peak measured heat transfer may not be the actual experimental peak values. The peak heat transfer location is predicted at $x = 9.86$, 9.85, and 9.81 cm respectively by thermally perfect, non-reactive, and Park I models. The prediction of the heat transfer at the aft cone is within the experimental uncertainty for all three models.

The predicted surface pressure on the forward cone is in close agreement with the experiment for all three models. The separation region is underpredicted by all three models. The predicted plateau pressure is identical for all three models and in good agreement with the experimental measurement. The peak surface pressure is overpredicted by all models from

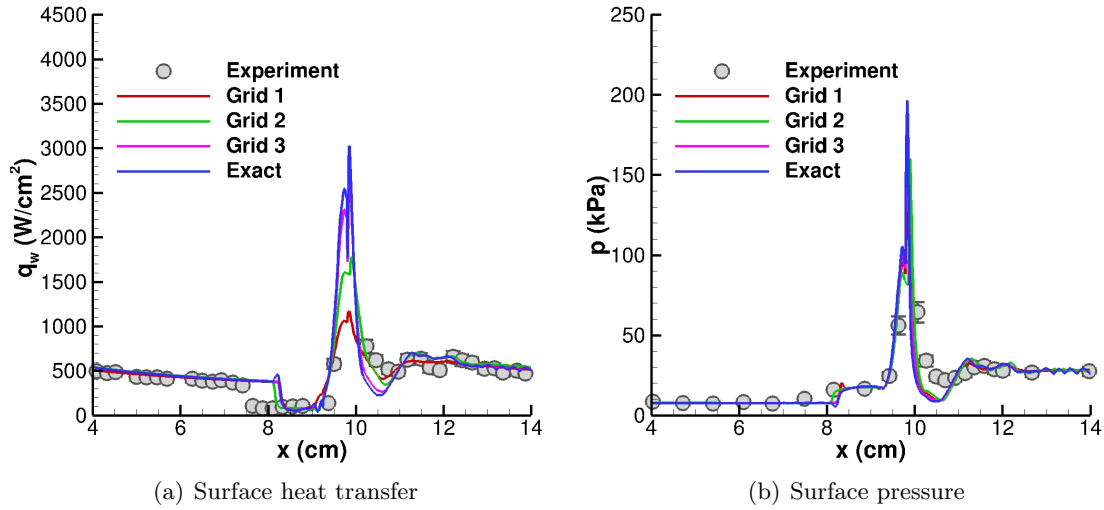


Figure 5.7: Grid study for Run 4 (21.77 MJ/kg) for non-reactive model

185% to 220%. However, as mentioned several times, the comparison of the numerical and experimental peak pressure values is indeterminant. The distance between the gauge with the maximum pressure reading and the gauge before and after is 0.20 and 0.43 cm which is about 50 times larger than the numerical grid spacing. Thus, the measured peak surface pressure may not be the actual maximum pressure. The location of the peak pressure in the numerical simulations is 9.85, 9.83, and 9.79 cm respectively for thermally perfect, non-reactive, and Park I models, while the location of the experimental peak pressure is 10.06 cm. The predicted pressures at the aft cone for the three models are in close agreement with the experimental measurement.

5.4.3 Analysis of Flow Structure

Figure 5.11 presents the Mach contours of thermally perfect, non-reactive, and Park I models for Run 2 (9.65 MJ/kg). The results of Grid 3 are presented. The flow structure is similar for the three models. The adverse pressure at the end of the forward cone creates a separation region. This separation region creates a separation shock which interacts with the oblique shock of the forward cone. The resultant shock interacts with the strong detached bow shock formed in front of the aft cone. As a result of this interaction, a transmitted shock forms toward the aft cone which interacts with the reattachment shock before it reaches

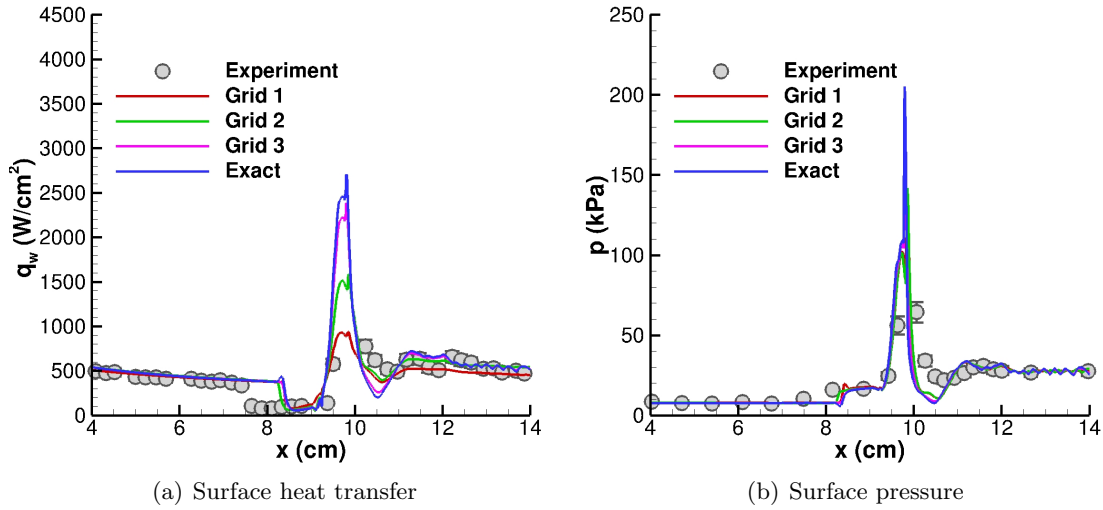


Figure 5.8: Grid study for Run 4 (21.77 MJ/kg) for Park I model

to the wall. A supersonic jet forms due to these interactions and impinges on the aft cone surface, creates a region of high pressure over the body. The supersonic jet undergoes a series of compression and expansion waves which can be seen better in Figure 5.12. The white lines in Figure 5.11 and the pink lines in Figure 5.12 are Mach one isolines, enclosing the subsonic regions after the bow shock, near the wall, and in the separation region. The separation and reattachment shocks are shown respectively with pink and brown lines in Figure 5.11.

Although the flow structure of the three models is similar, it is apparent that the separation region length in the thermally perfect is larger. The separation region starts at 69.64, 76.76, and 76.95 mm respectively for thermally perfect, non-reactive, and Park I models. The distance between the first triple point and the junction of the two cones along the second cone is 13.63, 9.59, and 9.59 mm, respectively for thermally perfect, non-reactive, and Park I models. The normal distance of the triple point to the aft cone surface is 3.90, 3.12, and 3.13 mm respectively for thermally perfect, non-reactive, and Park I models. The larger normal distance of the thermally perfect model is in agreement with the literature, increasing the ratio of the vibrational energy to the freestream kinetic energy decreases the shock standoff distance [103]. The larger standoff distance of the bow shock in the thermally perfect model compared to non-reactive and Park I models creates a shock-shock

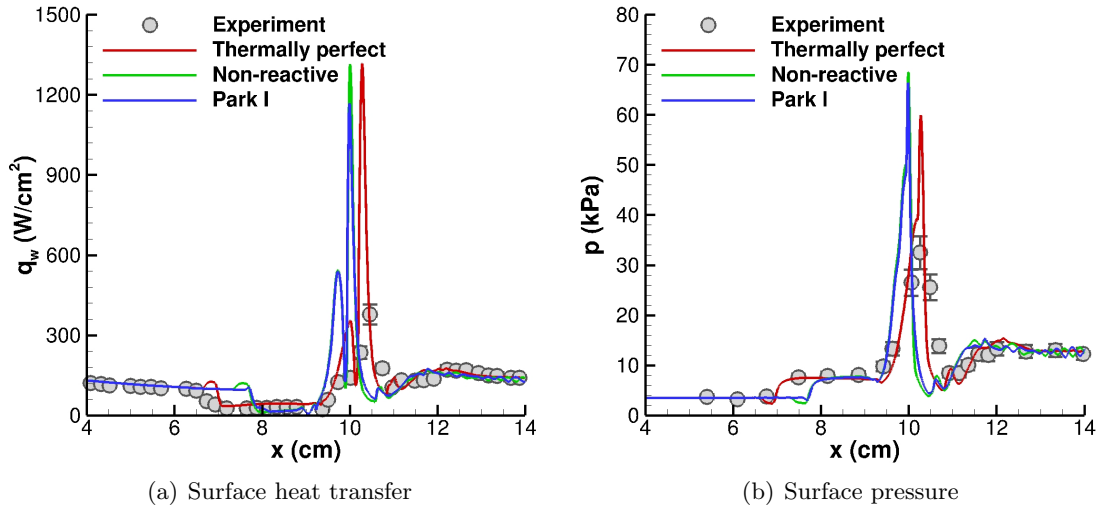


Figure 5.9: Effect of different models on prediction of surface pressure and surface heat transfer for Run 2 (9.65 MJ/kg)

interaction with different pressure gradient in comparison to the two other models. This difference in pressure gradient over the first cone results in the larger separation region for the thermally perfect model. Moreover, the larger distance of the triple point along the aft cone from the two cone junction and larger normal distance from the surface in thermally perfect model results into a larger distance for the supersonic jet to impinge on the surface of the aft cone in comparison to non-reactive, and Park I models. The larger distance along the aft cone from the junction corresponds to a larger axial distance x . Since the impinging location of the supersonic jet is the location of the peak surface pressure and heat transfer, thus, the peak location for the thermally perfect model is larger compared to non-reactive and Park I models.

To better understand the effect of the models, the models compared two by two so only one effect is considered at a time. First, to better understand the effect of the thermochemistry which is the difference between the non-reactive and Park I models, the mass fraction of species NO, N, and O which are the products of thermochemistry reaction are presented in Figure 5.13 for Run 2 (9.65 MJ/kg) along with the line contour flow structure. The maximum mass fraction of species NO, N, and O are 6.4%, 0.07%, and 5.5%, respectively. These numbers are small and thus it is not surprising that the difference between the predicted surface pressure and heat transfer of Park I and non-reactive is negligible.

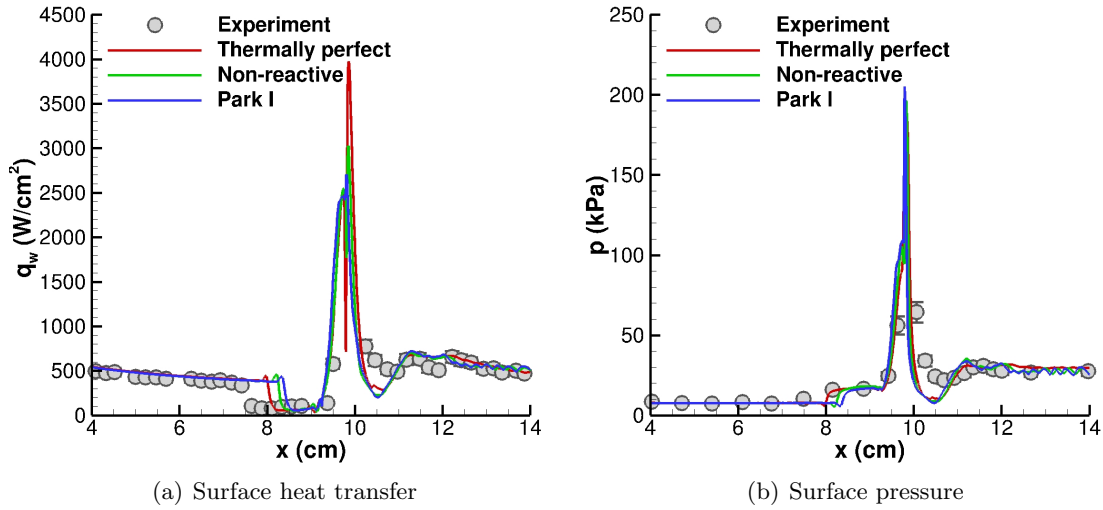


Figure 5.10: Effect of different models on prediction of surface pressure and surface heat transfer for Run 4 (21.77 MJ/kg)

Also, it is evident from Figure 5.13 that the dissociated gas does not reach the double cone surface. The enlarged views of the mass fractions contours show that the flow passed the portion of the bow shock that is almost a normal shock dissociate the gas. However, the supersonic jet separates this dissociated gas from the wall surface. Therefore, the effect of thermochemistry on surface pressure and heat transfer is negligible.

Second, to see the effect of vibrational-translational energy transfer which is the difference between the non-reactive and thermally perfect models, the logarithm of the ratio of Landau-Teller relaxation time of each species to the characteristic time of the flow, *i.e.* time required for the freestream flow to pass a distance equal to the axial length of the first cone, is plotted in Fig. 5.14 for the non-reactive and Park I models. The reason that Park I model results are also included is that thermochemistry results in the creation of diatomic species NO, the effect of thermochemistry on the vibrational-translational energy transfer can also be examined by this comparison. When the logarithm is positive, the time required for transferring energy between vibrational and translational-rotational mode is larger than the characteristic time. When the logarithm is negative, the required time for the energy transfer between two modes are smaller than the characteristic time and if it is zero, the characteristic time is equal to the required time for energy transfer. Since the non-reactive model does not include thermochemistry, there is no species NO in the flow and therefore

the non-reactive model has two vibrational temperatures for species N_2 and O_2 while the Park I model has three vibrational temperatures for species N_2 , O_2 , and NO . The areas enclosed with black lines in Fig. 5.14 are corresponding to the non-positive logarithm of the ratio of Landau-Teller relaxation time of each species to characteristic time. The enclosed areas for both model for species N_2 are small and thus the vibrational-translational effect is only important in regions near the shock-shock interactions. However, the effect of vibrational-translational effect for species O_2 and NO are important in a larger area including the shock-shock interaction region and after the bow shock. The maximum ratio of the sum of vibrational energy of each species times density of that species of the non-reactive model to the thermally perfect model and the Park I model to the thermally perfect model are about 10,000 in the shock-shock interaction region while it is about 1,000 after the bow shock but far from the wall, and less than 10 over the first cone.

Figures 5.15 and 5.16 show respectively the Mach and pressure contours for the thermally perfect, non-reactive, and the Park I models for Run 4 (21.77 MJ/kg) using Grid 3 which is the finest grid of the calculations. The flow structures of all three models are similar as observed for Run 2 (9.65 MJ/kg). The white lines in Fig. 5.15 are Mach one isolines. The pink and brown lines respectively make the separation and reattachment shock more visible.

Figure 5.15 shows that despite having similar flow structures, the thermally perfect model predicts a slightly larger separation region. The separation region starts at 79.58 mm, 81.92 mm, and 83.32 mm respectively for the thermally perfect, non-reactive, and the Park I models. As a result, the interaction of the resultant oblique shock and the bow shock occurs at slightly different locations. The distance between this point and the junction of the two cone along the second cone is 7.24 mm, 7.76 mm, and 7.59 mm, respectively for the thermally perfect model, non-reactive model, and the Park I model. The normal distance of the triple point to the wall is 2.82 mm, 2.06 mm, and 1.66 mm respectively for thermally perfect, non-reactive and Park I models. The normal distance of the triple point from the wall is in agreement with the literature shock standoff distance [103]. Again the larger shock standoff distance of the bow shock in the thermally perfect model explains the larger separation region size predicted by this model.

The combination of the normal distance of the triple point from the second cone wall and its distance along the wall from the junction of the two cones finalizes the location of the high pressure region at the wall. This distance is slightly larger for thermally perfect model compare to the two other models and Park I model has the smallest distance among the three models as seen in Fig 5.16. However, all these changes are less than 4% of the axial length of the first cone and thus the difference between the three models are negligible.

Figure 5.17 shows the mass fraction contours for Run 4 (21.77 MJ/kg) along with the line contour flow structure. The maximum mass fraction of species NO, N, and O are 12.4%, 15.7%, and 23.5%, respectively. These amount of dissociation and recombination is significant and therefore it is surprising that the predicted surface heat transfer and surface pressure of Park I and non-reactive models are close to each other for Run 4. However, it can be seen that the regions of highest mass fractions of NO, N, and O are separated from the wall by the supersonic jet. As a result, the predicted surface heat transfer and surface pressure only slightly differ between the two models.

Figure 5.18 shows the logarithm of the ratio of Landau-Teller relaxation time of each species to the characteristic time of the flow, *i.e.* time required for the freestream flow to pass a distance equal to the axial length of the first cone, for the non-reactive and Park I models. Since the non-reactive model does not include thermochemistry, there is no species NO in the flow and therefore the non-reactive model has two vibrational temperatures for species N_2 and O_2 while the Park I model has three vibrational temperatures for species N_2 , O_2 , and NO. The areas enclosed with black lines in Fig. 5.18 are corresponding to the non-positive logarithm of the ratio of Landau-Teller relaxation time of each species to characteristic time. The vibrational-translational energy transfer is important inside the enclosed line and therefore, for species N_2 , it is important for the shock-shock interaction region and the region after bow shock. The vibrational-translational energy transfer effect for species NO is important for larger area including the shock-shock interaction region, region after the bow shock and region above the separation region. However, for species O_2 , the vibrational-translational effect is important almost in all the area after the oblique shock over the first cone and bow shock of the second cone. Consequently, there is a big difference between the predicted peak heat transfer of the thermally perfect model and the non-reactive and the

Park I models due to the effect of vibrational-translational energy transfer between the two modes of energy. The maximum ratio of the sum of vibrational energy of each species times density of that species for the non-reactive model to the thermally perfect model is 439 and for the Park I model to the thermally perfect model is 247. The reason that we have more vibrational energy in the non-reactive model is that part of the energy of the flow in the Park I model is used for dissociation of molecules and therefore there is less energy in the vibrational modes of energy.

5.5 Conclusion

Three different models, namely, full non-equilibrium laminar Navier-Stokes with Park I thermochemistry denoted “Park I”, 2) non-reactive, and 3) thermally perfect are compared in terms of prediction of aerothermodynamic loading of double cone at Mach numbers of 10.90 and 12.82 with stagnation enthalpies of 9.65 MJ/kg and 21.77 MJ/kg. Surprisingly, the thermally perfect model gives the accurate prediction for the 9.65 MJ/kg case in comparison to the experimental measurement except for the peak values; however, the spacing between the experimental data in the vicinity of the peak values are so large that it is possible that the measured peak values are not the actual peak values. For the 21.77 MJ/kg case, although the prediction of the separation region is slightly underpredicted, however, the thermally perfect model still presents the best prediction among the three models.

The inclusion of vibrational-translation energy transfer into the modeling reduced the separation region size which makes the prediction worse in comparison to the thermally perfect gas. The inclusion of thermochemistry has a negligible effect on the aerothermodynamic loadings. This is because the jet forms by the interaction of the shock waves of the forward and aft cones creates a shield that does not allow the highly heated air with thermochemical reaction to reach the surface. Therefore, it can be concluded that this experiment is not a test for the thermochemistry model.

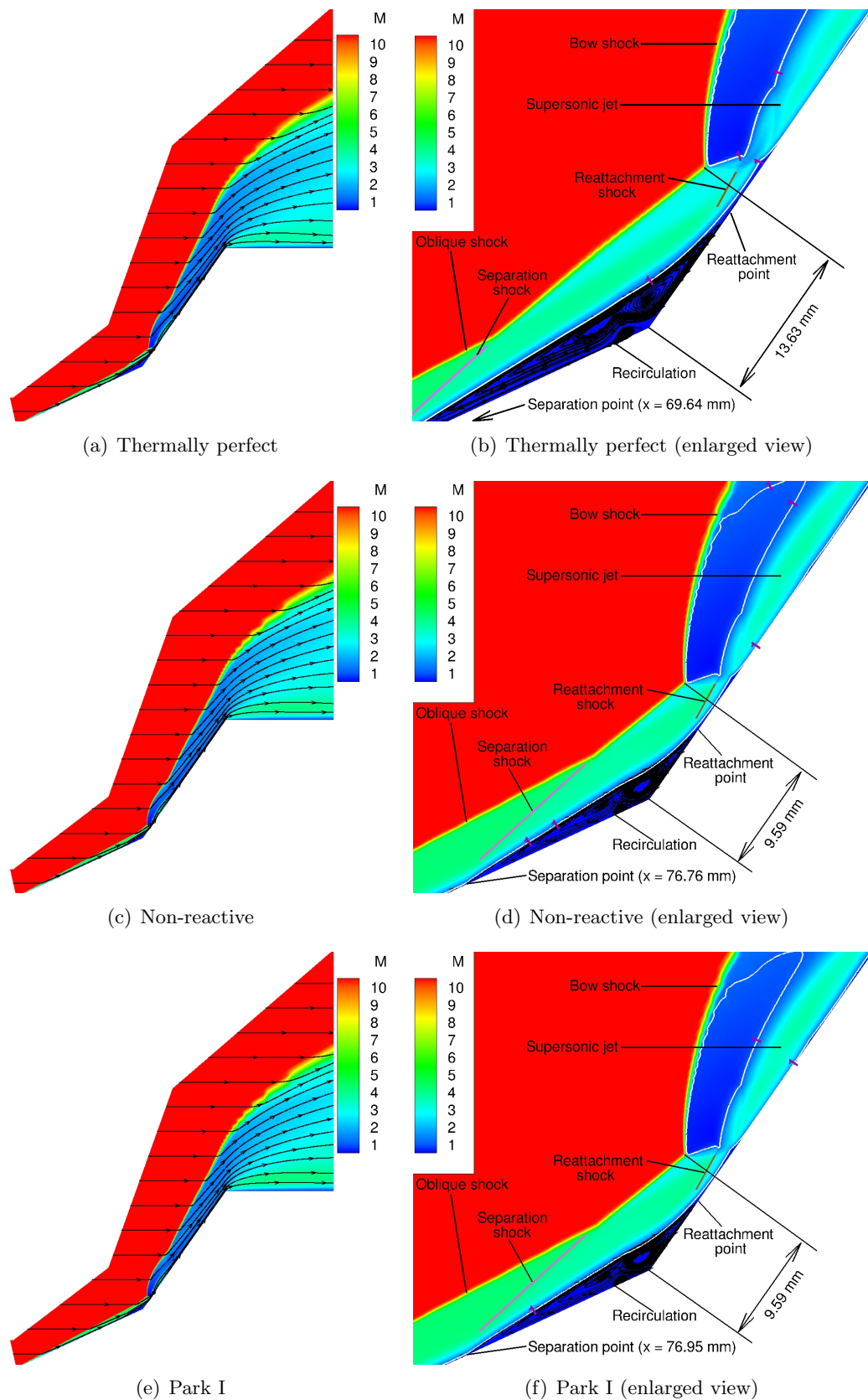
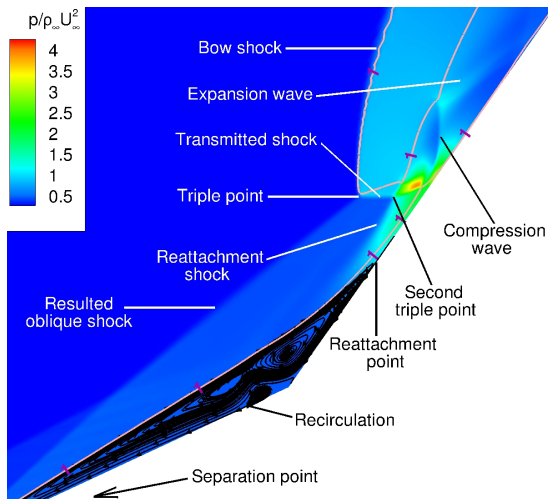
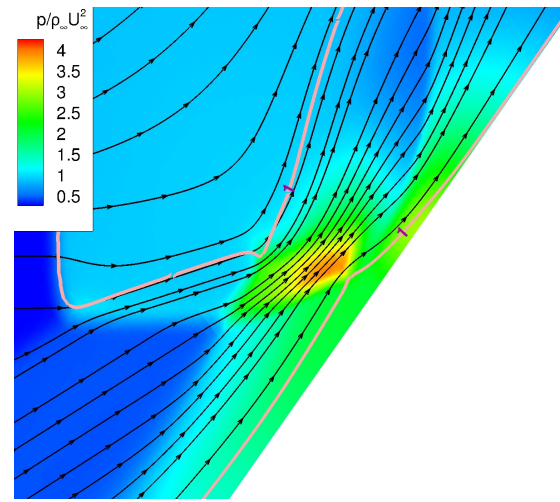


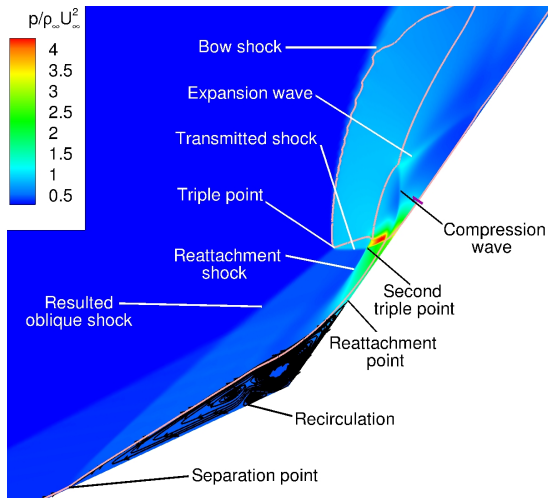
Figure 5.11: Mach contours for thermally perfect, non-reactive, and Park I models for Run 2 (9.65 MJ/kg)



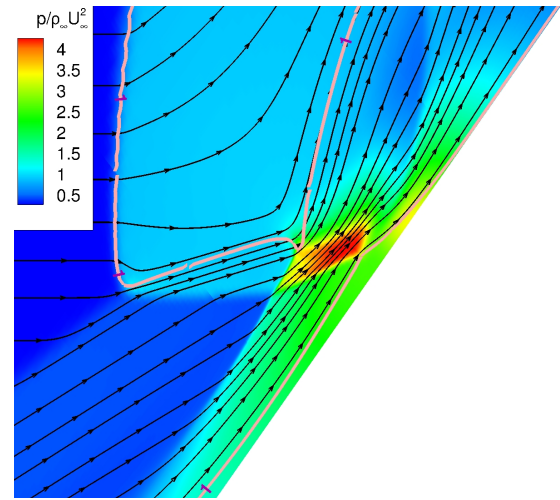
(a) Thermally perfect (enlarged view)



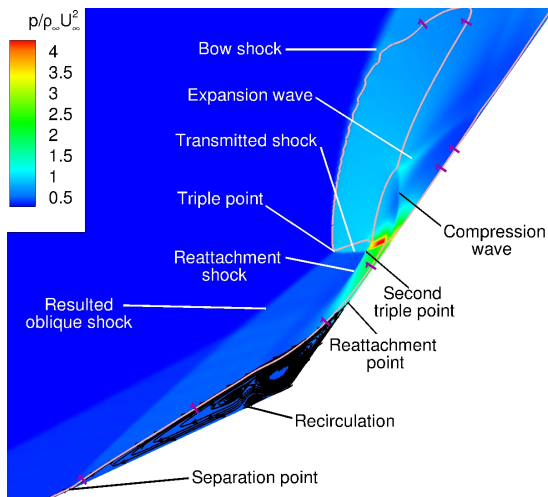
(b) Thermally perfect (extra enlarged view about peak pressure)



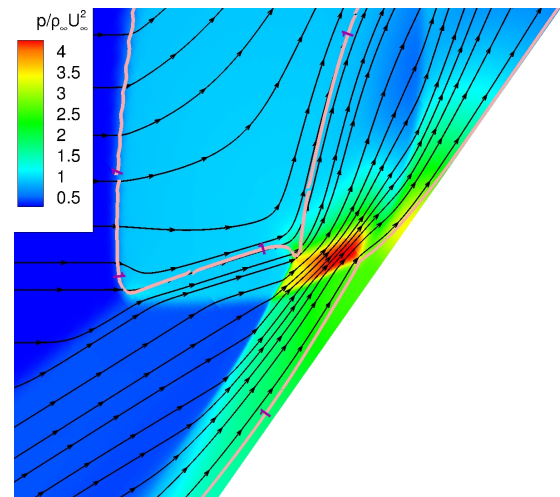
(c) Non-reactive (enlarged view)



(d) Non-reactive (extra enlarged view about peak pressure)

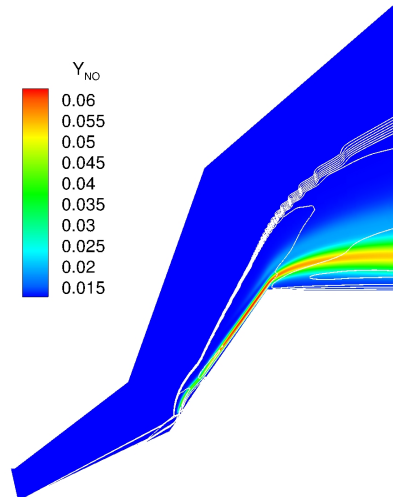


(e) Park I (enlarged view)

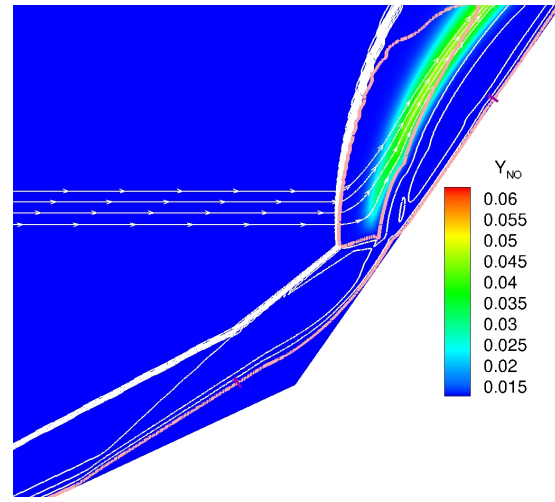


(f) Park I (extra enlarged view about peak pressure)

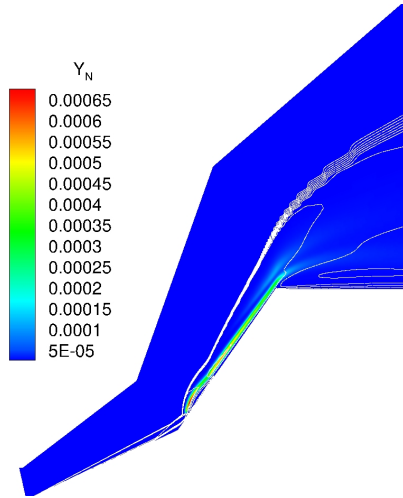
Figure 5.12: Pressure contours for thermally perfect, non-reactive, and Park I models for Run 2 (9.65 MJ/kg)



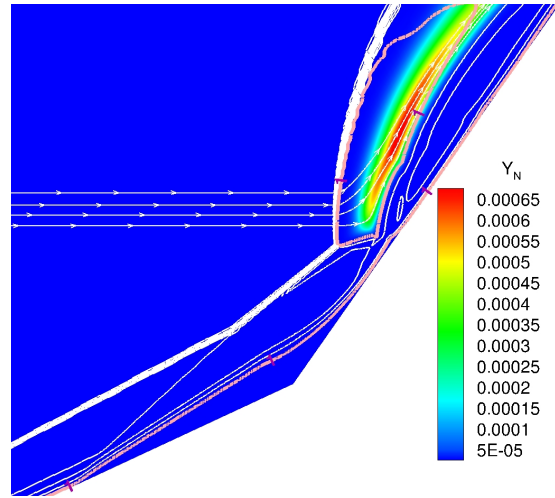
(a) Mass fraction of NO



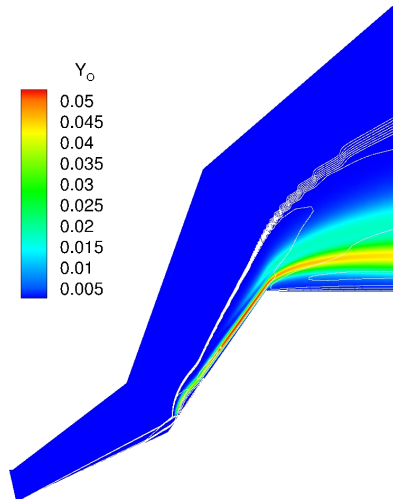
(b) Mass fraction of NO (enlarged view)



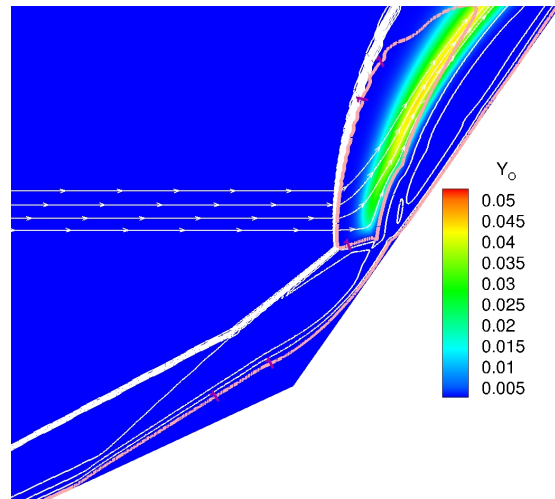
(c) Mass fraction of N



(d) Mass fraction of N (enlarged view)



(e) Mass fraction of O



(f) Mass fraction of O (enlarged view)

Figure 5.13: Mass fraction contours of NO, N, and O for Park I model for Run 2 (9.65 MJ/kg)

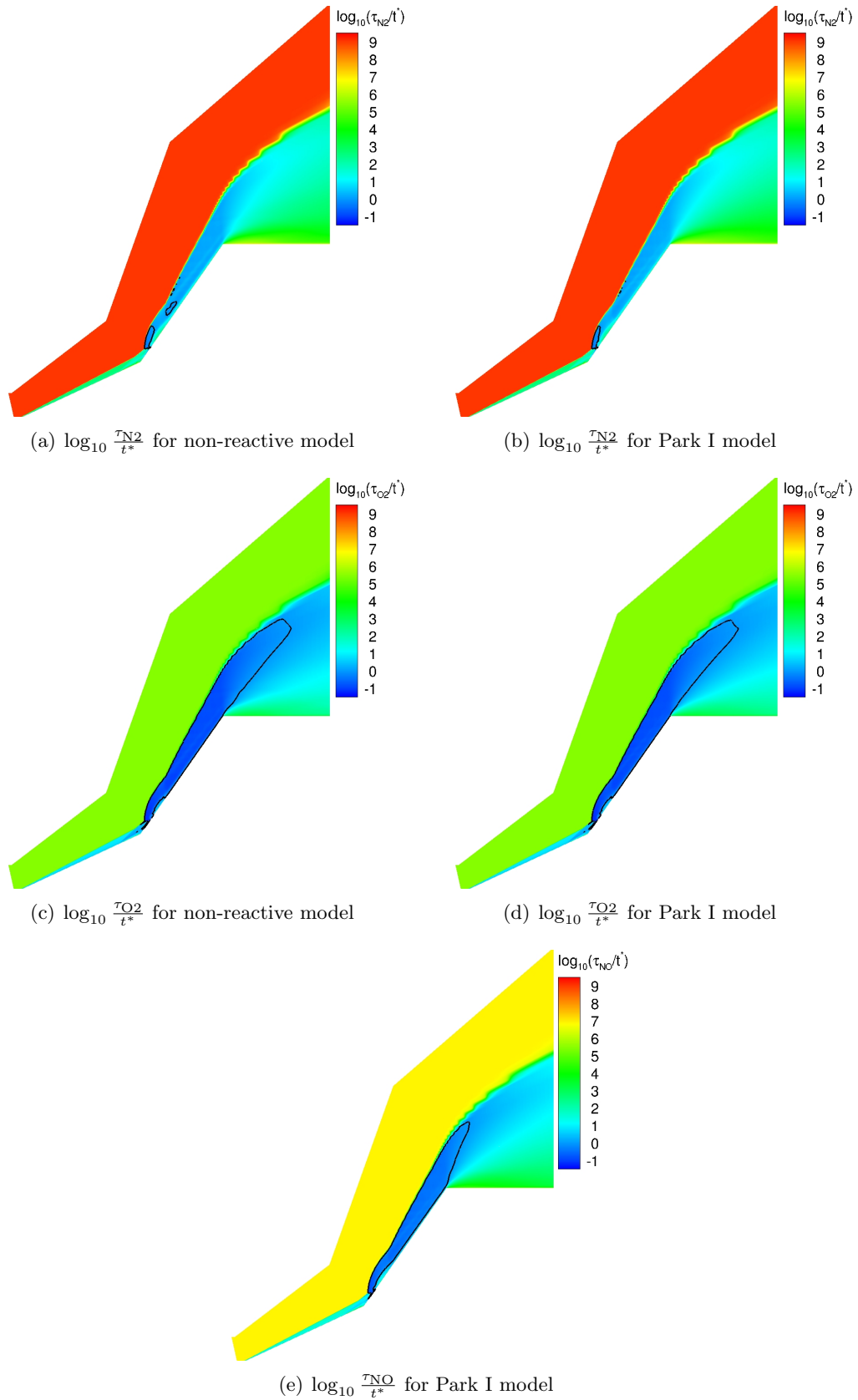


Figure 5.14: Logarithm of ratio of Landau-Teller relaxation and flow characteristic times contours for non-reactive and Park I models for Run 2 (9.65 MJ/kg)

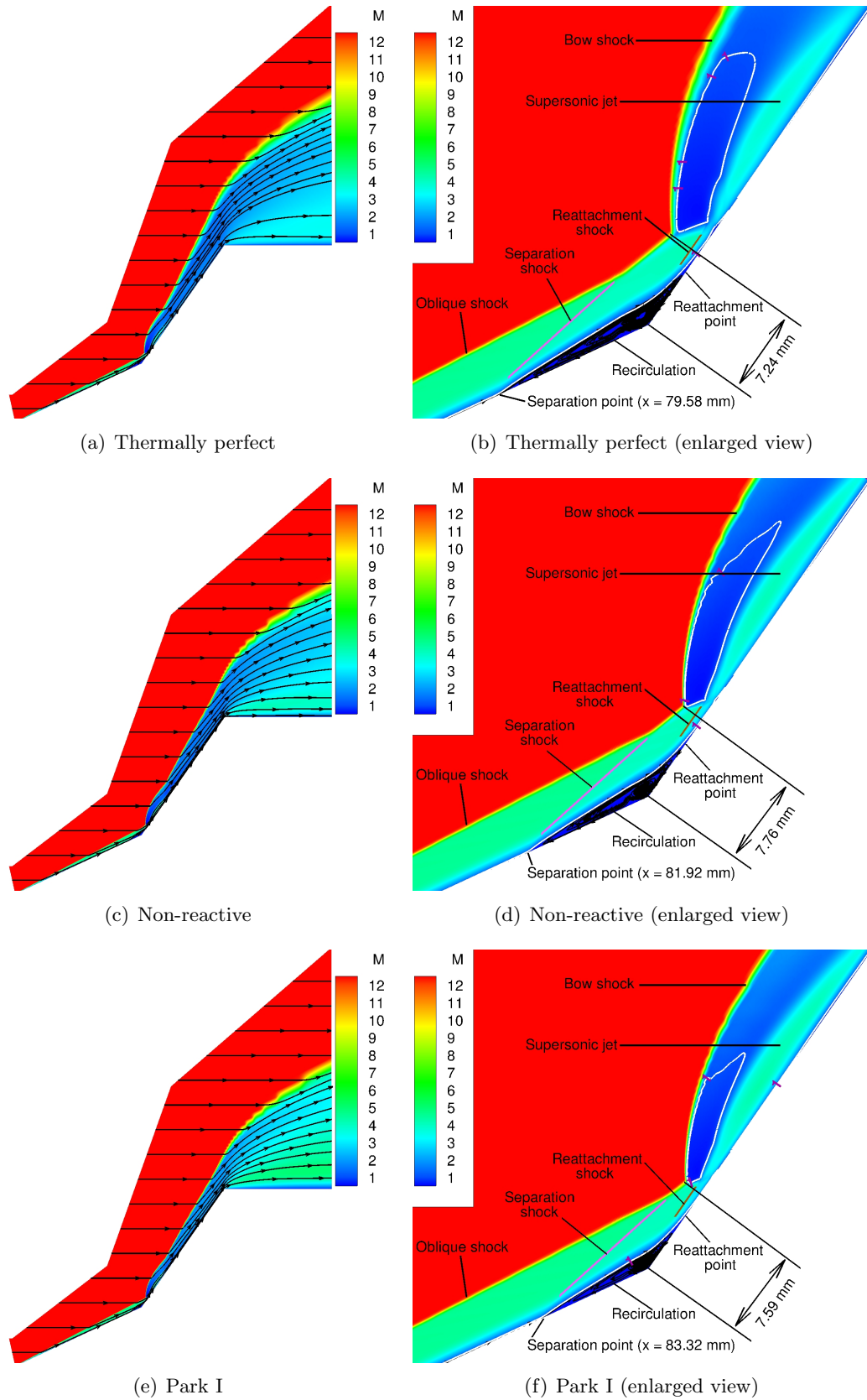
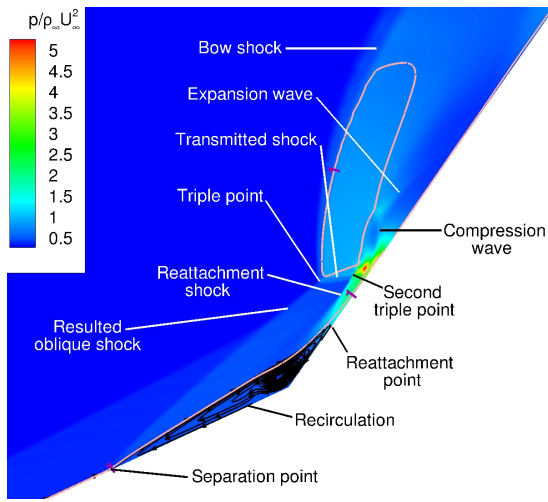
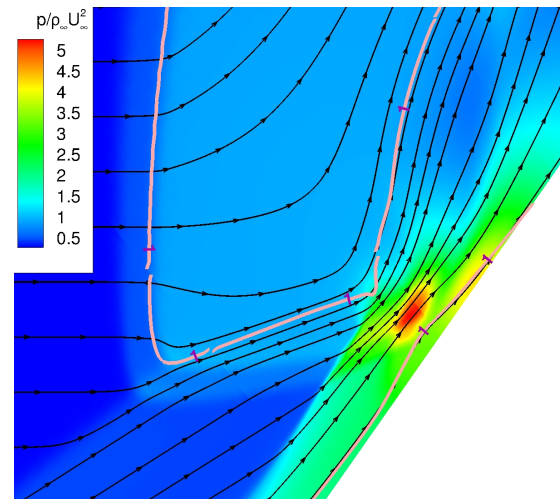


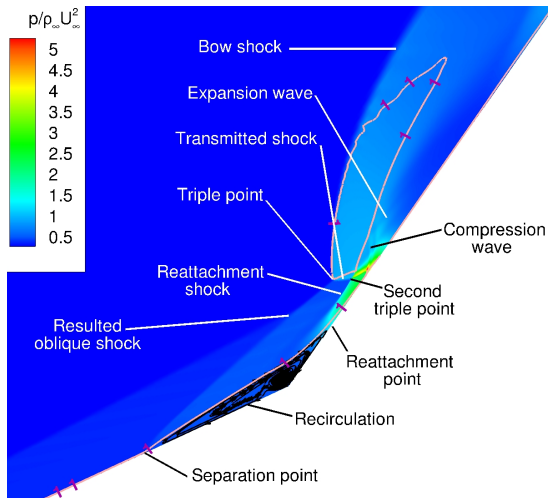
Figure 5.15: Mach contours for thermally perfect, non-reactive, and Park I models for Run 4 (21.77 MJ/kg)



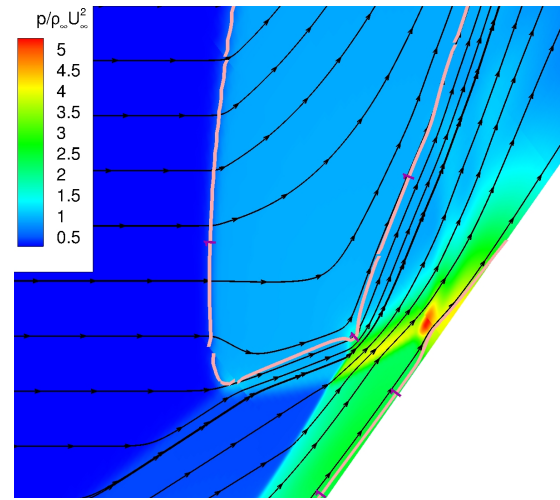
(a) Thermally perfect (enlarged view)



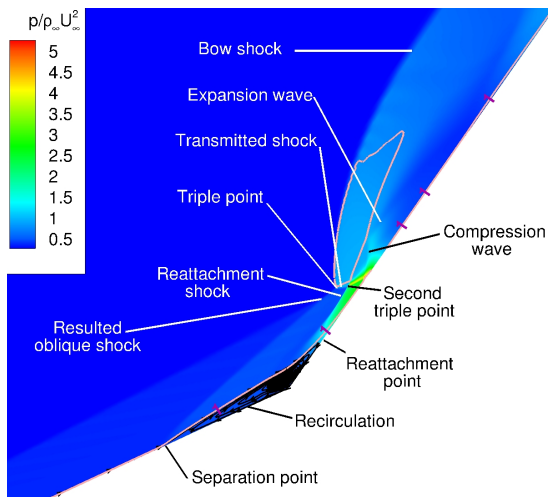
(b) Thermally perfect (extra enlarged view about peak pressure)



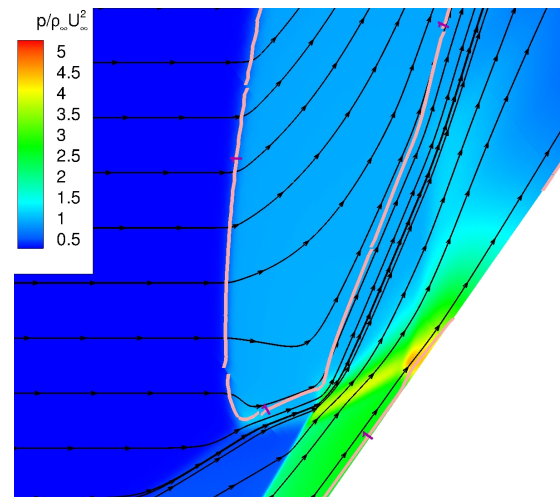
(c) Non-reactive (enlarged view)



(d) Non-reactive (extra enlarged view about peak pressure)

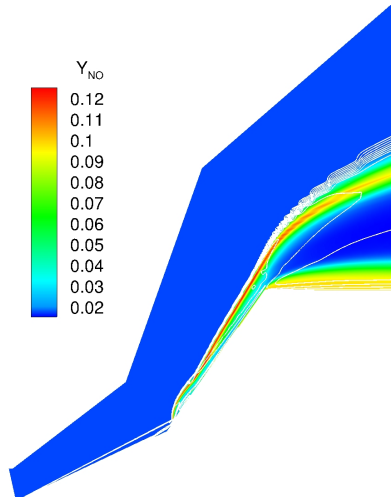


(e) Park I (enlarged view)

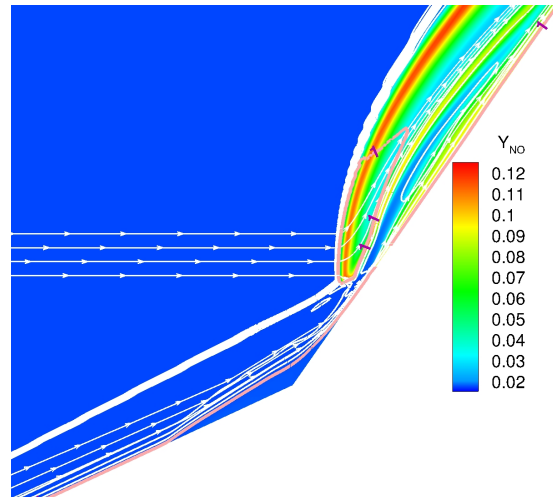


(f) Park I (extra enlarged view about peak pressure)

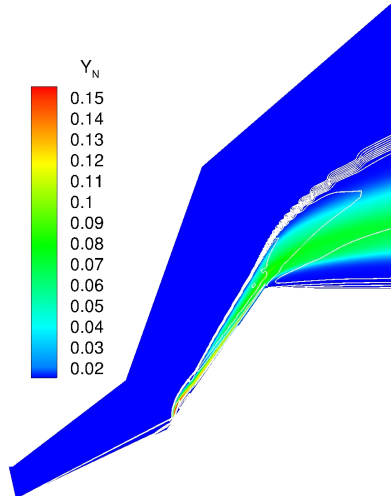
Figure 5.16: Pressure contours for thermally perfect, non-reactive, and Park I models for Run 4 (21.77 MJ/kg)



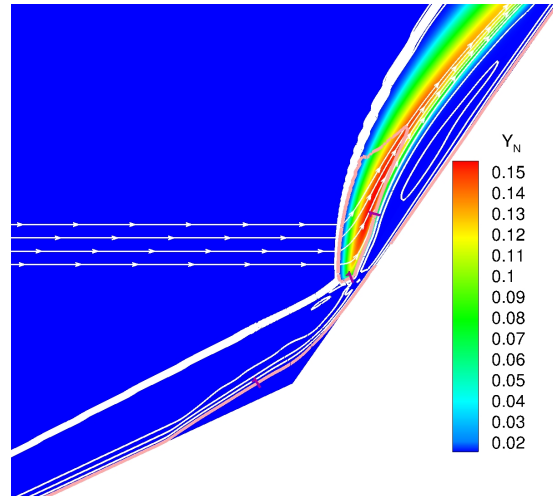
(a) Mass fraction of NO



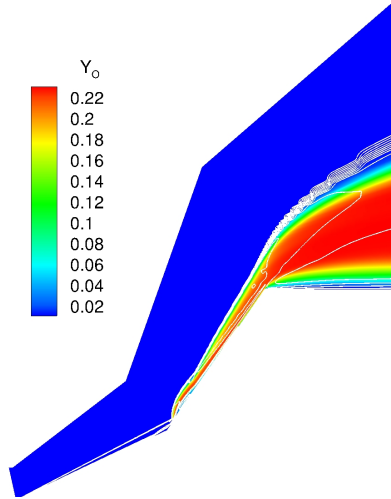
(b) Mass fraction of NO (enlarged view)



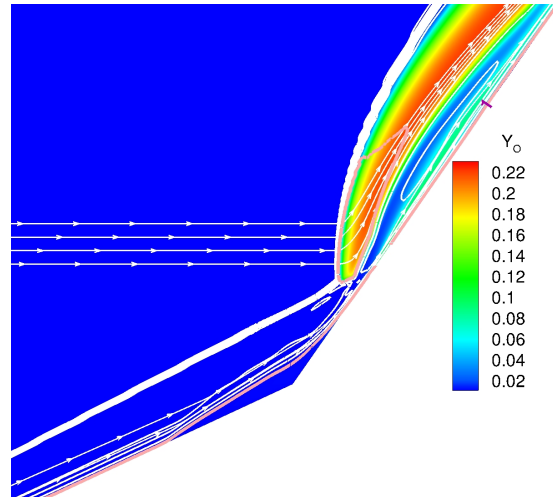
(c) Mass fraction of N



(d) Mass fraction of N (enlarged view)



(e) Mass fraction of O



(f) Mass fraction of O (enlarged view)

Figure 5.17: Mass fraction contours of NO, N, and O for Park I model for Run 4 (21.77 MJ/kg)

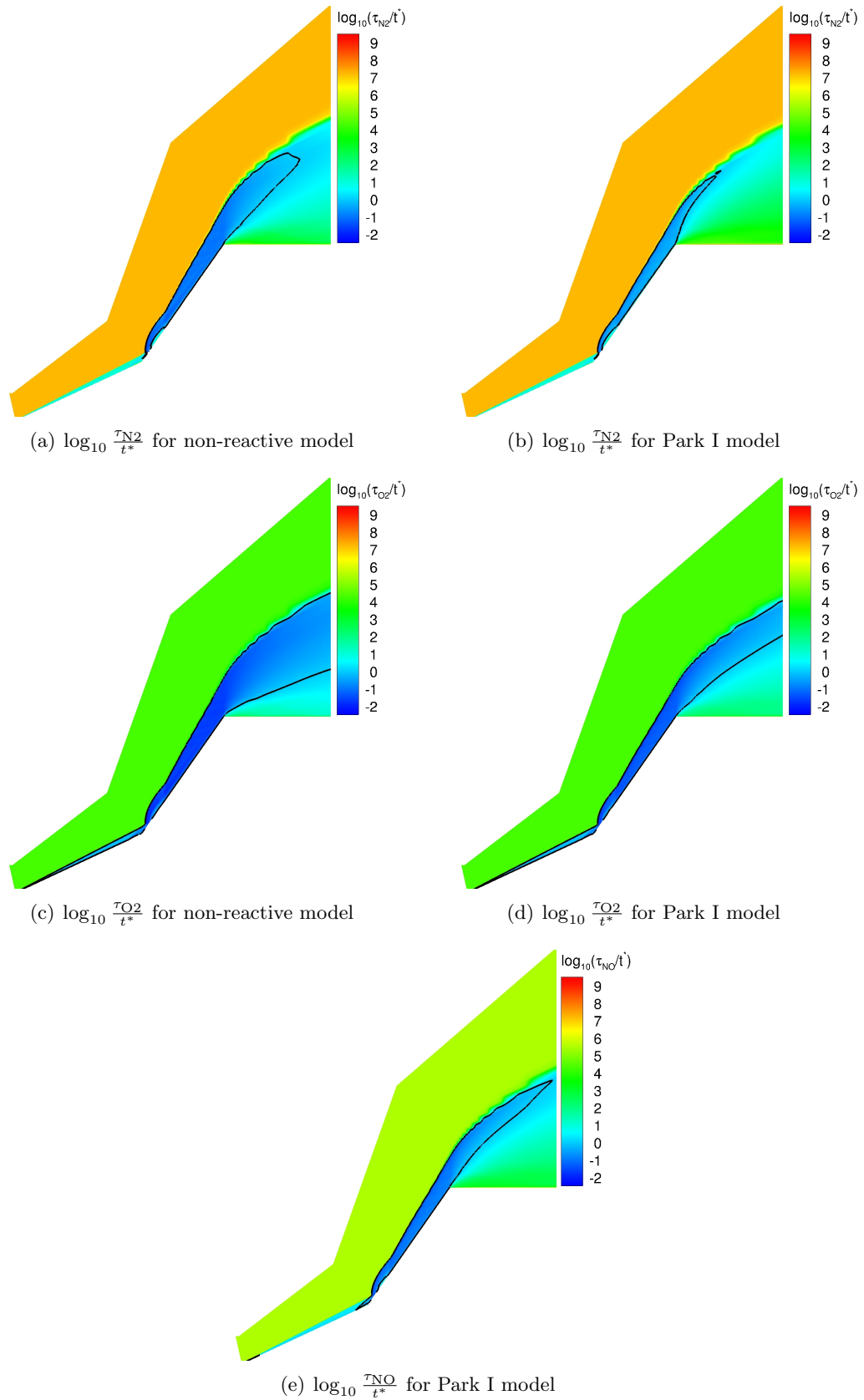


Figure 5.18: Logarithm of ratio of Landau-Teller relaxation and flow characteristic times contours for non-reactive and Park I models for Run 4 (21.77 MJ/kg)

Chapter 6

Prediction of Aerothermodynamic Loading on a Hemisphere Due to Edney III Shock-Shock Interaction

Accurate prediction of shock-shock interactions in hypersonic flows is also important. Due to the problematic behavior of these interactions, especially type III and IV of the Edney category, it is necessary to have a reliable CFD tool for accurate prediction of these interactions or at least know where are the shortcomings. In this chapter, the Edney III type interaction is investigated at Mach 14.6.

6.1 Introduction

Performing a flight test for a hypersonic vehicle is expensive. Therefore, the interest is to rely more on numerical simulation and minimize expensive experiments. However, the reliability and capability of the numerical models for consistent and accurate prediction of complicated phenomena such as shock-shock interaction have not yet been achieved. The failure in accurate prediction of the Edney III or Edney IV interaction can cause structural failure due to the high surface pressure and of heat transfer.

The objective of this chapter is to examine the numerical capability for prediction of an Edney III type interaction of an experiment performed at the Calspan University of Buffalo Research Center (CUBRC) at Mach 14.6. Several simulations are required due to uncertainty in the exact location of the incident shock (unless the simulation covered the entire experimental domain including shock generator at one simulation). The effect of different locations for impinged shock and some numerical aspects like temporal accuracy on the predicted surface pressure and surface heat transfer is evaluated.

6.2 Description of Experiment

The experimental model is a smooth hemisphere with a radius of 6 inches. The hemisphere surface is instrumented with sixty two heat transfer and eight pressure gauges to measure the surface heat transfer and surface pressure over the centerline of the hemisphere surface. A sixty-inch flat plate is used as a shock generator to form an oblique shock that impinges on the hemisphere shock. This flat plate is eighteen inches wide and has a leading edge curvature of 0.625 inches. The plate is installed at a ten-degree angle. Figure 6.1 shows the schematic of the hemisphere model and the shock generator installed in the tunnel. This experiment was performed in CUBRC's 48-Inch Shock Tunnel [104].

There are several data sets in this experiment for Edney III and IV types of interactions [1]. The values of A and B which are defined in Figure 6.1 determine the interaction type for each data set. For the purpose of the study in this chapter, Run 17 is chosen from this data set with the freestream conditions given in Table 6.1. Table 6.2 presents the values of A and B for Run 17. The hemisphere wall is considered as an isothermal wall at 292.7 K.

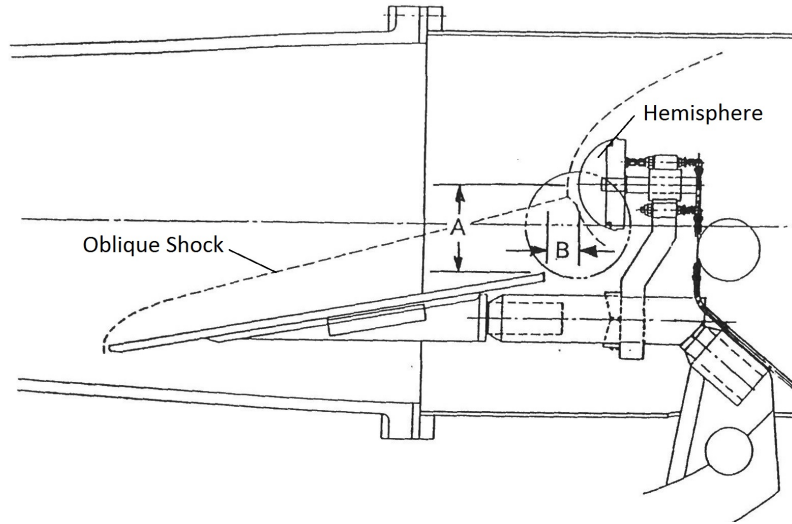


Figure 6.1: Schematic of hemisphere model in hypersonic shock tunnel [1]

Table 6.1: Flow conditions

Run No.	Total Enthalpy (MJ/kg)	Mach Number	Pitot Pressure (kPa)	Unit Reynolds ($/10^6 \text{ m}^{-1}$)	Velocity (km/s)	Density (g/m^3)	Temperature (K)
17	2.1498	14.616	0.9494	0.1419	2.052	0.241	47.37

Table 6.2: Experimental Location of Shock Generator Relative to Hemisphere Cylinder

Run No.	A (cm)	B (cm)
17	21.11248	9.11860

6.3 Methodology

The thermally perfect model (see 2.3.2) is used for this simulation. The total enthalpy of this flow is 2.1498 MJ/kg. This means that the maximum static temperature of this experiment does not exceed 2150 K. At this temperature, the reactions are expected to be minimal. Roe's method with the MUSCLp reconstruction method is used for the calculation of inviscid fluxes. The DPLR method is used to achieve high performance integration in time. The simulation is initialized with freestream conditions.

6.3.1 Computational Domain

Figure 6.2 shows the computational domain of this problem. In this problem, there is a plane of symmetry ($(x - y$ plane at $z = 0$) which allows us to simulate only half of the domain. The grid used for the computations of this chapter consists of 1.9 M cells and has stretching in the direction to the wall and also along the surface with the smallest spacing around the hemisphere tip. Table 6.3 resents the grid properties of the gird used for the simulations.

Table 6.3: Computational grid

Grid	il	jl	kl	Δr_{\min} in μm	$\Delta \theta_{\min}$ in deg	$\Delta \phi$ in deg	Δt in ns	Total No. Cells
Grid 1	80	600	40	40.785	0.7273	4.50	13.986	1,920,000

LEGEND

il	No. of cells along surface from hemisphere tip to the end of hemisphere
jl	No. of cells normal to the surface
kl	No. of cells in azimuthal direction about centerline axis

NOTE

Number of zones: 128

The boundary conditions are color coded in this figure. The outer surface of this semi-hemisphere with the red and green color is the fixed boundary condition. The red section indicates the fixed values at freestream while the green part is related to the fixed values after the oblique shock. The inner semi-hemisphere with the black color is the surface of

the hemisphere with the non-catalytic ($\partial Y_\alpha / \partial n = 0$ where n is the normal distance to the boundary) no-slip isothermal boundary condition. The blue arc shape surface is the zero-gradient outflow boundary condition and the yellow arc shape surface is the plane of symmetry with the symmetry boundary condition.

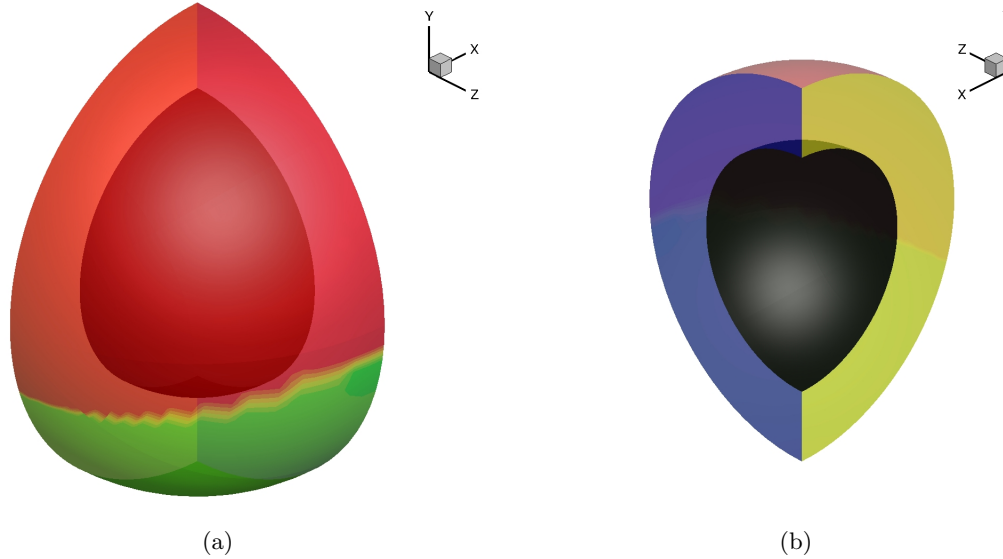


Figure 6.2: Computational domain

The location of the impinging shock which divides the inflow boundary condition is specified with two variables: 1) the angle of the impinging oblique shock measured from a separate shock generator simulation, and 2) the offset location of the oblique shock from the hemisphere center calculated as if there was no hemisphere in the way of the oblique shock. The offset location variable is shown in Figure 6.3. The offset location is adjusted until the location of the peak surface pressure and peak surface heat transfer coincide with the experimental data. Candler and Nompelis [105] and Gaitonde and Shang [106] used the same adjusting method to find the exact location of the impinging shock.

6.4 Results

Table 6.4 presents the two cases that are considered in this chapter for the impinging shock location. The shock angle is constant for both cases since it is measured from the shock generation simulation. However, the offset variable is changed to find the correct location

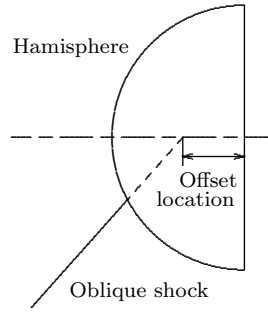


Figure 6.3: Definition of offset location variable used for specifying the location of the impinging shock

of the shock by matching the peak location of the surface pressure and heat transfer with experimental data.

Table 6.4: Impinging shock location parameters

Case	Shock angle (deg)	Offset variable ¹
1	13.6	0.46
2	13.6	0.56

NOTE

¹ Nondimensionalized by radius of the hemisphere

6.4.1 Results of Case 1

Figures 6.4 and 6.5 show the Mach, logarithm of the ratio of pressure to freestream pressure, and the ratio of temperature to the freestream temperature contour plots of the shock-shock interaction of the impinging shock and the bow shock forms in front of the hemisphere in the plane of symmetry for Case 1. Figure 6.4(b) shows the enlarged view of the interaction region. From this figure, the Edney III type of interaction is recognizable. The oblique shock interacts with the bow shock and a transmitted shock emanates from the first triple point. The flow downstream of the bow shock is subsonic while the flow passing through the transmitted shock is still supersonic. Therefore, a shear layer forms above the transmitted shock. This shear layer impinges on the hemisphere surface, creates a subsonic region with high pressure and high heat transfer. The isoline of Mach number equal to one is shown in Figures 6.4(b) and 6.5(a) while the streamlines of the flow are presented in figure 6.5(b).

Figure 6.6 shows the variation of dimensionless surface pressure and heat transfer versus time at point “P” in the vicinity of the location of peak pressure and peak heat transfer.

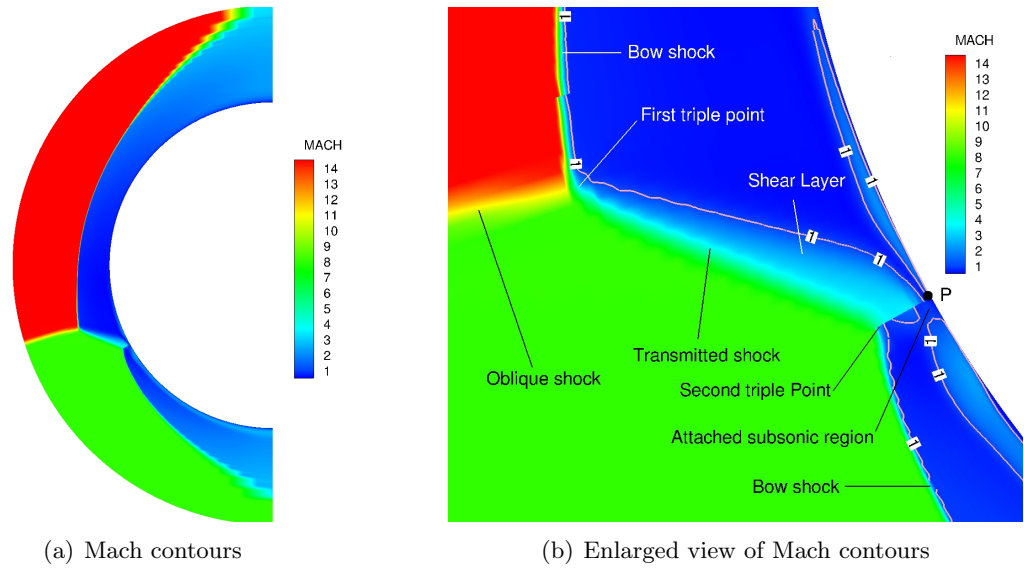


Figure 6.4: Mach contours in the symmetry plane for Case 1

Point P is shown in Figure 6.4. The profile of the surface pressure and heat transfer present an unsteady but statistically stationary behavior.

Figure 6.7 shows the instantaneous pressure coefficient and the dimensionless heat transfer over the hemisphere surface. The pressure coefficient C_p and the dimensionless heat transfer q/Q_{FR} are defined as

$$C_p = \frac{p_w - p_\infty}{\frac{1}{2}\rho_\infty U_\infty^2} \quad (6.1)$$

$$q/Q_{\text{FR}} = \frac{k_w \frac{\partial T}{\partial n}}{Q_{\text{FR}}} \quad (6.2)$$

where p_w is wall pressure, p_∞ is the freestream pressure, ρ_∞ is the freestream density, k_w is air conductivity at the wall, $\frac{\partial T}{\partial n}$ is the temperature gradient normal to the wall, and Q_{FR} is the Fay-Riddell heat transfer [107] given in Holden and Nowak [1]. Figure 6.7 illustrates the existence of a rectangular shape region with higher pressure and heat transfer. The values are the highest near the plane of symmetry of the hemisphere.

Figure 6.8 compares the time-averaged pressure coefficient and dimensionless heat transfer on the hemisphere surface in the plane of symmetry with the experimental data. In these graphs, $\theta = 0$ represents the hemisphere tip and negative values of θ are located below the tip where the interaction occurs. Although both pressure coefficient and dimensionless heat transfer profile have the same general behavior as the experimental data, the locations of

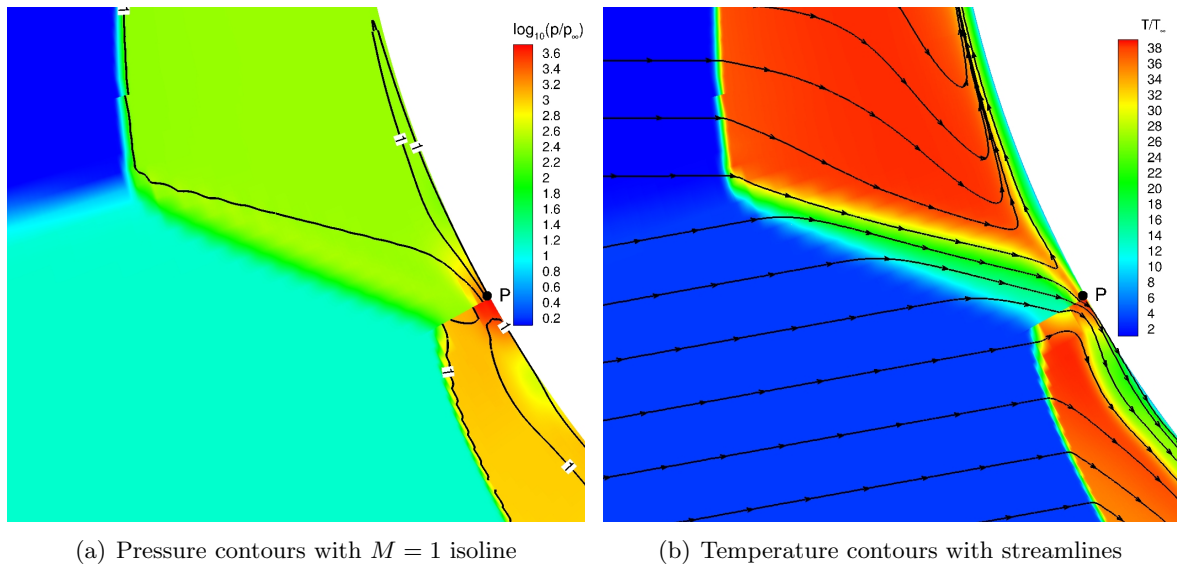


Figure 6.5: Pressure and temperature contours in the symmetry plane for Case 1

the peak values are off from the experimental peaks by three degrees. Moreover, the peak values are also overpredicted by about 130%.

Spectrum Analysis

A Fast Fourier Transform (FFT) analysis of the dimensionless surface heat transfer profile of point P versus time (Figure 6.6(b)) is performed to achieve a better understanding of the statistical behavior of the flowfield. The FFT result is shown in Figure 6.9 where f is the dimensionless frequency defines as

$$f = \frac{f^* R}{U_\infty} \quad (6.3)$$

and f^* is the dimensional frequency. There is a dominant frequency in this figure at $f = 0.345$ which is equal to $202.9 \mu\text{s}$ period. Kroll *et al.* [108] and Gaitonde and Shang [106] reported respectively the dimensionless frequencies of 0.049 and 0.79 for an Edney IV shock-shock interaction over a circular cylinder with two dimensional solvers. Moreover, the spectrum is discrete; *i.e.*, it has separate distinctive peaks in the range of analyzed frequencies. This is an indication that the flow is an *unsteady laminar* flow.

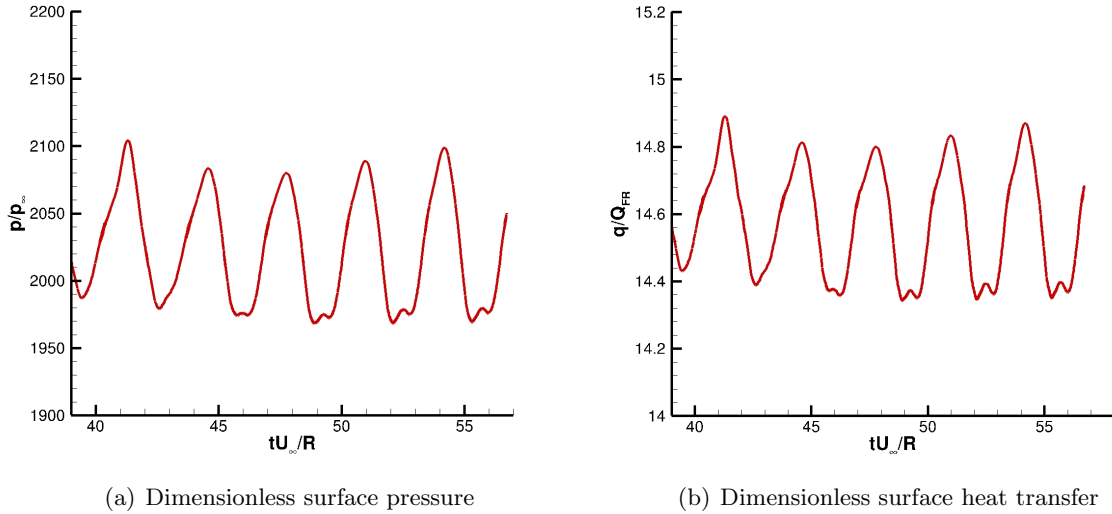


Figure 6.6: Dimensionless surface pressure and heat transfer *vs.* time for point P in the interaction region for Case 1

6.4.2 Results of Case 2

The location of the peak pressure and heat transfer has not coincided with the experimental location for Case 1. Therefore, a new location for the impinging shock is selected (Case 2 in Table 6.4). The instantaneous flow structure of this calculation at the dimensionless time of $\tau = tU_\infty/R = 197.665$ is shown in Figures 6.10 and 6.11. Although some vortices appear in the flowfield, the same Edney III structure is seen in the flowfield structure.

Figure 6.12 shows the variation of the pressure coefficient and dimensionless heat transfer on the hemisphere surface at point P. Point P which is located near the peak region of surface pressure and heat transfer is shown in Figure 6.10(b). From these graphs, there is no recognizable repeated behavior. The instantaneous pressure coefficient and dimensionless heat transfer coefficient on the hemisphere surface at $\tau = 198.265$ is illustrated in Figure 6.13. This figure shows that the maximum surface pressure and heat transfer, at least at this instant of time, is not located at the plane of symmetry.

The time-averaged (from dimensionless time of 201.467 to 338.465) pressure coefficient and dimensionless heat transfer is displayed in Figure 6.14. The adjusted impinging shock location predicts the peak location of surface pressure and heat transfer accurately. Moreover, the peak surface pressure coefficient and peak dimensionless heat transfer coefficients

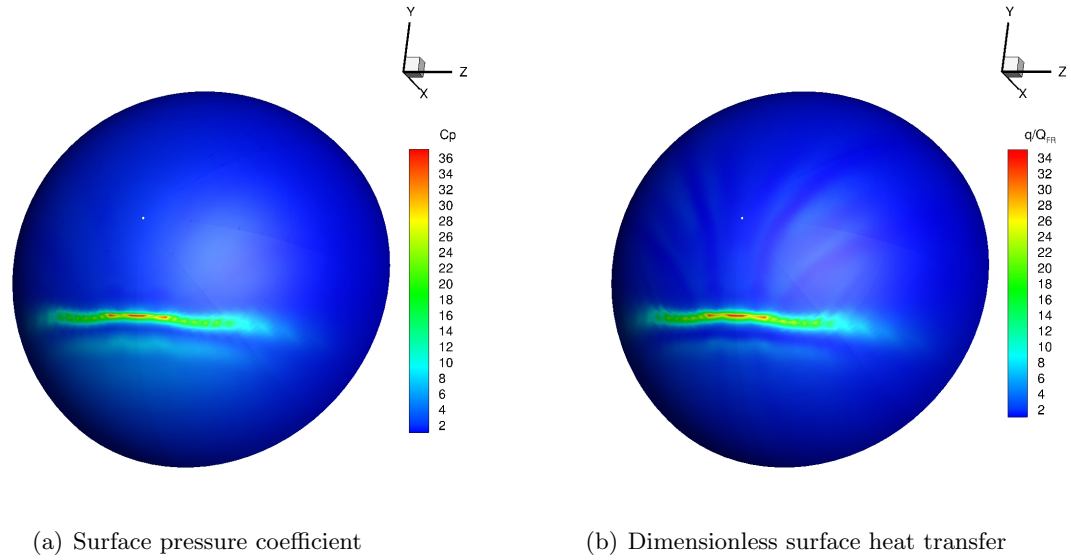


Figure 6.7: 3-D pressure coefficient and dimensionless heat transfer on hemisphere surface for Case 1

are closer to the experimental values.

Spectrum Analysis

The FFT analysis of the dimensionless surface heat transfer of point P (Figure 6.12(b)) is performed to better understand the flowfield for Case 2. Four FFT analysis is performed at four different time intervals of $\Delta\tau$ equal to a) 67, b) 134, c) 201, and d) 268. The results of these analyses are presented in Figure 6.15. The four spectra are in close agreement with each other indicating that the flow is statistically stationary. The general behavior of these profiles is suggesting a turbulent flow.

The instantaneous computed surface heat transfer q_w is a weighted sum of the static temperatures at the surface, the cell adjacent to the surface, and the cell immediately above that cell in accordance with the second order accurate discretization used to determine q_w . The wall is isothermal, and therefore the surface temperature is fixed. Hence, the instantaneous surface heat transfer is a weighted sum of the instantaneous temperature of the two next cells adjacent to the surface. Since the Prandtl number is $\mathcal{O}(1)$, the energy spectrum for the temperature fluctuations in the inertial subrange is [109]

$$E_\theta(k) = \beta N \epsilon^{-1/2} k^{-5/3} \quad (6.4)$$

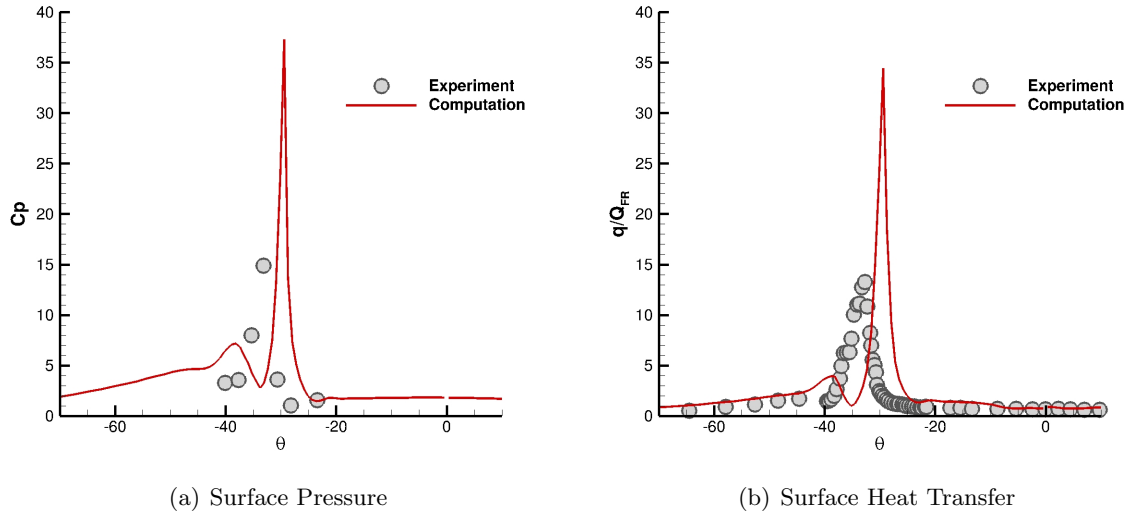


Figure 6.8: Comparison of Surface Pressure Coefficient and Dimensionless Heat Transfer on Plane of Symmetry of Hemisphere with Experimental Data for Case 1

where θ is the temperature fluctuations, β is a constant, N is the dissipation of temperature variance, ϵ is energy dissipation and k is the wavenumber. By the usual Taylor hypothesis, therefore

$$E_\theta \propto f^{-5/3} \quad (6.5)$$

where f is the dimensionless frequency. Equation (6.4) assumes the existence of an inertial subrange for wavenumbers k where

$$k\ell \gg 1 \quad (6.6)$$

$$k\eta \ll 1 \quad (6.7)$$

where ℓ is the characteristic length scale of the overall flowfield, and η is the Kolmogorov length scale. By analogy, this implies the existence of a range of dimensionless frequencies f_{inertial} in the inertial subrange satisfying

$$f_{\text{inertial}} \gg f_{\text{flowfield}} \quad (6.8)$$

$$f_{\text{inertial}} \ll f_{\text{dissipation}} \quad (6.9)$$

The value of $f_{\text{flowfield}}$ is $\mathcal{O}(1)$ from (6.3). The value of $f_{\text{dissipation}}$ may be estimated as follows.

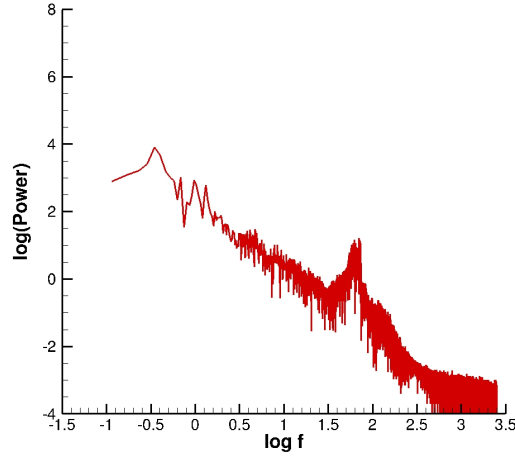


Figure 6.9: Fast Fourier Analysis of surface heat transfer *vs.* time for point P in the interaction region (Case 1)

The rate of dissipation of energy per unit volume by viscosity is

$$\epsilon = \frac{\partial \tau_{ij} u_i}{\partial x_j} \quad (6.10)$$

To a first approximation near the wall, the rate of dissipation of energy per unit mass is

$$\epsilon \approx \frac{\tau_w^2}{\mu_w \rho_w} \quad (6.11)$$

The dimensionless characteristic frequency is therefore

$$f_{\text{dissipation}} = \left(\frac{\epsilon}{\nu_w} \right)^{1/2} \frac{R}{U_\infty} \approx \frac{\partial u}{\partial n} \quad (6.12)$$

where $\partial u / \partial n$ is the dimensionless normal derivative of the tangential velocity at the wall.

A typical value at point P is $\mathcal{O}(100)$. Therefore an inertial subrange would correspond to

$$1 \ll f_{\text{inertial}} \ll 100 \quad (6.13)$$

In Figure 6.15 in addition to the four FFT analysis for the four time intervals from 67 to 268, a straight line corresponding to the slope of the expected spectrum of a turbulent flow is shown. In all these graphs, in the inertial subrange (indicated by two arrows in accordance with Equation (6.13)) the spectra are in close agreement with the calculated slope for the expected turbulent flow (see Equation (6.5)). Therefore, the conclusion is that the flow is turbulent for Case 2.

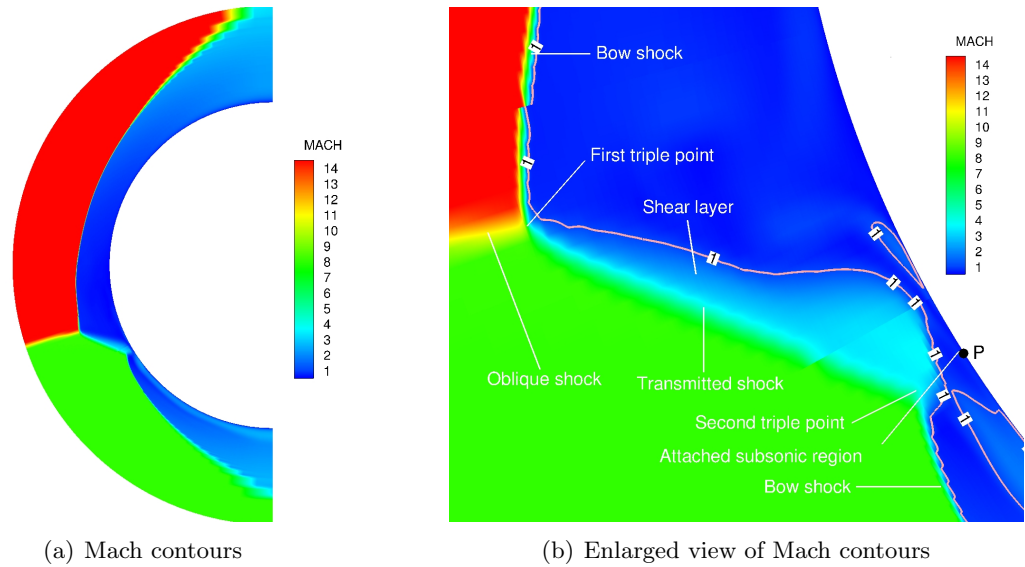


Figure 6.10: Mach contours in the symmetry plane for adjusted oblique shock location (Case 2)

Wavelet Analysis

Since FFT analysis does not consider the time evolution of the frequencies, therefore in the flowfield, it will not provide a complete understanding of the flow. However, there are other methods to consider the effect of time in the flow. One of these methods is wavelet analysis. Lau and Weng introduced a simple and easy method for using wavelet analysis [110]. There are four types of basic changes in any dataset, namely, 1) amplitude modulation, 2) frequency modulation, 3) abrupt change in frequency, and 4) abrupt change in time. Figure 6.16 presents these basic changes and their real Morse wavelet¹ transform scalograms. The change in the real dataset is a combination of these four basic changes.

A Morse wavelet, analysis is performed for surface heat transfer. Figure 6.17 shows the result. There are two major incidents visible in the absolute values scalogram. The first one starts at $\tau = 98.4$ and ends at 113.7. The dominant dimensionless frequency at this incident is in the range of 0.866 to 2.196. The second major incident starts at $\tau = 174.0$ and ends at 196.2 with dominant dimensionless frequencies in the range of 0.564 to 0.737. The real part scalogram provides different information, the type of changes that are introduced

¹There are several wavelet functions. Among these functions are Haar wavelet, Daubechies wavelet, Morlet wavelet, Gabor wavelet, and Morse wavelet.

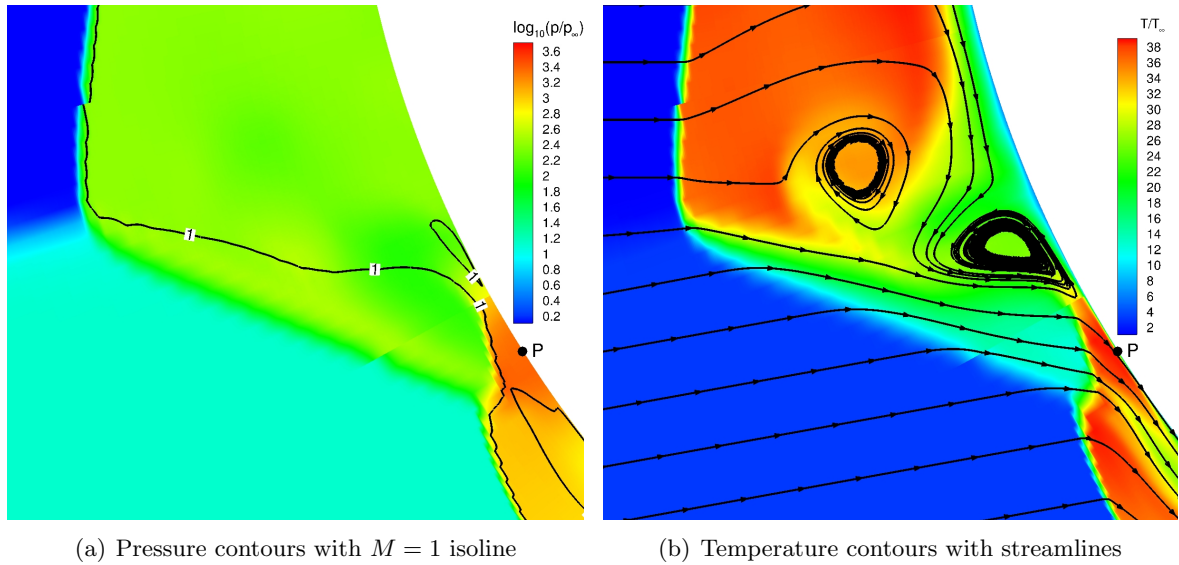


Figure 6.11: Pressure and temperature contours in the symmetry plane for adjusted oblique shock location (Case 2)

at specific times. Using Figure 6.16, the main features in the flowfields are follows: 1) an abrupt change in time at point A (similar to Figure 6.16(d)), 2) amplitude modulation in region B (similar to Figure 6.16(a)) starts at a moderate magnitude, goes to a quiescent mode and then returned with a very high magnitude, 3) abrupt change in frequencies in region C (similar to Figure 6.16(c)), and 4) frequency modulation in region D (similar to Figure 6.16(b)). In region D, only the rising part of the arc shape related to the frequency modulation is visible. There are some minor events also in the flowfield that doesn't describe here.

It should be explained here that since the wavelet analysis is performed using MATLAB, the limitation on the data size did not allow me to incorporate the entire dataset for heat transfer. The analysis performed in a way to read one data out of every several data. Even using this method cannot extend to the entire duration of numerical calculation.

6.4.3 Effect of Numerical Method

This section is specified to study the effect of the number of inner iterations and the effect of time accuracy on the predicted surface pressure and surface heat transfer.

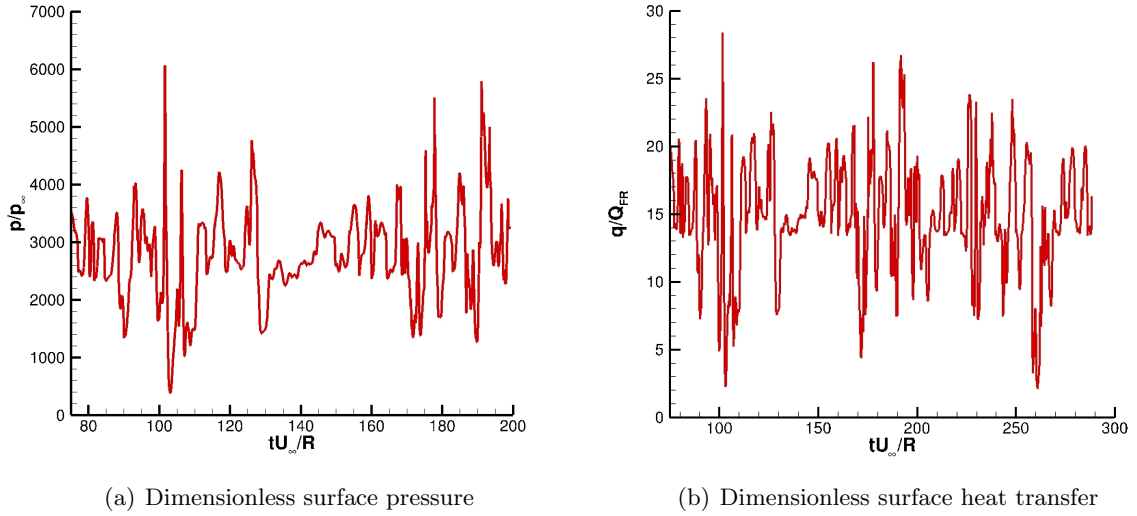


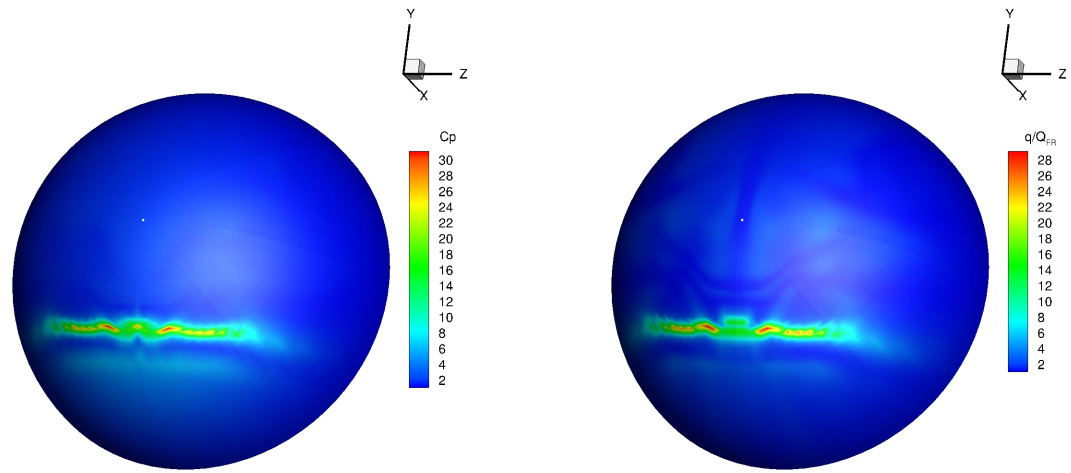
Figure 6.12: Dimensionless surface pressure and heat transfer *vs.* time for point P in the interaction region for adjusted oblique shock location

Effect of Inner Iteration

To study the effect of the number of inner iterations, the number of inner iterations per timestep in the first order DPLR method is chosen as 3, 5, and 8. Figure 6.18 shows the results of these three calculations for a dimensionless interval of 20. The conclusion from the surface pressure coefficient and dimensionless heat transfer is that the solution is independent of the number of inner iterations since the changes between the three solutions are negligible.

6.5 Conclusion

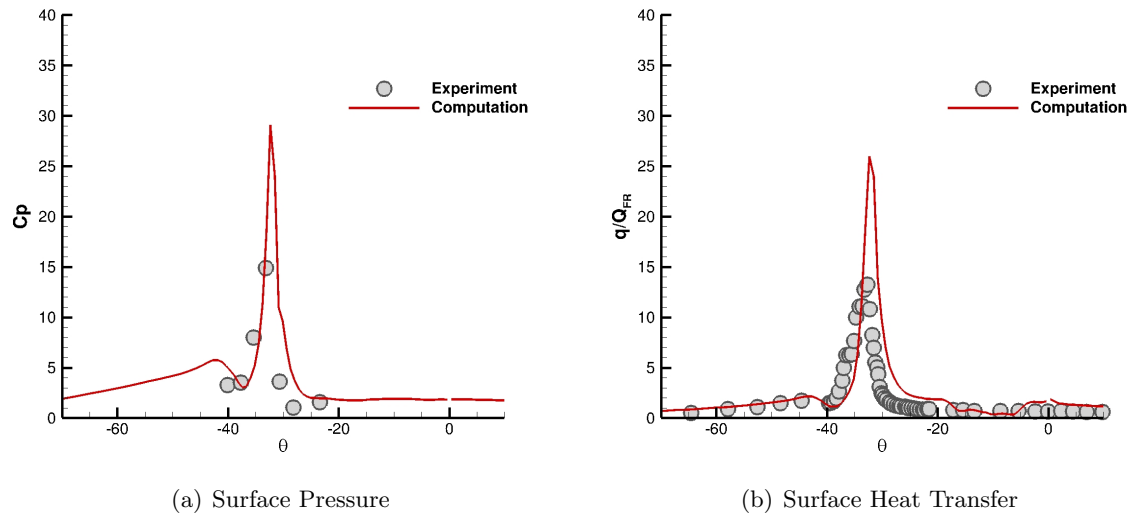
The study of Edney III interaction in this chapter enlightens the sensitivity of these complex structures to minor changes. By slightly moving the location of the interaction of the oblique shock and the bow shock, close agreement between the experimental and numerical surface pressure and heat transfer is achieved (except for overprediction of the peak values); however the flow regime changes completely, one calculation is laminar while the other one is turbulent. It is necessary to continue to study this type of interaction further.



(a) Surface pressure coefficient

(b) Dimensionless surface heat transfer

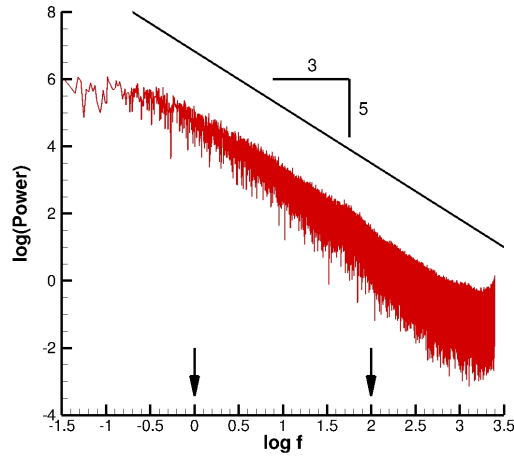
Figure 6.13: 3-D pressure coefficient and dimensionless heat transfer on hemisphere surface for adjusted oblique shock location (Case 2)



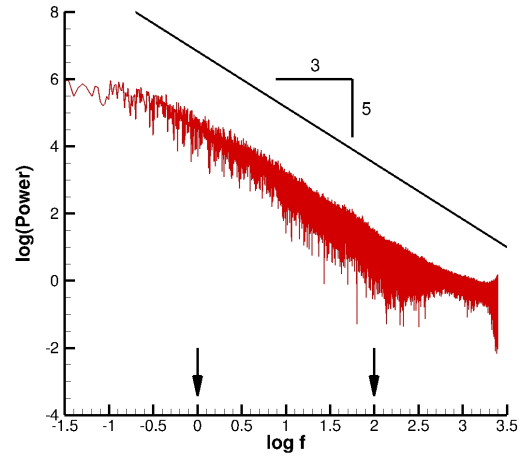
(a) Surface Pressure

(b) Surface Heat Transfer

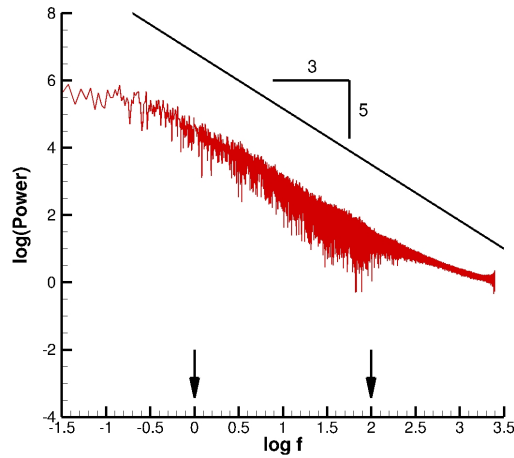
Figure 6.14: Comparison of Surface Pressure Coefficient and Dimensionless Heat Transfer on Plane of Symmetry of Hemisphere with Experimental Data for adjusted oblique shock location (Case 2)



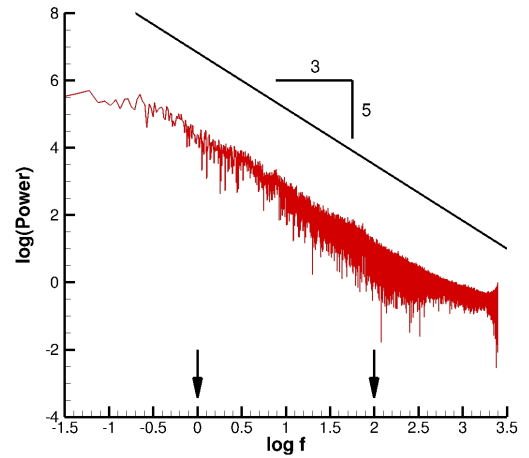
(a) FFT for time interval of 70 to 338



(b) FFT for time interval of 70 to 271



(c) FFT for time interval of 70 to 204



(d) FFT for time interval of 70 to 137

Figure 6.15: Fast Fourier Analysis of surface heat transfer *vs.* time for point P in the interaction region for adjusted oblique shock location (Case 2). The two arrows correspond to $f_{\text{flowfield}}$ and $f_{\text{dissipation}}$.

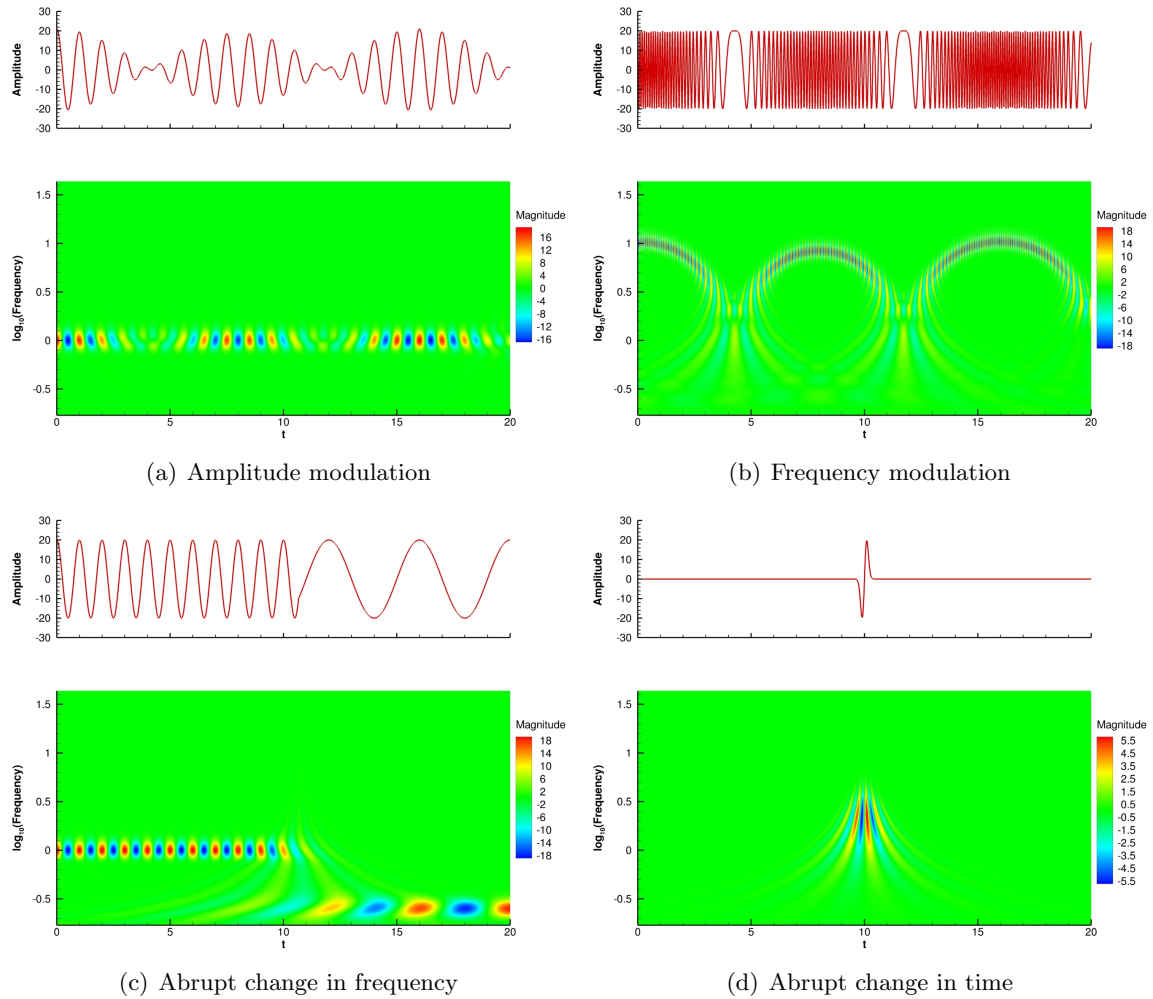
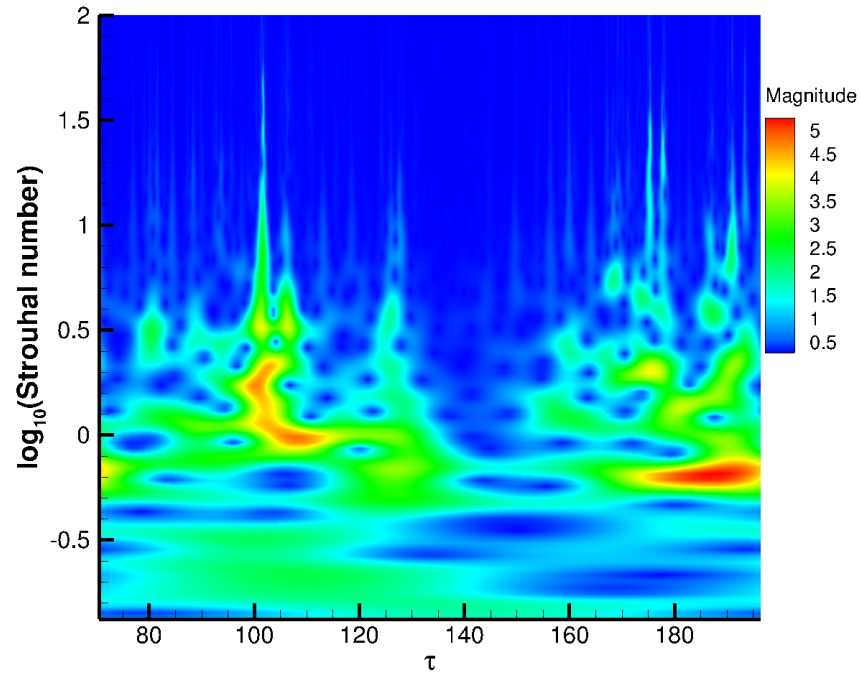
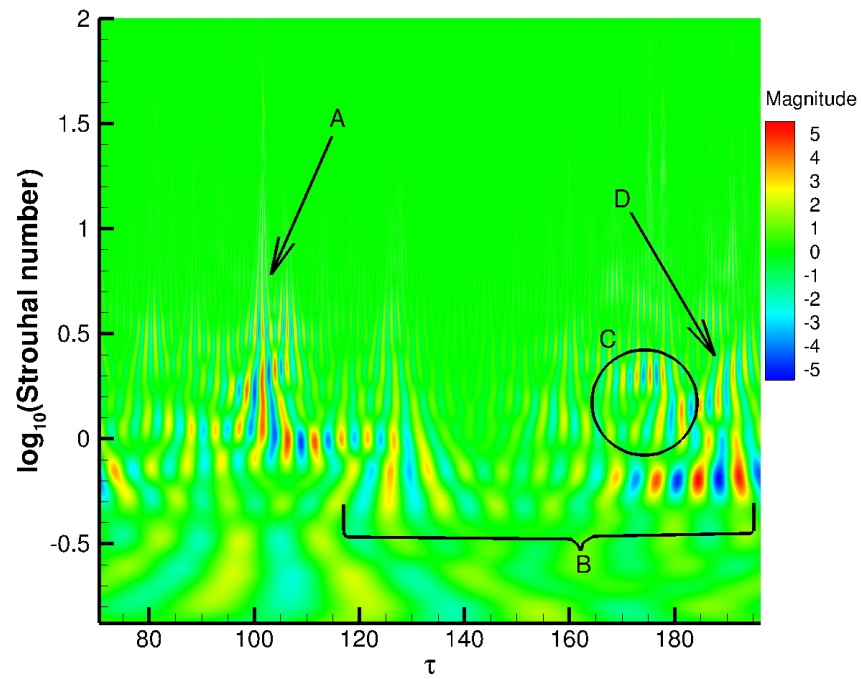


Figure 6.16: Sample signals and the real parts of their Morse wavelet transform scalograms



(a) Absolute value scalogram



(b) Real part scalogram

Figure 6.17: Continuous wavelet transform scalogram of the dimensionless surface heat transfer profile given in Figure 6.12(b)

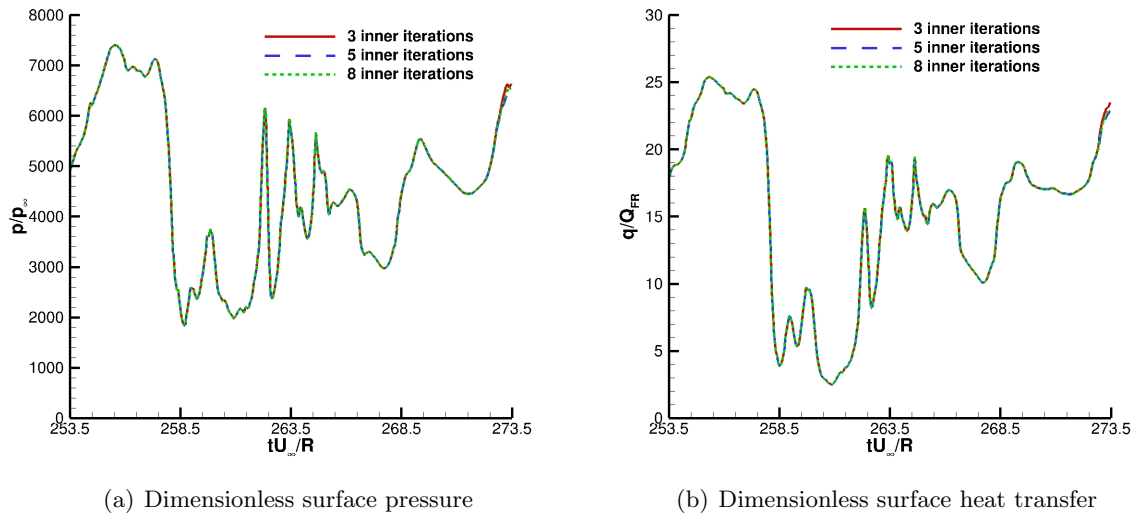


Figure 6.18: The effect of number of inner iteration on the dimensionless surface pressure and heat transfer *vs.* time for point P in the interaction region for adjusted oblique shock location (Case 2)

Part II

Energy Deposition for Flight Control in High Speed Flows

Chapter 7

Effect of a Laser Discharge Pulse on a Hemisphere Cylinder

In this chapter, the interaction of an off-body energy discharge with a hemisphere cylinder (both on and off axis) in supersonic flow is investigated. The objectives are 1) to study the effect of the amount of energy discharged on the efficiency (more accurately, energetic efficiency), 2) to investigate the effect of numerical modeling on the accuracy of the final results, and 3) to examine the effect of off axis energy discharge vs on axis discharge.

7.1 Introduction

The usage of energy discharge for drag reduction is well known. However, the efficiency of this method is not a well studied phenomenon. The reported drag reduction is varied over a vast range depend on so many factors including the amount of energy input inside the discharge, the efficiency of the method used for creation of the energy deposition, the method used for measuring drag reduction (*e.g.*, force measurement using force load, measuring stagnation pressure, etc.). Moreover, the accuracy of the models used in the simulations is not evaluated. In other words, can we model this interaction with a simple Euler equation and get a good measure of drag reduction, or do we need to utilize a non-equilibrium code to have a good estimation of the change in the forces?

The objective of this chapter is to first evaluate the efficiency of the energy deposition for drag reduction. The energetic efficiency is used as a scale for this validation. The only parameter changed in this study is the energy absorbed by the gas. Moreover, three different models are considered to evaluate how complicated the model should be so the results can be trusted. The three models used for this purpose are 1) full non-equilibrium Navier-Stokes equation with Park I thermochemistry, 2) non-reactive model (see section 2.3.3), and 3) thermally perfect model (see section 2.3.2).

7.2 Description of Problem

A test for a 1-inch radius hemisphere cylinder is in progress at the NASA Langley 20-inch Supersonic Wind Tunnel [111] at Mach 2. At this test, the actual energy absorbed by the gas, the impulse on the hemisphere cylinder due to a laser discharge interaction, and the energetic efficiency will be measured. For the details of the experiment, see Kianvashrad *et al.* [112]. The hemisphere cylinder model of this experiment is shown in Figure 7.1. The length of the cylinder is equal to the diameter of the hemisphere.

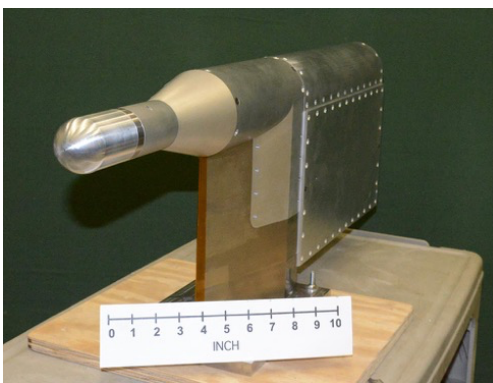


Figure 7.1: Hemisphere cylinder model

The nominal freestream conditions of the tunnel are given in Table 7.1. The surface of the hemisphere is isothermal at room temperature. Four sets of on axis energy discharges are added in front of the hemisphere cylinder. The energy discharge is modeled by instantaneous heating of a spherical region so that the energy added to the gas be equal to the energy absorbed by the gas. It is assumed that the energy absorbed by the gas increases translational and vibrational energies to the same level. Table 7.2 presents the energy absorbed by the gas, the location of the spherical region, and the temperature, density, and velocity inside the heated region. The pressure of the heated region calculated by Equation (2.33).

To study the effect of off axis energy discharge, 51 mJ of energy is discharged off axis according to Table 7.3. In this calculation, the freestream condition is the same as Table 7.1 except that the Reynolds number drops to 406022.

Table 7.1: Freestream conditions

Variables	Freestream condition
M_∞	2.0
T_∞	172.74 K
P_∞	17.635 kPa
ρ_∞	0.354 kg/m ³
Y_{N_2}	0.765
Y_{O_2}	0.235
Re_∞^*	406280
T_w	294.48 K

* Re_∞ is based on hemisphere radius $R=2.54$ cm

Table 7.2: Heated region initial conditions

Absorbed Energy	12.5 mJ	25 mJ	50 mJ	100 mJ
$T^{\text{vib}} = T$	833 K	1342 K	2234 K	3880 K
Radius of discharge	2.54 mm	2.54 mm	2.54 mm	2.54 mm
Discharge location upstream	0.84R	0.84R	0.84R	0.84R
Density	ρ_∞	ρ_∞	ρ_∞	ρ_∞
Velocity	U_∞	U_∞	U_∞	U_∞

7.3 Methodology

The governing equations are the non-equilibrium laminar Navier-Stokes equations. Three models are considered for simulations of the energy discharge in front of the hemisphere cylinder namely, 1) full non-equilibrium Navier-Stokes equation with Park I thermochemistry, 2) non-reactive model (see section 2.3.3), and 3) thermally perfect model (see section 2.3.2). The Roe's method with MUSCLp reconstruction is used for calculation of inviscid fluxes and the DPLR time integration method is used to achieve high efficiency.

The simulation is first converged to steady state in the absence of the energy discharge. Then energy is added instantaneously to the domain by increasing translational and vibrational temperatures to the same level so that the total amount of energy added to the spherical heated region be equal to the energy absorbed by the gas.

7.3.1 Computational Domain

Depending on the location of the energy discharge, the computational domain required for solving this problem is changed. For the on axis discharge, the problem is axisymmetric. However, the off axis energy discharge problem is fully three dimensional. Therefore, two

Table 7.3: Heated region initial conditions

Absorbed Energy	51 mJ
$T^{\text{vib}} = T$	2238 K
Radius of discharge	2.54 mm
Discharge location above axis	$1.0499R$
Discharge location upstream of hemisphere tip	$0.9643R$
Density	ρ_{∞}
Velocity	U_{∞}

computational domain is considered in this chapter, one for the on axis energy discharge and one for the off axis energy discharge.

The schematic of the computational domain for the on axis energy deposition is shown in Figure 7.2. The boundary conditions of this domain are axis from A to B, no-slip, non-catalytic isothermal wall with adiabatic for vibration from B to D, zero-gradient from D to E, and fixed at freestream condition from E to F and from F to A. The computational domain consists of 2.16 M cells and has uniform spacing along the surface and normal to the wall. The grid properties of this domain are provided in Table 7.4.

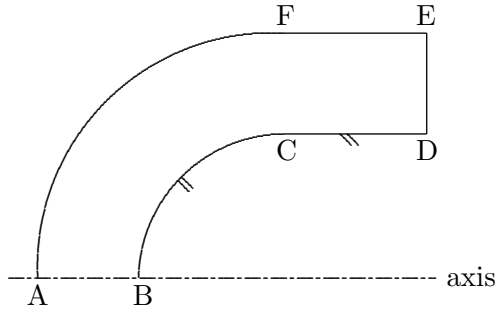


Figure 7.2: Computational domain

Table 7.4: Computational grid (2.16 M cells)

il	jl	kl	$\Delta\xi$ (μm)	$\Delta\eta$ (μm)	$\Delta\phi$ (in degree)
600	600	6	133.00	84.67	2

LEGEND

il	No. of points along surface
jl	No. of points away from surface
kl	No. of points in axisymmetric direction
ξ	Direction along surface
η	Direction away from surface
ϕ	Rotational direction about axis

The schematic of the computational domain for off axis energy deposition is shown in

Figure 7.3. In the three dimensional calculation, there exists a plane of symmetry, enable us to simulate only half of the hemisphere cylinder and the area around it. This computational domain is consists of 6.84 M cells and has uniform spacing along the surface and normal to the wall. The grid properties of this domain are given in Table 7.5.

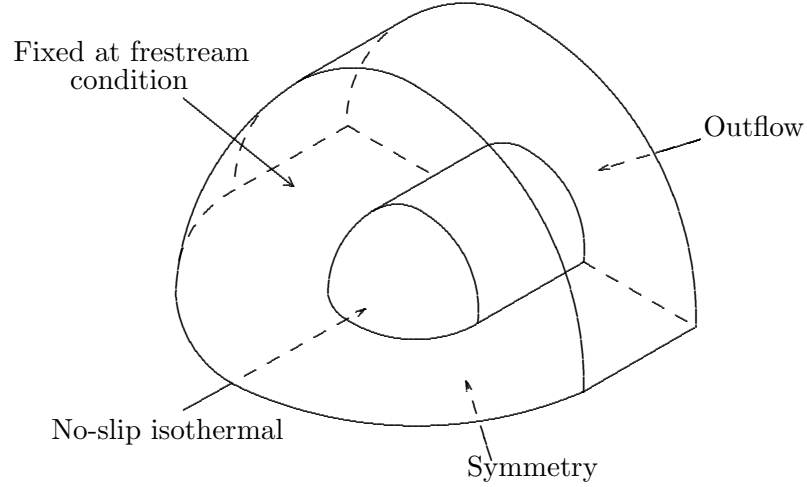


Figure 7.3: Computational domain for three-dimensional calculation

Table 7.5: Computational grid for three-dimensional calculation (6.84 M cells)

il	jl	kl	$\Delta\xi$ (μm)	$\Delta\eta$ (μm)	$\Delta\phi$ (in degree)
192	198	180	264.58	38.49	1

LEGEND

il	No. of cells along surface from hemisphere tip to the end of cylinder
jl	No. of cells away from surface
kl	No. of cells in azimuthal direction
ξ	Direction along surface
η	Direction away from surface
ϕ	Azimuthal cell angle

7.4 Results

This section is divided into two parts 1) on axis laser discharge with the axisymmetric computational domain and 2) off axis laser discharge with the three dimensional computational domain.

7.4.1 On Axis Laser Discharge

To better understand the physics of the interaction of the energy discharge with the hemisphere cylinder, moderate energy absorbed by the gas, namely 50 mJ of energy is used for explanation. Figures 7.4 and 7.5 present Mach contours on the top and vibrational temperature of species N_2 on the bottom at the specified time. Figures 7.6 and 7.7 show the numerical schlieren on the top and pressure to the freestream pressure ratio at the bottom at the same time sequences as Figures 7.4 and 7.5. Figures 7.4(a) and 7.6(a) show the contour plots at $t = 0.48 \mu s$. The heated region is visible upstream of the hemisphere. The blast wave is located so close to the heated region that it is unrecognizable. Figures 7.4(b) and 7.6(b) show the interaction of the blast wave with the bow shock. The vibrational temperature inside the heated region is almost constant suggesting that the flow is vibrationally frozen. The expansion of the heated region is profound. Yan *et al.* [113] study suggests that the expansion of the heated region is due to the radial velocity at the edge of the heated region. In Figures 7.4(c) and 7.6(c) the transmitted shock created by the interaction of blast wave and the bow shock impinge on the hemisphere surface creates a high pressure region. At the same time, the interaction of the heated region with the bow shock has started and resulted in the compression of the heated region. Since the Mach number inside the heated region is lower, the bow shock moves forward and a phenomenon is known as “lensing” observed. The interaction of the distorted bow shock and the original bow shock forms a λ -shock which is better visible in the numerical schlieren imaging.

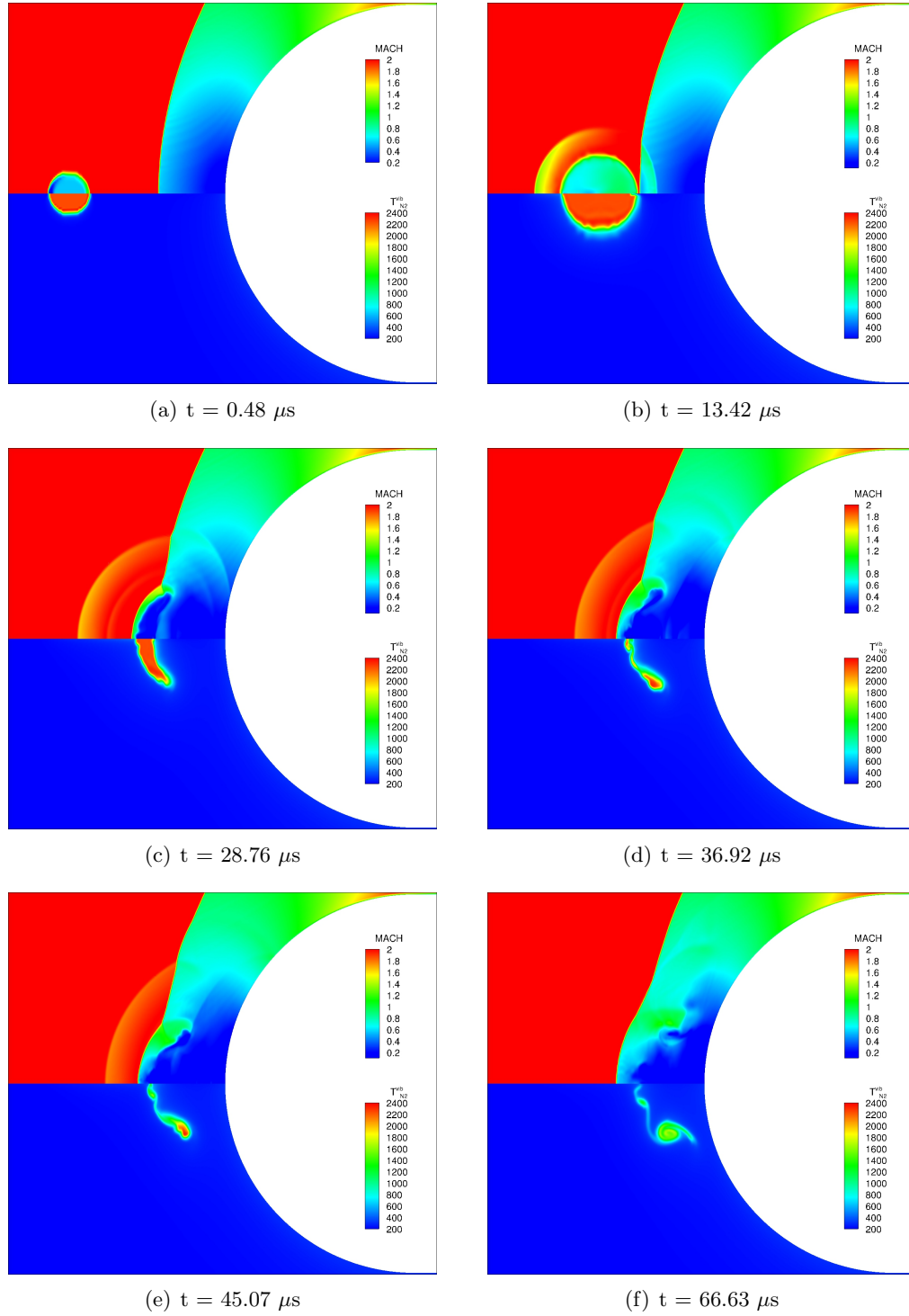


Figure 7.4: Contour plots of Mach number and vibrational temperature of N_2 for $\Delta E = 50$ mJ

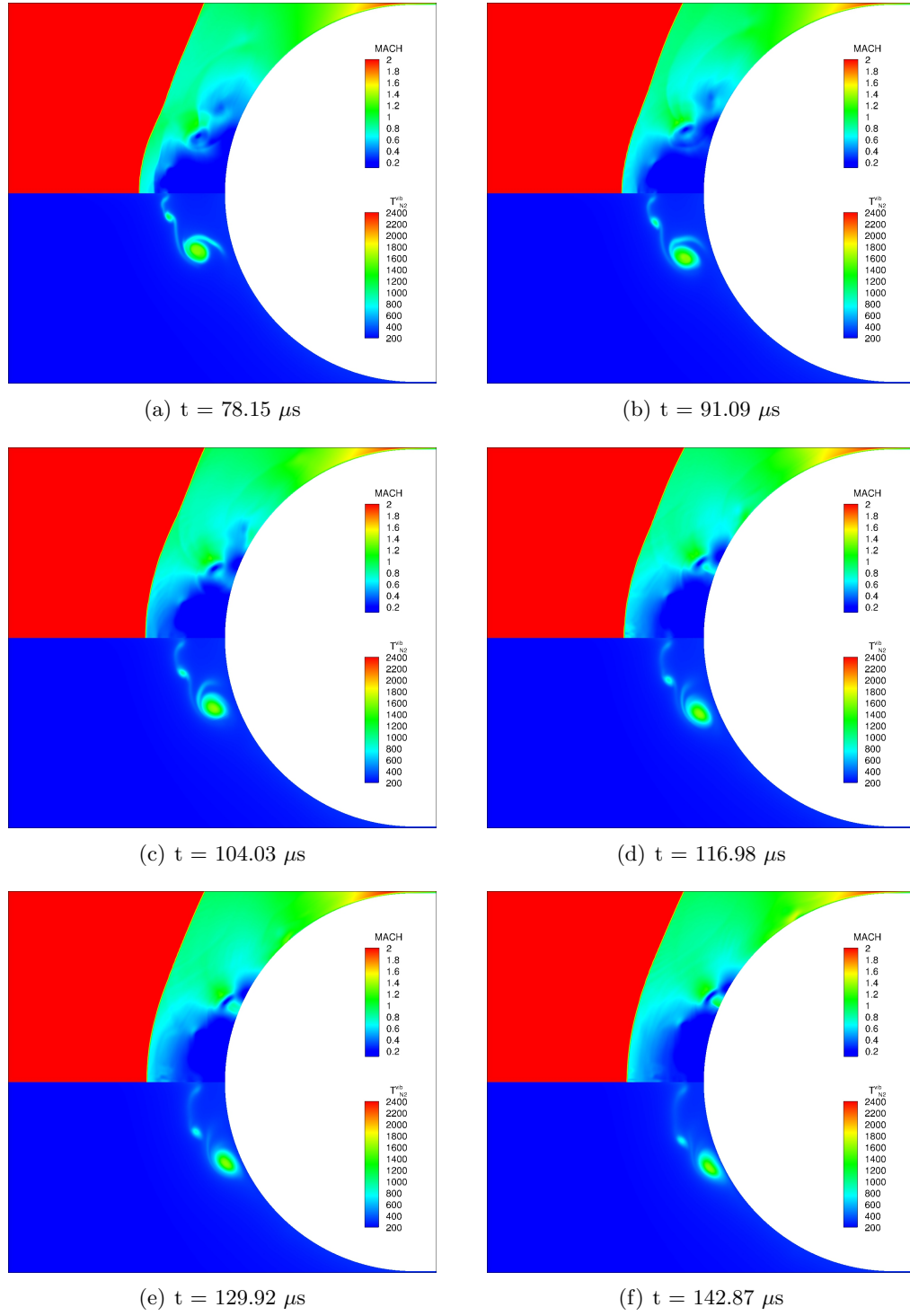


Figure 7.5: Contour plots of Mach number and vibrational temperature of N_2 for $\Delta E = 50$ mJ

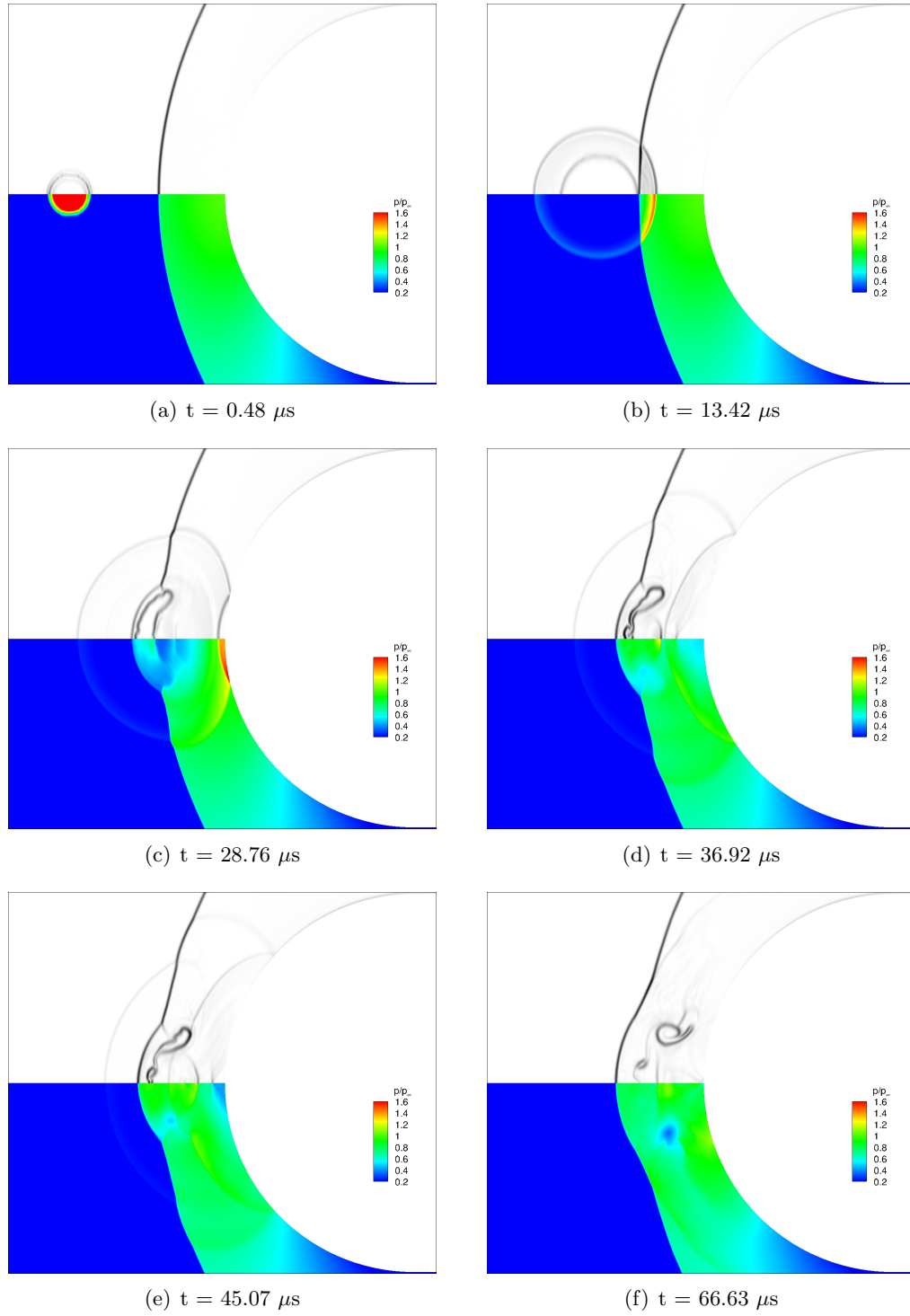


Figure 7.6: Numerical schlieren and contour plots of dimensionless pressure for $\Delta E = 50 \text{ mJ}$

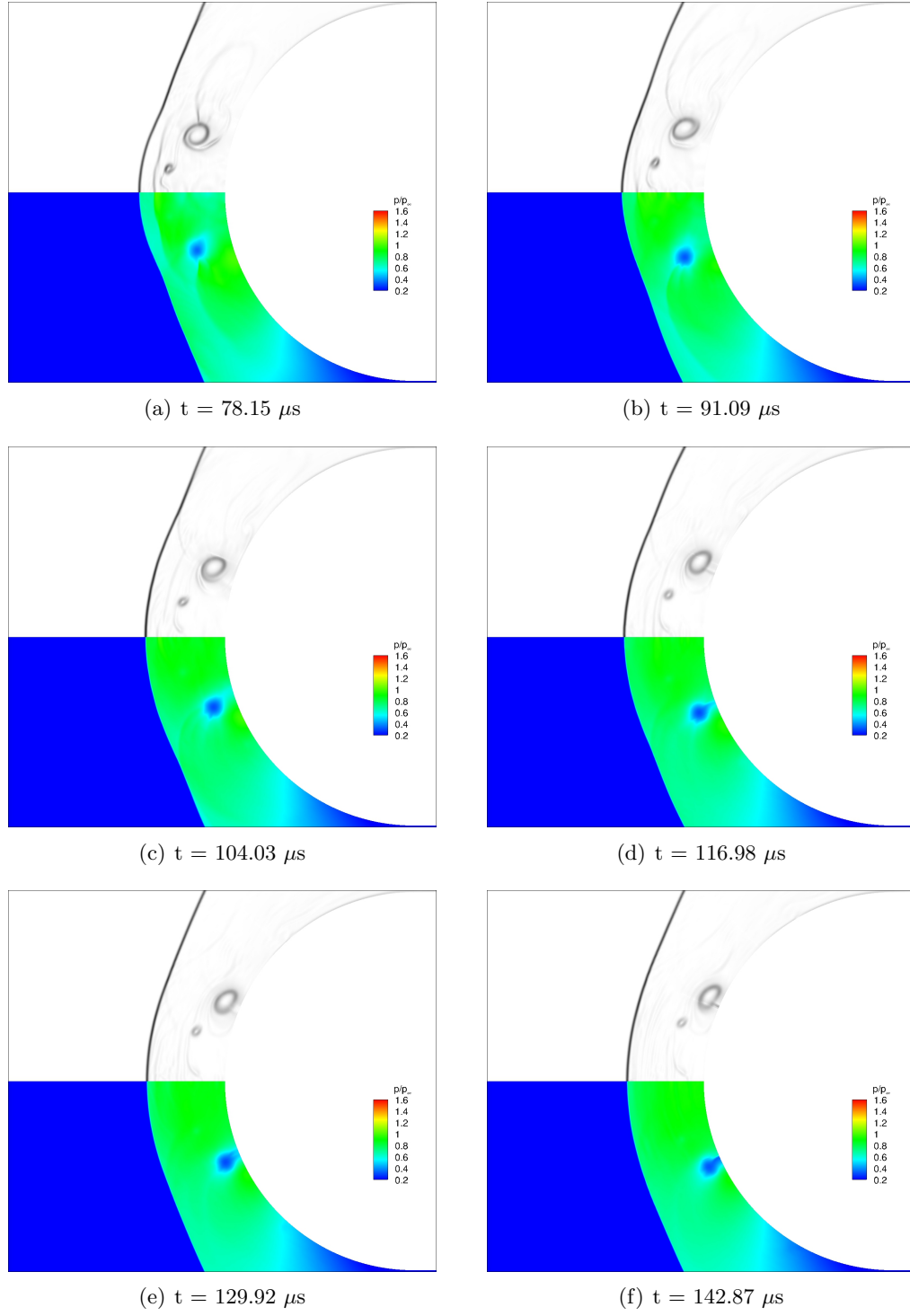


Figure 7.7: Numerical schlieren and contour plots of dimensionless pressure for $\Delta E = 50 \text{ mJ}$

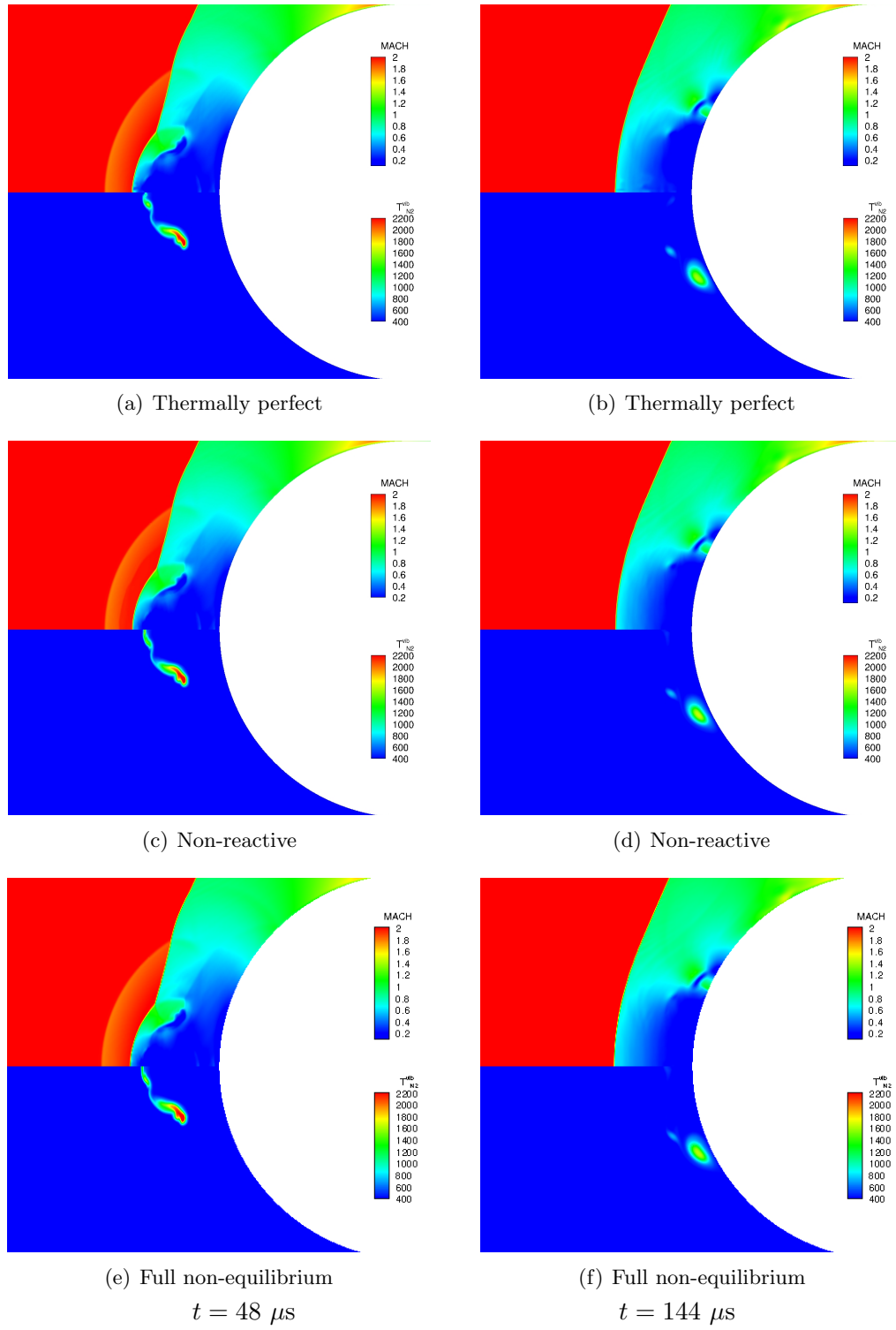


Figure 7.8: Contour plots of Mach number and vibrational temperature of N_2 for three models for $\Delta E = 50$ mJ

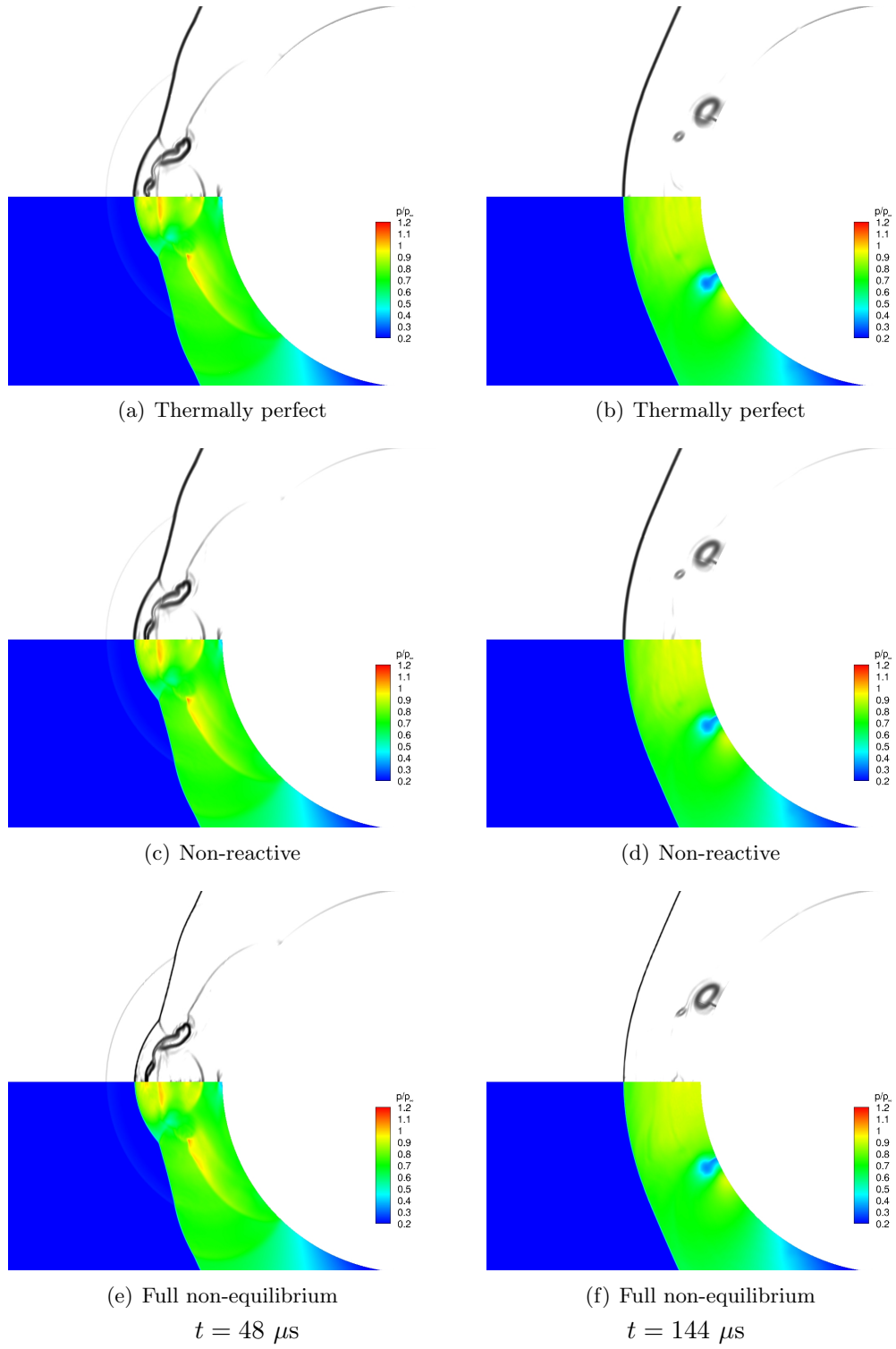


Figure 7.9: Schlieren images and contour plots of dimensionless pressure for three models for $\Delta E = 50 \text{ mJ}$

Figures 7.4(d)-(f) and 7.6(d)-(f) show the formation of the vortex ring. The difference in the density gradient initiates the Richtmyer-Meshkov instability which results in the creation of two vortex rings. Figures 7.4(f) and 7.6(f) show that at this point the blast wave completely passed the bow shock. Figures 7.5 and 7.7 demonstrate the movement of the vortex along the hemisphere surface. As the vortex moves forward, the bow shock returns to its original position. In Figures 7.5(f) and 7.7(f), the bow shock is back to its initial position.

Figures 7.8 and 7.9 compare the flow structure of the three models used for the simulations, namely, 1) full non-equilibrium with Park I thermochemistry, 2) non-reactive, and 3) thermally perfect are presented at two specified times $t = 48 \mu s$ and $t = 144 \mu s$ for 50 mJ absorbed energy by the gas. The difference between the figures are very insignificant and all the models represent the same result at each of the selected times.

Figure 7.10 shows the changes in the x -direction force due to energy discharge divided by the F_x^o which is the force in x -direction before adding the discharge versus time over the entire hemisphere cylinder. This value corresponds to the change in drag force. The negative values show the drag reduction and the positive values show the increase in the drag. The lower horizontal axis is dimensionless time tU_∞/R , where R is the hemisphere radius and the upper horizontal axis is the dimensional time in μs . The dashed line shows the zero change in the force, *i.e.*, the x -direction force is equal to the drag force of the hemisphere cylinder before adding the energy to the flow. In each of these graphs, the variation of the force versus time for the three models. It should be noted here there is no simulation for thermally perfect for 25 and 100 mJ energy deposition and thus there is no plot for these two cases.

The first peak in the forces is related to the impingement of the shock wave created as a result of the blast wave and the bow shock interaction on the hemisphere surface (see Figures 7.4(c) and 7.6(c)) which increase the pressure at the surface and therefore increases the drag force. The expansion wave forms due to the interaction of the heated region and the bow shock reached the surface and reduced the pressure and drag force (see Figures 7.4(e) and 7.6(e)) creates the minimum drag force. A comparison wave interacts with the hemisphere surface creates the second peak (see Figures 7.4(f) and 7.6(f)). The

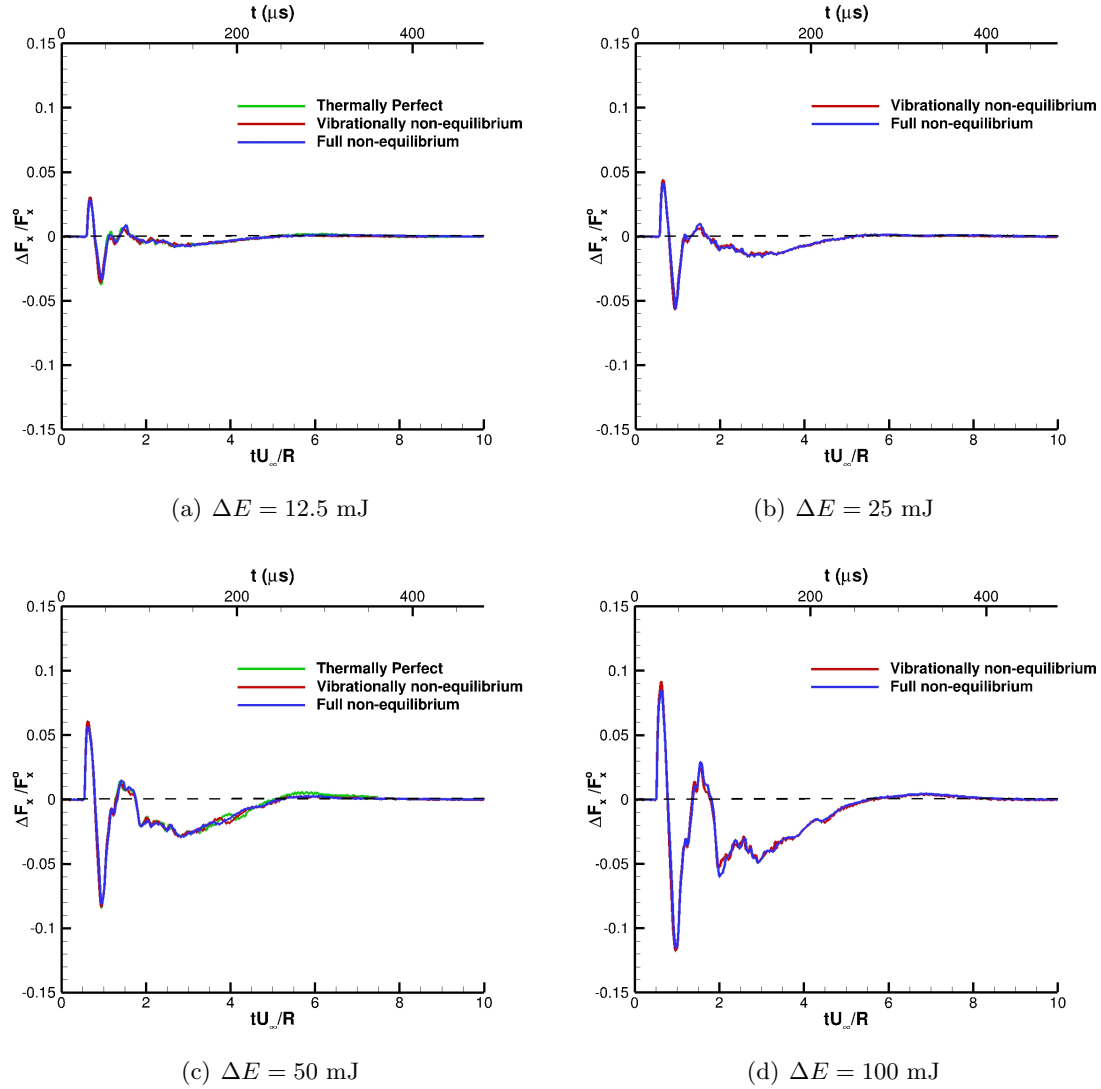


Figure 7.10: Dimensionless pressure force change versus time

creation of the vortex ring and its slow movement near the hemisphere surface forms the long lasting drag reduction (see Figures 7.5 and 7.7).

The comparison of the four graphs for four different energy absorbed by the gas of 12.5 mJ, 25 mJ, 50 mJ, and 100 mJ shows that increasing the energy absorbed by the gas increases the values at all the peaks location decreases the values at all the troughs. This is the direct result of having a stronger interaction due to a higher temperature heated region. Moreover, the drag reduction is significantly larger at the higher energies which is due to the creation of stronger vortices with lower core pressure. It is also visible that the effect

of the modeling is negligible and the change between the three models is insignificant.

The gas dynamic energetic efficiency (GDEF) defines as the ration of energy saved due to the interaction of the energy discharge to the energy absorbed by the gas. The energy saved is the negative of the impulse times the inflow velocity.

$$\text{GDEF} = -\frac{u_{\infty} \Delta \text{Impulse}}{\Delta E} \quad (7.1)$$

where the impulse is calculated using the area under graphs of Figure 7.10. Table 7.6 presents the gas dynamic energetic efficiency of the three models for the four energies absorbed by the gas. The increase in the energy absorbed by the gas from 12.5 mJ to 25 mJ increases the GDEF, however, increasing the absorbed energy from 25 mJ to 100 mJ has almost no effect on it. It seems that there is an asymptotic value for the GDEF and therefore there should be an optimized value of energy absorbed by the gas. Although the drag reduction is the highest for the 100 mJ case, however, since the energy absorbed by the gas itself is higher, the efficiency is not higher than the 25 mJ or 50 mJ cases. Additionally, the GDEF is virtually independent of the model. The calculated GDEF for all the models is almost the same except at 12.5 mJ case that thermally perfect calculation has slightly higher efficiency.

Table 7.6: Gas dynamic energetic efficiency of on-axis laser discharge

Absorbed energy (mJ)	GDEF *		
	Thermally perfect	non-reactive	Full non-equilibrium
12.5	2.7	2.3	2.5
25	—	3.0	3.0
50	3.2	3.0	3.0
100	—	2.9	2.9

* Uncertainty in calculations are ± 0.1

7.4.2 Off Axis Laser Discharge

To understand the physics of the interaction of the off axis energy discharge with the hemisphere cylinder, the contour plots of Mach number (on the left side) and the vibrational temperature of species N_2 (on the right side) are shown at specified times in Figure 7.11. The instant that energy discharge is added to the flow corresponds to $t = 0$. Figure 7.11(a) shows the contour plots at $t = 14.45\mu\text{s}$. The heated region is expanded and the blast wave

is formed. The blast wave is visible in the Mach contour plot close to the heated region. Figure 7.11(b) presents the interaction of the heated region with the bow shock at $t = 43.35 \mu\text{s}$. The lower Mach number inside the heated region moves the shock wave forward and creates the “lensing” phenomenon. Moreover, as a result of the interaction of the heated region and the bow shock, the heated region is compressed as seen in the vibrational temperature contour plots. The Richtmyer-Meshkov instability initiates the formation of a vortex. This vortex is more visible in the vibrational temperature contour plots. Passing the time, the vortex moves slowly downstream along the body and during this movement, the vibrational temperature of all species inside the vortex is reduced. Figure 7.11(c) shows the contour plots at $t = 120.41 \mu\text{s}$ when the heated region has completely passed the bow shock and thus the bow shock has returned to its original position. The vortex has passed the hemisphere and is over the cylinder at this time.

Figure 7.12 shows the change in the x and y -direction forces on the hemisphere as a result of the energy discharge interaction. These forces are calculated over the entire hemisphere cylinder and not the half part simulated in this chapter. The forces are divided by F_x° which is the force in the x -direction before adding the energy to the flowfield. The lower horizontal axis is dimensionless time tU_∞/R where R is the radius of the hemisphere. The upper horizontal axis is dimensional time in μs . The dashed line in the figure represents the zero change in the force, *i.e.*, in the x -direction, the force is equal to F_x° and in the y -direction, the force is equal to zero. The change in F_x represents drag reduction or increase in the drag while the change in the F_y represents side force and can be used for the creation of the pitching moment.

The interaction of the blast wave with the bow shock creates an interaction that reflects a shock toward the hemisphere cylinder. The interaction of this shock with the hemisphere surface rises the pressure locally which increases F_x and decreases F_y . The creation of the vortex and its slow movement along the body is the reason for long lasting drag reduction which lasts for about two dimensionless times. One dimensionless time is the time required for the freestream flow to pass a distance equal to the hemisphere radius. The pressure at the center of the vortex is lower than the ambient flow and thus creates a positive force in the y -direction. It should be noted that the maximum dimensionless force in the x and

y -directions are comparable.

7.5 Conclusion

The simulation of energy discharge in front of a hemisphere cylinder at supersonic speed gives us a better understanding of the physics of the interactions of a single pulse energy discharge with a blunt body. The takeaway from this chapter is that the final flow structure of the interaction and the calculated efficiency does not significantly depend on the model used in the simulations. Moreover, the energetic efficiency increases by increasing the energy absorbed by the gas until it reaches its asymptotic value. Off-axis energy discharge creates side force that its maximum value is comparable to the maximum drag reduction.

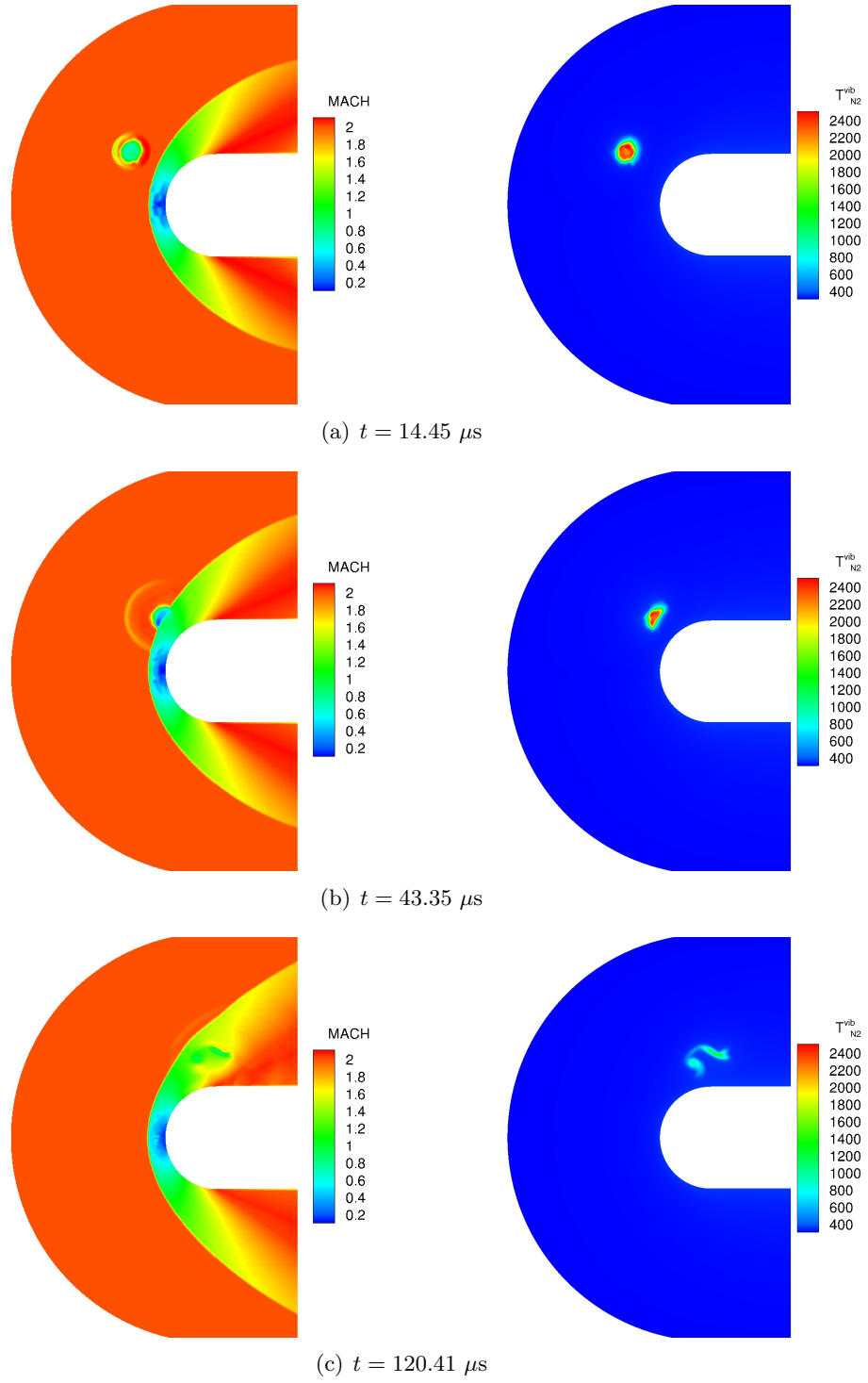


Figure 7.11: Contour plots of Mach number and vibrational temperature of N_2 for off-axis laser discharge

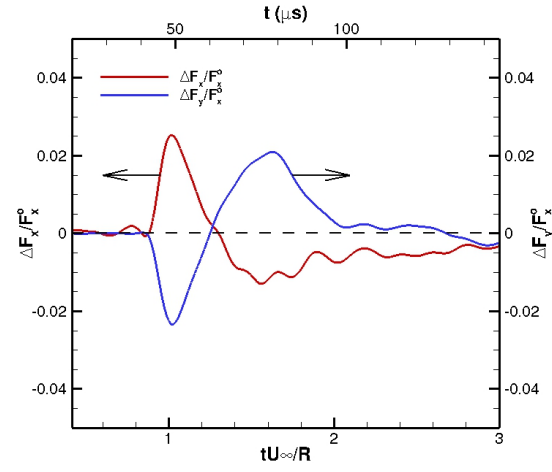


Figure 7.12: Dimensionless force change versus time for off-axis laser discharge

Chapter 8

Effect of a Laser Discharge Pulse on a Ogive Cylinder

In the previous chapter, it is shown that off-axis laser discharge can produce side force. This chapter is devoted entirely to the off axis energy discharge simulations to evaluate the possibility of using off axis energy deposition for flight control.

8.1 Introduction

As a starting point for evaluation of the possibility of the usage of energy discharge for flight control at high speed flows, there should be simulations to evaluate the effect of different parameters involved in the problem on the parameters showing the flight control such as pitching moment. Moreover, the accuracy of these calculations should also be evaluated. To achieve this purpose, the numerical investigation of the interaction of the off axis energy discharge in front of an ogive cylinder at Mach 3.4 is presented in this chapter. An ogive cylinder is chosen in this chapter since it is a streamlined body and resembled more to a designed vehicle at high speed flow. The parametric study of the effect of the energy discharge location and the amount of energy absorbed by the gas on the forces and pitching moment is performed. Moreover, the effect of the change in geometry is also evaluated. Finally, a qualitative evaluation of the numerical results is achieved by comparing the results with the experimental data.

8.2 Description of Problem

Figure 8.1 illustrates the schematic of adding an off axis energy discharge in front of an ogive cylinder. The diameter of the discharge is d_l and its location is defined by x_d and z_d . The freestream condition of the simulations is given in Table 8.1.

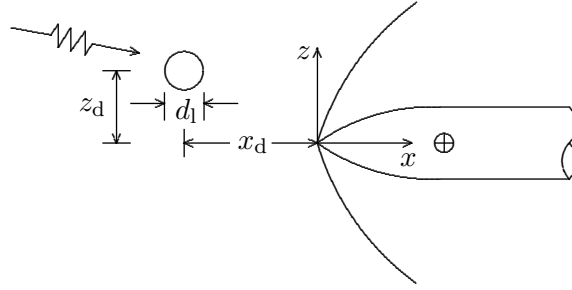


Figure 8.1: Schematic of off-axis laser discharge in front of an ogive cylinder

Table 8.1: Numerical freestream conditions

Variables	Freestream condition
M_∞	3.4
Y_{N_2}	0.76
Y_{O_2}	0.23
Y_{NO}	0.01
Re/L	$1.03 \cdot 10^7$
$\frac{T_w}{T_\infty}$	0.994

The schematic of the ogive cylinder is shown in Figure 8.2. This geometry is defined by the cylinder diameter D , cylinder length L_c , ogive length L , and the fineness ratio f where

$$f = \frac{L}{D}. \quad (8.1)$$

The radius of ogive curvature is defined as

$$R_c = D \left(f^2 + \frac{1}{4} \right) \quad (8.2)$$

Table 8.2 summarizes the properties of all the ogive cylinders used in this chapter.

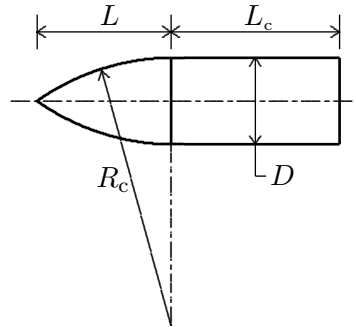


Figure 8.2: Schematic of ogive-cylinder geometry

The objectives of this study are to examine the effect of the energy of the discharge and the location of the discharge on the produced force and moment to better understand the

Table 8.2: Ogive cylinder properties and dimensions

Geometry	D (cm)	f	L_c/D	L_t/D
Ogive 1	5.08	2.0	1.0	3.0
Ogive 2	1.27	2.5	2.0	4.5

capability of energy discharge for flight control. Table 8.3 presents all the cases studied for this purpose. This study is performed on Ogive 1 geometry. To study the effect of the amount of energy on the forces and pitching moment, Case 1, 2, and 3 are used. The location of discharge is fixed while the energy added to the gas is changed. The parameter ϵ is the dimensionless energy added to the gas and defines as

$$\epsilon = \frac{\Delta E}{p_\infty V} \quad (8.3)$$

where $V = (\pi/6) d_1^3$ and ΔE is the energy added to the gas by laser discharge [78].

Table 8.3: Laser discharge initial conditions for Ogive 1

Case No.	ϵ	$\frac{T^{\text{vib}}}{T_\infty} = \frac{T}{T_\infty}$	$\frac{d_1}{D}$	$\frac{x_d}{D}$	$\frac{z_d}{D}$
Case 1	82.20	7.90	0.1	-0.433	0.25
Case 2	163.42	13.47	0.1	-0.433	0.25
Case 3	326.08	24.05	0.1	-0.433	0.25
Case 4	326.05	26.67	0.1	-0.433	0.50
Case 5	326.50	22.60	0.1	-0.433	0.75

To study the effect of the location of the laser discharge, Cases 3, 4, and 5 are used. In these cases, the energy added is the same while the vertical location of the discharge z_d is changed. It is well known in the literature that by increasing the horizontal distance, the first peak in the force history (as described in Chapter 7) which is the result of the interaction of the blast wave and the shock becomes weaker. In all of these five cases, the discharge is located in the plane of symmetry and it is added instantaneously by increasing the temperatures inside the heated region while the density and velocity remain as in the freestream density and velocity (because the addition of energy discharge *e.g.*, laser discharge is assumed instantaneous). The freestream condition is a converged steady state solution.

To understand the effect of geometry on the forces and pitching moment, the Ogive 2 model is used for simulation. In this series of simulations, the location of discharge is

changed at the same value of energy discharge. Table 8.4 shows these conditions. The values of this table are chosen in a way that Case 8 coincides with the experimental condition.

Table 8.4: Laser discharge initial conditions for Ogive 2

Case No.	ϵ	$\frac{T^{\text{vib}}}{T_{\infty}} = \frac{T}{T_{\infty}}$	$\frac{d_l}{D}$	$\frac{x_d}{D}$	$\frac{z_d}{D}$
Case 6	73.96	18.67	0.47	-0.11	-0.25
Case 7	74.37	18.67	0.47	-0.11	-0.50
Case 8	73.26	18.67	0.47	-0.11	-0.75

8.3 Description of Experiment

There is an experiment performed at Rutgers University Emil Buehler Supersonic wind tunnel. The operational condition of this tunnel is given in Table 8.5. The model is shown in Figure 8.3 and has the dimensions of Ogive 2. The energy deposition in this experiment is created using a Nd:YAG laser.

Table 8.5: SWT operation parameters

Parameter	Value
M	3.4
p_0	0.9 MPa
T_0	~ 290 K
q	109 kPa
Run time	< 20 s
Re	$5.82 \times 10^7/\text{m}$



Figure 8.3: Ogive cylinder test article

8.4 Methodology

The governing equations are the full non-equilibrium laminar Navier-Stokes equations. Roe's method with MUSCLp reconstruction is used for the calculation of inviscid fluxes. DPLR method is used to achieve high performance time integration with large timesteps. First, the calculation is converged to the steady state solution. This steady state solution is used as the initial condition for adding the instantaneous energy discharge. Energy discharge is added by increasing the translational and vibrational temperatures inside the spherical regions in the freestream condition. The center of the spherical region is specified by the location of the discharge.

8.4.1 Computational Domain

Two geometries - Ogive 1 and 2 - are considered in this chapter. Therefore, there are two computational domains, one for each of these two cases. Since this flow has the plane of symmetry, only half of the domain is simulated. The plane of symmetry for both geometries is located in $x - z$ as shown in Figure 8.1. The computational domain of Ogive 1 and 2 are respectively shown in Figures 8.4 and 8.5.

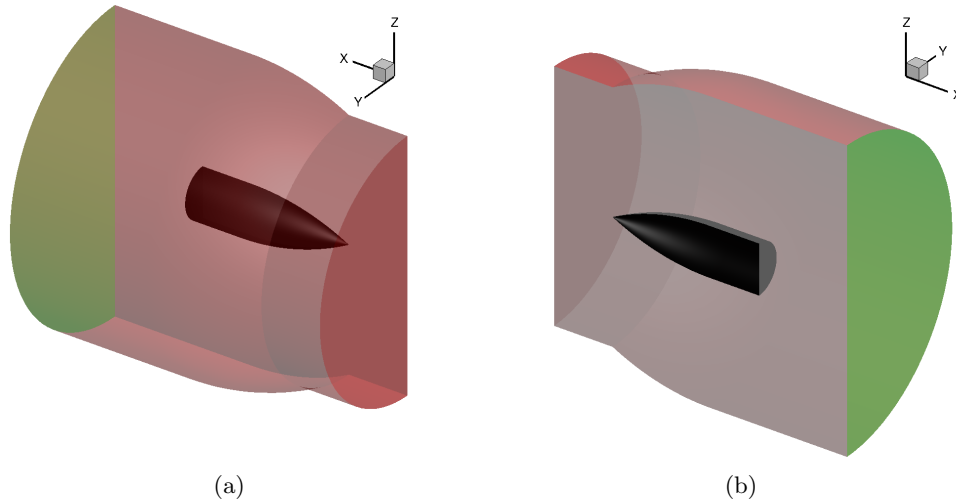


Figure 8.4: Computational domain for Ogive 1

The boundary conditions are color coded in Figures 8.4 and 8.5. The red and blue surfaces are fixed boundary condition at freestream conditions. The green surfaces are the

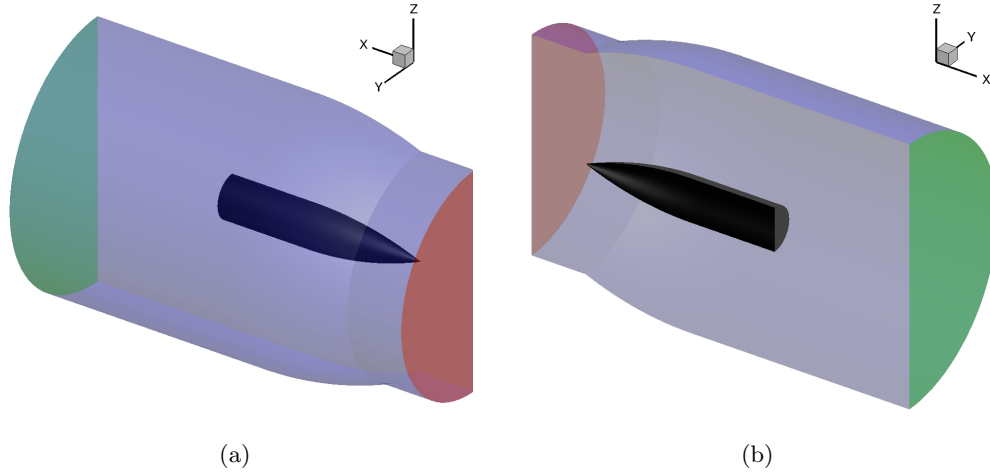


Figure 8.5: Computational domain for Ogive 2

zero-gradient outflow boundary condition. The black surfaces are the ogive cylinder surface which is the non-catalytic, no-slip isothermal wall. The gray surfaces are the planes of symmetry with the symmetry boundary conditions.

Three sets of grids are used for Ogive 1 geometry. The main computational domain (Grid 2) consists of 3.7 M cells. Grid 1 and Grid 3 are used for grid study. Table 8.6 presents the grid properties of the three computational domain.

Table 8.6: Computational grid Properties for Ogive 1

	No. cells	il	jl	kl	$\Delta\xi$ (μm)	$\Delta\eta_{\min}$ (μm)	$\Delta\phi$ (in degrees)
Grid 1	1.5 M	150	96	45	1004.0	225.0	4
Grid 2	3.7 M	300	120	45	502.0	125.5	4
Grid 3	7.5 M	300	120	90	502.0	125.5	2

LEGEND:

il No. of cells along surface from ogive tip to the end of cylinder.

jl No. of cells away from surface (normal to the wall).

kl No. of cells in azimuthal direction.

ξ Direction along surface.

η Direction away from surface.

ϕ Azimuthal cell angle.

M means millions.

For Ogive 2 geometry, only one set of grid is used. Table 8.7 gives the properties of the grid is used for these calculations. This grid consists of 5.3 M cells.

Table 8.7: Computational grid Properties (5.3 M cells)

il	jl	kl	$\Delta\xi$ (μm)	$\Delta\eta_{\min}$ (μm)	$\Delta\phi$ (in degree)
420	120	45	136.1	31.4	4

LEGEND

il	No. of cells along surface from ogive tip to the end of cylinder
jl	No. of cells away from surface
kl	No. of cells in azimuthal direction
ξ	Direction along surface
η	Direction away from surface
ϕ	Azimuthal cell angle

8.5 Results

The result section is divided into four main categories. First, the grid study is presented for Ogive 1. Then the effect of the amount of energy added to the gas and the effect of the location of discharge on forces and pitching moment are presented. Finally, the flow structure of the numerical results is compared with the experimental schlieren images.

8.5.1 Grid Study

A grid refinement study is performed using Grid 1, Grid 2, and Grid 3 which is presented in Table 8.6 for Ogive 1 geometry and the energy discharge condition of Case 1 in Table 8.3. Due to the limitation in computational resources, the grid refinement is not in all three directions in all the grid sets. The refinements in grids are performed in two steps. In the first step, from Grid 1 to Grid 2, the refinement is in the $\xi - \eta$ plane. In the second step, from Grid 2 to Grid 3, the refinement is performed in the azimuthal direction. Figure 8.6 shows the drag force, side force, and pitching moment coefficients versus dimensionless time for these three grids. The dimensionless time is defined as

$$\tau = \frac{tU_{\infty}}{D}. \quad (8.4)$$

and the drag force, side force, and pitching moment coefficients are defined as

$$C_D = \frac{F_x}{(1/2) \rho_{\infty} U_{\infty}^2 \pi D^2 / 4}, \quad (8.5)$$

$$C_Z = \frac{F_z}{(1/2) \rho_{\infty} U_{\infty}^2 \pi D^2 / 4}, \quad (8.6)$$

$$C_m = \frac{M_y}{(1/2) \rho_{\infty} U_{\infty}^2 L_t \pi D^2 / 4}. \quad (8.7)$$

where D is the diameter of the cylinder given in Table 8.2. The pitching moment is calculated about $x = L_t/2$ which is assumed to be the center of gravity. The forces and pitching moment coefficients are computed over the entire ogive cylinder. The change in the side force and pitching moment coefficients are negligible. However, changing the grid has a more visible effect on the drag coefficient especially after the interaction of the blast wave and heated region with the shock structure of the ogive cylinder which respectively represents the first peak and first trough. However, it should be noted that the change between the drag coefficient of the three grids is still less than 1%.

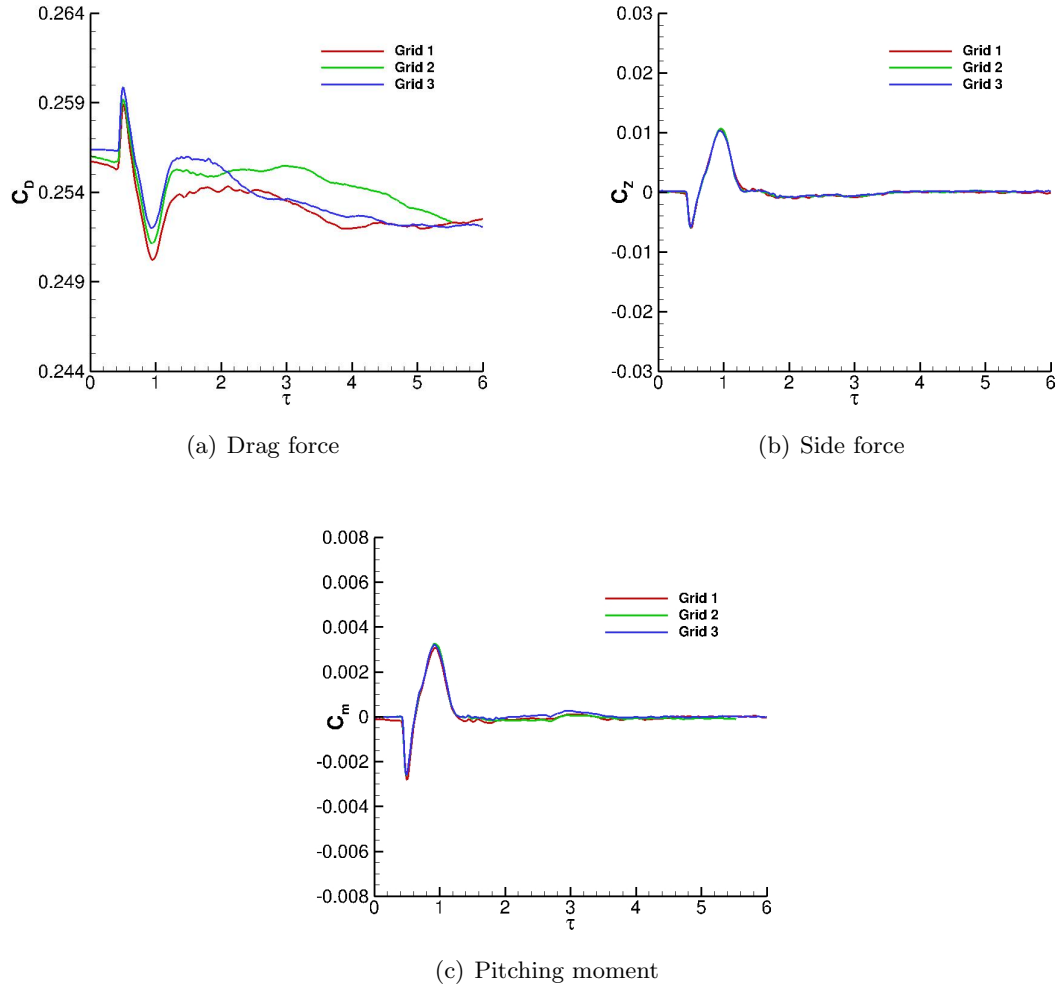


Figure 8.6: Drag force, side force, and pitching moment coefficients versus time for different grids

8.5.2 Effect of Energy Added to the Gas

To study the effect of the energy added to the gas on the forces and the pitching moment coefficients, Case 1, Case 2, and Case 3 (see Table 8.3) are compared in Figure 8.7. The calculations are performed on Grid 2 for Ogive 1. The interaction of the blast wave with the ogive cylinder curved oblique shock creates a transmitted shock that impinges on the surface of the ogive and increases the drag force coefficient and reduces the side force coefficient. The total effect of the increase in the drag and reduction in the side force is a negative pitching moment about the center of gravity.

The expansion wave forms as a result of the interaction of the heated region and the curved oblique shock decreases the pressure locally on the top surface and thus reduces the drag and increases the side force. A total positive pitching moment is created at this point. The Richtmyer-Meshkov instability creates a vortex that moves slowly along the body. The interaction of this vortex with the expansion fans and the separation region at the base of the body reduces the drag coefficient while the side force and pitching moment coefficients remain almost constant at zero. Increasing the energy added to the gas increases the peak values and decreases the trough values for drag force, side force, and pitching moment coefficients.

Figures 8.8 to 8.10 present the normalized pressure difference $(p - p_{nl})/p_{nl}$, the surface pressure distribution on the top and bottom surface at the plane of symmetry, and the top and bottom view of the surface pressure normalized by $\rho_{\infty}U_{\infty}^2$ for Case 1, Case 2, and Case 3, where p_{nl} is the undisturbed pressure before adding the energy discharge to the flow. All of these results correspond to $\tau = 1.0$ which is approximately the time of maximum pitching moment for all three cases (see Figure 8.7). From these figures, the low pressure region created by the expansion fan (forms due to the interaction of the heated region and the curved oblique shock) on the top surface is visible. This imbalance in the pressure distribution between the upper and the lower half of the ogive cylinder creates the upward side force and the desired pitching moment.

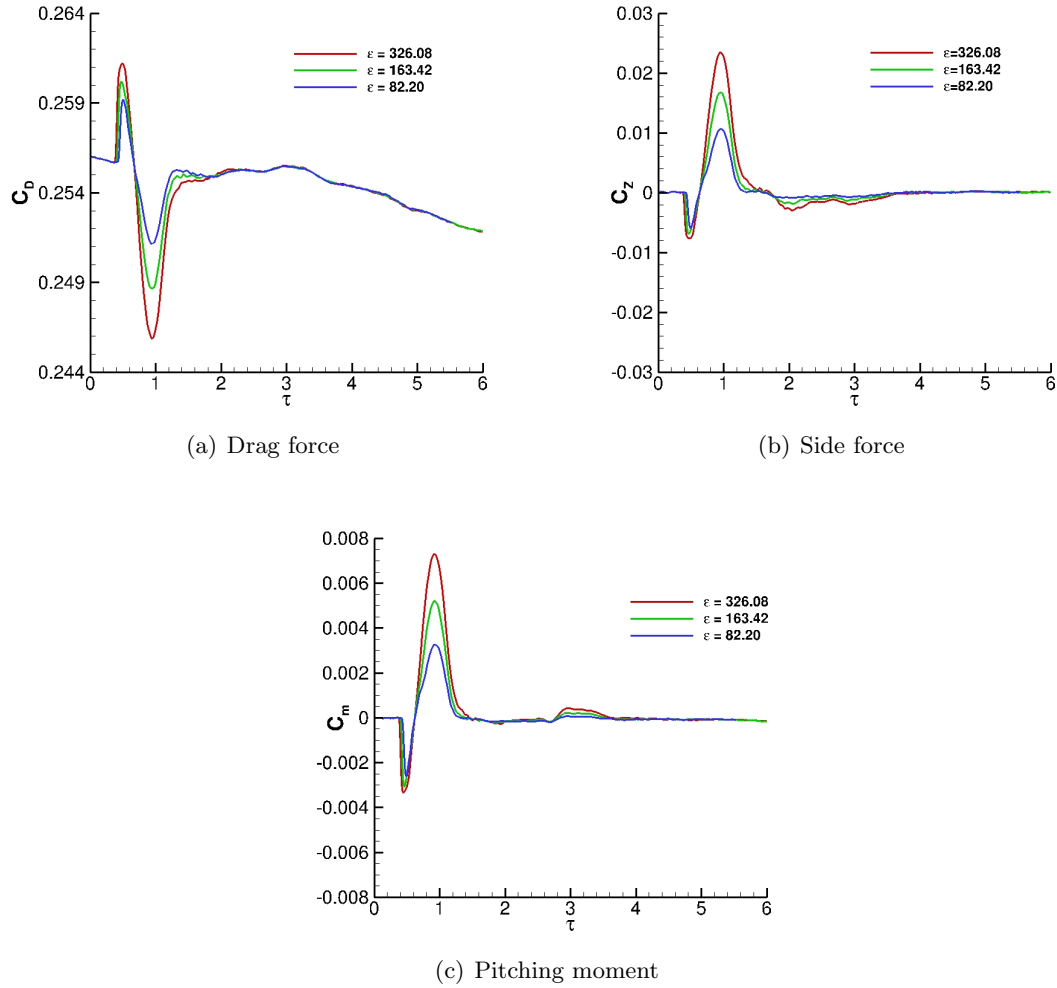
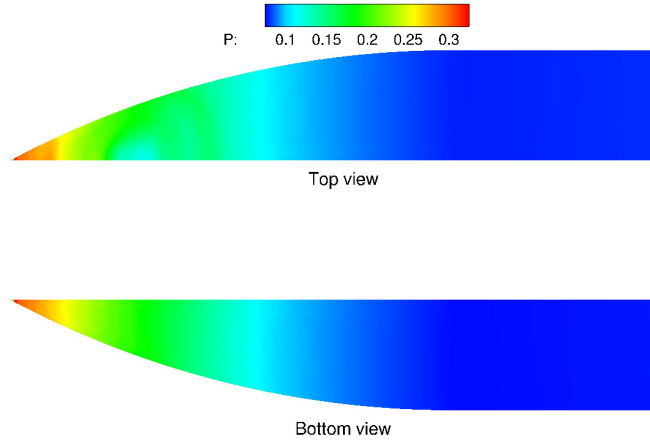
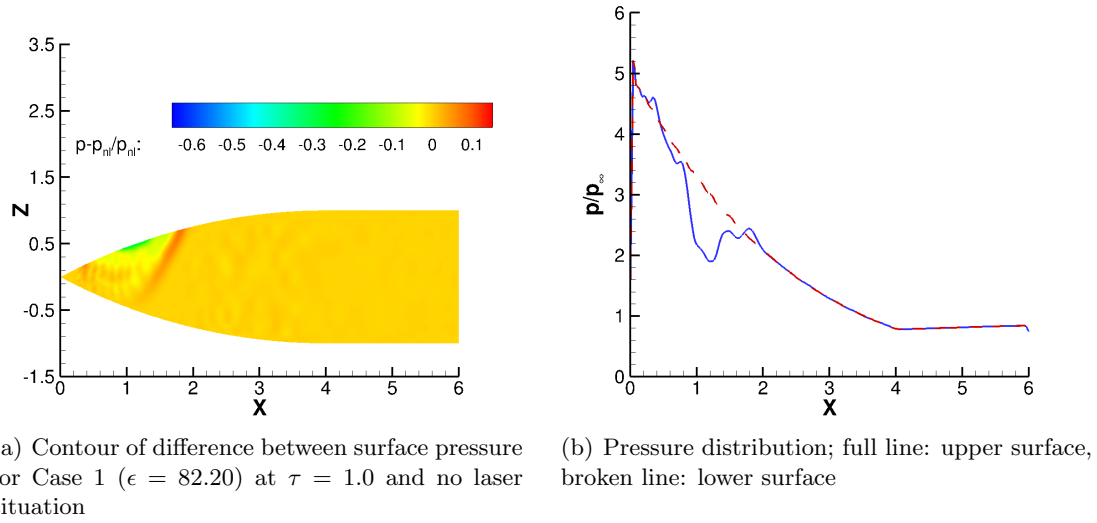


Figure 8.7: Drag force, side force, and pitching moment coefficients versus time for different energy absorbed by the gas

8.5.3 Effect of the Location of Energy Deposition

To understand the effect of the location of the energy discharge on the force and pitching moments affecting the ogive cylinder, Case 3, Case 4, and Case 5 of Table 8.3 are considered for Ogive 1 geometry. Moreover, to see if changing the geometry has any effect on the conclusion of the previous set of data, Case 6, Case 7, and Case 8 are also considered for Ogive 2 geometry. The comparison of the drag force, side force, and pitching moment coefficient of the three cases are shown in Figure 8.11 for Ogive 1. All the simulations are performed on Grid 2.

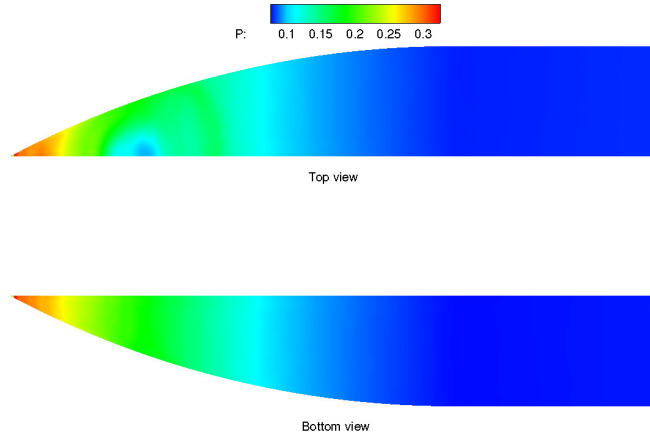
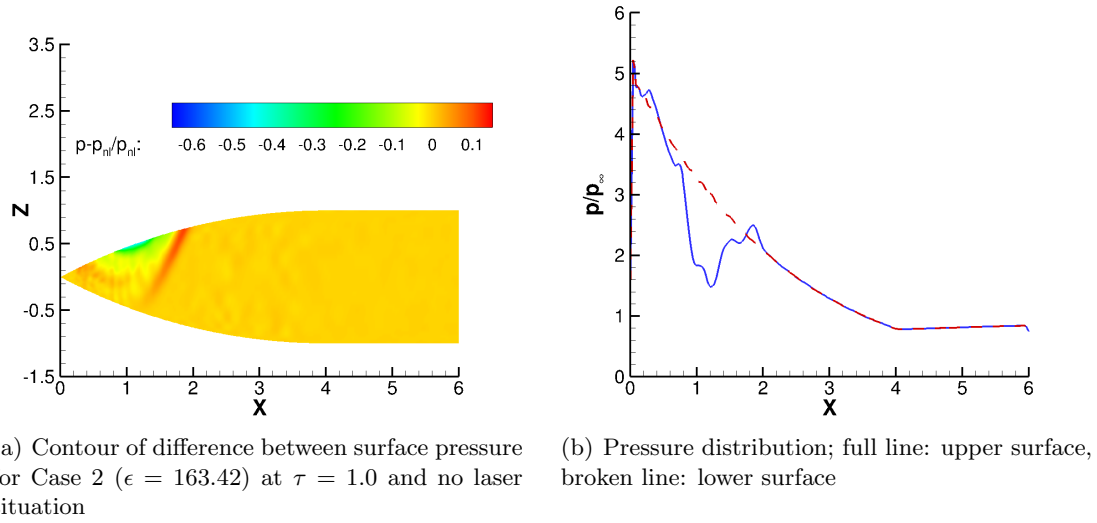
Increasing the vertical location z_d delays the change in the forces and pitching moment



(c) Top and bottom view of pressure contours

Figure 8.8: Pressure for Case 1 ($\epsilon = 82.20$) at $\tau = 1.0$

coefficients since the distance between the energy discharge and the curved oblique shock is increasing. Moreover, the higher the location of the discharge is, the lower is the drag reduction and the maximum side force and the maximum pitching moment coefficients are. In particular, for the vertical location of $z_d = 0.75D$ (the center of the discharge is above the body), the pitching moment remains negative during the entire interaction. Knowing that the on axis energy discharge produces no side forces, there should be an optimum location to create the maximum positive side force and pitching moment at a constant amount of energy added to the gas.

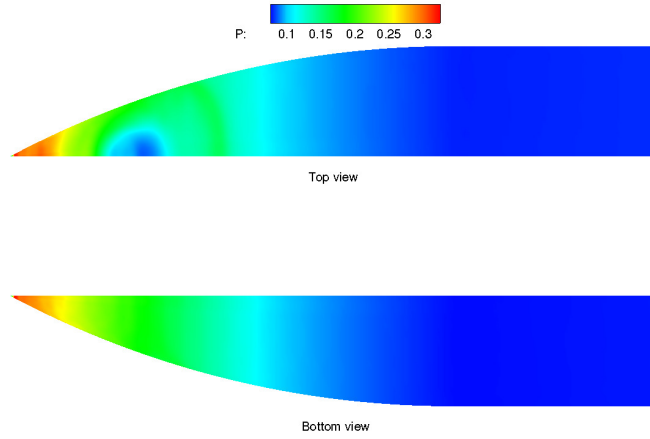
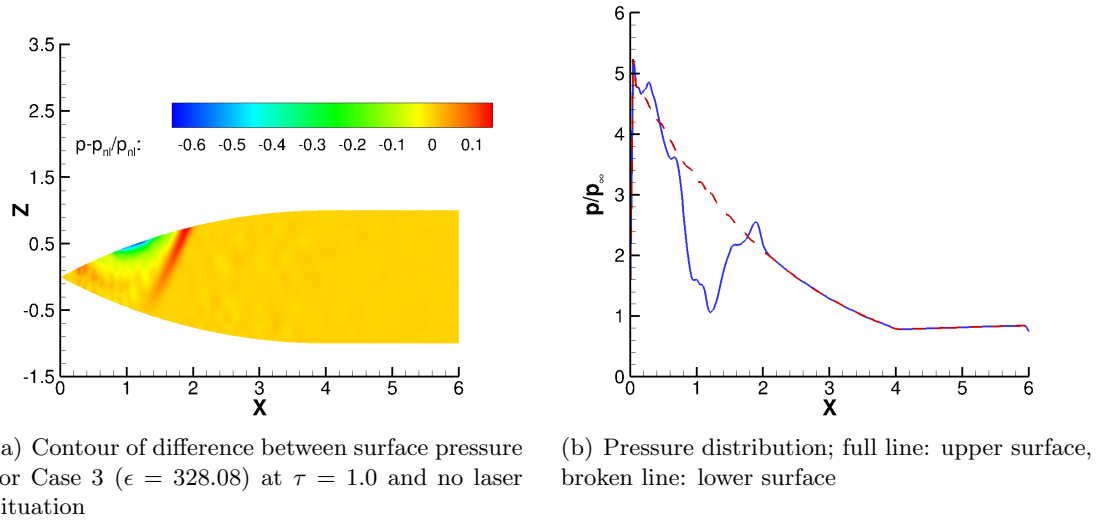


(c) Top and bottom view of pressure contours

Figure 8.9: Pressure for Case 2 ($\epsilon = 163.42$) at $\tau = 1.0$

Figures 8.10, 8.12, and 8.13 show the normalized pressure difference $(p - p_{nl})/p_{nl}$, pressure distribution on the upper and lower surface at the plane of symmetry, and the top and bottom view of normalized surface pressure $p/\rho_{\infty}U_{\infty}^2$ for Case 3, Case 4, and Case 5 at $\tau = 1.0, 1.5$, and 2.0 , respectively. These are approximately the times that the maximum pitching moment achieved for Case 3 and 4 and related to happening of the same phenomenon for Case 5 (Case 5 does not have maximum pitching moment).

Figure 8.14 shows the comparison of Case 6, Case 7, and Case 8 for Ogive 2 geometry. It should be noted here that the energy discharge is in the lower part of the ogive cylinder to match the calculation with the experiment. The same procedure is visible in these graphs



(c) Top and bottom view of pressure contours

Figure 8.10: Pressure for Case 3 ($\epsilon = 328.08$, $z_d/D = 0.25$) at $\tau = 1.0$

except that due to the change in the location of the energy discharge, the change in the side force is first positive due to the interaction of the blast wave and the shock wave and then negative due to the expansion fans form by the interaction of the heated region and the shock wave. The pitching moment graph is not available for these sets of data.

Again it is seen that increasing the vertical distance of the discharge delays the interaction and thus delays the change in the forces. Increasing the vertical distance monotonically increases the first peak in side force while there is a maximum at $z_d = 0.5D$ (at the same level as the surface of the cylinder). On the other hand, increasing the vertical distance reduces the drag reduction effect while there is an extremum minimum value for side force

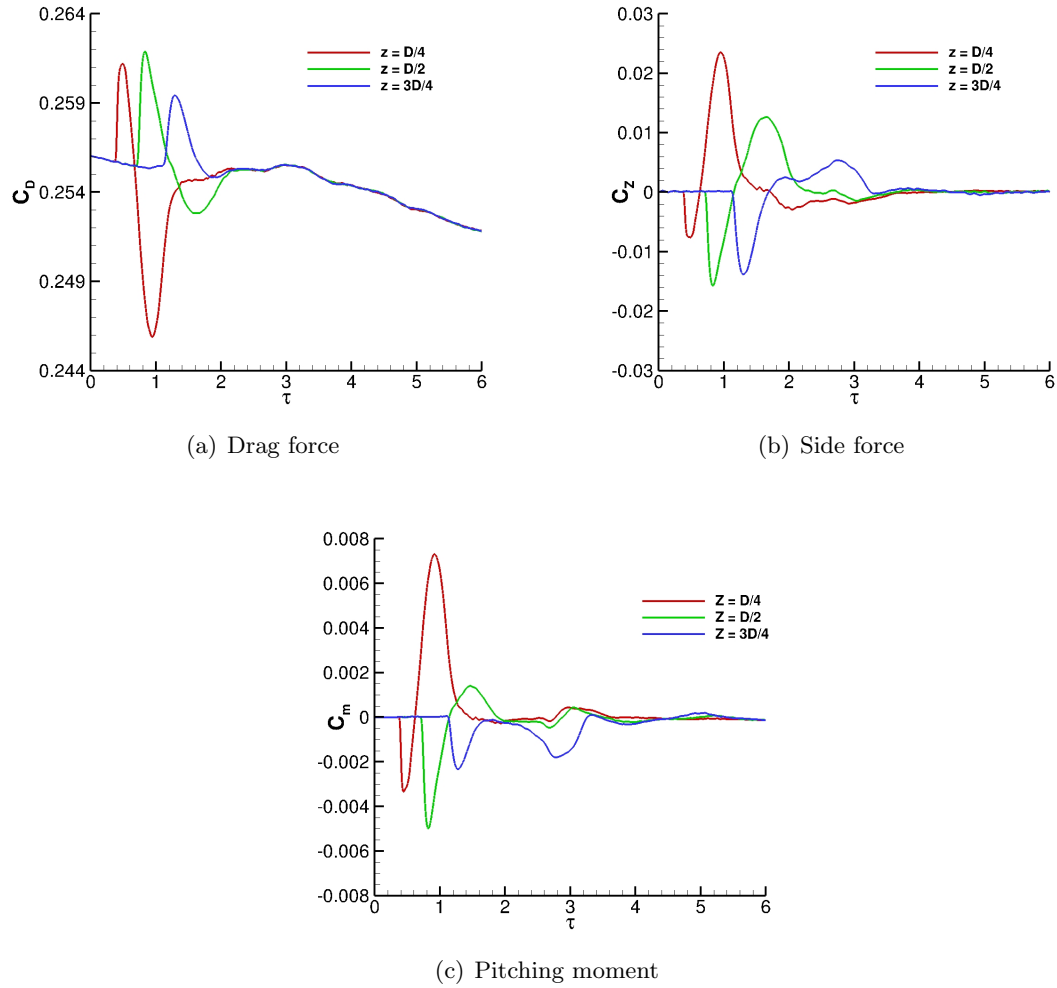
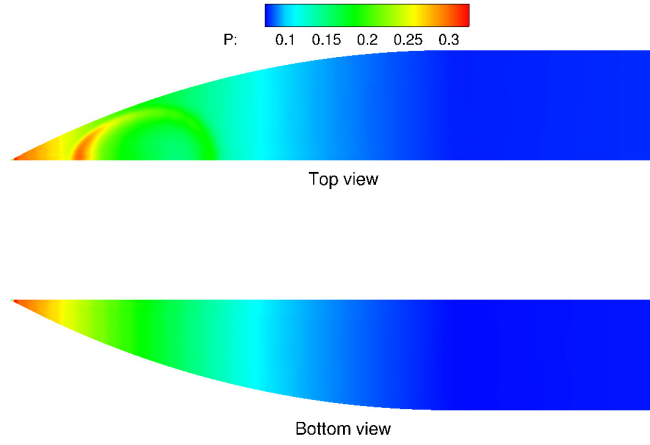
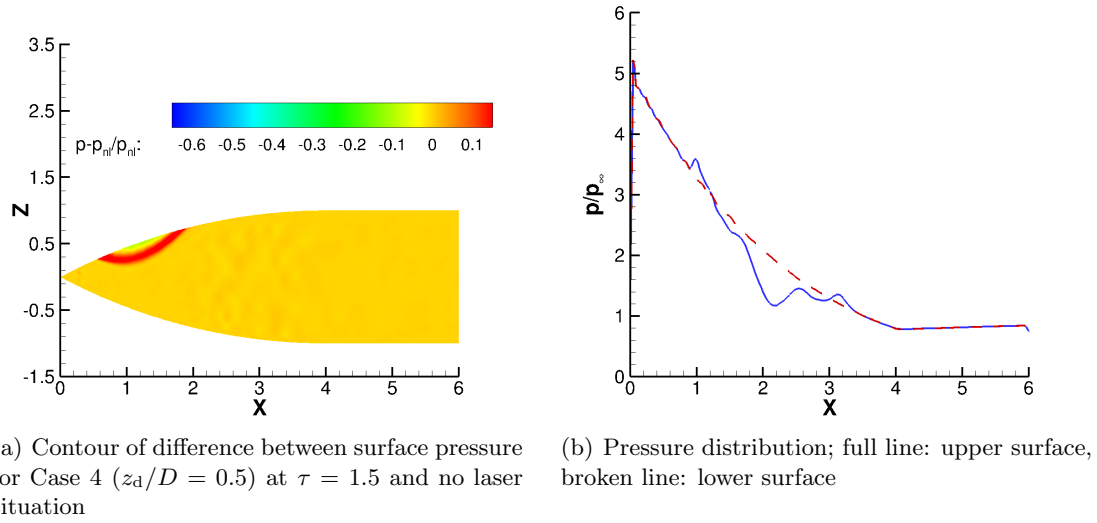


Figure 8.11: Drag force, side force, and pitching moment coefficients versus time for different laser discharge location

at $z_d = 0.5D$.

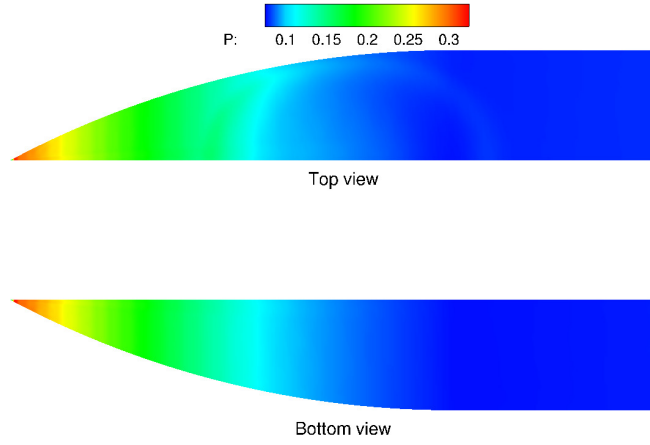
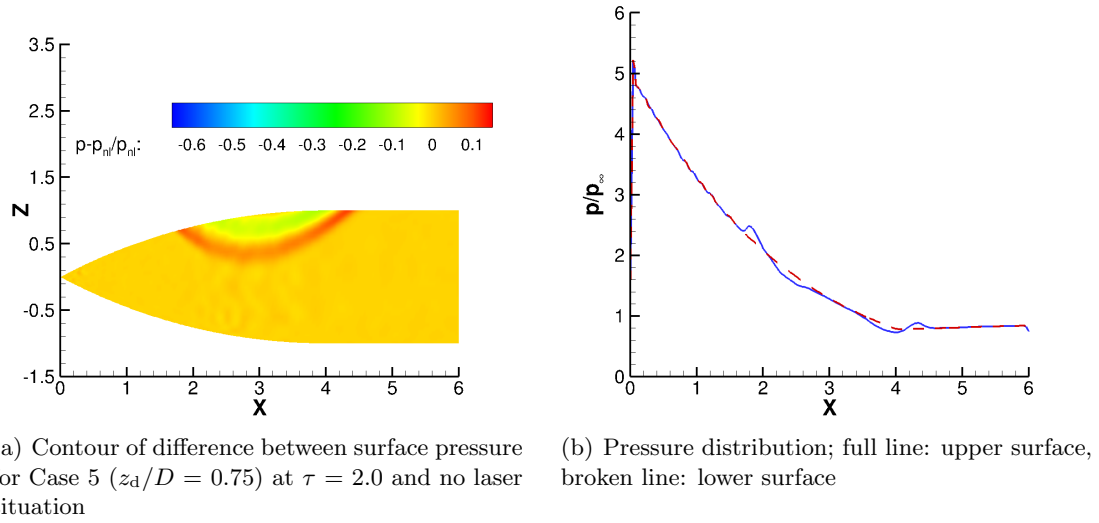
By comparison of Figures 8.11 and 8.14, it can be seen that although the general behavior is the same, there are some small changes between the two side force graphs which may depend on the difference between the geometries and need more investigation. There is an extremum value for the force resulted from the interaction of the blast wave with the shock system of the ogive cylinder for Ogive 1 which not exist for Ogive 2. On the other hand, there exists an extremum for the side force created as a result of the interaction of the heated region and the ogive's shock for Ogive 2 which does not appear in the Ogive 1 case.



(c) Top and bottom view of pressure contours

Figure 8.12: Pressure for Case 4 ($z_d/D = 0.5$) at $\tau = 1.5$

In summary, from Figures 8.7, 8.11, and 8.14, it is evident that adding energy in the upstream of an object can modify the drag force, side force and pitching moment of the body. This pitching moment may use a flight control method. The side forces created in these experiments are in the order of one-tenth of the undisturbed drag and the time interval that the side force and pitching moment are effective is in the order of $\Delta\tau = 2$. This dimensionless time is equal to the time required for the ogive cylinder to travel a distance equal twice its diameter which is two-third of its length for Ogive 1 and less than half its length for Ogive 2. Assuming that the actuation time for deflection of a conventional controlling surface is 0.1 s and the ogive cylinder is flying at sea level, the actuation time



(c) Top and bottom view of pressure contours

Figure 8.13: Pressure for Case 5 ($z_d/D = 0.75$) at $\tau = 2.0$

is equal to $\Delta\tau = 22$ which is more than the time required for Ogive 1 to travel seven times its length and for Ogive 2 is about the time required to travel five times its length. The actuation times of a deflecting surface is 11 times slower than the time required for creating the pitching moment using the energy discharge. Therefore, this study shows the possibility of assessing rapid maneuvering using energy deposition.

8.5.4 Flow Structure

Figures 8.15 and 8.16 compare the flow structure of Case 8 with the experimental shadowgraph images. In the experiment, 116 mJ of energy added to the flow using a laser.

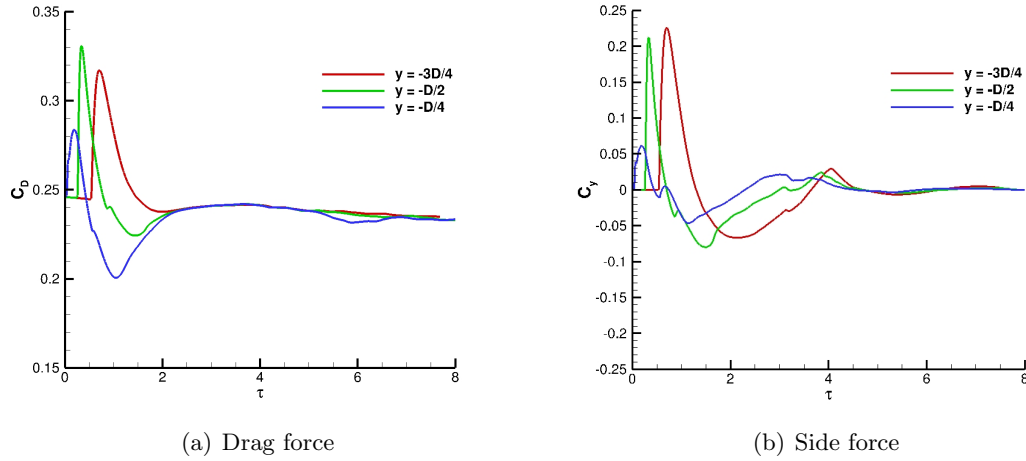


Figure 8.14: Drag force and side force coefficients change versus time for different laser discharge locations

Figure 8.15(a) is the instant of adding energy to the flow. Figure 8.15(b) shows the expansion of the heated region and the blast wave and the starting point of the interaction of the blast wave with the curved oblique shock. The “lensing” phenomenon illustrated in Figures 8.15(c) and 8.16(a). As described in Chapter 7, the interaction of the heated region and the shock wave moved the shock forward creates a lensing effect. Figures 8.16(b) and 8.16(c) illustrate the formation of a vortex due to the Richtmyer-Meshkov instability and the movement of the vortex along the ogive cylinder body. The comparison of the numerical and experimental flow structures shows a good agreement within the two.

8.6 Conclusion

The effect of off axis energy discharge in front of an ogive cylinder is examined. The amount of the energy put into the flow, the location of the discharge, and the shape of the ogive all have an effect on the final drag force, side force and pitching moment. The increase in the amount of energy added to gas will increase the force and moment peak values. However, while increasing the vertical distance of the discharge from the axis of the body decreases the drag reduction effect, but its effect on the side force depends on the shape and geometry of the ogive cylinder itself. But the existence of the optimum location of the discharge to achieve maximum effective side force is evident. The evidence of the possibility of using

energy discharge as a method for rapid maneuvering is also presented.

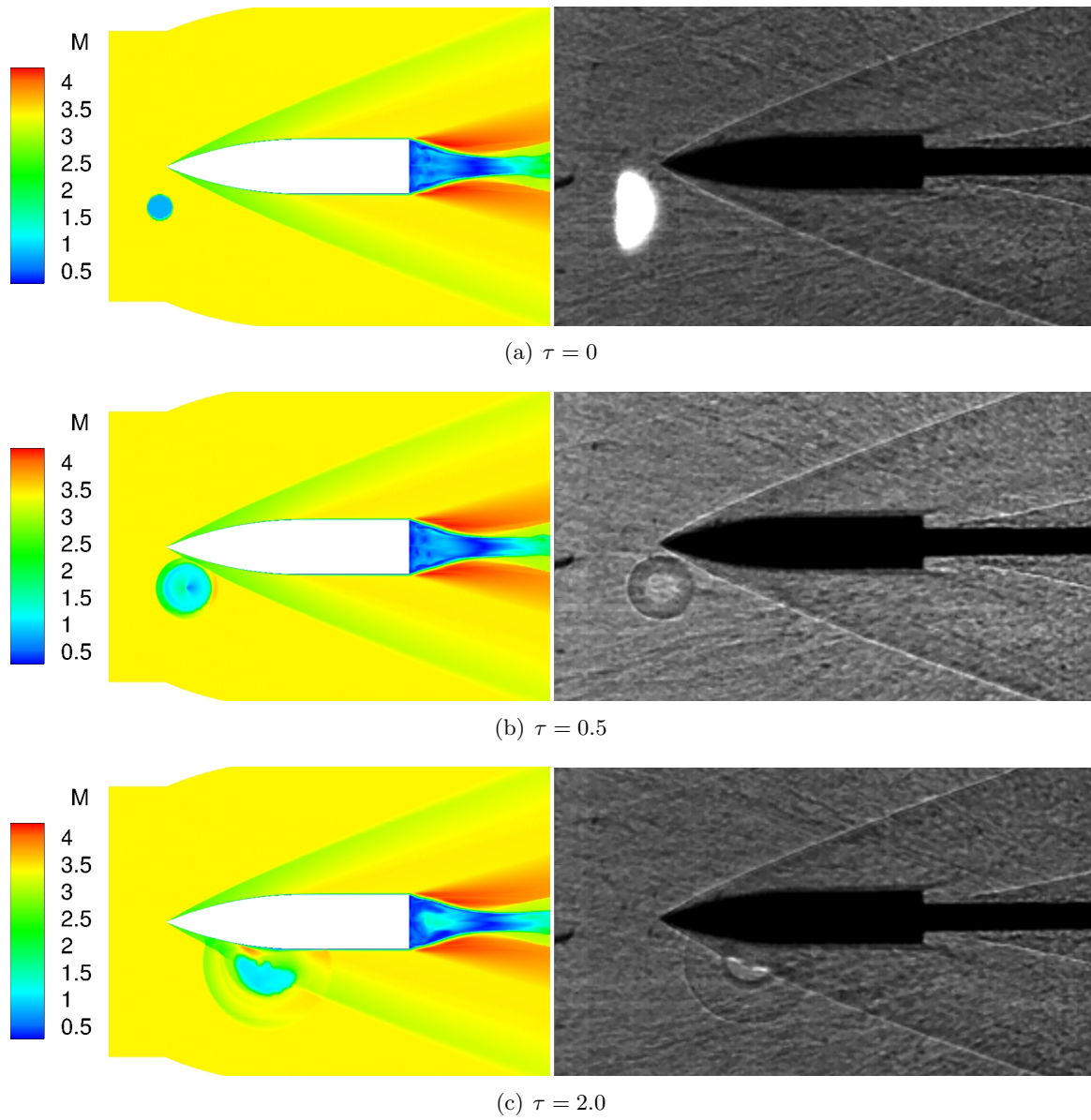


Figure 8.15: Contour plots of Mach number in comparison with shadowgraph images

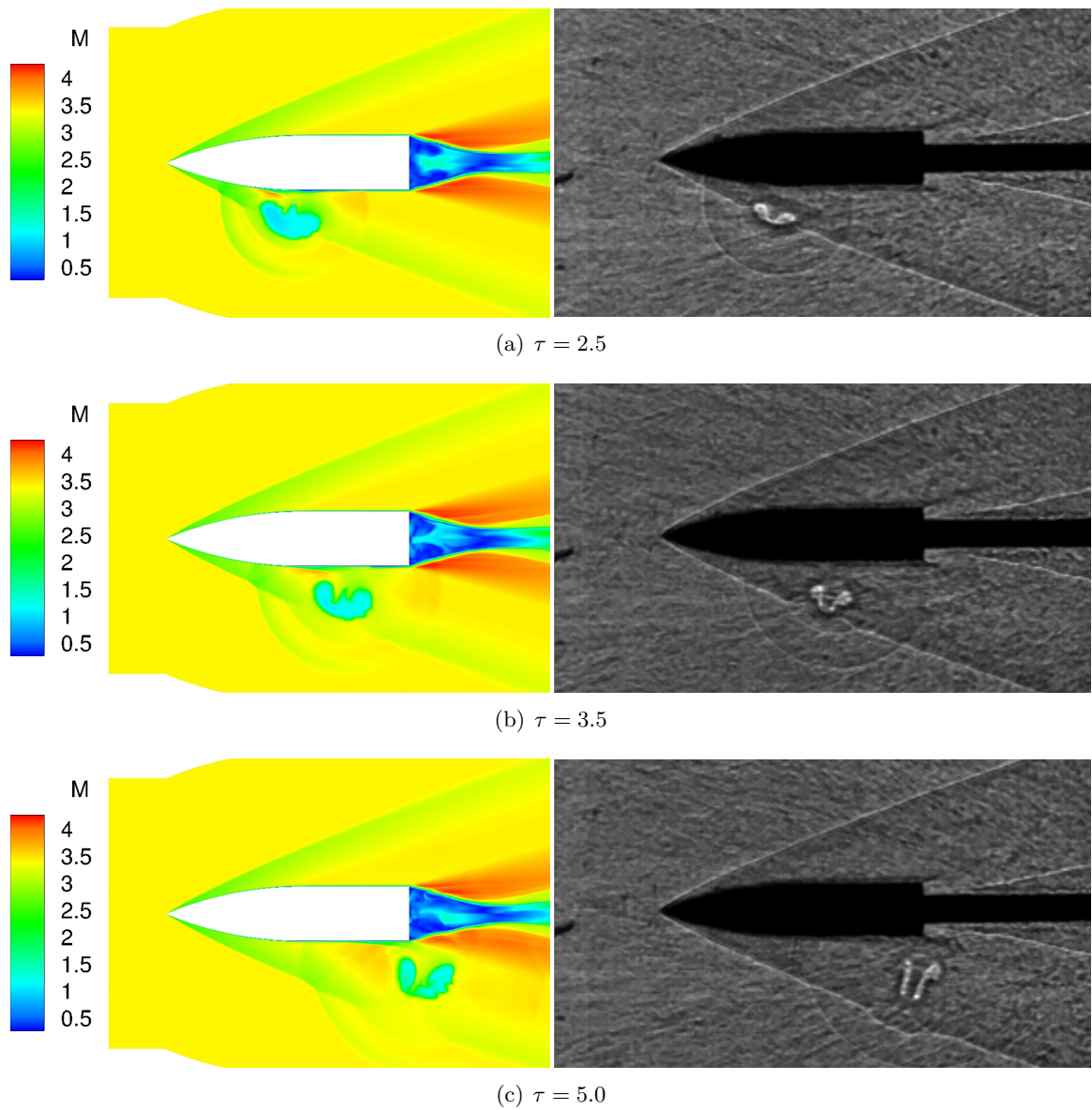


Figure 8.16: Contour plots of Mach number in comparison with shadowgraph images

Chapter 9

Conclusion

In this dissertation, high speed flows were simulated. In the first part, the focus was on the prediction of aerothermodynamic loading in hypersonic flows due to shock-shock or shock wave boundary layer interaction. The effect of physical modeling was examined by considering four main categories of modeling: 1) full non-equilibrium flow with Park I thermochemistry (denoted as Park I), 2) non-reactive model, 3) thermally perfect, and 4) calorically perfect. It was shown that for both experiments chosen for this dissertation, namely double cone and hollow cylinder flare performed at CUBRC, the effect of the thermochemistry and vibrational-translational effect is insignificant. For the double cone geometry, the reason is that a supersonic jet forms as a result of the interaction of the shock waves which prevent the dissociated gas to reach to the wall. In the case of hollow cylinder flare, the interactions are not strong and therefore, the mass fraction of dissociated gas is small. For the double cone, the thermally perfect model has the best prediction for the separation region length while the Park I and non-reactive underpredict the separation region length. For hollow cylinder flare, all models except the calorically perfect model predict the separation length accurately. The calorically perfect model overpredicted the length of the separation region. It has shown for hollow cylinder flare the usage of either isothermal for vibration or adiabatic for vibration boundary condition for vibrational energy at the isothermal wall does not affect on the final prediction of the aerothermodynamic database. Moreover, it was shown (by having two models for calorically perfect gas) that direct application of the isothermal boundary condition or using ghost cell has a significant effect on the predicted peak values, since the temperature gradient is high at the wall, using ghost cell predict higher peak values. Finally, neither of these two geometries was a test case for non-equilibrium models. In the future, the new experiment should consider in which the non-equilibrium effect is

important near the wall.

The study of the Edney III shock-shock interaction enlightened the importance of the location of the impinging shock. Due to uncertainty in the location of the impinging shock, two calculation is performed to find the correct location of the shock by matching the peak values for surface pressure and heat transfer. The slight change in the location of shock change the surface pressure and heat transfer to coincide well with the experimental data, however, the flowfield was changed from laminar to turbulent. Further study of this problem is needed to fully understand the turbulent behavior. Moreover, the grid refinement analysis should perform to show the independence of the results from the grid.

The second part of this dissertation was focused on the flow and flight control using energy deposition. Since during the response time of typical controlling surface, supersonic and especially hypersonic vehicles will travels several times their length, there is a need for the development of new methods. Using energy, rapid maneuvering is achievable. The analysis in this dissertation showed that there is an optimum amount of energy and optimum location for energy discharge. Even the shape of the object affects the efficiency of the method. Further studies are needed to understand the possibility of this method. The most important question is how much energy is needed for a real size vehicle? What is the efficiency of this method at large scale?

Chapter 10

List of Publications

Refereed Journal Publication

- **Kianvashrad, N.** and Knight, D., "Numerical Simulation of Laser Energy Discharge for Flight Control", *Journal of Physics D: Applied Physics*, Vol. 52, No.49, 2019, pp. 494005 (14pp).
- **Kianvashrad, N.** and Knight, D., "Nonequilibrium Effects on Prediction of Aerothermodynamic Loading for a Double Cone", *AIAA Journal*, Vol. 57, No.7, 2019, pp. 2946-2963.
- **Kianvashrad, N.** and Knight, D., "Simulation of Hypersonic Shock-Wave-Laminar-Boundary-Layer Interaction on Hollow Cylinder Flare", *AIAA Journal*, Vol. 55, No.1, 2017, pp. 322-326.

Referred Conference Proceedings

- **Kianvashrad, N.**, and Knight, D., "Shock-Shock Interaction over a Hemisphere in Hypersonic Flow - Part II", AIAA Paper No. 2020-2056, *AIAA 2020 SciTech Forum*, 6-10 January, 2020, Orlando, Florida, USA, DOI: 10.2514/6.2020-2056.
- **Kianvashrad, N.** and Knight, D., "Interaction of Energy Discharge and Hypersonic Vehicle", *8th European Conference for Aeronautics and Space Sciences (EUCASS)*, 1-4 July, 2019, Madrid, Spain, DOI: 10.13009/EUCASS2019-0235.
- **Kianvashrad, N.**, Pournadali Khamseh, A., DeMauro, E., and Knight, D., "Flight Control Using Off-Axis Laser Discharge", AIAA Paper No. 2019-3225, *AIAA AVIATION 2019 Forum*, 17-21 June, 2019, Dallas, Texas, USA, DOI: 10.2514/6.2019-3225.

- **Kianvashrad, N.** and Knight, D., "Shock-Shock Interaction over a Hemisphere in Hypersonic Flow", AIAA Paper No. 2019-0890, *AIAA 2019 SciTech Forum*, 7-11 January, 2019, San Diego, California, USA, DOI: 10.2514/6.2019-0890.
- **Kianvashrad, N.** and Knight, D., "Non-Equilibrium Effects of Interaction of Laser Discharge with Hemisphere-Cylinder in Supersonic Flow", AIAA Paper No. 2018-3708, *2018 Flow Control Conference*, 25-29 June, 2018, Atlanta, Georgia, USA, DOI: 10.2514/6.2018-3757.
- **Kianvashrad, N.** and Knight, D., "Simulation of Hypersonic Shock-Shock Interaction over a Hemisphere", AIAA Paper No. 2018-3708, *2018 Fluid Dynamics Conference*, 25-29 June, 2018, Atlanta, Georgia, USA, DOI: 10.2514/6.2018-3708.
- Knight, D., **Kianvashrad, N.**, "Prediction of Aerothermodynamic Loading in Hypersonic Shock Wave Laminar Boundary Layer Interaction", *53rd 3AF International Conference on Applied Aerodynamics*, 26-28 March, 2018, Salon-de-Provence, France.
- **Kianvashrad, N.** and Knight, D., "The Effect of Thermochemistry on Prediction of Aerothermodynamic Loading over a Double Cone in a Laminar Hypersonic Flow", AIAA Paper No. 2018-1812, *56th AIAA Aerospace Science*, 8-12 January, 2018, Kissimmee, Florida, USA, DOI: 10.2514/6.2018-1812.
- **Kianvashrad, N.** and Knight, D., "Effect of Off-Body Laser Discharge on Drag Reduction of Hemisphere Cylinder in Supersonic Flow - Part II", AIAA Paper No. 2018-1433, *56th AIAA Aerospace Science*, 8-12 January, 2018, Kissimmee, Florida, USA, DOI: 10.2514/6.2018-1433.
- **Kianvashrad, N.** and Knight, D., "Effect of Vibrational Temperature Boundary Condition of Isothermal Wall on Hypersonic Shock Wave Laminar Boundary Layer Interaction of a Hollow Cylinder Flare", *Seventh European Conference for Aeronautics and Aerospace Sciences (EUCASS)*, 3-6 July, 2017, Milan, Italy, DOI: 10.13009/EUCASS2017-97.
- **Kianvashrad, N.**, Knight, D., Wilkinson, S., Chou, A., Horne, R., Herring, G., Beeler, G. and Jangda, M., "Effect of Off-Body Laser Discharge on Drag Reduction of Hemisphere Cylinder in Supersonic Flow", AIAA Paper No. 2017-3478, *48th AIAA*

Plasmadynamics and Lasers Conference, 5-9 June, 2017, Denver, Colorado, USA, DOI: 10.2514/6.2017-3478.

- **Kianvashrad N.**, and Knight, D., "Simulation of Hypersonic Shock Wave Laminar Boundary Layer Interaction on Hollow Cylinder Flare, Part II", AIAA Paper No. 2017-3975, *47th AIAA Fluid Dynamics Conference*, 5-9 June, 2017, Denver, Colorado, USA, DOI: 10.2514/6.2017-3975.
- **Kianvashrad, N.** and Knight, D., "Simulation of Hypersonic Shock Wave Laminar Boundary Layer Interaction on Hollow Cylinder Flare", AIAA Paper No. 2016-0349, *54th AIAA Aerospace Sciences Meeting*, 4-8 January, 2016, San Diego, California, USA, DOI: 10.2514/6.2016-0349.
- **Kianvashrad, N.** and Knight, D., "Simulation of Hypersonic Shock Wave Laminar Boundary Layer Interactions", *Sixth European Conference for Aerospace Sciences*, 29 June-3 July, 2015, Krakow, Poland.

Conference Oral Presentation

- Knight, D., **Kianvashrad, N.**, Wilkinson, S., Chou, A., Herring, G. and Horne, R., "Modeling Laser Discharge in Quiescent Air", *55th AIAA Aerospace Sciences Meeting*, 9-13 January, 2017, Grapevine, Texas, USA.

Appendix A

Appendix

A.1 Park I Model

Table A.1: Thermochemistry Model Reactions

Reaction	C ($\text{m}^3/\text{kg}\cdot\text{mole}\cdot\text{s}$)	η	ϵ/k (K)	α	β	A_1	A_2	A_3	A_4	A_5
$N_2 + N_2 \rightarrow N + N + N_2$	$3.70 \cdot 10^{18}$	-1.6	113200	0.5	0.5	10.81	-12.61	0.683	-0.118	0.006
$N_2 + N \rightarrow N + N + N$	$1.11 \cdot 10^{19}$	-1.6	113200	0.5	0.5	10.81	-12.61	0.683	-0.118	0.006
$N_2 + NO \rightarrow N + N + NO$	$3.70 \cdot 10^{18}$	-1.6	113200	0.5	0.5	10.81	-12.61	0.683	-0.118	0.006
$N_2 + O_2 \rightarrow N + N + O_2$	$3.70 \cdot 10^{18}$	-1.6	113200	0.5	0.5	10.81	-12.61	0.683	-0.118	0.006
$N_2 + O \rightarrow N + N + O$	$1.11 \cdot 10^{19}$	-1.6	113200	0.5	0.5	10.81	-12.61	0.683	-0.118	0.006
$N_2 + O \rightarrow NO + N$	$3.18 \cdot 10^{10}$	0.1	37700	1.0	0.0	2.349	-4.828	0.455	-0.075	0.004
$O_2 + N_2 \rightarrow O + O + N_2$	$2.75 \cdot 10^{16}$	-1.0	59500	0.5	0.5	8.243	-4.127	-0.616	0.093	-0.005
$O_2 + N \rightarrow O + O + N$	$8.25 \cdot 10^{16}$	-1.0	59500	0.5	0.5	8.243	-4.127	-0.616	0.093	-0.005
$O_2 + NO \rightarrow O + O + NO$	$2.75 \cdot 10^{16}$	-1.0	59500	0.5	0.5	8.243	-4.127	-0.616	0.093	-0.005
$O_2 + O_2 \rightarrow O + O + O_2$	$2.75 \cdot 10^{16}$	-1.0	59500	0.5	0.5	8.243	-4.127	-0.616	0.093	-0.005
$O_2 + O \rightarrow O + O + O$	$8.25 \cdot 10^{16}$	-1.0	59500	0.5	0.5	8.243	-4.127	-0.616	0.093	-0.005
$NO + O \rightarrow N + O_2$	$2.16 \cdot 10^5$	1.29	19220	1.0	0.0	0.215	-3.657	0.843	-0.136	0.007
$NO + N_2 \rightarrow N + O + N_2$	$2.30 \cdot 10^{14}$	-0.5	75500	0.5	0.5	8.457	-7.784	0.228	-0.043	0.002
$NO + NO \rightarrow N + O + NO$	$2.30 \cdot 10^{14}$	-0.5	75500	0.5	0.5	8.457	-7.784	0.228	-0.043	0.002
$NO + O_2 \rightarrow N + O + O_2$	$2.30 \cdot 10^{14}$	-0.5	75500	0.5	0.5	8.457	-7.784	0.228	-0.043	0.002
$NO + N \rightarrow N + O + N$	$4.60 \cdot 10^{14}$	-0.5	75500	0.5	0.5	8.457	-7.784	0.228	-0.043	0.002
$NO + O \rightarrow N + O + O$	$4.60 \cdot 10^{14}$	-0.5	75500	0.5	0.5	8.457	-7.784	0.228	-0.043	0.002

NOTES

$$k_f = CT_a^\eta e^{-\epsilon/kT_a}, \quad T_a = T^\alpha T_{\text{vib}}^\beta, \quad k_e = \exp(A_1 + A_2 z + A_3 z^2 + A_4 z^3 + A_5 z^4) \text{ where } z = 10^4/T$$

References

- [1] Holden, M. and Nowak, R., “Studies of Shock/Shock Interaction on Smooth and Transpiration-cooled Hemispherical Nostetips in Hypersonic Flow,” AIAA Paper 91-1765, American Institute of Aeronautics and Astronautics, June 1991.
- [2] Sippel, M., Klevanski, J., and Steelant, J., “Comparative Study on Options for High-Speed Intercontinental Passenger Transports: Air-Breathing- vs. Rocket-Propelled,” Tech. Rep. IAC-05-D2.4.09, DLR, October 2005.
- [3] Sippel, M., Schwanekamp, T., Trivailo, O., and Lentsch, A., “Progress of SpaceLiner Rocket-Powered High-Speed Concept,” Tech. Rep. IAC-13-D2.4.05, DLR, September 2013.
- [4] “LAPCAT A2 Facts and Figures,” Reaction Engines Limited, Oxfordshire, England, 2008.
- [5] “ZEHST High-Speed Transport Concept Study,” EADS INNOVATION WORKS and ASTRIUM, Munich, Germany, 2011.
- [6] Steelant, J., Langener, T., Matteo, F. D., Hannemann, K., Riehmer, J., Kuhn, M., Ditter, C., Jung, W., Marini, M., Pezzella, G., Cicala, M., and Serre, L., “Conceptual Design of the High-Speed Propelled Experimental Test Vehicle HEXAFLY,” AIAA Paper 2015-3539, American Institute of Aeronautics and Astronautics, July 2015.
- [7] Pezzella, G., Marini, M., Reimann, B., and Steelant, J., “Aerodynamic Design Analysis of the HEXAFLY-INT Hypersonic Glider,” AIAA Paper 2015-3644, American Institute of Aeronautics and Astronautics, July 2015.
- [8] Steelant, J., Villace, V., Kallenbach, A., Wagner, A., Andro, J., di Benedetto, S., Saracoglu, B., Chernyshev, S., Gubanov, A., Talyzin, V., Voevodenko, N., Kukshinov, N., Prokhorov, A., Grigoriev, N., Neely, A., Verstraete, D., and Buttsworth, D., “Flight Testing Designs in HEXAFLY-INT for High-Speed Transportation,” HiSST Paper 2018-3101064, HiSST: International Conference on High-Speed Vehicle Science & Technology, November 2018.
- [9] Walker, S. and Rodgers, F., “Falcon Hypersonic Technology Overview,” AIAA Paper 2005-3253, American Institute of Aeronautics and Astronautics, May 2005.
- [10] Walker, S., Sherk, J., Shell, D., Schena, R., Bergmann, J., and Gladbach, J., “The DARPA/AF Falcon Program: The Hypersonic Technology Vehicle # 2 (HTV-2) Flight Demonstration Phase,” AIAA Paper 2008-2539, American Institute of Aeronautics and Astronautics, January 2008.
- [11] Longo, J., “Present Results and Future Challenges of the DLR SHEFEX Program,” AIAA Paper 2009-7226, American Institute of Aeronautics and Astronautics, October 2009.

- [12] Dittert, C., Böhrk, H., and Elsässer, H., “Design of a Transpiration Cooled Sharp Leading Edge for SHEFEX III,” *8th European Conference on Aerothermodynamics for Space Vehicles*, 2015.
- [13] Button, K., “Making a Money Saver,” *Aerospace America*, June 2016, pp. 16–19.
- [14] Perrett, B., Sweetman, B., and Fabey, M., “U.S. Navy Sees Chinese HGV as Part of Wider Threat,” *Aviation Week and Space Technology*, January 2014.
- [15] Jackson, K., Gruber, M., and Buccellato, S., “Mach 6-8+ Hydrocarbon-Fueled Scramjet Flight Experiment: The HIFiRE Flight 2 Project,” *Journal of Propulsion and Power*, Vol. 31, No. 1, January-February 2015, pp. 36–53.
- [16] Juliano, T., Adamczak, D., and Kimmel, R., “HIFiRE-5 Flight Test Results,” *Journal of Spacecraft and Rockets*, Vol. 52, No. 3, May-June 2015, pp. 650–663.
- [17] Bond, A., “Skylon Users’ Manual,” Tech. Rep. SKY-REL-MA-0001, Reaction Engines Limited, September 2009.
- [18] “X-51A WaveRider,” Boeing Defense, Space & Security, St. Louis, MO, 2012.
- [19] MacCormack, R., “Numerical Solution of the Interaction of a Shock Wave with a Laminar Boundary Layer,” *Proceedings of the Second International Conference on Numerical Methods in Fluid Dynamics*, edited by M. Holt, Vol. 8 of *Lecture Notes in Physics*, Springer Berlin Heidelberg, 1971, pp. 151–163.
- [20] Shang, J. and Scherr, S., “Navier-Stokes Solution for a Complete Re-Entry Configuration,” *Journal of Aircraft*, Vol. 23, No. 12, December 1986, pp. 881–888.
- [21] Maus, J., Griffith, B., Szema, K., and Best, J., “Hypersonic Mach number and real gas effects on Space Shuttle Orbiteraerodynamics,” *Journal of Spacecraft and Rockets*, Vol. 21, No. 2, 1984, pp. 136–141.
- [22] “STS-1 Anomaly Report,” Tech. Rep. SSVEO IFA List Date 27 February 2003, OV-103, Columbia, National Aeronautics and Space Administration, 2003.
- [23] Thompson, M., *At the Edge of Space: The X-15 Flight Program*, Smithsonian Institution Press, Washington, DC, 1992.
- [24] Edney, B., “Anomalous Heat Transfer and Pressure Distributions on Blunt Bodies at Hypersonic Speed in the Presence of an Impinging Shock,” Tech. Rep. FFA Report 115, Aeronautical Research Institute of Sweden, 1968.
- [25] Liepmann, H., “The Interaction Between Boundary Layer and Shock Waves in Transonic Flow,” *Journal of the Aeronautical Sciences*, Vol. 13, No. 12, December 1946, pp. 623–637.
- [26] Babinsky, H. and Harvey, J., *Shock Wave-Boundary-Layer Interactions*, Cambridge University Press, New York, 2011.
- [27] Knight, D., Chazot, O., Austin, J., Badr, M., Candler, G., Celik, B., de Rosa, D., Donelli, R., Komives, J., Lani, A., Levin, D., Nompelis, I., Panesi, M., Pezzella, G., Reimann, B., Tumuklu, O., and Yuceil, K., “Assessment of Predictive Capabilities for

- Aerodynamic Heating in Hypersonic Flow,” *Progress in Aerospace Sciences*, Vol. 90, April 2017, pp. 39–53.
- [28] Grasso, F. and Marini, M., “Analysis of Hypersonic Shock-Wave Laminar Boundary-Layer Interaction Phenomena,” *Journal of Computers and Fluids*, Vol. 25, No. 6, 1996, pp. 561–581.
 - [29] Holden, M. and Moselle, J., “Theoretical and Experimental Studies for the Shock Wave-Boundary Layer Interaction on Compression Surfaces in Hypersonic Flow,” Tech. Rep. ARL 70-0002, Aerospace Research Laboratories, Wright-Patterson AFB, OH, 1970.
 - [30] Chanetz, B., “Study of Axisymmetric Shock Wave/Boundary Layer Interaction in Hypersonic Laminar Flow,” Tech. Rep. RT 42/4362 AN, Office National D’Etudes et de Recherches Aerospatiales, 1995.
 - [31] Chanetz, B., Benay, R., Bousquet, J.-M., Bur, R., Pot, T., Grasso, F., and Moss, J., “Experimental and Numerical Study of the Laminar Separation in Hypersonic Flow,” *Aerospace Science and Technology*, Vol. 3, 1998, pp. 205–218.
 - [32] Olejniczak, J., Candler, G., Wright, M., Leyva, I., and Hornung, H., “Experimental and Computational Study of High Enthalpy Double-Wedge Flows,” *Journal of Thermophysics and Heat Transfer*, Vol. 13, No. 4, October-December 1999, pp. 431–440.
 - [33] Park, C., “On Convergence of Computation of Chemically Reacting Flow,” AIAA Paper 1985-0247, American Institute of Aeronautics and Astronautics, January 1985.
 - [34] Park, C., “Two-Temperature Interpretation of Dissociation Rate Data for N_2 and O_2 ,” AIAA Paper 1988-0458, American Institute of Aeronautics and Astronautics, January 1988.
 - [35] Bortner, M., “A Review of Rate Constants of Selected Reactions of Interest in Re-Entry Flow fields in Atmosphere,” NBS TN 484, NBS, 1969.
 - [36] Wright, M., Sinha, K., Olejniczak, J., Candler, G., Magruder, T., and Smits, A., “Numerical and Experimental Investigation of Double-Cone Shock Interactions,” *AIAA Journal*, Vol. 38, No. 12, December 2000, pp. 2268–2276.
 - [37] Marini, M., “Analysis of Hypersonic Compression Ramp Laminar Flows Under Sharp Leading Edge Conditions,” *Aerospace Science and Technology*, Vol. 5, No. 4, June 2001, pp. 257–271.
 - [38] Holden, M., “A Study of Flow Separation in Regions of Shock Wave-Boundary Layer Interaction in Hypersonic Flow,” AIAA Paper 78-1169, American Institute of Aeronautics and Astronautics, January 1978.
 - [39] Marini, M., “Effects of Flow and Geometry Parameters on Shock-Wave Boundary Layer Interaction Phenomena,” AIAA Paper 98-1570, American Institute of Aeronautics and Astronautics, January 1998.
 - [40] Holden, M. and Wadhams, T., “Code Validation Study of Laminar Shock/Boundary Layer and Shock/shock Interactions in Hypersonic Flow Part A: Experimental Measurements,” AIAA Paper 2001-1031, American Institute of Aeronautics and Astronautics, January 2001.

- [41] Harvey, J., Holden, M., and Wadhams, T., “Code Validation Study of Laminar Shock/Boundary Layer and Shock/shock Interactions in Hypersonic Flow Part B: Comparison with Navier-Stokes and DSMC Solutions,” AIAA Paper 2001-1031, American Institute of Aeronautics and Astronautics, January 2001.
- [42] Gaitonde, D., Canupp, P., and Holden, M., “Heat Transfer Prediction in a Laminar Hypersonic Viscous/Inviscid Interaction,” *Journal of Thermophysics and Heat Transfer*, Vol. 16, No. 4, October-December 2002, pp. 481–489.
- [43] Holden, M., “Experimental Studies of Laminar Separated Flows Induced by Shock Wave/Boundary Layer and Shock/Shock Interaction in Hypersonic Flows for CFD Validation,” AIAA Paper 2000-0930, American Institute of Aeronautics and Astronautics, January 2000.
- [44] Roy, C., Bartel, T., Gallis, M., and Payne, J., “DSMC and Navier-Stokes Predictions for Hypersonic Laminar Interacting Flows,” AIAA Paper 2001-1030, American Institute of Aeronautics and Astronautics, January 2001.
- [45] Roy, C., Gallis, M., Bartel, T., and Payne, J., “Navier-Stokes and Direct Simulation Monte-Carlo Predictions for Laminar Hypersonic Separation,” *AIAA Journal*, Vol. 41, No. 6, June 2003, pp. 1055–1063.
- [46] Holden, M., Wadhams, T., Harvey, J., and Candler, G., “Comparisons between Measurements in Regions of Laminar Shock Wave Boundary Layer Interaction in Hypersonic Flows with Navier-Stokes and DSMC Solutions,” AIAA Paper 2002-0435, American Institute of Aeronautics and Astronautics, January 2002.
- [47] Candler, G., Nompelis, I., Druguet, M.-C., Holden, M., Wadhams, T., Boyd, I., and Wang, W.-L., “CFD Validation for Hypersonic Flight: Hypersonic Double-Cone Flow Simulations,” AIAA Paper 2002-581, American Institute of Aeronautics and Astronautics, January 2002.
- [48] Nompelis, I., Candler, G., Holden, M., and Wadhams, T., “Computational Investigation of Hypersonic Viscous/Inviscid Interactions in High Enthalpy Flows,” AIAA Paper 2003-3642, American Institute of Aeronautics and Astronautics, June 2003.
- [49] Nompelis, I., Candler, G., and Holden, M., “Effect of Vibrational Nonequilibrium on Hypersonic Double-Cone Experiments,” *AIAA Journal*, Vol. 41, No. 11, November 2003, pp. 2162–2169.
- [50] Schaaf, S. and Chambre, P., *Flow of Rarefied Gases*, Princeton University Press, Princeton, NJ, 1966.
- [51] Druguet, M.-C., Candler, G., and Nompelis, I., “Effects of Numerics on Navier-Stokes Computations of Hypersonic Double-Cone Flows,” *AIAA Journal*, Vol. 43, No. 3, March 2005, pp. 616–623.
- [52] Knight, D., Longo, J., Drikakis, D., Gaitonde, D., Lani, A., Nompelis, I., Reimann, B., and Walpot, L., “Assessment of CFD Capability for Prediction of Hypersonic Shock Interactions,” *Progress in Aerospace Sciences*, Vol. 48–49, 2012, pp. 8–26.

- [53] Reimann, B. and Hannemann, V., “Numerical Investigation of Double-Cone and Cylinder Experiments in High Enthalpy Flows Using the DLR TAU Code,” AIAA Paper 2010-1282, American Institute of Aeronautics and Astronautics, January 2010.
- [54] MacLean, M., Holden, M., and Dufrene, A., “Comparison between CFD and Measurements for Real-Gas Effects on Laminar Shock Wave Boundary Layer Interaction, I,” Oral Presentation, AIAA Aviation 2014, Atlanta, GA, 2014.
- [55] Nompelis, I. and Candler, G., “US3D Predictions of Double-Cone and Hollow Cylinder-Flare Flows at High Enthalpy,” AIAA Paper 2014-3366, American Institute of Aeronautics and Astronautics, June 2014.
- [56] Knight, D. and Chazot, O., “Assessment of Predictive Capabilities for Aerodynamic Heating of Hypersonic Systems,” STO Technical Report TR-AVT-205, NATO Science and Technology Organization, November 2015.
- [57] Swantek, A. and Austin, J., “Heat Transfer on a Double Wedge Geometry in Hypervelocity Air and Nitrogen Flows,” AIAA Paper 2012-0284, American Institute of Aeronautics and Astronautics, January 2012.
- [58] Komives, J., Nompelis, I., and Candler, G., “Numerical Investigation of Unsteady Heat Transfer on a Double Wedge Geometry in Hypervelocity Flows,” AIAA Paper 2014-2354, American Institute of Aeronautics and Astronautics, June 2014.
- [59] Tumuklu, O., Levin, D., and Austin, J., “Shock-Shock Interactions for a Double Wedge Configuration in Different Gases,” AIAA Paper 2015-1520, American Institute of Aeronautics and Astronautics, January 2015.
- [60] Mason, M. and Berry, S., “Global Aeroheating Measurements of ShockShock Interactions on Swept Cylinder,” *Journal of Spacecraft and Rockets*, Vol. 53, No. 4, July 2016, pp. 678–692.
- [61] Windisch, C., Reinartz, B., and Müller, S., “Investigation of Unsteady Edney Type IV and VII Shock-Shock Interactions,” *AIAA Journal*, Vol. 54, No. 6, 2016, pp. 1846–1861.
- [62] Hao, J., Wang, J., and Lee, C., “Numerical Simulation of High-Enthalpy Double-Cone Flows,” *AIAA Journal*, Vol. 55, No. 7, July 2017, pp. 2471–2475.
- [63] Marrone, P. and Treanor, C., “Chemical Relaxation with Preferential Dissociation from Excited Vibrational Levels,” *The Physics of Fluids*, Vol. 6, No. 9, September 1963, pp. 1215–1221.
- [64] Xiao, F., Li, Z., Zhu, Y., and Yang, J., “Hypersonic Type-IV Shock/Shock Interactions on a Blunt Body with Forward-Facing Cavity,” *Journal of Spacecraft and Rockets*, Vol. 54, No. 2, March 2017, pp. 506–512.
- [65] Hao, J., Wang, J., and Lee, C., “Numerical Simulation of High-Enthalpy Hollow-Cylinder/Flare Flows,” *AIAA Journal*, Vol. 56, No. 8, August 2018, pp. 3337–3341.
- [66] Park, C., *Nonequilibrium Hypersonic Aerothermodynamics*, John Wiley & Sons, New York, 1990.

- [67] Paoli, R., “Numerical Simulations of Shock-Shock Interactions,” *Open Journal of Fluid Dynamics*, Vol. 8, No. 4, December 2018, pp. 392–403.
- [68] Durna, A. and Celik, B., “Effects of Double-Wedge Aft Angle on Hypersonic Laminar Flows,” *AIAA Journal*, Vol. 0, No. 0, 0, pp. 1–15.
- [69] Knight, D., *Energy Deposition for High-Speed Flow Control*, Cambridge University Press, New York, 2019.
- [70] Tretyakov, P., Garanin, A., Kraynev, V., Tupikin, A., and Yakovlev, V., “Investigation of Local Laser Energy Release Influence on Supersonic Flow by Methods of Aerophysical Experiments,” *International Conference on Methods of Aerophysical Research, Novosibirsk, Russia*, 1996.
- [71] Riggins, D., Nelson, H., and Johnson, E., “Blunt-Body Wave Drag Reduction Using Focused Energy Deposition,” *AIAA Journal*, Vol. 37, No. 4, 1999, pp. 460–467.
- [72] Lashkov, V., Mashek, I., Anisimov, Y., Ivanov, V., Kolesnichenko, Y., Ryvkin, M., and Gorynya, A., “Gas Dynamic Effect of Microwave Discharge on Supersonic Cone-shaped Bodies,” *AIAA Paper 2004-0671*, American Institute of Aeronautics and Astronautics, January 2004.
- [73] Adelgren, R., Yan, H., Elliott, G., Knight, D., Beutner, T., and Zheltovodov, A., “Control of Edney IV Interaction by Pulsed Laser Energy Deposition,” *AIAA Journal*, Vol. 43, No. 2, 2005, pp. 256–269.
- [74] Yan, H. and Gaitonde, D., “Effect of Energy Pulse on 3-D Edney IV Interaction,” *AIAA Journal*, Vol. 46, No. 6, 2008, pp. 1424–1431.
- [75] Knight, D., Kolesnichenko, Y., Brovkin, V., Khmara, D., Lashkov, V., and Mashek, I., “Interaction of Microwave-Generated Plasma with a Hemisphere Cylinder at Mach 2.1,” *AIAA Journal*, Vol. 47, No. 12, 2009, pp. 2996–3010.
- [76] Schüle, E., Zheltovodov, A., Pimonov, E., and Loginov, M., “Experimental and Numerical Modeling of the Bow Shock Interaction with Pulse-Heated Air Bubbles,” *International Journal of Aerospace Innovations*, Vol. 2, No. 3, 2010, pp. 165–188.
- [77] Kim, J., Matsuda, A., Sakai, T., and Sasoh, A., “Wave Drag Reduction with Acting Spike Induced by Laser-Pulse Energy Depositions,” *AIAA Journal*, Vol. 49, No. 9, 2011, pp. 2076–2078.
- [78] Anderson, K. and Knight, D., “Plasma Jet for Flight Control,” *AIAA Journal*, Vol. 50, No. 9, 2012, pp. 1855–1872.
- [79] Girgis, I., Shneider, M., Macheret, S., Brown, G., and Miles, R., “Steering Moments Creation in Supersonic Flow by Off-Axis Plasma Heat Addition,” *Journal of Spacecraft and Rockets*, Vol. 43, No. 3, May-June 2006, pp. 607–613.
- [80] Starikovskiy, A., Limbach, C., and Miles, R., “Trajectory Control of Small Rotating Projectiles by Laser Discharges,” *AIAA Paper 2016-4308*, American Institute of Aeronautics and Astronautics, June 2016.

- [81] Elias, P., Severac, N., Luyssen, J., André, Y., Doudet, I., Wattellier, B., Tobeli, J., Albert, S., Mahieu, B., Bur, R., Mysyrowicz, A., and Houard, A., “Improving Supersonic Flights with Femtosecond Laser Filamentation,” *Science Advances*, Vol. 4, No. 11, November 2018, pp. 1–5.
- [82] Haynes, W., *CRC Handbook of Chemistry and Physics, 97th Edition (2016-2017)*, CRC Press, New York, 2016.
- [83] Hirschfelder, J., Curtiss, C., and Bird, R., *Molecular Theory of Gases and Liquids*, John Wiley & Sons, New York, 1954.
- [84] Molvik, G. and Merkle, C., “A Set of Strongly Coupled, Upwind Algorithms for Computing Flows in Chemical Nonequilibrium,” AIAA Paper 89-0199, American Institute of Aeronautics and Astronautics, January 1989.
- [85] Wilke, C., “A Viscosity Equation for Gas Mixtures,” *Journal of Chemical Physics*, Vol. 18, No. 4, April 1950, pp. 517–519.
- [86] Vincenti, W. and Kruger, C., *Introduction to Physical Gas Dynamics*, Krieger Publishing Company, Malabar, Florida, 1965.
- [87] Millikan, R. and White, D., “Systematics of Vibrational Relaxation,” *Journal of Chemical Physics*, Vol. 39, 1953, pp. 3209–3213.
- [88] Gupta, R., Yos, J., Thompson, R., and Lee, K., “A Review of Reaction Rates and Thermodynamic and Transport Properties for an 11-Species Air Model for Chemical and Thermal Nonequilibrium Calculations to 30000 K,” Reference Report 1232, NASA, 1990.
- [89] “GASPeX Version 5.1.2 Reference Guide,” Aerosoft, Inc., Blacksburg, VA, 2014.
- [90] Liou, M. and Steffen, C., “A New Flux Splitting Scheme,” *Journal of Computational Physics*, Vol. 107, No. 1, 1993, pp. 23–29.
- [91] Roe, P., “Approximate Riemann Solvers, Parameter Vectors, and Difference Schemes,” *Journal of Computational Physics*, Vol. 43, 1981, pp. 357–372.
- [92] Knight, D., *Elements of Numerical Methods for Compressible Flows*, Cambridge University Press, New York, 2006.
- [93] Wright, M., Bose, D., and Candler, G., “A Data-Parallel Line Relaxation Model for the Navier-Stokes Equations,” *AIAA Journal*, Vol. 36, No. 9, 1998, pp. 1603–1609.
- [94] Withington, J., Yang, V., and Shuen, J., “A Time-Accurate Implicit Method for Chemically Reacting Flows at All Mach Numbers,” AIAA Paper 1991-581, American Institute of Aeronautics and Astronautics, January 1991.
- [95] Hoffmann, K. and Chiang, S., *Computational Fluid Dynamics-Volume I*, Engineering Education System; 4th edition, Wichita, 2004.
- [96] MacLean, M., Holden, M., and Dufrene, A., “Comparison between CFD and Measurements for Real-Gas Effects on Laminar Shock Wave Boundary Layer Interaction, I,” Oral Presentation, AIAA Aviation 2014, Atlanta, GA, 2014.

- [97] MacLean, M., Holden, M., and Dufrene, A., "Comparison between CFD and Measurements for Real-Gas Effects on Laminar Shock Wave Boundary Layer Interaction, II," Oral Presentation, AIAA Aviation 2014, Atlanta, GA, 2014.
- [98] MacLean, M., Private Communication, 22 November 2015.
- [99] Dufrene, A., MacLean, M., Parker, R., Wadhams, T., Mundy, E., and Holden, M., "Characterization of the New LENS Expansion Tunnel Facility," AIAA Paper 2010-1564, American Institute of Aeronautics and Astronautics, January 2010.
- [100] Dufrene, A., MacLean, M., Parker, R., and Holden, M., "Experimental Characterization of the LENS Expansion Tunnel Facility including Blunt Body Surface Heating," AIAA Paper 2011-626, American Institute of Aeronautics and Astronautics, January 2011.
- [101] Youssefi, M. R. and Knight, D., "Assessment of CFD Capability for Hypersonic Shock Wave Laminar Boundary Layer Interactions," *Aerospace*, Vol. 4, No. 2, April 2017.
- [102] Knight, D. and Kianvashrad, N., "Prediction of Aerothermodynamic Loading in Hypersonic Shock Wave Laminar Boundary Layer Interaction," Tech. Rep. FP55-AERO2018-Knight, 3AF International Conference, March 2018.
- [103] Houwing, A., Nonaka, S., and Takayama, H. M. K., "Effects of Vibrational Relaxation on Bow Shock Standoff Distance for Nonequilibrium Flows," *AIAA Journal*, Vol. 38, No. 9, August 2000, pp. 1760–1763.
- [104] "Calspan Hypersonic Shock Tunnel, Description and Capabilities Brochure," 1975.
- [105] Candler, G. and Nompelis, I., "CFD Validation for Hypersonic Flight - Real Gas Flows," AIAA Paper 2002-434, American Institute of Aeronautics and Astronautics, January 2002.
- [106] Gaitonde, D. and Shang, J., "The Performance of Flux-Split Algorithms in High-Speed Viscous Flows," AIAA Paper 1992-186, American Institute of Aeronautics and Astronautics, January 1992.
- [107] Fay, J. and Riddell, F., "Theory of Stagnation Point Heat Transfer in Dissociated Air," *Journal of the Aerospace Sciences*, Vol. 25, No. 2, 1958, pp. 73–85.
- [108] Kroll, N., Gaitonde, D., and Aftosmis, M., "A Systematic Comparative Study of Several High Resolution Schemes for Complex Problems in High Speed Flows," AIAA Paper 1991-636, American Institute of Aeronautics and Astronautics, January 1991.
- [109] Tennekes, H. and Lumley, J., *A First Course in Turbulence*, The MIT Press, Cambridge, Massachusetts, 1983.
- [110] Lau, K.-M. and Weng, H., "Climate Signal Detection Using Wavelet Transform: How to Make a Time Series Sing," *Bulletin of the American Meteorological Society*, Vol. 76, No. 12, December 1995, pp. 2391–2402.
- [111] Dillon, J., Trimpi, R., and Schultz, A., "The NASA-Langley 20-Inch Supersonic Wind Tunnel," AIAA Paper 86-0765, American Institute of Aeronautics and Astronautics, March 1986.

- [112] Kianvashrad, N. and Knight, D., “Simulation of Hypersonic Shock-Wave-Laminar-Boundary-Layer Interaction on Hollow Cylinder Flare,” *AIAA Journal*, Vol. 55, No. 1, January 2017, pp. 322–326.
- [113] Yan, H., Adelgren, R., Boguszko, M., Elliott, G., and Knight, D., “Laser Energy Deposition in Quiescent Air,” *AIAA Journal*, Vol. 41, No. 10, 2003, pp. 1988–1995.